

NASA Contractor Report 4716

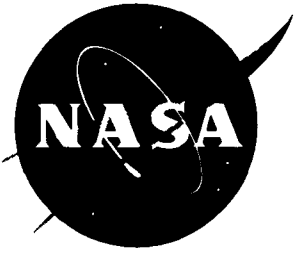
1N-18
67537
180 p

Vulnerability of Space Station *Freedom* Modules: A Study of the Effects of Module Perforation on Crew and Equipment

J. Serrano, D. Liquornik, and W.P. Schonberg

Contract NCC8-28
Prepared for Marshall Space Flight Center

February 1996



Vulnerability of Space Station *Freedom* Modules: A Study of the Effects of Module Perforation on Crew and Equipment

J. Serrano, D. Liquornik, and W.P. Schonberg
University of Alabama in Huntsville
Huntsville, Alabama 35899

PREFACE

The effort described in this report was supported by the Structural Development Branch (ED52) and the Laboratory Support Branch (EH15) at the NASA/Marshall Space Flight Center in Huntsville, Alabama. The Contracting Officer's Technical Representatives for this program were Mr. Richard Dotson (ED51) and Dr. Joel Williamsen (ED52). This report consists of two parts. The first describes the experimental effort, which was performed at the Aerophysics Research Center of the University of Alabama in Huntsville in Huntsville, Alabama. The second describes the development of an analytical model for the various internal effects that accompany the perforation of a habitable module by an orbital debris particle. Each part was originally issued as a separate volume by the performing organization (the UAH Aerophysics Research Center and the UAH Civil & Environmental Engineering Department, respectively).

ACKNOWLEDGMENTS

The authors would like to acknowledge the assistance of J.D. Johnson at the Los Alamos National Laboratory in obtaining the equation-of-state for air. The authors are also grateful to Mr. Werner Dahm (NASA/Marshall Space Flight Center) for his many helpful comments during the course of this effort. The authors would like to thank Dr. Joel E. Williamsen of the NASA/MSFC Structural Development Branch (ED52) for his guidance and many valuable suggestions during the course of this project. Finally, the authors would like to acknowledge the assistance of Mssrs. Daniel Gala and Richard Hayami (UAH Aerophysics Research Center), and Quint Davenport (UAH Mechanical and Aerospace Engineering Department) during the course of this study.

TABLE OF CONTENTS

PREFACE	iii
ACKNOWLEDGMENTS	v
 <i>PART ONE – EXPERIMENTAL PROGRAM</i>	
1.0 INTRODUCTION	1
2.0 REPORT FORMAT	1
3.0 EXPERIMENTAL SET-UP	1
3.1 Facility	1
3.2 Target Chamber	2
3.3 Test Conditions	2
3.4 Instrumentation Set-up	2
3.5 Data Acquisition	7
3.6 Spacecraft Shield Targets	7
4.0 TEST RESULTS AND OBSERVATIONS	9
4.1 Test Results	9
4.2 Environment Effects on Crew	16
5.0 CONCLUSIONS	18
6.0 REFERENCES	18

PART TWO – ANALYTICAL MODELING OF INTERNAL EFFECTS

1.0 INTRODUCTORY COMMENTS	19
2.0 INITIAL IMPACT SHOCK LOADING AND RELEASE MODELING	23
2.1 Shock Loading Due to High Speed Impact	23
2.2 Shock Release Using the Mie-Gruneisen Equation-of-State	26
3.0 MODELING OF PRIMARY AND SECONDARY DEBRIS CLOUDS	29
3.1 Primary Debris Cloud Mass	29
3.2 Primary Debris Cloud Characteristic Velocities	29
3.2.1 Conservation of Momentum and Energy	30
3.2.2 Elementary Shock Physics	32
3.2.3 Effective Applied Pressure Wall Velocity	33
3.2.4 Observations and Comments	34
3.3 Secondary Debris Cloud Mass	35
3.3.1 The Mass Factor κ_1	37
3.4 Secondary Debris Cloud Characteristic Velocities	37
3.4.1 Axial Velocities	39
3.4.2 Comments on the Axial Velocity Calculations	41
3.4.3 Expansion Velocities	43
3.5 Debris Cloud Spread Angles	46
4.0 PRESSURE WALL IMPACT SHOCK LOADING AND RELEASE MODELING	48
5.0 MODELING OF INDIVIDUAL INTERNAL EFFECTS: SHOCK WAVE PASSAGE	50
5.1 Pressure Wall Impulsive Loading Effect	50
5.2 Pressure Wall Impact Loading Effect	51
5.2.1 Impedance Matching Technique	51
5.3 Shock Wave Induced Pressure and Temperature Changes	54
5.4 Attenuation of Shock Wave Induced Pressures and Temperatures	56
5.4.1 Pressure and Temperature Values at a Specified Location	59

6.0 MODELING OF INDIVIDUAL INTERNAL EFFECTS: INTERNAL DEBRIS CLOUD PASSAGE	63
6.1 Debris Cloud Induced Pressure and Temperature Changes	63
6.2 Attenuation of Debris Cloud Induced Pressures	65
6.2.1 Pressure Wall Hole-Out Mass	67
6.2.2 Onset of Pressure and Temperature Attenuation	69
6.2.3 Pressure and Temperature Values at a Specified Location	71
6.2.4 Definition of Shock Wave Position	72
7.0 SUPERPOSITION OF INDIVIDUAL INTERNAL EFFECTS	82
7.1 Energy Partitioning	82
7.2 Initial Shock Wave Pressures and Temperatures	86
7.2.1 Peak Pressures and Temperatures	86
7.2.2 Attenuated Pressures and Temperatures	87
7.2.3 Pressure and Temperature Values at a Specified Location	88
7.3 Internal Debris Cloud Pressures and Temperatures	88
7.3.1 Peak Pressures and Temperatures	88
7.3.2 Attenuated Pressures and Temperatures	89
7.3.3 Pressure and Temperature Values at a Specified Location	90
7.4 Cumulative Pressures and Temperatures at a Specified Location	91
8.0 COMPARISON WITH EXPERIMENTAL RESULTS	92
8.1 Test Configurations and Impact Parameters	92
8.2 Model Parameter Values	93
8.3 Comparison of Model Predictions with Experimental Results	99
8.4 Internal Effects Model Modifications	102
8.4.1 Model Modifications	102
8.4.2 Empirical Constant Adjustments	103
8.5 Comparison of Modified Model Predictions with Experimental Results	104
9.0 SUMMARY AND RECOMMENDATIONS	107
9.1 Summary	107
9.2 Recommendations	108

10.0 REFERENCES	111
11.0 APPENDICES	113
APPENDIX A -- TEST DATA	
APPENDIX B -- FLASH X-RAY PHOTOGRAPHS	
APPENDIX C -- INTEFF.FOR	
APPENDIX D -- SAMPLE INPUT FILE	
APPENDIX E -- SAMPLE OUTPUT FILE	

PART ONE -- EXPERIMENTAL PROGRAM

1. INTRODUCTION

Studies by Kessler¹ and others indicate that the likelihood of orbital debris penetration increases with increased spacecraft size and time of exposure in low Earth orbit. With this increased likelihood of debris impact comes a responsibility on the part of the manned spacecraft designer to (1) provide effective shielding to prevent the likelihood of penetration to the maximum practical extent, and (2) to reduce the hazardous effects on the crew should a penetration occur. The latter responsibility requires detailed information on the magnitude of the atmospheric hazard associated with orbital debris penetration and the effects of such factors as internal equipment and crew proximity on increasing the likelihood of their survival following a penetration.

The primary objective of this study was to establish through experimentation the level of spacecraft cabin over pressure, light, and temperature that accompanies penetration of typical orbital debris shielding as a function of distance from the source of penetration. A secondary objective was to examine the effectiveness of internal equipment and/or spall blankets in reducing the levels of these hazardous effects on the crew. The data from these experiments will be used in future research efforts to establish a model for the level of hazardous internal effects as a function of orbital debris impact parameters (debris diameter and velocity), spacecraft shield design, and crew distance from the point of penetration. The availability of such a model for predicting the magnitude of atmospheric hazard levels following the remote likelihood of a penetration allows the spacecraft designer to adapt his design to improve the survivability of spacecraft occupants from these hazards should they occur.

2.0 REPORT FORMAT

This report consists of the main body which describes the experiments and summarizes the results obtained plus Appendices which presents all of the processed data from each of the tests performed on this program. Appendix A includes the Target Plate photographs, the test chamber temperature profiles, the test chamber pressure profiles, and the UV and visible band radiometric data. Appendix B includes the available flash X-Ray photographs for the test series.

As mentioned in the preface, this document comprises Volume I, Experimental Program portion of the Final Report "Vulnerability of Space Station Freedom Modules, A Study of the Effects of Perforation on Crew and Equipment" for this contract. Volume II, Analytical Modeling of Internal Debris Cloud Effects of the Final Report "Vulnerability of Space Station Freedom Modules, A Study of the Effects of Perforation on Crew and Equipment" by Dr. Wm. P. Schonberg is available under separate cover.

3.0. EXPERIMENTAL SETUP

3.1 FACILITY

In order to meet these objectives, the Marshall Space Flight Center (MSFC) and the University of Alabama in Huntsville (UAH) conducted a series of hypervelocity impact tests at the UAH Aerophysics Research Center (ARC), located on Redstone Arsenal near Huntsville, Alabama. The ARC features a variety of light gas gun systems capable of accelerating projectiles to speeds in excess of 7.5 km/sec. The particular gun chosen for this test series features a launch tube capable of firing particles up to 3.0 cm in size at near 7 km/s and a target chamber approximately 2 meters in diameter and 4 meters in length.

3.2 TARGET CHAMBER

Figure 1 shows a photograph of the external view of the target chamber looking at the chamber from the North West side. The pulser for the flash X-ray and the 17 GHz Doppler radar can be seen in the foreground. Figure 2 shows a photograph of the internal arrangement of the target chamber for Test # 1 without the equipment Rack Simulant and Test #5 with the equipment rack simulant. Note that the internal surfaces of the chamber were lined with 1 cm polyurethane foam panels. These panels reduced the "noise" in the over pressure readings considerably when compared to several checkout tests without the foam liners, and so were utilized through the tests reported here. Note also the presence of a square fiberboard witness panel hung from the chamber ceiling approximately 2.6 meters downrange of the point of penetration in order to characterize the mass characteristics within the debris cloud from the penetrating particle and shield target assembly.

3.3 TEST CONDITIONS

Prior to the test, the target chamber was carefully sealed with a ballistic test article simulating a "typical" orbital debris shield in order to maintain an approximate 1 atm internal (absolute) pressure as the test chamber upstream of the impact tank was pumped down to a near vacuum condition. The bumper shield plate and enhancer materials were held on frames in the two feet diameter tube which served as a mount for the bumper shields and the hull plate. The hull plate provided the seal for the test chamber at ambient atmosphere from the vacuum on the gun side of the hull plate. The range chamber uprange of the hull plate was connected to a 8' diameter by ~200' long chamber which was pumped down to act as a large vacuum dump, thereby simulating the infinite vacuum of space as the hull plate was perforated. In this fashion, the penetrating projectile simulates the passage of a space debris particle from the vacuum of space into a crew cabin. All hypervelocity impact tests within this series were conducted using 7075 Al spheres moving at approximately 6.5 km/sec.

3.4 INSTRUMENTATION SET UP

Figures 4 and 5 show cross-sectional top views of the test chamber for the cases without and with the simulated internal equipment cabinets respectively. Pressure and temperature sensors were paired in six positions within the target tank, three pairs along each side. For most tests, pressure and temperature sensors 1E and 1W were located on the east and west walls (respectively) of the tank at an approximate "line of sight" distance of 62 cm from the pressure bearing surface (pressure wall) of the shield target. Sensors 2E and 2W were approximately 136 cm from the pressure wall of the shield target; sensors 3E and 3W were approximately 253 cm from the target pressure wall. Notable exceptions to these general sensor locations included (1) the position of temperature sensor 3W, which was lengthened subsequent to Test 1 to measure the temperature directly along the centerline of the test chamber, and (2) the position of temperature and pressure sensors 1W in Tests 10 and 13, which were also extended to measure the over pressure inside an equipment rack mockup very near the point of penetration (see Figure 2). A low speed video camera (30 frames/sec) was trained at the target plate through a Plexiglas window and mirror arrangement at the roof of the target chamber.

The pressure sensor used was a Dytran Model 2200V1, with a frequency response of 500 kHz and capable of measuring a peak output level of 100 psi (690 kPa) with a resolution of approximately 0.01 psi (0.07 kPa). The temperature sensor used was an Omega Type E thermocouple with a frequency response of 2 msec and capable of measuring a peak output level of 600 degrees C with a resolution of approximately 0.1 degrees C.

Three UDT Model UV50 radiometers that were used to measure the magnitude of (1) visible light when directly facing the penetration point, (2) ultraviolet (UV) light when directly facing the penetration point, and (3) visible light when facing 90 degrees away from the penetration point. The visible light detector bandwidth was set at 400 to 750 nm and the UV detector bandwidth was set at 250 to 360 nm. The sensors were located from 155 to 190 cm from the point of penetration.

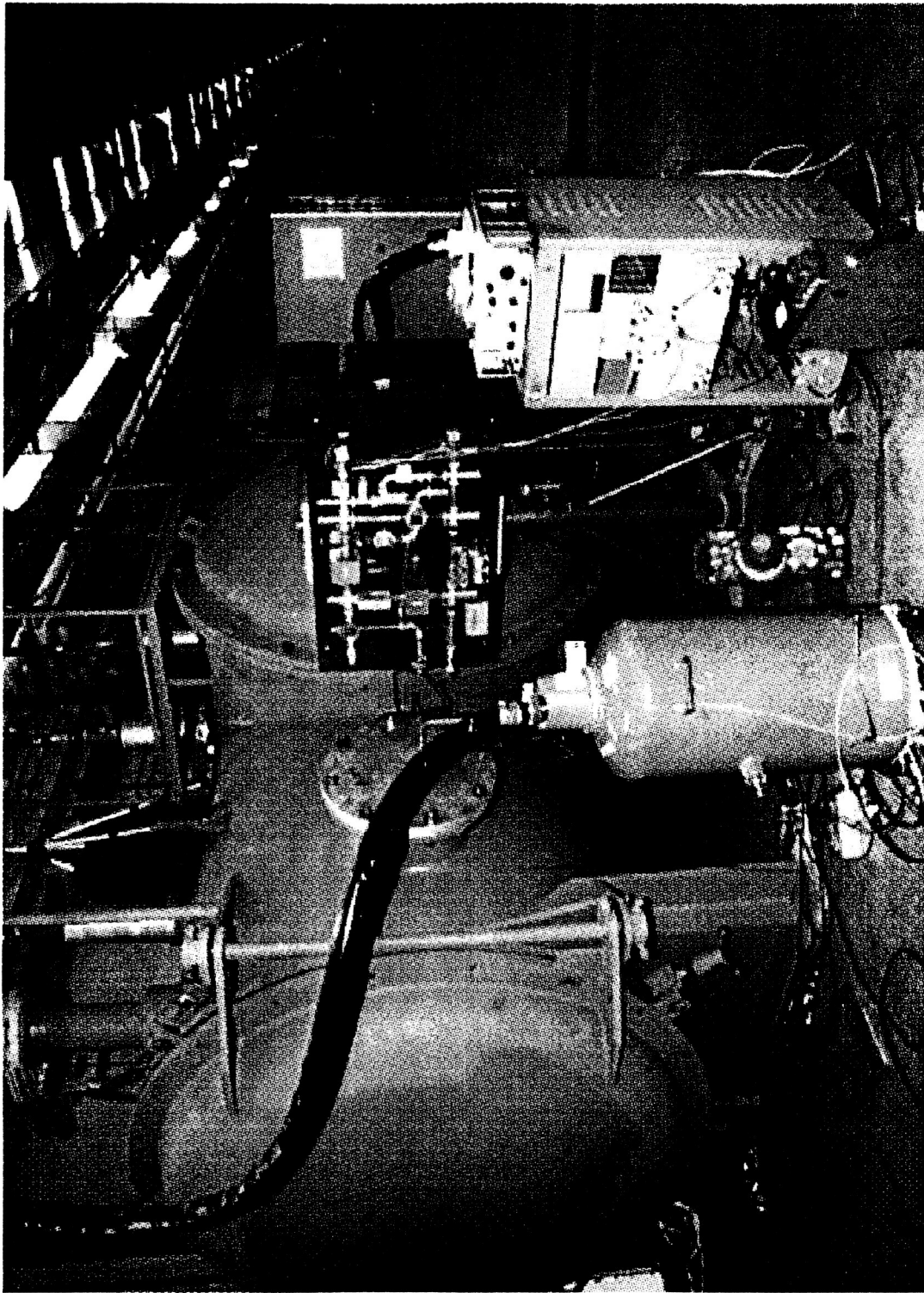


Figure 1 Photograph of the UAH Target Chamber for the 108 mm Gun System used in this Test Series

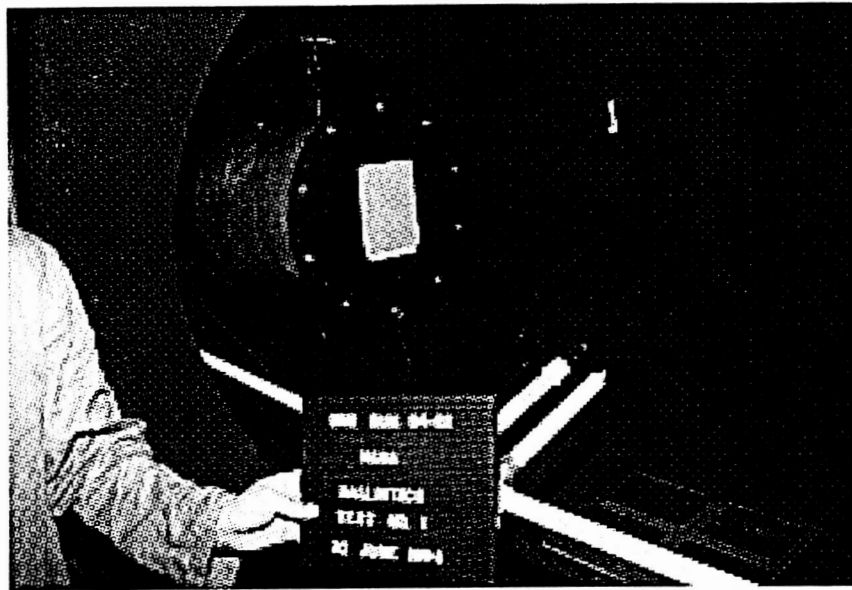


Figure 2 View of Impact Chamber Interior Without Equipment Rack Simulant

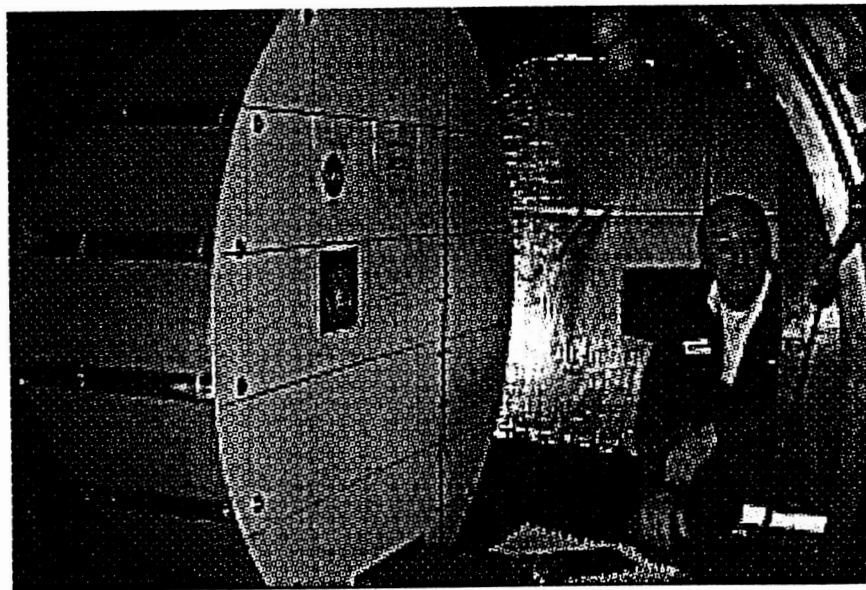


Figure 3 View of Impact Chamber Interior With Equipment Rack Simulant

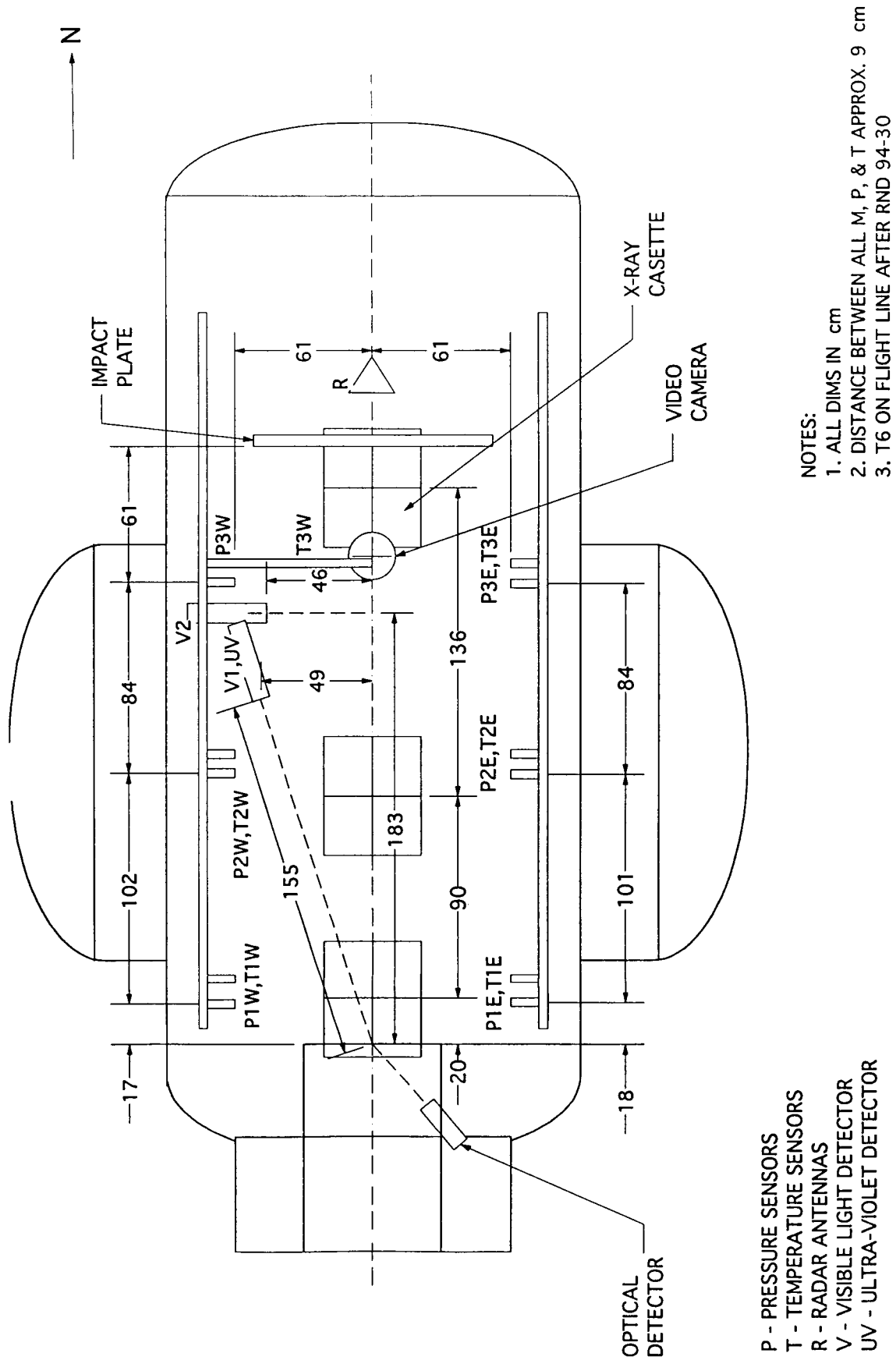


Figure 4 Cross Sectional Top Down View of Test Chamber Without Equipment Rack Simulant

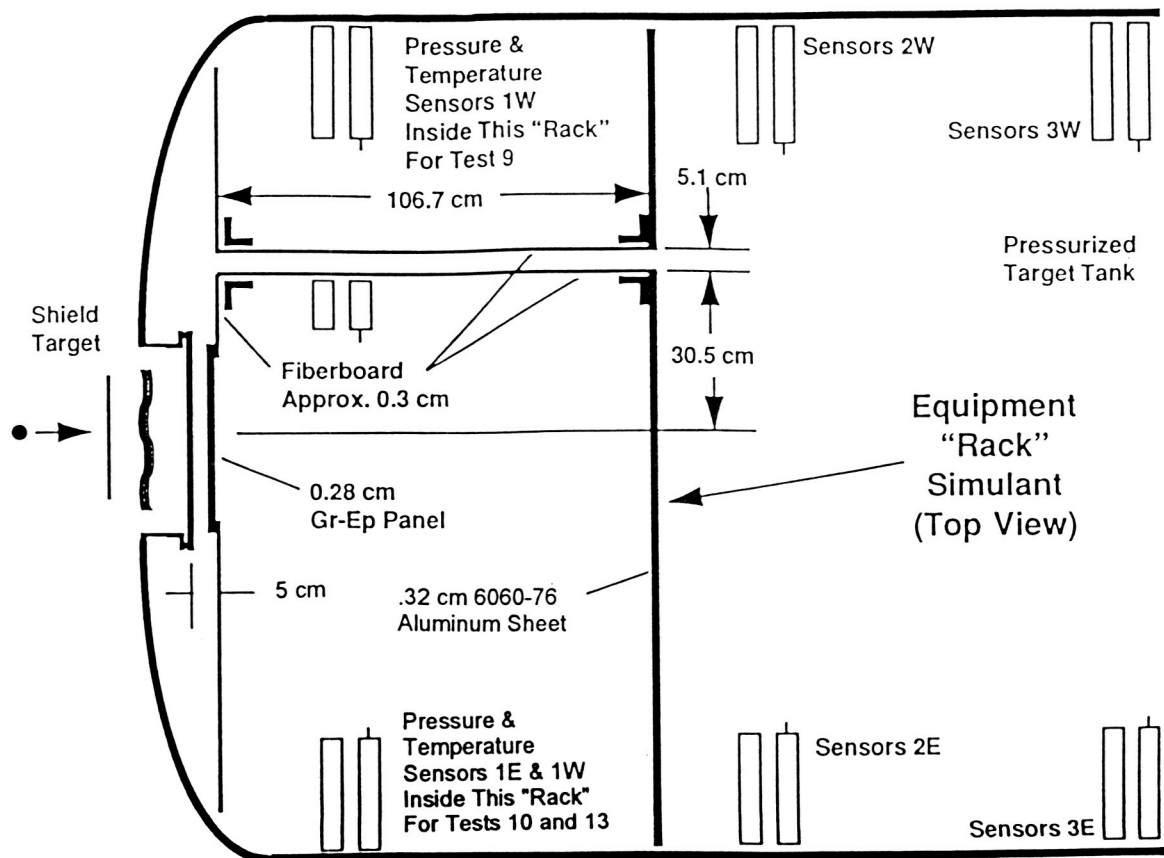


Figure 5 Cross Sectional Top Down View of Test Chamber With Equipment Rack Simulant

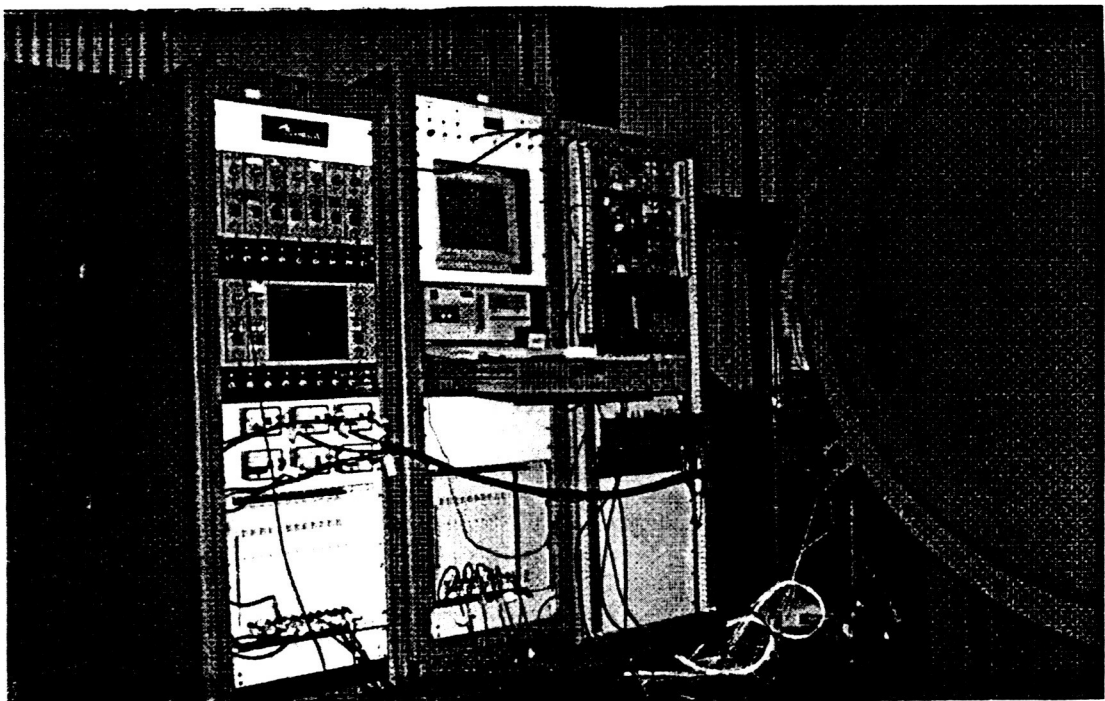


Figure 6 Photograph of Digital Acquisition System

In order to obtain a measure of the residual energy in the debris cloud from the penetration of the target plate, a 17 GHz Doppler radar was installed to view the motion of the witness plate during the tests. This data is presented in Figure 13.

The deflection of the pressure hull plate was measured using a Doppler radar operating at 17 GHz in an interferometric mode as the uprange side was pumped down to < 0.01 Torr with atmospheric pressure in the test chamber. This plate deflection data is shown in A39 of Appendix A.

Flash X-rays were obtained on most tests. The available flash X-ray data are presented in Appendix B.

3.5 DATA ACQUISITION

Data acquired by the various sensors were recorded on a Nicolet Digital Data Acquisition system which has a maximum sampling rate of 10 MSamples/s, 12 bit resolution and 1 Mbyte memory per channel. The actual sampling rate was adjusted depending on the expected data recording time. The instrumentation rack which contains the data acquisition system is shown in Figure 6.

3.6 SPACECRAFT SHIELD TARGETS

Figure 7 shows a sketch of the three types of spacecraft shield targets that were featured in this test series. Shield target 1 is essentially a simple two-wall bumper shield, with the second wall acting as the pressure bearing surface of the spacecraft. The ballistic limit (size of aluminum sphere that will marginally penetrate this type of target) for shield target 1 is approximately 1.0 cm (at 6.5 km/sec). Shield target 2 is an enhanced orbital debris shield that features intermediate layers of Nextel, Kevlar, and graphite between the outer bumper and rear pressure wall. These layers increase the ballistic limit of this shield package to approximately 1.35 cm (at 6.5 km/sec). Shield target 3 is a simple single pressure wall with no bumpers. The ballistic limit of this target is very low, requiring only a 0.1 cm spherical aluminum particle to penetrate this shield target.

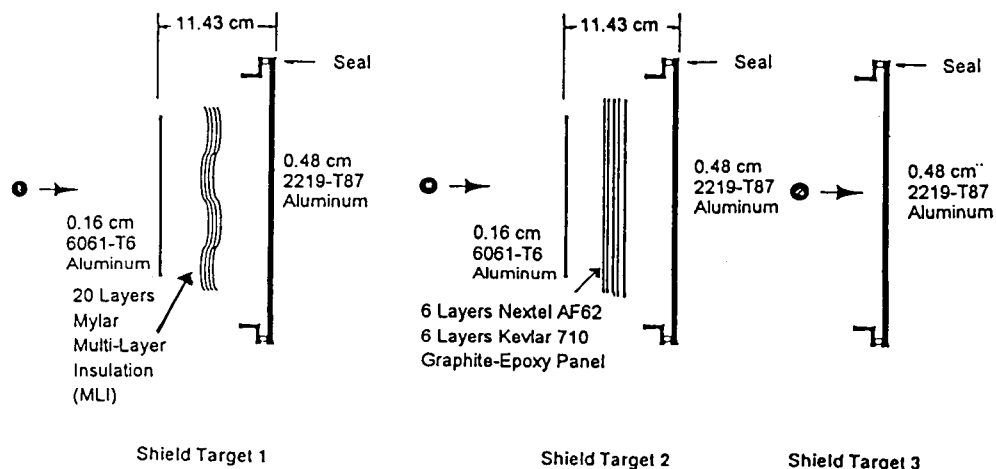


Figure 7 Sketch of Three Space Craft Shield Targets

Figure 8 shows photographs of the internal arrangement of the target chamber for Test 5. Note that the internal surfaces of the chamber were lined with 1 cm thick polyurethane acoustic attenuating foam panels. These panels reduced the “noise” in the over pressure readings considerably compared to several checkout shots without the foam liners, and so were utilized through the tests reported here. Note also the presence of a square fiberboard witness plate hung from the chamber ceiling approximately 2.6 meters downrange the point of penetration in order to determine the mass characteristics within the debris cloud from the penetrating particle and shield assembly.

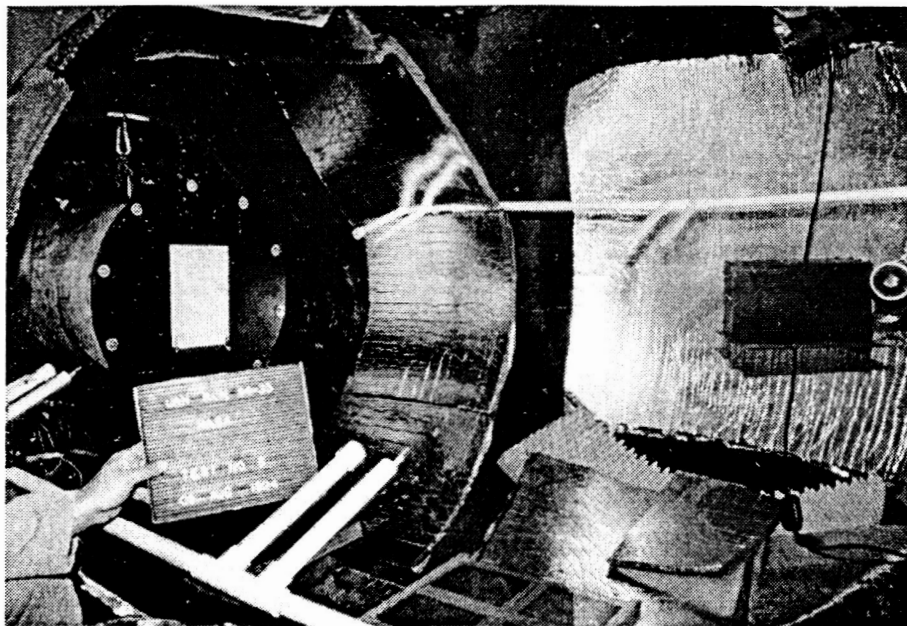


Figure 8a Photograph of Target Chamber for Test 5 - View Towards Shield Target

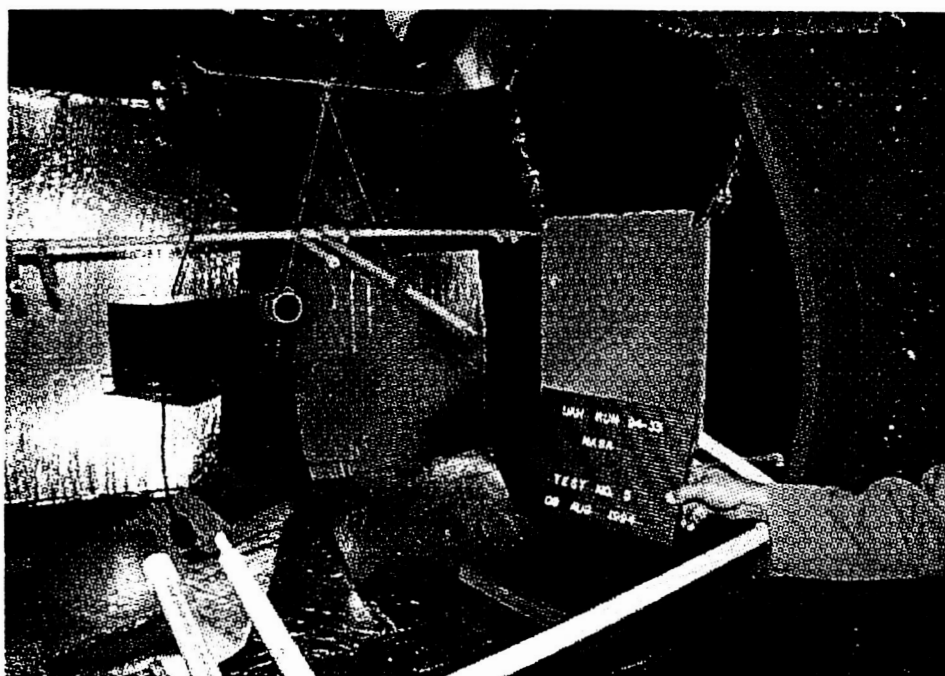


Figure 8b Photograph of Target Chamber for Test 5 - View Away from Shield Target (Downrange)

In several tests, a mockup was used to simulate an empty interior spacecraft equipment rack. The objective of these tests was to observe how interior equipment could reduce the hazardous levels of over pressure, light, and temperature on the crew. Figure 4 shows that the "back" wall of this rack (the surface nearest the penetration) consisted of a 0.28 cm graphite epoxy panel, similar in construction to the equipment rack used in the U.S. Lab module of Space Station Freedom. The "front" wall of the rack (nearest a prospective crew member) was 0.32 cm 6061-T6 Aluminum sheet, similar to the material used as a cover panel over Space Station Freedom equipment or experiment racks. In a variation of the internal equipment test, a 45 cm square Kevlar spall blanket (0.4 gm/cm^2) was placed on the inboard surface of the pressure wall with adhesive around its outer circumference to test for possible reduction of atmospheric hazards should the blanket be penetrated.

4.0 TEST RESULTS AND OBSERVATIONS

4.1 TEST RESULTS

Tables 1, 2, and 3 show a summary of test conditions and results obtained from these experiments, including the shield targets used in each test. Test parameters were directed primarily towards characterizing the hazards for the "baseline" two-wall shield (target 1). Another consideration was an attempt to compare the levels of interior hazards for differing targets with similar levels of ballistic energy "overmatch". For example, in Test 1 the target was hit by a particle that had approximately $22,000 \text{ kg-m}^2/\text{sec}^2$ of kinetic energy over and above the kinetic energy required to penetrate the target ($28,000 \text{ kg-m}^2/\text{sec}^2$). Tests 5 and 8 had a similar amount of ballistic energy overmatch-- $37,000$ and $21,000 \text{ kg-m}^2/\text{sec}^2$ respectively (by contrast, Tests 3 and 6 had a ballistic energy overmatch of approximately $70,000 \text{ kg-m}^2/\text{sec}^2$). By testing similar levels of ballistic overmatch within differing targets, it was hoped that a "simple" model of overpressure as a function of this parameter might be achievable.

Figures 9 and 10 show typical overpressure profiles for sensors 1 and 3. The test measurements for peak overpressure and pulse duration (for sensor 1) and peak overpressure (for sensors 2 and 3) are recorded in Table 1. Figures 11 and 12 show typical temperature profiles for sensors 1 and 3. The measurements shown in these figures (peak delta temperature, time to peak temperature, total product of temperature x duration under the curve) appear in Table 2.

In tests without internal equipment racks, the over pressure within the target chamber peaked at sensor position 1, was lower at sensor position 2, and lowest of all at sensor position 3 (farthest downstream). Over pressure is clearly decreasing with distance from the penetration event, similar to explosively-driven shocks in air (though perhaps not at the same rate). These over pressure peaks corresponded roughly in time to the passage of the fragments from the internal debris cloud associated with the penetration, which was traveling at peak velocities of approximately 1.0 km/sec . Observed asymmetries in this debris cloud could account for the variances recorded in over pressure between sensors E and W (opposite sides of the target chamber). The hole in the pressure wall was approximately 64 mm in diameter, and the amount of mass lost in the pressure wall was

Table 1. Over pressure Test Results

Test Number		1	1	1	2	3	1 +Blanket	1+ Rack	2+ Rack	2+ Rack
		1	3	6	5	8	11	10	9	13
Projectile Diameter		1.27 cm .500 in	1.59 cm .625 in	1.59 cm .625 in	1.59 cm .625 in	0.95 cm .375 in	1.27 cm .500 in	1.59 cm .625 in	1.59 cm .625 in	1.59 cm .625 in
Velocity (k/s)		6.70	6.42	6.50	6.58	6.64	6.46	6.63	6.21	6.52
Sensor 1E	Peak Over pressure	117 kPa 17 psi	141 kPa 20.5 psi	110 kPa 16.0 psi	234 kPa 34.0 psi	262 kPa 38.0 psi	38 kPa 5.5 psi	55 kPa 8.0 psi	-	145 kPa 21.0 psi
	Duration of Peak	0.35 ms	0.50 ms	0.45 ms	0.45 ms	0.35 ms	0.20 ms	0.10 ms	-	0.10 ms
Sensor 1W	Peak Over pressure	121 kPa 17.5 psi	148 kPa 21.5 psi	214 kPa 31.0 psi	276 kPa 40.0 psi	193 kPa 28.0 psi	-	97 kPa 14.0 psi	3 kPa * 0.4 psi	207 kPa 30.0 psi
	Duration of Peak	0.35 msec	0.50 msec	0.40 msec	0.40 msec	0.40 msec	-	0.10 msec	0.10 * msec	0.10 msec
Sensor 2E	Peak Over pressure	31 kPa 4.5 psi	117 kPa 17.0 psi	103 kPa 15.0 psi	69 kPa 10.0 psi	48 kPa 7.0 psi	-	9 kPa 1.3 psi	5 kPa 0.7 psi	10 kPa 1.4 psi
Sensor 2W	Peak Over pressure	41 kPa 6.0 psi	145 kPa 21.0 psi	97 kPa 14.0 psi	103 kPa 15.0 psi	45 kPa 6.5 psi	124 kPa 18.0 psi	9 kPa 1.3 kPa	3 kPa 0.5 psi	6kPa 0.9 psi
Sensor 3E	Peak Over pressure	21 kPa 3.0 psi	55 kPa 8.0 psi	83 kPa 12.0 psi	21 kPa 3.0 psi	7 kPa 1.0 psi	34 kPa 5.0 psi	9 kPa 1.3 psi	10 kPa 1.5 psi	8 kPa 1.2 psi
Sensor 3W	Peak Over pressure	17 kPa 2.5 psi	55 kPa 8.0 psi	48 kPa 7.0 psi	28 kPa 4.0 psi	7 kPa 1.0 psi	21 kPa 3.0 psi	9 kPa 1.3 psi	3 kPa 0.5 psi	4 kPa 0.6 psi

* Pressure sensor located in adjacent rack (see Figure 2)

Table 2. Temperature Test Results

Target		1	1	1	2	3	1 + Blanket	1 + Rack	2 + Rack	2 + Rack
Test Number		1	3	6	5	8	11	10	9	13
Projectile Diameter		1.27 cm .500 in	1.59 cm .625 in	1.59 cm .625 in	1.59 cm .625 in	0.95 cm .375 in	1.27 cm .500 in	1.59 cm .625 in	1.59 cm .625 in	1.59 cm .625 in
Velocity (km/s)		6.70	6.42	6.50	6.58	6.64	6.46	6.63	6.21	6.52
Sensor 1E	Peak delta temp. (deg C)	25	105	20	65	20	40	280+	--	--
	Time to peak temp. (msec)	15	10	20	15	10	20	400	--	--
	Temp x time (deg C - secs)	0.4	7.0	3.0	3.0	1.0	3.0	380.0	--	--
Sensor 1W	Peak delta temp. (deg C)	30	115	65	55	15	15	--	5 *	280+
	Time to peak temp. (msec)	20	15	25	20	10	20	--	20 *	1800
	Temp x time (deg C - secs)	0.5	4.5	3.5	4.5	0.9	1.0	--	5 *	330.0
Sensor 2E	Peak delta temp. (deg C)	25	140	50	35	15	75	15	0	5
	Time to peak temp. (msec)	20	10	90	20	12	70	20	--	20
	Temp x time (deg C - secs)	0.7	16.0	5.1	2.0	0.9	4.1	1.5	0	0.5
Sensor 2W	Peak delta temp. (deg C)	20	95	65	220	10	--	20	0	5
	Time to peak temp. (msec)	20	10	50	250	20	--	20	--	20
	Temp x time (deg C - secs)	0.6	11.3	4.5	23.0	0.5	--	4.0	0	0.5
Sensor 3E	Peak delta temp. (deg C)	45	--	280+	10	10	280+	--	0	5
	Time to peak temp. (msec)	1200	--	250	20	270	180	--	--	20
	Temp x time (deg C - secs)	46.3	--	185.0	1.1	9.0	122.0	--	0	0.5
Sensor 3W	Peak delta temp. (deg C)	45+	270	--	25	70	280+	5	10	15
	Time to peak temp. (msec)	300	300	--	20	200	200	1.5	3000	3000
	Temp x time (deg C - secs)	66.5+	131.5	--	1.5	45.0	155	6.0	3.0	4.5

Notes: - All temperatures reported to nearest 5 deg C. interval.
- All times reported to nearest 5 millisecond interval
* Sensors located in adjacent equipment rack (see Figure 3).

Table 3 Radiometric Results and Hole Characteristics

Target	1	1	1	2	3	1 + Blanket	1 + Rack	2+ Rack	2 + Rack
Test Number	1	3	6	5	8	11	10	9	13
Projectile Diameter	1.27 cm .500 in	1.59 cm .625 in	1.59 cm .625 in	1.59 cm .625 in	0.95 cm .375 in	1.27 cm .500 in	1.59 cm .625 in	1.59 cm .625 in	1.59 cm .625 in
Velocity (k/s)	6.70	6.42	6.50	6.58	6.64	6.46	6.63	6.21	6.52
Direct Visible Light (Watts per Steradian)	—	--	40,000	48,000	—	40,000	Lower *	Lower *	Lower *
Indirect Visible Light, 90 deg. from Direct (Watts per Steradian)	30	—	17	14	—	13	—	—	—
Direct Ultraviolet Light (Watts per Steradian)	26	58	—	—	--33	42	8	0.3	—
Effective Pressure Wall Hole Diameter	5.9 cm 2.3 in	6.1 cm 2.4 in	6.3 cm 2.5 in	12.2 cm 4.8 in	3.2 cm 1.3 in	6.1 cm 2.4 in	6.6 cm 2.6 in	8.1 cm 3.3 in	7.1 cm 2.8 in
Maximum Tip-to-tip Crack Length	15.3 cm 6.0 in	8.7 cm 3.4 in	14.2 cm 5.6 in	24.9 cm 9.8 in	No Crack	7.9 cm 3.1 in	9.7 cm 3.8 in	22.6 cm 8.9 in	25.1 cm 9.9 in
Mass Removed from Pressure Wall	37 g	39 g	42 g	—	12 g	42 g	52 g	6 g	7 g

* Radiometer data not available, but video tape indicates that direct light flash levels were severely reduced.

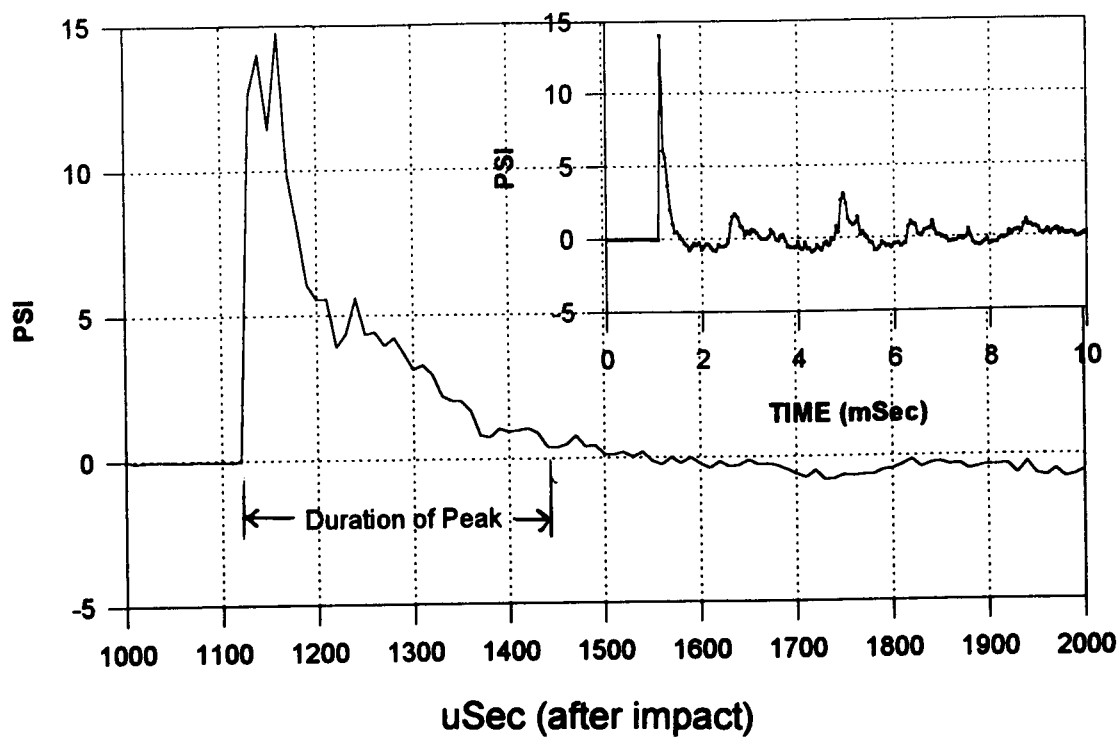


Figure 9 Typical Over Pressure Profiles from Sensor Position 1 (No Internal Equipment Simulant)

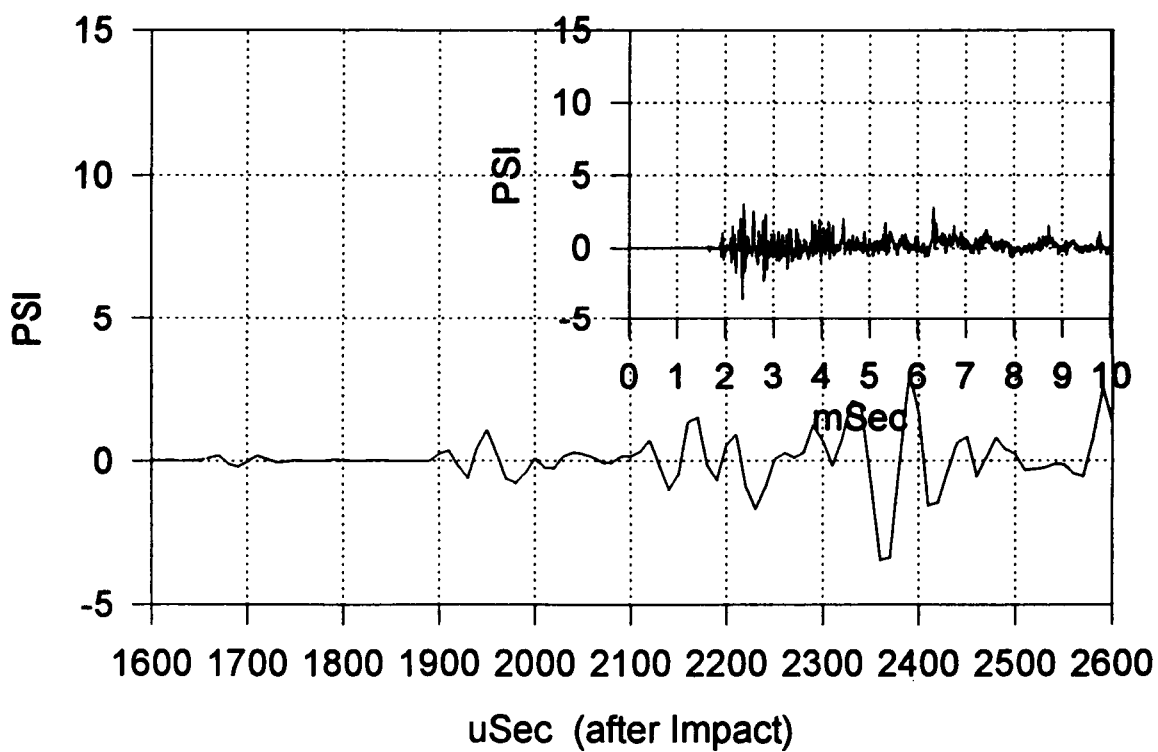


Figure 10 Typical Over Pressure Profiles from Sensor Position 3 (No Internal Equipment Simulant)

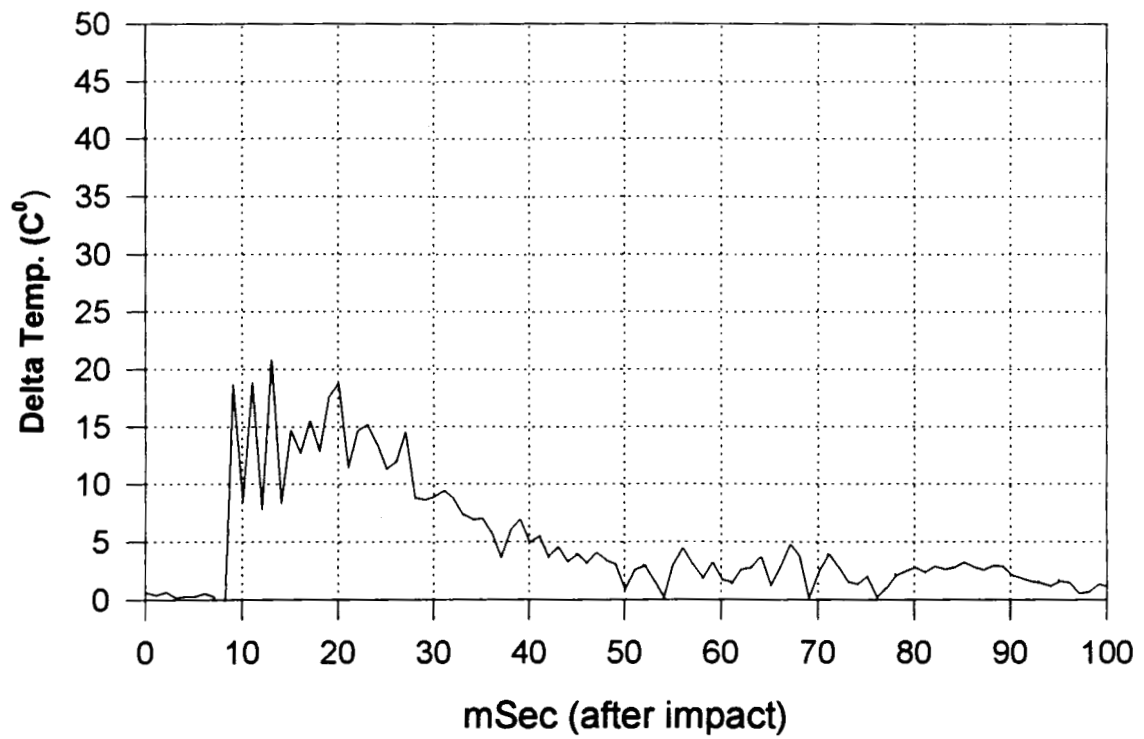


Figure 11 Typical Temperature Profiles from Sensor Position 1 (No Internal Equipment Simulant)

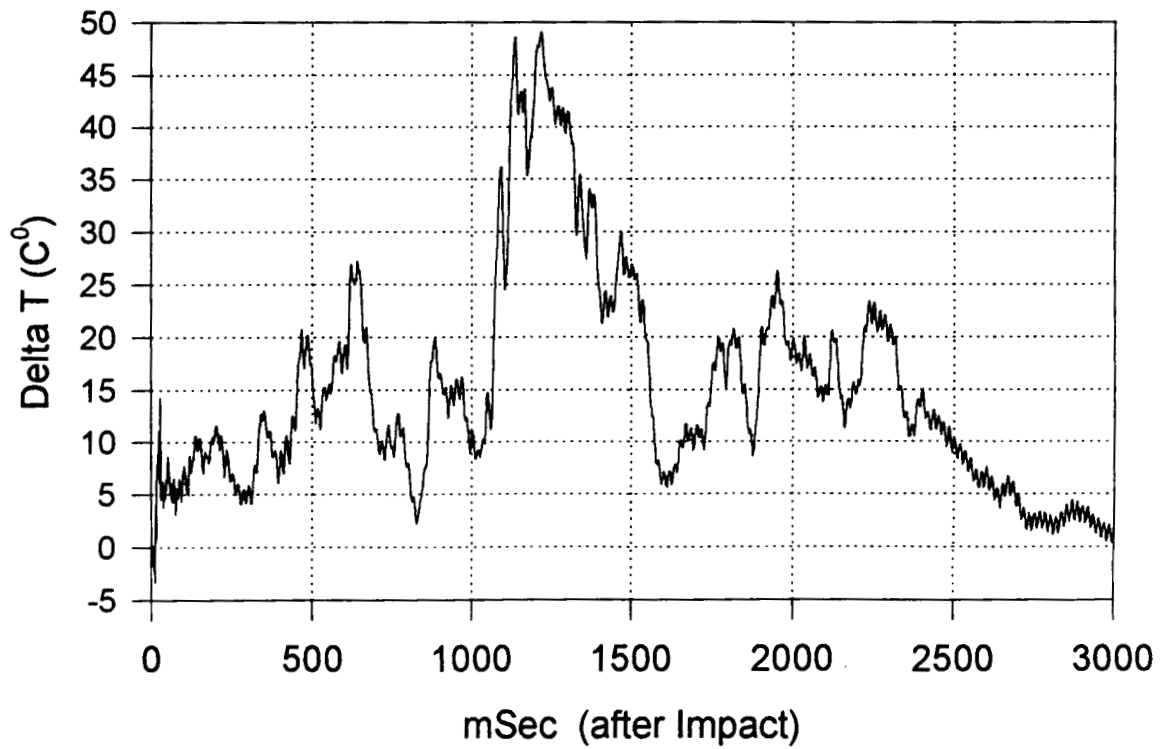


Figure 12 Typical Temperature Profiles from Sensor Position 3 (No Internal Equipment Simulant)

approximately 40 grams (also true for all tests of shield type 2). Despite this large amount of initial mass in the debris cloud, the one meter square fiberboard witness panel (weighing 2700 gms) located at 2.7 meters from the impact point was relatively undamaged, with one small (< 0.1 gram) particle imbedded within it. This lack of mass in the witness panel was curious, and consistent throughout the tests of all target types. This observation is supported by the Doppler radar measurement of the witness plate motion. The projectile mass was 3.0 gms and actual velocity was 6.69 km/s, resulting in projectile momentum of 2×10^6 gm-cm/s. The witness plate mass was 2702 gms and measured velocity was 20 cm/s, resulting in momentum of 67,550 gm-cm/s. The target momentum measurement presented in Figure 13 shows very low (~3.3% of the projectile momentum) momentum transfer to the witness plate.

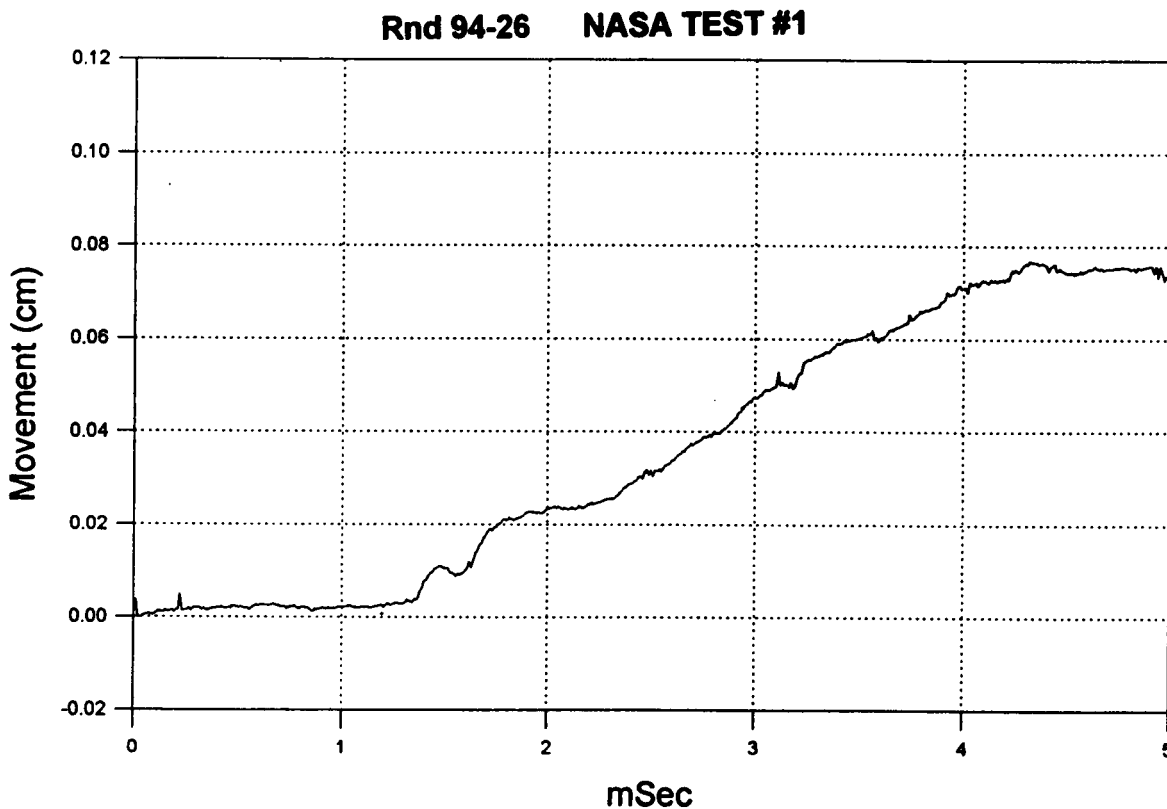


Figure 13 Doppler Radar data on Witness Plate Motion

One possible explanation for this apparent lack of post-test debris mass downrange might be that the debris cloud had a high radial component to its velocity vector--that is, the debris "spread out" quickly to the sides of the chamber and did not proceed directly along the centerline of the target chamber where the witness plate was located. It is difficult to discount this explanation without better flash X-ray characterization of the debris cloud and/or witness plates located along the inner walls of the test chamber; however, relatively little debris was noted to be imbedded within the polyurethane foam lining the chamber walls following the tests. A low speed (30 frames/second) video from these tests indicated a roughly even radial distribution of visible debris fragments particles emerging from the target into the 1 meter field of view of the camera (downrange). Another interesting possibility is that the fine debris cloud particles "burned up" as well slowed down

through drag deceleration in flying through the ambient air atmosphere of the target chamber at high velocity, and only rarely reached the witness plate. This explanation is attractive because of the highly exothermic reaction of hot aluminum particles with oxygen in the air atmosphere generating ~400 kilo-calories per mole of reacting aluminum. This is manifested by the over pressure, temperature, and light energy data witnessed in the tests. MSFC is sponsoring additional flash X-ray characterization tests to better typify the mass distribution within debris clouds traveling in a vacuum versus those traveling through a spacecraft interior atmosphere.

Another interesting observation concerning the effect of debris cloud mass on overpressure level may be drawn from comparing the low levels of overpressure at sensor position 3 in Test 5 (shield target 2) and Test 8 (shield target 3) to higher overpressure levels for sensor position 3 in Tests 1, 3 and 6 (shield target 1). Table 3 shows that even though the effective hole size is larger in shield type 2 due to its larger petals (see Figure 4), the amount of mass lost in the wall (and thus the amount of mass in the debris cloud) is an order of magnitude lower in shield type 2 than in shield type 1. The same is true for Test 8, where the mass missing from the pressure wall is very low compared to Tests 1, 3 and 6 (shield type 1). Thus, the lower overpressure downrange for Test 5 and for Test 8 (shield types 2 and 3 respectively) validates our reasoning that overpressure may be directly related to debris cloud mass.

Why the higher overpressure for these tests (5 and 8) at sensor position 1 compared to Tests 1, 3 and 5 (shield target 1)? One may theorize that these higher overpressures near the target are occurring for different reasons, unrelated to debris cloud mass. In Test 5, the formation and motion of large petals attached to the pressure wall may be causing a short range multiplying effect on the over pressure level near the wall (note the severely reduced overpressure at sensor position 2. In Test 6, the initial velocity of the debris cloud was much higher--approximately 6 km/sec (velocity of the impacting particle). This higher velocity led to a stronger air shock to be induced near the pressure wall, though its effects dissipated quickly.

4.2 ENVIRONMENT EFFECTS ON CREW

Overpressure levels of the magnitudes shown in Table 1 (ranging from 10 to 270 kPa) can have varying affects on incapacitating crew members (i.e., rendering crew incapable of rescuing themselves from the depressurizing spacecraft). While none of these overpressure levels appeared to be of sufficient duration to cause damage to lungs or other internal organs, they are of sufficiently high magnitude and duration to cause serious damage to the eardrum, inner ear, and cranium.²

Table 2 shows that for tests performed without simulated internal equipment racks, the peak air temperature at sensor position 2 reached generally higher levels than those at sensor position 1, with highest values recorded at sensor position 3. Air temperature peaks at sensor 1 generally occurred at around 20 milliseconds (ms) after pressure wall penetration; temperature peaks at sensor position 2 occurred at approximately 50 ms; they occurred at sensor position 3 at approximately 250 ms. These temperature and time readings indicate that the heated, shocked air from upstream (nearest the target) appeared to move downstream more slowly than the debris cloud (10 m/s, versus 1000 m/s for the debris cloud). As it moves downstream, this slower moving mass of heated air combines with additionally shocked air (downstream) to reach increasingly high overall air temperatures (280+ deg C in some cases). However, the highest observed product of air temperature x duration observed (185 deg C-secs for sensor position 3 in Test 6) did not exceed the air temperature levels that might reasonably be expected to induce second degree burns (1200 deg C-secs).³

Table 3 shows that the light levels for the tests without the internal equipment rack varied strongly with viewing angle. Visible light levels exceeded 40Kwatts per steradian (27.2 million candles) when directly viewing the target. UV light levels were much lower; the light flash phenomenon appears to be occurring primarily in the visible regime. This direct visible light level is roughly equivalent to that from the Sun as viewed from outside the Earth's atmosphere, and is certainly

sufficient to cause temporary blindness and other incapacitating effects⁴. However, the level of light as viewed from 90 degrees (i.e., from the side) is on the order of 20 watts per steradian (14,000 candles)--three orders of magnitude less than a direct view of the penetration event, and well within safe levels. Of course, the actual level of "off-axis" light flash observed will probably vary from case to case, depending on the reflectivity of the surrounding spacecraft cabin interior surfaces. Nevertheless, these results point to the dramatic relevance of viewing angle on observed light flash levels following a penetration.

In Test 11, a spall blanket consisting of 12 layers of Kevlar 120 was placed directly on the inboard (target chamber) side of the pressure wall using a two inch Velcro strip (one layer sewn to the spall blanket, the other glued to the pressure wall). The spall blanket in Test 11 was penetrated, creating a two inch hole in the Kevlar and separating the blanket from the wall. Remarkably, both layers of Velcro were still attached to the pressure wall; the joint failure occurred in the nylon thread used to attach the Kevlar blanket to the Velcro strip. Because the spall blanket was penetrated, the overpressure, temperature, and light levels were little effected, with one notable exception--little overpressure was measured at sensor position 1. This could have been caused by the considerable amount of aluminum debris from the pressure wall that was trapped in the spall blanket. With this mass trapped in the blanket, it was unavailable to cause large overpressure (shock waves) as it moved through the air near the target wall.

The presence of the internal equipment rack simulant in Tests 9, 10, and 13 had a large effect on reducing overpressure, temperature, and light flash levels at sensor positions 2 and 3 (outside the equipment rack). Of these tests, the only equipment rack completely penetrated was in Test 13, where a single 0.5 cm hole was induced in the outboard surface of the equipment rack. Once again, reducing the mass of the debris cloud within the target chamber (in this case, to nearly zero) has led to a reduced overpressure and temperature downrange. Note also that the magnitude of the overpressure inside the penetrated equipment rack is lower than that produced had there been no equipment rack (Test 5). In this case, even though penetrated, the rear wall of the equipment rack has reduced the velocity (and probably the mass) of the debris cloud impinging into the equipment rack, reducing the overpressure.

The close proximity of the pressure wall to the graphite epoxy panel on the rear face of the rack simulant (5 cm) also produced a limiting effect on effective hole size in the pressure wall for Tests 9 and 13 (shield target 2). Following these tests, the petals from the pressure wall were imbedded and actually curled around the interior circumference of the hole in the graphite panel (it was very difficult to separate the pressure wall from the rear surface of the equipment rack simulant following the tests). This same contact constrained the formation of petals in the pressure wall for Tests 9 and 13, forcing the effective hole diameters to be 30 percent smaller in these tests than in Test 5. This result is significant--it indicates that equipment racks located behind spacecraft shields similar to target 2 will hinder hole growth (and decompression losses) in spacecraft using these designs. However, repair of the pressure wall in these modules following penetration will be severely hindered by an impaired ability to separate the equipment racks from the pressure wall due to the petalling of the pressure wall around the hole in the back of the equipment rack.

Note however that the temperature at sensor position 1 (within the equipment rack) is considerably larger than in previous tests without the rack. By containing the debris cloud, the equipment rack has contained most of the heat transferred from the kinetic energy of the penetrating particle and debris cloud. Because the volume of the equipment rack is considerably smaller than the target tank, the product of total temperature x duration at sensor position 1 is approximately twice as high as measured for previous tests at sensor position 3 (without the equipment rack).

Unfortunately, light flash measurements from the visible radiometers are unavailable for tests with the equipment rack in place. However, the levels of direct UV light measured were considerably

lower than for tests without equipment racks in place, and the video taped results of these tests provide convincing evidence that far less light flash passed outside of the equipment rack than was seen in tests without the equipment rack.

5. CONCLUSIONS

This series of internal effects tests was successful in meeting its primary and secondary objectives: (1) to establish through experimentation the level of spacecraft cabin overpressure, light, and temperature that accompanies penetration of typical orbital debris shielding as a function of distance from the source of penetration, and (2) to examine the effectiveness of internal equipment in reducing the levels of these hazardous effects on the crew. In addition, the tests led to valuable observations on how debris cloud mass and velocity (and other penetration parameters) affect the levels of overpressure and temperature within a spacecraft atmosphere following orbital debris penetration. This information will be used by MSFC and UAH to formulate a first order relationship between penetration parameters (projectile energy, shielding type, hole size, etc.) and the levels of temperature and overpressure hazards resulting at a given distance from the penetration event.

6. REFERENCES

1. D. Kessler, "Orbital Debris Environment for Spacecraft Designed to Operate in Low Earth Orbit," NASA Technical Memorandum 100-471, 1989.
2. G. Weibull, "A Proposal for Blast Incapacitation Criteria Concerning Soldiers Inside Armoured Vehicles", Proceedings of the Ninth International Symposium on Ballistics, Shrivenham, U.K., May 1986.
3. B. Lawton and M. Laird, "Assessment of Skin Burns Behind Defeated Armour," Proceedings on the Fourteenth International Symposium on Ballistics, Quebec, Canada, September 1993.
4. A. R. Coronado, et al, "Space Station Integrated Wall Design and Penetration Damage Control", Final Report, NASA Contract NAS8-36426, July 1987.
5. Joel Williamsen & John Serrano, "Atmospheric Effects in Spacecraft Interiors Following Orbital Debris Penetration" presented in the Space Environmental, Legal and Safety Session of the Aero-Sense 95 Symposium sponsored by the Society of Photographic Instrumentation Engineers at Orlando FL on 17-18 April 1995. Published in SPIE Proceedings Volume 2483, Paper #2483-06

***PART TWO – ANALYTICAL MODELING OF INTERNAL
EFFECTS***

1.0 INTRODUCTORY COMMENTS

In this part of the report, a first-principles based model is developed to predict the overpressure and temperature effects of a perforating orbital debris particle impact within a pressurized habitable module. While the effects of a perforating debris particles on crew and equipment can be severe, only a limited number of empirical studies focusing on space vehicles have been performed to date (see, e.g. [1-3]). Traditionally, crew loss or incapacitation due to a perforating impact has primarily been of interest to military organizations and as such have focused on military vehicles and systems (see, e.g. [4]).

The module wall considered in this study is initially assumed to be a standard Whipple-type dual-wall system in which the outer wall protects the module and its inhabitants by disrupting impacting particles. The model is developed in a way such that it sequentially characterizes the phenomena comprising the impact event, including the initial impact, the creation and motion of a debris cloud within the dual-wall system, the impact of the debris cloud on the inner wall, the creation and motion of the debris cloud that enters the module interior, and the effects of the debris cloud within the module on module pressure and temperature levels. This is accomplished through the application of elementary shock physics and thermodynamic theory.

Consider the normal hypervelocity impact of a projectile on the outer wall or 'bumper' of a dual-wall system as shown in Figure 1. Upon impact, shock waves are set up in the projectile and bumper materials (Figure 1a). The pressures associated with these shocks typically exceed the strengths of the materials by several orders of magnitude. For example, in an 8 km/sec

aluminum-on-aluminum impact, the ratio of the impact pressure (116.5 GPa=1.15 MBar) to the strength of the material (310 MPa for aluminum 6061-T6) is approximately 375, or roughly 2.5 orders of magnitude. As the shock waves propagate, the projectile and bumper materials are heated adiabatically and non-isentropically. The release of the shock pressures occurs isentropically through the action of rarefaction waves that are generated as the shock waves interact with the free surfaces of the projectile and bumper (Figure 1b). This process leaves the materials in high energy states and can cause either or both to fragment, melt or vaporize, depending on the material properties, geometric parameters, and the velocity of impact.

In this manner, a debris cloud consisting of fragmented, melted, or vaporized projectile and bumper material (referred to from here on as the 'primary debris cloud') is created. This debris cloud travels towards, impacts, and perforates an inner bumper. For this study, this bumper consists of either a blanket of multi-layer thermal insulation (MLI) or a multi-material composite wall ('Type A' and 'Type B' inner bumpers, respectively). In addition to providing thermal insulation, the inner bumper also serves to trap some or most of the primary debris cloud particles. The debris cloud exiting the inner bumper is referred to from here on as the 'secondary debris cloud'.

Eventually, the secondary debris cloud impacts the inner or 'pressure' wall of the dual-wall system. The material in the secondary debris cloud and the portion of the pressure wall impacted by the secondary debris cloud are shocked and released in a manner similar to that of the initial impact on the bumper. In some instances this causes a perforation of the pressure wall. If this were to occur in an orbiting habitable module, then the debris cloud created as a result of the pressure wall perforation (hereafter referred to as the 'internal debris cloud') would be ejected

into the module interior. In addition to the motion of the internal debris cloud within the module, a shock wave would also be created in the module due to the presence of the module air.

The focus of the model developed herein is on the motion of the internal debris cloud within the module and its effects on pressure and temperature within a pressurized habitable module. Thus, the model to be developed will consider:

- 1) the shock loading and release of projectile and bumper material due to the initial impact on the bumper;
- 2) the creation and motion of the primary debris cloud created by the initial impact on the bumper;
- 3) the impact of the primary debris cloud on the inner bumper;
- 4) the composition and motion of the secondary debris cloud;
- 5) the shock loading and release of the secondary debris cloud and pressure wall material caused by the impact of the secondary debris cloud on the pressure wall;
- 6) the module internal pressure and temperature increase at a specific location due to the passage of the shock wave induced by the motion of the module pressure wall;
- 7) the module internal pressure and temperature increase at a specific location due to the passage of an internal debris cloud; and,
- 8) the module internal pressure and temperature increase at a specific location due to the combined presence of an internal debris cloud and a shock wave.

Section 2.0 presents the shock loading and release analysis that will be applied to the initial impact of the projectile on the bumper. The motion of the primary debris cloud is discussed in Section 3.0 with an emphasis on obtaining an appropriate velocity value to characterize the

forward motion of the primary debris cloud. This is a critical value because it is eventually used as input for the pressure wall shock loading and release analysis, the results of which are in turn used directly in the modeling of the module internal effects due to a perforation (i.e. the pressure and temperature increases). Thus, an incorrect primary debris cloud velocity value could have a disastrous effect on all subsequent calculations. Section 3.0 concludes with a discussion of the impact of the primary debris cloud on the inner bumper and the creation and motion of the secondary debris cloud. In Section 4.0, the shock loading and release analysis developed for the initial impact in Section 2.0 are applied to the impact of the secondary debris cloud on the pressure wall. Sections 5.0 and 6.0 present the modeling of the pressure and temperature increases due to shock wave motion and internal debris cloud passage, respectively. Section 7.0 presents the manner in which the individual effects models developed in Sections 5.0 and 6.0 are combined to give the cumulative effect of shock wave motion and internal debris cloud passage. Finally, Section 8.0 presents a comparison of the predictions of the internal effects model and experimental data. Modifications to the model that are required to bring its predictions in closer agreement with the experimental results are also presented and discussed.

2.0 INITIAL IMPACT SHOCK LOADING AND RELEASE MODELING

2.1 Shock Loading Due to High Speed Impact

In calculating the shock loading and subsequent release of the projectile and bumper materials, the shock waves are considered to be initially planar. This simplification allows one-dimensional relationships to be used for analyzing the creation and release of shock pressures. In this manner, the shock pressures, energies, etc., in the projectile and bumper materials are calculated using the three 1-D shock-jump conditions, a linear relationship between the shock wave velocity and particle velocity in each material, and continuity of pressure and velocity at the projectile/target interface.

Specifically, if we consider the 1-D impact of a projectile with velocity v_0 on a stationary target plate, conservation of mass, momentum, and energy across the shock fronts in the projectile and in the target yields

<u>Projectile</u>	<u>Target</u>	
$u_{sp}/V_{op} = (u_{sp} - u_{pp})/V_{Hp}$	$u_{st}/V_{ot} = (u_{st} - u_{pt})/V_{Ht}$	(1a,b)
$P_{Hp} = P_{op} + u_{sp}u_{pp}/V_{op}$	$P_{Ht} = P_{ot} + u_{st}u_{pt}/V_{ot}$	(2a,b)
$E_{Hp} = E_{op} + (P_{Hp} + P_{op})(V_{op} - V_{Hp})/2$	$E_{Ht} = E_{ot} + (P_{Ht} + P_{ot})(V_{ot} - V_{Ht})/2$	(3a,b)

where $V=1/\rho$ is specific volume, u_s and u_p are shock and particle velocity, respectively;

V_H, P_H, E_H and V_O, P_O, E_O are the density, pressure and energy states associated with the shocked and initial material states. In equations (1-3), the subscripts 'p', and 't' refer to projectile and target quantities, respectively. In the development of equations (1-3), the shock velocity in the projectile is taken relative to a 'stationary' projectile.

The linear shock velocity-particle velocity relationships for the projectile and bumper materials are taken to be in the form

$$u_s = c_0 + k u_p \quad (4)$$

where $c_0 = \sqrt{KV_0}$ is the material bulk speed of sound, $K = E/3(1-2\nu)$ is the adiabatic bulk modulus, E and ν are Young's modulus and Poisson's ratio, respectively, and k is an empirically-derived constant. The general equations (1-4) are applied to the initial impact on the bumper of a dual-wall system in the following manner. Upon impact, pressure equilibrium at the projectile/target interface implies that

$$P_{Hp} = P_{Ht} \quad (5)$$

while material continuity at the interface implies that

$$v_0 = u_{pp} + u_{pt} \quad (6)$$

Because the individual bumper plates in a dual-wall system are free from any initial mechanical stress (they are merely supported at their four corners a fixed distance away from the inner pressure wall), the initial conditions ahead of the projectile and target shock waves are taken to be zero (with the exception, of course, of the initial material densities). Solving equations (1-6) simultaneously yields expressions for projectile and target particle velocities which can then be used to calculate shock velocities, pressures, internal energies, and material densities after the passage of a shock wave. For example, using this procedure to solve for initially for u_{pt} yields

$$u_{pt} = (b - \sqrt{\Delta})/2a \quad (7)$$

where

$$a = k_p - k_t(\rho_{ot}/\rho_{op}) \quad (8a)$$

$$b = 2k_p v_0 + c_{op} + c_{ot}(\rho_{ot}/\rho_{op}) \quad (8b)$$

$$\Delta = b^2 - 4a(c_{op}v_o + k_p v_o^2) \quad (8c)$$

Then it follows that

$$u_{pp} = v_o - u_{pt} \quad (9a)$$

$$u_{st} = c_{ot} + k_t u_{pt} \quad (9b)$$

$$u_{sp} = c_{op} + k_p u_{pp} \quad (9c)$$

The shocked densities of the projectile and target materials are found by substituting equations (7,9a-c) into equations (1a,b) to yield

$$\rho_{Hp} = 1 / V_{Hp} = \frac{u_{sp} / V_{op}}{u_{sp} - u_{pp}} \quad (10a)$$

$$\rho_{Ht} = 1 / V_{Ht} = \frac{u_{st} / V_{ot}}{u_{st} - u_{pt}} \quad (10b)$$

Finally, equations (2a,b) and (3a,b) are then used to define the pressure and energy in the projectile and target materials, respectively, associated with the passage of the shock waves created by the initial impact. This completely defines the shocked states of the projectile and target materials due to the initial impact.

While the shock loading of a material is an irreversible process that results in an increase of the internal energy of the shocked material, the release of a shocked material occurs isentropically along an 'isentropes' or 'release adiabat'. The difference between the area under the isentropes and the energy of the shocked state is the amount of residual energy that remains in the material and can cause the material to melt or even vaporize. In order to calculate the release of the projectile and target materials from their respective shocked states (each characterized by P_H , E_H , and V_H), an appropriate equation-of-state is needed for each material. To keep the analysis relatively simple, the Mie-Gruneisen equation-of-state [5] was used in this study.

2.2 Shock Release Using the Mie-Gruneisen Equation-of-State

The Mie-Gruneisen equation-of-state (EOS) is an accurate thermodynamic description of most metals in the solid regime and is relatively easy to use. It has the form

$$P = P_H + \rho \Gamma (E - E_H) \quad (11)$$

where the time-dependent Gruneisen coefficient Γ is given for most metals as

$$\Gamma = \Gamma_0 \rho_0 / \rho \quad (12)$$

where $\Gamma_0 = K\beta/\rho_0 C_p$ is the ambient Gruneisen coefficient, K is the adiabatic bulk modulus, $\beta = 3\alpha$ is the volumetric coefficient of thermal expansion, and C_p is specific heat at constant pressure. Invoking the Second Law of Thermodynamics

$$dE = TdS - PdV \quad (13)$$

along with the isentropic constraint $dS=0$ for the release process allows us to construct the release isentrope in P - V space for a material referenced to the material Hugoniot in P - V space and a given initial shocked state defined by P_H , V_H , E_H . Using the procedure outlined in Reference [5], the pressure P_i and internal energy E_i at a specific position 'i' along the isentrope can be shown to be given by

$$P_i = [P_{Hi} + (\Gamma/V)_i (E_{i-1} - P_{i-1} \Delta V/2 - E_{Hi})] / [1 + (\Gamma/V)_i \Delta V/2] \quad (14)$$

where ΔV is the incremental change in volume used to create the release isentrope, and P_{Hi} and E_{Hi} are the pressure and energy along the Hugoniot corresponding to the i -th position in the release process. The release process is continued using equation (15) until the release isentrope so determined crosses the V -axis.

It should be noted that based on its thermodynamic origins, the Mie-Gruneisen EOS cannot be expected to give accurate results in a highly expanded liquid regime or in a vapor re-

gime. This is because as impact energy increases, the assumption that the Gruneisen coefficient is a function of density alone is no longer valid. At high impact energies, the Gruneisen coefficient is a function of internal energy as well as density. Experience has shown, however, that it does yield fairly accurate end-state results even when there is a small percentage of molten material present [6].

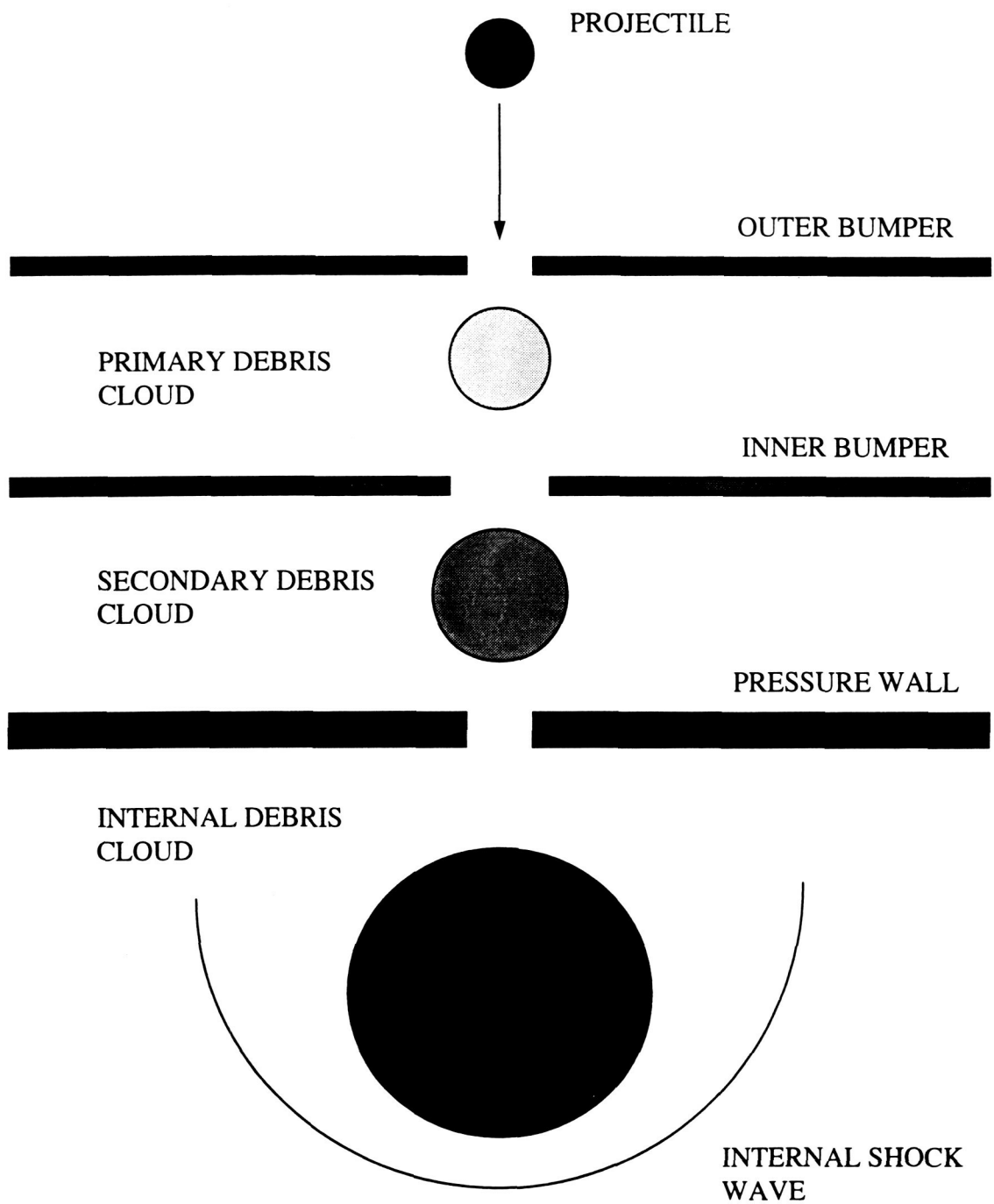


Figure 1. Hypervelocity Impact of a Module Wall System

3.0 MODELING OF PRIMARY AND SECONDARY DEBRIS CLOUDS

3.1 Primary Debris Cloud Mass

The mass of the primary debris cloud consists of the mass of the original impacting projectile plus the mass of the removed bumper material. No mass is considered lost to backsplash of the bumper and projectile materials; hence, since all of the mass is presumed to be directed in towards the pressure wall, the model to be developed should yield conservative results. The contribution of the bumper material to the primary debris cloud mass can be determined once the bumper hole diameter is known. This diameter can be calculated using any one of a number of empirical equations for hole diameter in a thin plate due to a high speed impact (see, e.g. [7]). The particular equation used in this study is given as follows [8]:

$$D_h/d_p = 3.4(t_b/d_p)^{0.333}(v_p/c_b)^{0.333}(1.0-0.0308\rho_b/\rho_p) \quad (15)$$

where c_b is the speed of sound in the bumper material. This equation was chosen because it is applicable over a wide range of projectile/bumper material combinations, impact velocities, and t_b/d_p ratios.

3.2 Primary Debris Cloud Characteristic Velocities

The characteristic velocities of interest for the debris clouds considered in this model are the axial and expansion velocities. These values can be determined in any number of different ways. Naturally, the various methods provide slightly different results. The 'correct' or most appropriate method is that which will provide characteristic velocity values that when used in subsequent calculations will provide pressure and temperature increases that are most consistent

with experimental results. The following sections present three methods to calculate characteristic velocities specifically for the primary debris cloud.

3.2.1 Conservation of Momentum and Energy

Because the initial impact occurs at such a high velocity, momentum transfer to the bumper itself can be ignored. As a result, the momentum balance along the axial direction before and after the initial impact is written as follows:

$$m_p v_o = (m_p + m_b) v_{mc}^{prim} \quad (16)$$

where v_{mc}^{prim} is the momentum conservation based axial velocity for the primary debris cloud. In fact, it is also the debris cloud center-of-mass velocity. Solving equation (16) for v_{mc}^{prim} yields

$$v_{mc}^{prim} = m_p v_o / (m_p + m_b) \quad (17)$$

We note that v_{mc}^{prim} can be viewed as the average axial velocity of the entire debris cloud mass.

Furthermore, because of the rapidity of the impact event, the only significant energy losses are to the accompanying light flash and the shock heating of the bumper and projectile materials. If we neglect the energy associated with the light flash, then the following energy balance can be written before and after the initial impact.

$$E_{impact} = E_{proj}^{sh\&rl} m_p + E_{bmpr}^{sh\&rl} m_b + E_{debcl d}^{prim,ax} + E_{debcl d}^{prim,exp} \quad (18)$$

where $E_{impact} = m_p v_o^2 / 2$ is the energy of the impacting projectile, m_p is the projectile mass, m_b is the bumper hole out mass, $E_{proj}^{sh\&rl}$ and $E_{bmpr}^{sh\&rl}$ are the residual energies per unit mass in the projectile and bumper materials following shock heating and release; $E_{debcl d}^{prim,ax}$ and $E_{debcl d}^{prim,exp}$

are the energies associated with the axial motion and radial expansion, respectively, of the primary debris cloud. By neglecting energy losses such as those due to light flash, the results obtained herein should also be conservative in nature.

If we let $v_{\text{exp}}^{\text{prim}}$ denote the expansion velocity of the primary debris cloud, then we can write

$$E_{\text{debclcd}}^{\text{prim,exp}} = (m_p + m_b)(v_{\text{exp}}^{\text{prim}})^2 / 2 \quad (19a)$$

$$E_{\text{debclcd}}^{\text{prim,ax}} = (m_p + m_b)(v_{\text{mc}}^{\text{prim}})^2 / 2 \quad (19b)$$

Substituting equations (19a,b) into equation (18) and solving for v_{exp} yields

$$v_{\text{exp}}^{\text{prim}} = \sqrt{\{m_p v_o^2 / 2 - [E_{\text{proj}}^{\text{sh\&rl}} m_p + E_{\text{bmpr}}^{\text{sh\&rl}} m_b + (m_p + m_b)(v_{\text{mc}}^{\text{prim}})^2 / 2]\} / [(m_p + m_b) / 2]} \quad (20)$$

We note that the expression under the radical in equation (20) is the difference of two terms. Because this difference is in an expression that is under a radical, there are three possibilities of which the user of the model being developed herein must be aware.

First, the difference is positive. In this case, the radical yields a real value that corresponds to the expansion velocity of the primary debris cloud.

Second, the difference is zero. In this case, the kinetic energy of the impacting projectile is not high enough so that there is no energy available for debris cloud expansion. This would result if the impact were at a velocity low enough so that the projectile passed through the bumper relatively unscathed (i.e. without any significant lateral dispersion).

Third, the difference is negative. In this case, the radical yields an imaginary value; however, the expansion velocity must be a real number. This implies that there is an error in the portion of the model that has been developed thus far. For example, depending on the impact

velocity, it is conceivable that only a portion of the projectile mass and only some fraction of the bumper hole-out mass are shocked and released. Implementing some adjustment factors to account for partial shock heating and release for m_p and m_b could significantly reduce the amount of energy being subtracted in equation (20). Or, for example, the hole diameter equation may be producing a diameter value that is too large. Correcting the hole diameter equation would also alter the amount of energy being subtracted. Finally, it is possible that the debris cloud axial velocity is too large. Including the momentum due to backsplash and the momentum transferred to the bumper plate would certainly alter the value of the debris cloud axial velocity.

Finally, we note that the spread of the primary debris cloud (in this case the half-angle defining the spread) can be estimated using the following relationship between the calculated primary debris cloud expansion and axial velocities:

$$\theta_{dc}^{prim} = \tan^{-1}(v_{exp}^{prim} / v_{mc}^{prim}) \quad (21)$$

3.2.2 Elementary Shock Physics

As the shock wave created by the initial impact strikes the rear surface of the bumper, it creates a rarefaction wave that travels back into the bumper and eventually in some form back into the projectile. This action and interaction of the shock wave and the free surface impacts a velocity u_{fst} to the target rear surface equal to the sum of the particle velocity in the target material due to the shock wave u_{pt} and the particle velocity due to the rarefaction wave u_{rt} :

$$u_{fst} = u_{pt} + u_{rt} \quad (22)$$

Since $u_{rt} \approx u_{pt}$ [5], an alternative form for equation (18) is

$$u_{fst} = 2u_{pt} \quad (23)$$

As in Reference [9], because the material along the leading edge of the primary debris

cloud is in fact the material at and directly behind the bumper rear free surface, the velocity of the leading edge of the primary debris cloud v_{le}^{prim} is approximated with u_{fst} , that is,

$$v_{le}^{prim} = u_{fst} = 2u_{pt} \quad (24)$$

Unfortunately, while the leading edge velocity may be used to characterize the axial velocity of the primary debris cloud, there does not exist a means by which the debris cloud expansion velocity can be calculated using the equations of elementary shock physics.

3.2.3 Effective Applied Pressure Wall Velocity

In a manner similar to Reference [10], the momentum of the primary debris cloud material before impact with the pressure wall is balanced with the momentum of the debris cloud material and the portion of the pressure wall affected by the debris cloud impact after the debris cloud impact. In this calculation, the presence and effect of an inner bumper are temporarily ignored. In this manner, the following expression is obtained:

$$(m_p + m_b) v_{mc}^{prim} = (m_p + m_b + m_w') v_{pw} \quad (25)$$

where m_w' is the pressure wall mass affected by the debris cloud impact and v_{pw} is the resultant velocity applied to the wall. Substituting for v_{mc}^{prim} according to equation (17) and solving for v_{pw} yields

$$v_{pw} = m_p v_o / (m_p + m_b + m_w') \quad (26)$$

The portion of pressure wall material affected by the debris cloud impact is taken to be the mass of the wall material directly beneath the impact footprint of the debris cloud on the wall, that is,

$$m_w' = \pi (r_w')^2 t_w \rho_w \quad (27a)$$

where

$$r_w' = S \tan \theta_{dc}^{\text{prim}} \quad (27b)$$

In equation (27b), S is the stand-off distance between the outer bumper and pressure wall.

3.2.4 Observations and Comments

A parametric study was performed using a 1.0 cm diameter aluminum projectile impacting an all-aluminum dual-wall system with a 0.16 cm thick bumper, a 0.48 cm thick pressure wall, and a stand-off distance of 11.43 cm at velocities between 1 and 16 km/sec. Table 1 provides the values of v_{mc}^{prim} , $v_{\text{exp}}^{\text{prim}}$, v_{le}^{prim} and v_{pw} for the velocity regime considered.

Table 1. Comparison of Primary Debris Cloud Characteristic Velocities

v_o (km/s)	v_{mc}^{prim} (km/s)	$v_{\text{exp}}^{\text{prim}}$ (km/s)	v_{le}^{prim} (km/s)	v_{pw} (km/s)
1	0.896	0.276	1.0	0.111
2	1.689	0.644	2.0	0.160
3	2.428	1.048	3.0	0.198
4	3.096	1.474	4.0	0.230
5	3.735	1.916	5.0	0.258
6	4.340	2.372	6.0	0.282
7	4.917	2.840	7.0	0.305
8	5.467	3.317	8.0	0.326
9	5.996	3.802	9.0	0.345
10	6.504	4.296	10.0	0.363
11	6.994	4.797	11.0	0.379
12	7.468	5.303	12.0	0.395
13	7.926	5.815	13.0	0.410
14	8.370	6.330	14.0	0.424
15	8.801	6.849	15.0	0.438
16	9.220	7.370	16.0	0.451

As can be seen in Table 1, $v_{le}^{\text{prim}} = v_o$ for like-on-like impacts so its use as the debris cloud impact velocity would most likely yield unreasonably high pressure wall impact stresses.

Conversely, v_{pw} is very low and would yield pressure wall impact stresses that would probably be too low to transfer significant amounts of energy into a module following a pressure wall perforation. The characteristic velocities produced by the momentum and energy conservation based calculation appear to be more physically reasonable and will be used to characterize the impact velocity of the primary debris cloud.

3.3 Secondary Debris Cloud Mass

The mass of the secondary debris cloud consists of a portion of the primary debris cloud mass plus the mass of the removed inner bumper material. No mass is considered lost to backplash of the inner bumper and primary debris cloud material. As discussed in Section 1.0, the inner bumper serves to trap a certain portion of the primary debris cloud particles. This fraction of trapped particles can be significant, especially for Type B inner bumpers. The reduction in mass of the primary debris cloud as it transforms into the secondary debris cloud is obtained using a simple multiplicative reduction factor. The nature of this factor, denoted by κ_1 , is discussed in Section 3.3.1.

The contribution of the inner bumper material to the secondary debris cloud mass can be determined once the inner bumper hole diameter is known. This diameter is calculated using the following fundamental empirical equation for hole diameter in a thin plate due to a high speed impact [11]:

$$d_h/d_p = 0.45V(t_s/d_p)^{0.666} + 0.90 \quad (28)$$

where V is the impact velocity and t_s is the thickness of the impacted plate. This equation was chosen because it is applicable over a wide range of projectile/bumper material combinations, impact velocities, and t_s/d_p ratios.

To render equation (28) applicable to the impact of the primary debris cloud on the inner bumper, some simplifying assumptions must be made. First, the velocity V in equation (28) is taken to be the characteristic velocity of the primary debris cloud as given by equation (17). Second, because the inner bumper is placed relatively close to the outer bumper, the primary debris cloud is in a relatively compact form when it impacts the inner bumper. This can give rise to a fair amount of “thickness” in the leading edge of the primary debris cloud as short-time X-ray photographs of expanding debris clouds have previously shown (see, e.g., [12]). Thus, for the purposes of this model, it is assumed that the thickness ratio in equation (28) is unity, or $t_s/d_p=1.0$. Finally, it is assumed that the perforation of the inner bumper occurs primarily as a result of the impact of the primary debris cloud leading edge material that is concentrated near the centerline. For the purposes of this study, this material is presumed to be contained within an area whose diameter is approximately equal to that of the hole in the bumper plate. In this manner, the “projectile diameter” in equation (28) is taken to be equal to D_h as calculated by equation (15), or $d_p=D_h$.

Making use of the terminology and simplifying assumptions discussed in the preceding paragraph reduces equation (28) to the following form:

$$d_h = (0.45 v_{mc}^{prim} + 0.90) D_h \quad (29)$$

Thus, the total mass of the secondary debris cloud is given by

$$m_{debcd}^{sec on} = \kappa_1 (m_p + m_b) + \pi \Lambda_{ib} d_h^2 / 4 \quad (30)$$

where Λ_{ib} is the areal mass density of the inner bumper material. The component of the secondary debris cloud whose origin can be traced back to the primary debris cloud is hereafter referred to as “the first component” while the inner bumper material contribution to the secondary

debris cloud is hereafter referred to as “the second component”.

3.3.1 The Mass Factor κ_1

From the discussion of the experimental results in Volume I of this report, it is apparent that a Type A inner wall traps only a small amount of the primary debris cloud material, while Type B traps a more significant quantity of material. One of the most distinguishing differences between the two inner bumper types (and a direct consequence of their respective composition) is their areal densities: $\Lambda_A=0.072 \text{ gm/cm}^2$ for the Type A inner bumper while $\Lambda_B=1.02 \text{ gm/cm}^2$ for the Type B inner bumper. Thus, it appears that the trapping capability of the inner bumpers is directly related to their areal densities. The following expression for κ_1 appears to capture this feature:

$$\kappa_1 = \left(1 - \frac{\Lambda_{ib}}{\Lambda_w}\right)^n \quad (31)$$

where n is a positive rational number, Λ_{ib} is the areal mass density of the inner bumper, and $\Lambda_w=\rho_w t_w$ is the areal mass density of the pressure wall. For example, if we consider an aluminum pressure wall with $t_w=0.48 \text{ cm}$ and $n=1$, then if $\Lambda_{ib}=\Lambda_A$, it follows that $\kappa_1=0.946$, which is only a slight reduction in debris cloud mass (approximately 5%). Alternatively, if $\Lambda_{ib}=\Lambda_B$, then $\kappa_1=0.237$, which is a more significant reduction in debris cloud mass (approximately 76%). Ultimately, the validity of this manipulation and, more specifically, the appropriate choice of the exponent ‘ n ’ will be ascertained when the predictions of the model are compared with experimental results.

3.4 Secondary Debris Cloud Characteristic Velocities

As in the case of the primary debris cloud, the characteristic velocities of interest for the

secondary debris cloud are the axial and expansion velocities. These values can be determined in a manner analogous to the procedure presented in Section 3.2.1. However, there is a significant difference between the method developed herein for the secondary debris cloud and that for the primary debris cloud in Section 3.2.1. This difference stems from the difference in the material composition of the two debris clouds.

For the purposes of this model, the primary debris cloud was tacitly assumed to be homogeneous and spherical; although it could possibly contain two different materials, both the projectile and bumper material that comprised the primary debris cloud were presumed to be evenly distributed throughout the cloud. As a result, only one axial velocity and one radial velocity were required to characterize its motion and expansion, respectively. However, the secondary debris cloud is comprised of two very distinct material types: the primary debris cloud material that passes through the inner bumper (i.e. the first component) and the inner bumper material itself (i.e. the second component), which is typically some form of composite material. Thus, in this case, it is necessary to develop axial and radial velocities for each component of the secondary debris cloud.

The procedures for calculating the axial and expansion velocities are very similar. In both cases, we first determine an average velocity quantity of interest (i.e. the average axial motion velocity or the average expansion velocity for the entire secondary debris cloud). In the case of the axial velocity, this is done by conserving momentum before and after the impact of the primary debris cloud on the inner bumper; for the expansion velocity, this is done using energy conservation before and after the inner bumper impact. Next, we postulate in both cases that the velocity quantities of interest for both components are proportional to the velocity quantity just

calculated and solve for the proportionality constants by conserving appropriate momentum and energy quantities.

As in the case of the primary debris cloud calculations, losses due to the light flash and backsplash accompanying the impact of the primary debris cloud on the inner bumper are ignored, as are losses due to the shock heating (or burning) of the primary debris cloud and inner bumper materials. As a result, the state of the primary debris cloud material that does pass through the inner bumper to become part of the secondary debris cloud remains unchanged by the impact on the second bumper. However, we do include the lost energy of the trapped primary debris cloud material is included in the energy balance equations. The next two sections present the details in this procedure for calculating the secondary debris cloud axial and expansion velocities.

3.4.1 Axial Velocities

To begin, we apply momentum conservation in the axial direction before and after the impact of the primary debris cloud on the inner bumper:

$$(m_p + m_b) v_{mc}^{prim} = m_{debcl d}^{sec on} v_{mc}^{sec} \quad (32)$$

where $m_{debcl d}^{sec on}$ is given by equation (30) and where v_{mc}^{sec} is the average axial velocity for the secondary debris cloud. Solving equation (32) for v_{mc}^{sec} yields

$$v_{mc}^{sec} = (m_p + m_b) v_{mc}^{prim} / m_{debcl d}^{sec on} \quad (33)$$

We note that momentum transfer to the inner bumper itself has again been ignored due to the rapidity of the impact event. We now rewrite equation (32) in terms of the axial velocities of the individual secondary debris cloud components:

$$(m_p + m_b)v_{mc}^{prim} = \kappa_1(m_p + m_b)v_{mc}^{sec1} + m_{ib}v_{mc}^{sec2} \quad (34)$$

where v_{mc}^{sec1} and v_{mc}^{sec2} refer to the axial velocities of the secondary debris cloud components, respectively, and where from equation (30)

$$m_{ib} = \pi \Lambda_{ib} d_h^2 / 4 \quad (35)$$

Next, we write

$$v_{mc}^{sec1} = C_1 v_{mc}^{sec} \quad (36a)$$

and

$$v_{mc}^{sec2} = C_2 v_{mc}^{sec} \quad (36b)$$

where C_1 and C_2 are the proportionality constants that need to be determined. Substituting equations (36a,b) into equation (34) and rearranging yields

$$\kappa_1(m_p + m_b)C_1 + m_{ib}C_2 = (m_p + m_b) \left(\frac{v_{mc}^{prim}}{v_{mc}^{sec}} \right) \quad (37)$$

A second equation for C_1 and C_2 is obtained by conserving the kinetic energy associated with the axial motion of the primary and secondary debris clouds. This equation is written as follows:

$$(m_p + m_b)(v_{mc}^{prim})^2 / 2 = \kappa_1(m_p + m_b)(v_{mc}^{sec1})^2 + m_{ib}(v_{mc}^{sec2})^2 + E_{lost}^{pr,ax} \quad (38)$$

where the final term on the right hand side of equation (38) refers to the axial kinetic energy lost due to the fact that the inner bumper stops a portion of the primary debris cloud mass. This energy loss is written as

$$E_{lost}^{pr,ax} = (1 - \kappa_1)(m_p + m_b)(v_{mc}^{prim})^2 / 2 \quad (39)$$

Substituting equations (36a,b) and (39) into equation (38) and rearranging yields

$$\kappa_1(m_p + m_b)C_1^2 + m_{ib}C_2^2 = \kappa_1(m_p + m_b)\left(\frac{v_{mc}^{prim}}{v_{mc}^{sec}}\right)^2 \quad (40)$$

Solving equations (37) and (40) yields

$$C_1 = \frac{\xi_a - \beta C_2}{\alpha} \quad (41a)$$

$$C_2 = \frac{\xi_a \left[\frac{\beta}{\alpha} \pm \sqrt{\Delta} \right]}{\beta \left(\frac{\beta}{\alpha} + 1 \right)} \quad (41b)$$

where

$$\Delta = \left(\frac{\beta}{\alpha} \right) \left[\left(\frac{\beta}{\alpha} + 1 \right) \kappa_1^2 - 1 \right] \quad (42)$$

and where

$$\alpha = \kappa_1(m_p + m_b), \quad \beta = m_{ib}, \quad \xi_a = (m_p + m_b) \left(\frac{v_{mc}^{prim}}{v_{mc}^{sec}} \right) \quad (43a,b)$$

Thus, equations (36a,b), together with equations (41a,b), (42), and (43a,b,c) define the axial velocities of the two secondary debris cloud components.

3.4.2 Comments on the Axial Velocity Calculations

In solving equations (37) and (40) for the constants C_1 and C_2 , the manipulations result in a single quadratic equation for C_2 . The general solution of such an equation has two roots as indicated by the \pm in equation (41b). Naturally, the choice of sign in equation (41b) will affect the outcome of C_1 according to equation (41a). Since C_1 must be a positive number, it follows from equation (41b) that $C_2 < \xi_a / \beta$. Substituting for C_2 according to equation (41b) yields the

inequality $\pm\sqrt{\Delta} < 1$. Obviously, if we keep the '-' sign, this inequality is always true. Of course, if we keep the '+' sign and substitute for Δ according to equation (42), we will obtain a relationship between the mass reduction constant κ_1 , the mass of the primary debris cloud, and the mass of the first component of the secondary debris cloud that will also make the inequality true. For the sake of simplicity, the model will consider only the '-' sign in equation (41b) since this will also allow the model to operate in its most general form.

Once it has been decided to keep the '-' sign in equation (41b), another issue arises, namely, we must ensure that C_2 is, in fact, a positive number. According to equation (41b), C_2 will be positive so long as

$$\frac{\beta}{\alpha} - \sqrt{\Delta} > 0 \quad (44)$$

Substituting for Δ according to equation (42) and simplifying, the inequality in equation (44) reduces to simply $1 > \kappa_1^2$. Since the definition of κ_1 is based on the premise that $\kappa_1 < 1$, the inequality in equation (44) is always true, which in turn implies that C_2 will always be a positive number if we keep the '-' sign in equation (41b).

The final issue that needs to be discussed is raised by the presence of the radical in equation (41b), namely, we must be sure that $\Delta > 0$. According to equation (42), this will be true only if

$$\kappa_1^2 > \frac{1}{\frac{\beta}{\alpha} + 1} \quad (45)$$

Substituting for α and β in equation (45) according to equations (43a,b) yields the following quadratic inequality:

$$\kappa_1^2 + \gamma\kappa_1 - 1 > 0 \quad (46a)$$

where

$$\gamma = \frac{m_{ib}}{m_p + m_b} \quad (46b)$$

Therefore, in order for the inequality in equation (45) to be true, we must have

$$\kappa_1 > \frac{-\gamma + \sqrt{\gamma^2 + 4}}{2} \quad (47)$$

We note that, since $\kappa_1 > 0$ by definition, the root with the '-' sign in front of the radical has been discarded. In addition, the discriminant in equation (47) is always positive (so there is no need to be concerned about complex roots) and the numerator is always positive (so there is no need to be concerned about negative κ_1 values. Thus, if the choice of the exponent 'n' in equation (31) results in a mass reduction factor κ_1 that violates equation (47) (i.e. the exponent is too large and the resulting reduction factor is too small), then the exponent needs to be reduced in order to increase the reduction factor value to an acceptable level.

3.4.3 Expansion Velocities

To begin, we conserve energy before and after the impact of the primary debris cloud on the inner bumper. This energy balance is written as follows:

$$E_{\text{impact}}^{\text{prim}} = E_{\text{debclld}}^{\text{sec,ax}} + E_{\text{debclld}}^{\text{sec,exp}} + E_{\text{lost}}^{\text{prim}} \quad (48)$$

where $E_{\text{impact}}^{\text{prim}}$ is the total kinetic energy of the impacting primary debris cloud (i.e. axial motion and expansion components combined), while $E_{\text{debclld}}^{\text{sec,ax}}$ and $E_{\text{debclld}}^{\text{sec,exp}}$ refer to the kinetic energies associated with the axial motion and radial expansion, respectively, of the secondary debris cloud.

The lost energy of the trapped primary debris cloud particles, $E_{\text{lost}}^{\text{prim}}$, consists of both components of primary debris cloud motion, and is given by

$$E_{\text{lost}}^{\text{prim}} = (1 - \kappa_1)(m_p + m_b)(v_{\text{mc}}^{\text{prim}})^2 / 2 + (1 - \kappa_1)(m_p + m_b)(v_{\text{exp}}^{\text{prim}})^2 / 2 \quad (49)$$

If we let $v_{\text{exp}}^{\text{sec}}$ denote the average expansion velocity of the secondary debris cloud, then we can write

$$E_{\text{debcd}}^{\text{sec,exp}} = m_{\text{debcd}}^{\text{sec on}} (v_{\text{exp}}^{\text{sec}})^2 / 2 \quad (50a)$$

where $m_{\text{debcd}}^{\text{sec on}}$ is given by equation (30). Since

$$E_{\text{debcd}}^{\text{sec,ax}} = m_{\text{debcd}}^{\text{sec on}} (v_{\text{mc}}^{\text{sec}})^2 / 2 \quad (50b)$$

we substitute equations (49) and (50a,b) into equation (48) and solve for $v_{\text{exp}}^{\text{sec}}$ to obtain

$$v_{\text{exp}}^{\text{sec}} = \sqrt{\{\kappa_1[(m_p + m_b)(v_{\text{mc}}^{\text{prim}})^2 + (m_p + m_b)(v_{\text{exp}}^{\text{prim}})^2] - m_{\text{debcd}}^{\text{sec on}} (v_{\text{mc}}^{\text{sec}})^2\} / m_{\text{debcd}}^{\text{sec on}}} \quad (51)$$

We again note that the expression under the radical in equation (51) is the difference of two terms. Because this difference is in an expression that is under a radical, care must again be taken to ensure that the difference is in fact positive.

To determine the expansion velocities of the two secondary debris cloud components, we again write

$$v_{\text{exp}}^{\text{sec 1}} = D_1 v_{\text{exp}}^{\text{sec}} \quad (52a)$$

and

$$v_{\text{exp}}^{\text{sec 2}} = D_2 v_{\text{exp}}^{\text{sec}} \quad (52b)$$

where $v_{\text{exp}}^{\text{sec } 1}$ and $v_{\text{exp}}^{\text{sec } 2}$ are the expansion velocities of the two secondary debris cloud components, and D_1 and D_2 are the corresponding respective proportionality constants that need to be determined.

Next, we conserve the kinetic energy associated with the expansion of the two secondary debris cloud components:

$$(m_p + m_b)(v_{\text{exp}}^{\text{prim}})^2 / 2 = \kappa_1(m_p + m_b)(v_{\text{exp}}^{\text{sec } 1})^2 / 2 + m_{ib}(v_{\text{exp}}^{\text{sec } 2})^2 / 2 + E_{\text{lost}}^{\text{pr,exp}} \quad (53)$$

where the final term on the right hand side of equation (53) refers to the expansion kinetic energy lost due to the fact that the inner bumper traps a portion of the primary debris cloud mass. This energy loss is written as

$$E_{\text{lost}}^{\text{pr,exp}} = (1 - \kappa_1)(m_p + m_b)(v_{\text{exp}}^{\text{prim}})^2 / 2 \quad (54)$$

Substituting equations (52a,b) and equation (54) into equation (53), yields

$$\kappa_1(m_p + m_b)D_1^2 + m_{ib}D_2^2 = \kappa_1(m_p + m_b)\left(\frac{v_{\text{exp}}^{\text{prim}}}{v_{\text{exp}}^{\text{sec}}}\right)^2 \quad (55)$$

A second equation for D_1 and D_2 is obtained by conserving the momentum associate with the expansion of the primary and secondary debris clouds:

$$(m_p + m_b)v_{\text{exp}}^{\text{prim}} = \kappa_1(m_p + m_b)v_{\text{exp}}^{\text{sec } 1} + m_{ib}v_{\text{exp}}^{\text{sec } 2} \quad (56)$$

Substituting equations (51a,b) into equation (56) yields

$$\kappa_1(m_p + m_b)D_1 + m_{ib}D_2 = (m_p + m_b)\left(\frac{v_{\text{exp}}^{\text{prim}}}{v_{\text{exp}}^{\text{sec}}}\right) \quad (57)$$

Thus, the constants D_1 and D_2 are found by solving equations (55) and (57). However, if we

compare the equation pair (55,57) to the equation pair (37,40), we find them to be identical with the exception that equations (55) and (57) are written in terms of expansion velocities while equations (37) and (40) are in terms of axial motion velocities. Other than that difference, their basic forms are identical. Therefore, the solution for the constants D_1 and D_2 is written down directly from equations (41) through (43) as follows:

$$D_1 = \frac{\xi_e - \beta D_2}{\alpha} \quad (58a)$$

$$D_2 = \frac{\xi_e \left[\frac{\beta}{\alpha} \pm \sqrt{\Delta} \right]}{\beta \left(\frac{\beta}{\alpha} + 1 \right)} \quad (58b)$$

where

$$\Delta = \left(\frac{\beta}{\alpha} \right) \left[\left(\frac{\beta}{\alpha} + 1 \right) \kappa_1^2 - 1 \right] \quad (59)$$

and where

$$\alpha = \kappa_1(m_p + m_b), \quad \beta = m_{ib}, \quad \xi_e = (m_p + m_b) \left(\frac{v_{\text{exp}}^{\text{prim}}}{v_{\text{exp}}^{\text{sec}}} \right) \quad (60a,b)$$

Thus, equations (51a,b), together with equations (58a,b), (59), and (60a,b,c) define the axial velocities of the two secondary debris cloud components.

3.5 Debris Cloud Spread Angles

Finally, the spread angles of the two secondary debris cloud components (in this case the half-angles defining the spreads) can be estimated using the following relationships between the calculated secondary debris cloud expansion and axial velocities:

$$\theta_{dc}^{sec 1} = \tan^{-1}(v_{exp}^{sec 1} / v_{mc}^{sec 1}) \quad (61a)$$

$$\theta_{dc}^{sec 2} = \tan^{-1}(v_{exp}^{sec 2} / v_{mc}^{sec 2}) \quad (62b)$$

Based on equations (27a,b), the portions of pressure wall material affected by the impacts of the two secondary debris cloud components are given by:

$$m_{w1} = \pi r_{w1}^2 t_w \rho_w \quad (63a)$$

$$m_{w2} = \pi r_{w2}^2 t_w \rho_w \quad (63b)$$

respectively, where

$$r_{w1} = S_2 \tan \theta_{dc}^{sec 1} \quad (64a)$$

$$r_{w2} = S_2 \tan \theta_{dc}^{sec 2} \quad (64b)$$

In equations (64a,b), S_2 is the stand-off distance between the inner bumper and pressure wall.

4.0 PRESSURE WALL IMPACT SHOCK LOADING AND RELEASE MODELING

In modeling the shock loading and subsequent release of the secondary debris cloud and pressure wall materials, it is again presumed that the shock waves are initially planar. This simplification again allows one-dimensional relationships to be used for analyzing the creation and release of shock pressures. The process used to calculate shock pressures, energies, etc. in the debris cloud and pressure wall materials is identical to that used in modeling the initial impact of the projectile on the bumper, with the following exceptions.

1) Only the secondary debris cloud material component consisting of primary debris cloud material that passed through the inner bumper contributes to the impact loading of the pressure wall. As such, the properties of that component of the secondary debris cloud and pressure wall properties are used in place of projectile and bumper properties, respectively.

2) The initial density of the secondary debris cloud material considered in the impact analysis is taken as the average of the final densities after release from their respective shocked states of the projectile and bumper materials in the primary debris cloud.

3) The secondary debris cloud axial velocity calculated using the momentum conservation method developed in Section 3.4.1 is used as the impact velocity in the impact analysis.

4) The component of the secondary debris cloud consisting of inner bumper material contributes to the loading of the pressure wall in the form of an impulsively delivered velocity. This causes additional motion of the pressure wall and so affects only the shock wave created at the pressure wall/module wall interface.

5) Unlike the stress-free bumper plate, the pressure wall of a pressurized habitable module experiences an initial bi-axial state of stress due to the internal ambient pressure. However, because the pressure wall is thin (i.e. on the order of 5 mm in thickness), it may be assumed that the stress *through the thickness* of the plate is nearly zero and may be ignored. Since the shock waves in the pressure wall propagate through the thickness as well, it appears reasonable to presume that the initial conditions ahead of the pressure wall shock wave are also zero.

6) The release of the pressure wall material from its shocked state terminates when the pressure in the wall material reaches a level corresponding to that which induced in the wall by the motion of the rarefaction wave through the shocked material. Since the pressure wall is backed by module air at 1 atm, this value is not zero as in the case of the bumper which was surrounded by a vacuum. The means of obtaining this value is presented in the next section.

5.0 MODELING OF INDIVIDUAL INTERNAL EFFECTS: SHOCK WAVE PASSAGE

As discussed in Chapter 4, the magnitude of the shock wave induced in the module by the motion of the pressure wall is the combined result of two phenomena. The first is the impulsive loading imparted to the pressure wall by the impact of the secondary debris cloud inner bumper material component. The second is the impact of the secondary debris cloud material component consisting of primary debris cloud material on the pressure wall. The motion of the pressure wall due to the impulsive loading is discussed in Section 5.1 while the effects of the impact loading are discussed in Section 5.2. The application of these two phenomena to the creation, propagation, and attenuation of a shock wave in the module interior is presented in Sections 5.3 and 5.4.

5.1 Pressure Wall Impulsive Loading Effect

In a manner similar to Section 3.2.3, the effect of the impulsive loading imparted to the pressure wall by the impact of the second secondary debris cloud component is characterized by an instantaneously applied velocity. This velocity is obtained by balancing the momentum of the second component of the secondary debris cloud material before its impact on the pressure wall with the momentum of the debris cloud material and the portion of the pressure wall affected by the impact after the debris cloud impact. In this manner, the following expression is obtained:

$$m_{ib} v_{mc}^{sec 2} = (m_{ib} + m_{w2}) u_{pw} \quad (65)$$

where $v_{mc}^{sec 2}$, m_{ib} , and m_{w2} are given by equations (36b), (35), and (63b), respectively, and u_{pw} is the resultant velocity that is applied to the wall. Solving for u_{pw} yields

$$u_{pw} = m_{ib} v_{mc}^{sec 2} / (m_{ib} + m_{w2}) \quad (66)$$

The application of this velocity to the creation of the module interior shock wave is presented in Section 5.3.

5.2 Pressure Wall Impact Loading Effect

As the shock wave generated by the impact of the first component of the secondary debris cloud on the pressure wall front surface propagates through the pressure wall, it encounters the pressure wall rear surface. In addition to creating a rarefaction wave that is reflected back into the pressure wall to relieve shock pressures, a shock wave is transmitted into the air that is adjacent the pressure wall rear surface. The properties of the reflected and transmitted waves are found using a technique based on the method of impedance matching (see, e.g., [9]). In this technique, continuity of pressure and particle velocity are enforced at the pressure wall/module air interface.

The equations governing the reflection and transmission of shock waves at material interfaces are presented in the following section. In this development, all materials are assumed to be stationary. As such, the superposition of the effect of an additional pressure wall velocity is deferred until Section 5.3 where the results of the development to follow are combined with the results of the preceding section.

5.2.1 Impedance Matching Technique

Figure 2a shows an incoming shock wave in material A, a reflected wave from the A/B interface, and a transmitted shock wave into material B. Shock wave I is shown moving into undisturbed material (denoted with a '0' subscript). The shocked state of the material in its wake is denoted by a '1' subscript. The reflected wave II moves back into this shocked material and leaves behind it material whose state is denoted by a subscript of '2'. The transmitted shock wave

III moves into undistributed material (denoted by a '4' subscript); the condition of the shocked material behind it is labeled with a '3' subscript. Figure 2b shows the same configuration only all motion is shown under steady conditions.

Across shock front I we have

$$\rho_1(U_1 - u_1) = \rho_0^A(U_1 - u_0) \quad (67a)$$

$$P_1 - P_0 = \rho_0^A(U_1 - u_0)(u_1 - u_0) \quad (67b)$$

as well as the constitutive relationship between the shock wave speed U_1 and the particle velocity u_1 induced in the shocked material

$$U_1 = c_0^A + k^A u_1 \quad (68)$$

In equations (67a,b), ρ_0 has been replaced by ρ_0^A , the ambient density of material A. Assuming stationary conditions at zero pressure ahead of the shock wave (i.e. $u_0 = P_0 = 0$) and that P_1 is known (it is the pressure associated with the impact of the initial debris cloud on the pressure wall as calculated in Section 4.0), equations (67-68) can be used to solve for u_1 and ρ_1 as follows:

$$u_1 = -(c_0^A/2k^A)\{1 - [1 + 4k^A P_1 / \rho_0^A (c_0^A)^2]^{1/2}\} \quad (69a)$$

$$\rho_1 = \rho_0^A U_1 / (U_1 - u_1) \quad (69b)$$

This completely defines the state of the material behind shock wave I. For shock wave II we have

$$\rho_1(U_2 + u_1) = \rho_2(U_2 + u_2) \quad (70a)$$

$$P_2 - P_1 = \rho_1(U_2 + u_1)(u_1 - u_2) \quad (70b)$$

and for shock wave III we have

$$\rho_3(U_3 - u_3) = \rho_0^B(U_3 - u_4) \quad (71a)$$

$$P_3 - P_4 = \rho_0^B(U_3 - u_4)(u_3 - u_4) \quad (71b)$$

$$U_3 = c_0^B + k^B u_3 \quad (71c)$$

where ρ_4 has been replaced by ρ_0^B , the ambient density of material B. In anticipation of the fact that material B will represent the module air, we assume stationary conditions but a non-zero pressure ahead of shock wave III. Enforcing pressure and velocity continuity at the A/B material interface (i.e. $P_3=P_2$ and $u_3=u_2$) reduces equations (71a-c) to

$$\rho_3(U_3-u_2) = \rho_0^B U_3 \quad (72a)$$

$$P_2 = P_4 + \rho_0^B U_3 u_2 \quad (72b)$$

$$U_3 = c_0^B + k^B u_2 \quad (72c)$$

Equations (70a,b) and equations (72a-c) form a system of 5 equations in 6 unknowns ($P_2, \rho_2, U_2, u_2, \rho_3, U_3$). The elimination of one unknown is illustrated graphically in Figure 3. In Figure 3, Curves A and B are the Hugoniot of materials A and B, and Curve A' is the Hugoniot of materials A reflected about point C which denotes the initial shocked state in material A (i.e. prior to the passage of the reflected wave). The shocked state of material B must lie at the intersection of its Hugoniot (Curve B) and the reflected Hugoniot for material A (Curve A'). This state is denoted by point D. The particle velocity corresponding to point D is the interface velocity $u_2=u_3$ while the pressure corresponding to point D is the interface pressure $P_2=P_3$.

Knowing that curve A' is the reflection of Curve A, that is, it passes throughout the points $(u_p=u_1, P=P_1)$, $(u_p=2u_1, P=0)$, and $(u_p=0, P=2\rho_0^A u_1(c_0^A+2k^A u_1))$, allows us to obtain the following functional form for Curve A' in P- u_p space:

$$P_{A'} = 2\rho_0^A u_1(c_0^A+2k^A u_1) - \rho_0^A(c_0^A+4k^A u_1-k^A u_p)u_p \quad (73)$$

Thus, when we set $P_{A'}$ equal to the functional form of Curve B in P- u_p space, we have an equation for the particle velocity that corresponds to point D. Solving for this particle velocity yields:

$$u_D = (\beta - \sqrt{\beta^2 - 4\alpha\gamma}) / 2\alpha \quad (74)$$

where

$$\alpha = \rho_0 A_k A - \rho_0 B_k B \quad (75a)$$

$$\beta = \rho_0 A_{c_0} A + \rho_0 B_{c_0} B + 4\rho_0 A_k A_{u_1} \quad (75b)$$

$$\gamma = 2\rho_0 A_{u_1} (c_0 A + 2k A_{u_1}) - P_4 \quad (75c)$$

in which u_1 , of course, is known. Setting $u_2 = u_D$ in equations (70a,b) and (72a-c) allows us to solve for all the remaining quantities:

$$U_3 = c_0 B + k B_{u_2} \quad (76a)$$

$$P_3 = P_4 + \rho_0 B U_3 u_2 \quad (76b)$$

$$\rho_3 = \rho_0 B U_3 / (U_3 - u_2) \quad (76c)$$

$$U_2 = (P_1 - P_2) / \rho_1 (u_1 - u_2) - u_1 \quad (77a)$$

$$\rho_2 = \rho_1 (U_2 + u_1) / (U_2 + u_2) \quad (77b)$$

5.3 Shock Wave Induced Pressure and Temperature Changes

The analysis in Sections 5.1 and 5.2 is applied to the reflection and transmission of shock waves from the pressure wall/module air interface as follows. Clearly, material A is the pressure wall material (aluminum) and, as mentioned previously, material B is air. Since the axial velocities of the two secondary debris cloud components are not equal, the pressure wall impact event occurs at a time either before or after the impulsive loading event. As a result, it may be presumed that the impact event does not affect the impulsive loading event and vice versa. This implies that the total pressure wall rear surface velocity may be written as simply the sum of the two velocities u_3 and u_{pw} as follows:

$$u_{pa} = u_3 + u_{pw} \quad (78)$$

This in turn is then also the total particle velocity in the module air immediately adjacent to the pressure wall rear surface. The velocity of the shock wave in the module air due to the combined effects of the impact and impulsive loadings is then given simply as

$$u_{sa} = c_0^B + k^B u_{pa} \quad (79)$$

while the initial pressure behind the shock front in the module air is given as

$$P_{Ha} = P_4 + \rho_0^B u_{sa} u_{pa} \quad (80)$$

It is also noted that $P_3 = P_2$ is the pressure level in the pressure wall material at which the release process for the pressure wall material terminates. For the purposes of this model, the shock wave is presumed to emanate spherically from the center of the pressure wall perforation. Naturally, the shock wave decays as it travels into the module environment. However, prior to its decay, the temperature increase in the immediate vicinity of the pressure wall is given by

$$\Delta T = (E_{Ha} - E_{Oa}) / C_{pa} \quad (81)$$

where $E_{Oa} = C_{pa} T_0$ is the ambient module air energy (note: $T_0 = 297$ -deg Kelvin; all temperatures are measured in degrees Kelvin), $C_{pa} = 0.24$ cal/gm°C is the specific heat of air, and E_{Ha} is given by

$$E_{Ha} = E_{Oa} + \frac{1}{2} (P_{Ha} + P_{Oa}) (1/\rho_{Oa} - 1/\rho_{Ha}) \quad (82)$$

In equation (82), $\rho_{Oa} = 1.22 \times 10^{-3}$ gm/cm³ is the ambient density of air, $P_{Oa} = 1$ atm is the ambient module air pressure ahead of the shock wave, and

$$\rho_{Ha} = \frac{u_{sa} \rho_{Oa}}{u_{sa} - u_{pa}} \quad (83)$$

is the density of the shocked air. Thus, ΔT as calculated by equation (81) and $\Delta P = P_{Ha} - P_{Oa}$, where P_{Ha} is given by equation (80), define the change in pressure and temperature due to a

shock wave originating at the rear surface of the pressure wall in a pressurized module in the immediate vicinity of the pressure wall itself. The attenuation of the pressure increase as a function of distance away from the shock wave is discussed in the following section.

5.4 Attenuation of Shock Wave Induced Pressures and Temperatures

Figure 4 shows a sketch of a generic shock wave and its attenuation with distance. The decay with distance of the initial pressure and temperature induced by the shock wave in the module are obtained using the non-dimensional attenuation curve for normally incident spherical air blast waves [14]. A closed-form analytical expression of the tabular P_s' vs R' data in [14] was obtained through a curve-fitting exercise for four regimes in R' with the following results:

$$0.01 \leq R' \leq 0.10 \quad \dots \quad P_s' = 3.803(R')^{-1.2627} \quad (84a)$$

$$0.10 \leq R' \leq 1.0 \quad \dots \quad P_s' = 0.476(R')^{-2.2416} \quad (84b)$$

$$1.0 \leq R' \leq 10.0 \quad \dots \quad P_s' = 0.441(R')^{-1.3821} \quad (84c)$$

$$10.0 \leq R' \leq 1000.0 \quad \dots \quad P_s' = 0.241(R')^{-1.1120} \quad (84d)$$

The initial pressure P_{Ha} is attenuated as a function of distance R away from the origination point of the shock wave by scaling values of P_s' calculated using equations (84a-d) to P_{Ha} using the maximum value of P_s' , i.e., the value of P_s' at $R'=0.01$, as follows:

$$P_a(R) = \frac{P_s'(R')}{P_s'(R'=0.01)} P_{Ha} \quad (85)$$

where $P_a(R)$ refers to the pressure in the module at a distance R away from the origination point of the shock wave. The dimensional distance R is obtained from its non-dimensional counterpart R' using the relationship in [14], that is,

$$R = R'(E/P_{oa})^{1/3} \quad (86)$$

where 'E' refers to the amount of energy that has been transformed into a shock wave blast. This quantity can be easily calculated by performing an energy balance before and after the impact of the first secondary debris cloud component on the pressure wall. If energy losses due to light flash are again ignored, this energy balance is written as follows:

$$E_{debcd}^{sec on 1} = \kappa_2 [E_{pwall}^{sh \& rl} m_{w1} + E_{debcd}^{sh \& rl} \kappa_1 (m_p + m_b)] + E_{shwave}^{initial} \quad (87)$$

where $E_{debcd}^{sec on 1}$ is the total kinetic energy of the secondary debris cloud component considered in the impact analysis (i.e. it is the sum of the axial and expansion energies of the first secondary debris cloud component) prior to its impact on the pressure wall, $E_{pwall}^{sh \& rl}$ and $E_{debcd}^{sh \& rl}$ are the residual energies per unit mass in the pressure wall and the secondary debris cloud following release from their respective shocked states, $E_{shwave}^{initial}$ is the initial energy of the shock wave (i.e. in the immediate vicinity of the pressure wall), and m_{w1} is the mass of the pressure wall material subjected to shock heating and release as defined by equation (63a). The quantities $E_{pwall}^{sh \& rl}$ and $E_{debcd}^{sh \& rl}$ are calculated using the 1-D shock physics equations developed in Section 2.0. A constant $\kappa_2 \leq 1$ has been inserted into equation (87) to allow for the possibility that not all of the secondary debris cloud and pressure wall materials will be loaded to a fully shocked state. The placement of κ_2 outside the square brackets implies that the fractions of shocked and released material for the pressure wall and the secondary debris cloud material are assumed to be equal. Then, solving for $E_{shwave}^{initial}$ yields

$$E = E_{shwave}^{initial} = E_{debcl d}^{sec, ax} + E_{debcl d}^{sec, exp} - \kappa_2 [E_{pwall}^{sh \& rl} m_{w1} + E_{debcl d}^{sh \& rl} \kappa_1 (m_p + m_b)] \quad (88)$$

We note that the quantity E as required by equation (86) and defined by equation (88) must be a positive number. Therefore, the fact that the right hand side is a difference between initial and expended energies is a signal that care must be taken to ensure that sufficient energy remains to allow shock wave creation and propagation. If, for example, the mass of the pressure wall material that is shocked and release is too large, it is conceivable that the right hand side of equation (88) may be a negative number. If this were the case, then the situation must be corrected either by decreasing κ_2 or by decreasing m_{w1} . The latter would be accomplished, for example, by decreasing the spread angle of the appropriate secondary debris cloud component.

To find temperature decay with distance R , we use the following slightly modified forms of equations (81) and (82):

$$\Delta T = [E_a(R) - E_{oa}] / C_{pa} \quad (89)$$

where $P_a(R)$ is given by equation (85),

$$E_a(R) = E_{oa} + \frac{1}{2} [P_a(R) + P_{oa}] [1/\rho_{oa} - 1/\rho_a(R)] \quad (90)$$

is the energy behind a decaying shock wave as a function of the distance R , and $\rho_a(R)$ is the corresponding shocked air density. In this case, the density of the air behind a decaying shock wave is given as a function of R by the following modified form of equation (83):

$$\rho_a(R) = \frac{u_s(R) \rho_{oa}}{u_s(R) - u_p(R)} \quad (91a)$$

where

$$u_s(R) = c_{oa} + k_a u_p(R) \quad (91b)$$

is the speed of the decaying shock wave as a function of R and u_p is the corresponding particle velocity (also a function of the distance R). Finally, the particle velocity as a function of distance is found by substituting equation (91b) into the following alternate expression for $P_a(R)$:

$$P_a(R) = P_{oa} + \rho_{oa}u_s(R)u_p(R) \quad (92)$$

Solving for $u_p(R)$ thus yields

$$u_p(R) = \frac{-\rho_{oa}c_{oa} + \sqrt{\Delta}}{2k_a\rho_{oa}} \quad (93a)$$

where

$$\Delta = (\rho_{oa}c_{oa})^2 - 4k_a\rho_{oa}[P_{oa}-P_a(R)] \quad (93b)$$

5.4.1 Pressure and Temperature Values at a Specified Location

Because the shock wave is presumed to propagate with spherical symmetry from the point on the pressure wall corresponding to the center of impact by the initial debris cloud, determining pressure and temperature values due to the passage of a decaying shock wave at a specific point of interest merely involves checking the radial distance from the decaying shock front to the point of interest. As the attenuation process progresses, if the point of interest is over-run by the shock wave, then a simple interpolation of the pressures and temperatures before and after the point of interest should yield a valid approximation of the pressure and temperature at that point. If the pressure jump across the shock wave has decayed to less than 1% of ambient and the point of interest has not yet been reached, then the attenuation process stops and we presume we are at ambient conditions. In this case, personnel at the point of interest will not feel any effect from the shock wave.

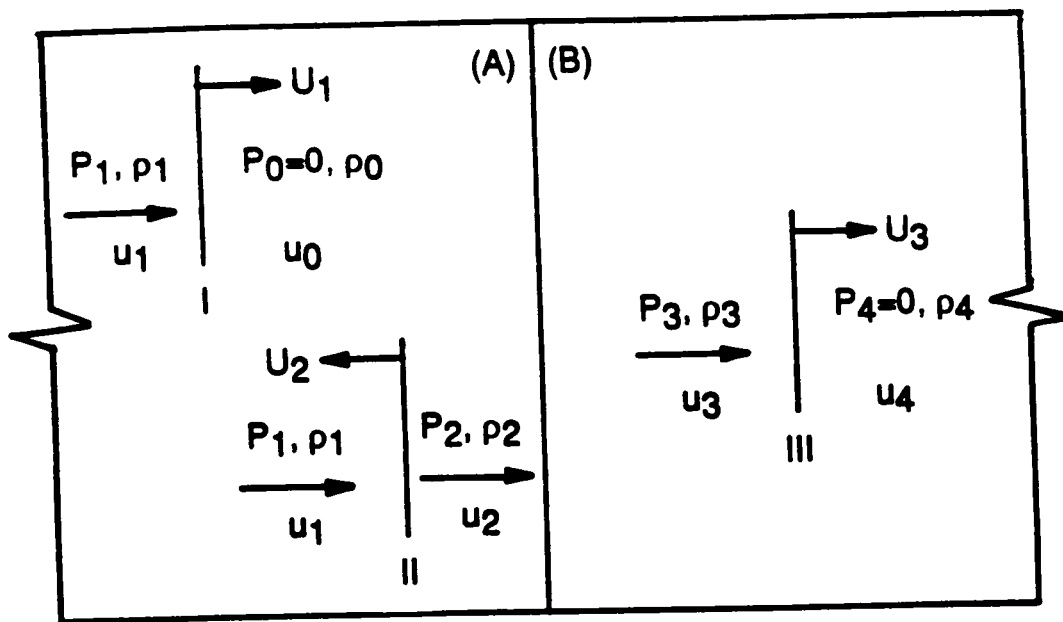


Figure 2a. Shock Wave Reflection and Transmission at a Material Interface -- Unsteady Conditions

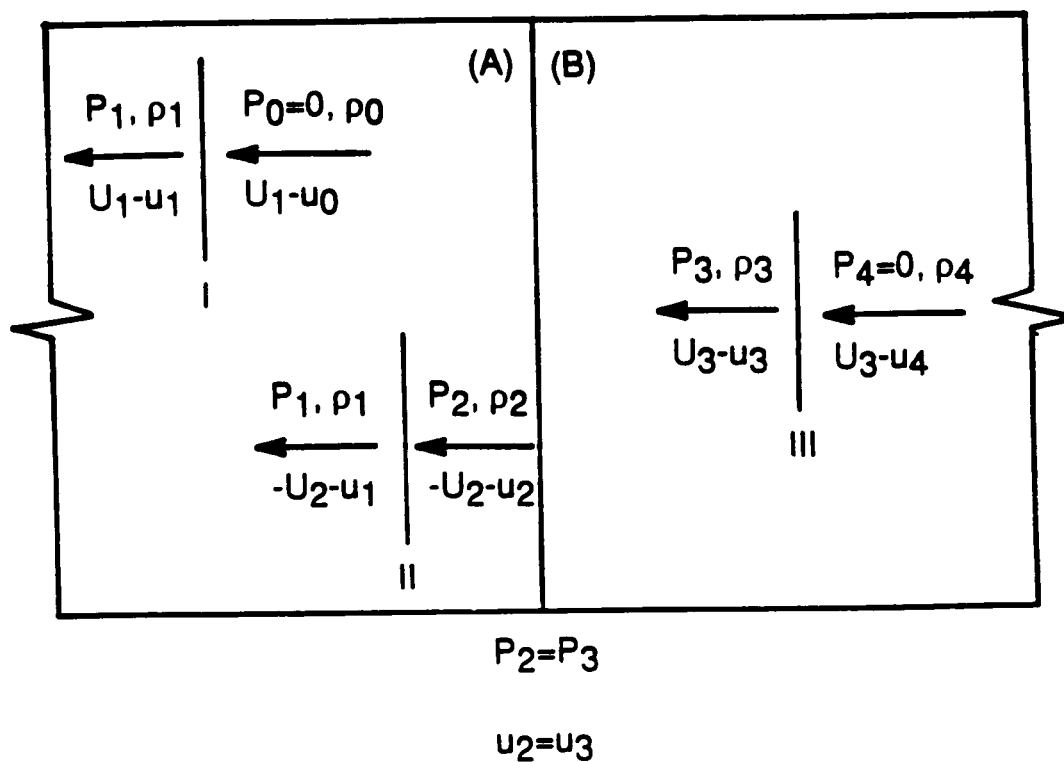


Figure 2b. Shock Wave Reflection and Transmission at a Material Interface -- Steady Conditions

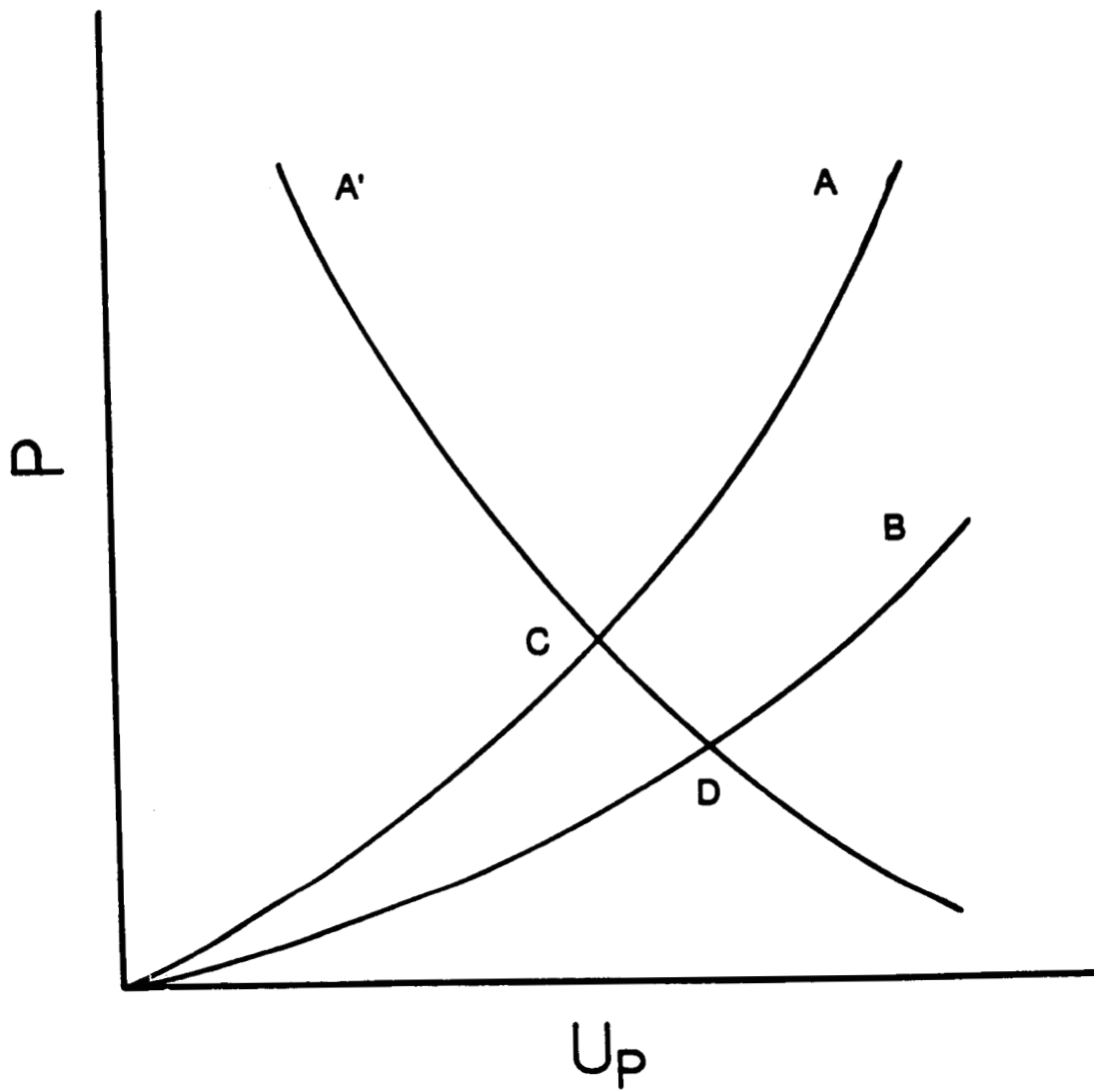
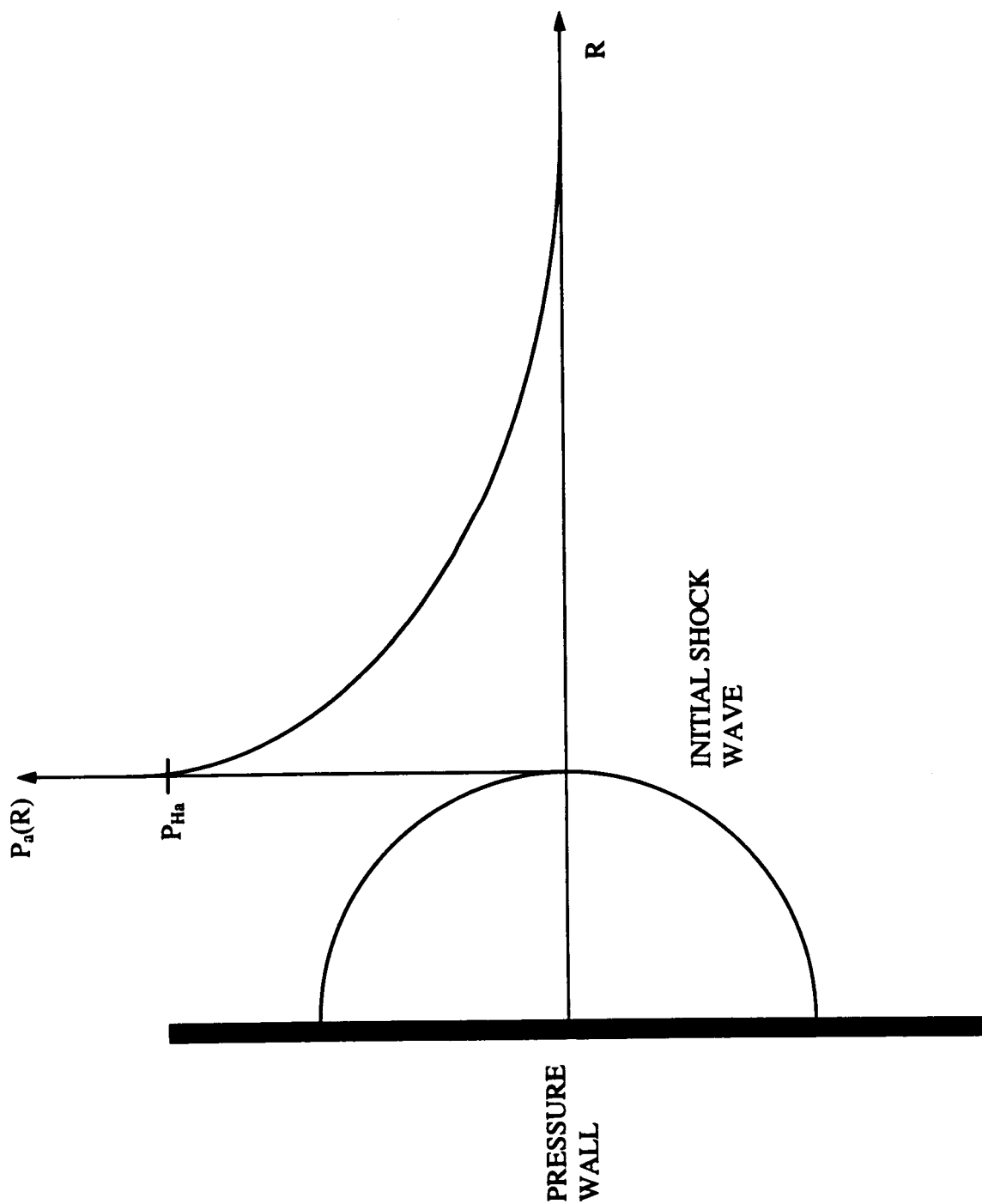


Figure 3. Impedance Mismatch at a Material Interface -- Generic Sketch



6.0 MODELING OF INDIVIDUAL INTERNAL EFFECTS:

INTERNAL DEBRIS CLOUD PASSAGE

6.1 Debris Cloud Induced Pressure and Temperature Changes

In the event that module wall perforation results in a debris cloud entering the module interior, the temperature rise and pressure increase accompanying the passage of a shock wave created by the motion of such a debris cloud are determined as follows.

First, the speed of the shock wave created by the motion of the internal debris cloud through the module air is taken to be equal to the leading edge velocity of the debris cloud. As discussed previously, this can be approximated by the particle velocity at the pressure wall/module air interface calculated using the impedance matching technique described previously, that is, $u_{sdc}=u_2=u_3$. While this may be presumed to be only valid in the immediate vicinity of the leading edge of the debris cloud near its centerline, applying this equality to the entire shock wave generated by the debris cloud should yield conservative results. Furthermore, we do not add the pressure wall velocity u_{pw} to u_3 to obtain the particle velocity at the pressure wall/module air interface. The velocity u_{pw} is assumed to affect only the creation and movement of the internal shock wave that is created by pressure wall motion.

Second, it is further assumed that the speed of the debris cloud and its accompanying shock wave do not decay until it reaches a certain distance away from the perforated pressure wall. If this distance is less than a module diameter, then the debris cloud effectively “runs out of steam” at this location and the velocity drops quickly to zero. It is at this distance (and point in

time) that the attenuation of the shock wave induced pressures and temperatures begin. The methods for calculating this distance is presented subsequently in Section 6.2.2. This assumption allows us to treat the shock wave velocity as essentially constant, which is consistent with the conservative nature of the model being developed.

Figure 5 shows a sketch of a generic debris cloud moving through the interior of a module and the shock wave accompanying its motion. Following the definition of the shock wave velocity given in the preceding paragraphs, the particle velocity in the air induced by the shock wave is given by

$$u_{pdc} = (u_{sdc} - c_{oa})/k_a \quad (94)$$

from which the pressure behind the shock is given by

$$P_{Ha} = P_{oa} + \rho_{oa} u_{sdc} u_{pdc} \quad (95)$$

where $c_{oa} = 0.33$ km/s, $k_a = 1.07$ and as before $P_{oa} = 1$ atm. The shocked density is again given by

$$\rho_{Ha} = \frac{u_{sdc} \rho_{oa}}{u_{sdc} - u_{pdc}} \quad (96)$$

As before, the energy associated with the passage of the shock wave induced by the internal debris cloud is

$$E_{Ha} = E_{oa} + \frac{1}{2} (P_{Ha} + P_{oa}) (1/\rho_{oa} - 1/\rho_{Ha}) \quad (97)$$

and the associated temperature change is again

$$\Delta T = (E_{Ha} - E_{oa})/C_{pa} \quad (98)$$

Thus, ΔT as calculated by equation (98) and $\Delta P = P_{Ha} - P_{oa}$ as calculated in equation (95) define the change in pressure and temperature due to a internal debris cloud traveling within a pressurized module in the immediate vicinity of the debris cloud itself. The attenuation of the

pressure increase as a function of distance away from the debris cloud is discussed in the following section.

6.2 Attenuation of Debris Cloud Induced Pressures

As the debris cloud moves through the module interior, it continuously sets up a shock wave in the module air. Thus, attenuation of the shock wave so created can occur only when there is no longer any debris cloud motion. In keeping with the assumption of constant debris cloud velocity, it is presumed that debris cloud motion ceases either when the debris cloud impacts an obstacle such as the far module wall or when the drag force due to the presence of air within the module exhausts the axial kinetic energy of the debris cloud, whichever comes first. It is at this instant that the attenuation of the shock wave is begun. Figure 6 shows a sketch of this scenario and the geometric parameters required to perform this calculation.

As can be seen in Figure 6, the distance parameter for the attenuation of the shock wave is η , not R as in Section 5.1.3. In fact, the decay of the pressure and temperature near the shock wave generated by the motion of an internal debris cloud in the module as a function of the distance η is actually obtained using the same procedure as that which was developed for the attenuation of the initial shock wave induced pressure and temperature. The only notable differences in the procedure are: 1) the quantity R in equation (86) is replaced by η and refers to the distance away from the shock wave along the direction of travel (i.e. in the x -direction) of the internal debris cloud as shown in Figure 6; and, 2) the quantity E in equation (86) now refers to the total kinetic energy of the internal debris cloud (i.e. the sum of the axial motion and expansion energies). Thus, it is presumed for the purposes of this model that the decaying shock wave keeps its shape and direction of motion during decay; only pressure and temperature magnitudes

associated with the shock wave decrease with distance once attenuation has begun.

The energy quantity required by equation (86) is found by applying momentum and energy conservation in a manner similar to that in Section 3.2.1. First, we conserve momentum before and after the impact of the first component of the secondary debris cloud on the pressure wall. Thus, we have

$$\kappa_1(m_p + m_b)v_{mc}^{sec1} = [\kappa_1(m_p + m_b) + m_{wh}]u_{mc} \quad (99)$$

where v_{mc}^{sec1} is the axial velocity of the secondary debris cloud first component, m_{wh} is the mass of the pressure wall hole-out material, and u_{mc} is the axial velocity of the internal debris cloud. We note that in equation (99) it has been assumed that the entire mass of the secondary debris cloud component used in the impact event analysis has been assumed to enter the module as part of the internal debris cloud. Second, once u_{mc} is known the kinetic energy associated with the axial motion of the internal debris cloud can be written as

$$E_{debcd}^{int,ax} = [\kappa_1(m_p + m_b) + m_{wh}]u_{mc}^2 / 2 \quad (100)$$

Next, energy conservation is applied before and after the impact of the secondary debris cloud on the pressure wall as follows:

$$E_{debcd}^{sec1,ax} + E_{debcd}^{sec1,exp} = \kappa_2[E_{pwall}^{sh\&rl}m_{wl} + E_{debcd}^{sh\&rl}\kappa_1(m_p + m_b)] + E_{debcd}^{int,ax} + E_{debcd}^{int,exp} \quad (101)$$

If we let u_{exp} denote the expansion velocity of the internal debris cloud, then we can write

$$E_{debcd}^{int,ax} = [\kappa_1(m_p + m_b) + m_{wh}]u_{mc}^2 / 2 \quad (102)$$

Substituting equations (102) into equation (101) and solving for u_{exp} yields

$$u_{exp} = \sqrt{\{E_{debcl d}^{sec l, ax} + E_{debcl d}^{sec l, exp} - (\kappa_2[E_{pwall}^{sh \&rl} m_{wl} + E_{debcl d}^{sh \&rl} \kappa_1(m_p + m_b)] + E_{debcl d}^{int, ax})\} / \{\kappa_1(m_p + m_b) + m_{wh}\} / 2} \quad (103)$$

Then, the energy quantity required by equation (86) is given by

$$E = E_{debcl d}^{int, ax} + E_{debcl d}^{int, exp} \quad (104)$$

where $E_{debcl d}^{int, ax}$ and $E_{debcl d}^{int, exp}$ are given by equations (100) and (102), respectively.

We note that the expression under the radical in equation (103) again is in the form of a difference between two quantities. Thus, there again exists a potential for spurious results if sufficient attention is not paid to, as before, the proper modeling of debris cloud velocities and, in this particular case, to the mass of the pressure wall hole-out material. The latter issue is addressed in the next sub-section.

6.2.1 Pressure Wall Hole-Out Mass

A question now arises as to what is the value of m_{wh} , the mass of the pressure wall hole-out material. Clearly, its exact value is a function of material properties as well as geometry and the conditions of the initial projectile impact. However, previous high speed impact testing of aluminum dual-wall structures at impact velocities between 6 and 8 km/sec has revealed an the following two features of the nature of pressure wall perforation in dual-wall systems under hypervelocity impact.

1) If an inner bumper is not placed between the bumper and the pressure wall, then the post-perforation pressure wall is relatively flat and its perforation consists of a single, well-defined, jagged hole in the center of the pressure wall damage area. In this case, a significant amount of mass is in fact removed from the pressure wall itself.

2) If a relatively light inner bumper is placed between the bumper and the pressure wall

(e.g. a Type A inner bumper), then a pressure wall perforation again consists of a single, well-defined jagged hole in the center of the pressure wall damage area. In this case, a significant amount of mass is removed from the pressure wall.

3) If a relatively heavy metallic or multi-material composite panel (e.g. a Type B inner bumper) is placed between the bumper and the pressure wall, then the perforated pressure wall is severely petalled. For impact velocities in excess of 6.5 km/s and projectile diameters greater than 1 cm this results in huge through-holes. However, observation of the petals themselves has shown them to be mostly sharp, and not at all stubby or short. This implies that if the petals were to be bent back to their original flat positions, they would very nearly meet at the center of impact. In these cases, therefore, almost no pressure wall mass is lost despite the inordinately large holes created.

Since the dual-wall construction to be used on the International Space Station is most likely to include some sort of thermal insulation and/or an inner bumper between the bumper and the pressure wall, it is assumed for the purposes of this study that the amount of pressure wall hole-out mass can be written as a fraction of the mass of pressure wall material that is subjected to shock heating and release by the impact of the secondary debris cloud, that is,

$$m_{wh} = \kappa_3(\kappa_2 m_{w1}) \quad (105)$$

where $\kappa_3 < 1$. For a Type A inner bumper, κ_3 can be as large as 0.5 or 0.8 while for a Type B inner bumper, κ_3 can be as small as 0.1 or 0.2.

As mentioned in the preceding section, an improper choice of κ_3 could have an adverse on the resulting internal debris cloud expansion velocity value. For example, if κ_3 is too small (i.e. we are underestimating the mass of the pressure wall hole-out material), then according to

equation (99), u_{mc} will be too large and it is conceivable that the radical in equation (99) may yield an imaginary value, which is clearly not acceptable. Naturally, there is more than one value of κ_3 that will yield expansion velocity values that are physically appropriate. However, the one that is ultimately most correct is the one that yields pressure and temperature values that are most in line with experimental results.

6.2.2. Onset of Pressure and Temperature Attenuation

Referring to Figure 6, the distance away from the pressure wall at which the attenuation of the shock wave induced pressures and temperatures begins is denoted by 'H'. This distance is calculated by balancing the axial kinetic energy of the debris cloud and the work done by the drag force due to the presence of the module air as the debris cloud moves through the module. Naturally, if the value so calculated exceeds, for example, the distance from the impact site on the pressure wall to the nearest obstacle within the module (such as, for example, the far module wall), then the distance H would simply be the distance to the nearest obstacle.

Thus, we write

$$E_{debclcd}^{int,ax} = F_D H \quad (106a)$$

where $E_{debclcd}^{int,ax}$ is the axial kinetic energy of the internal debris cloud and F_D is the drag force due to the module air. Elementary fluid dynamics provides the following expression to calculate the drag force:

$$F_D = \rho_a C_D A_p V^2 / 2 \quad (106b)$$

where $\rho_a = 1.22 \text{ kg/m}^3$ is the density of air, C_D is the drag coefficient, A_p is the presented area of the moving object, and V is the velocity of motion through the air. The drag coefficient is

typically a function of the Reynolds number Re which itself is given by

$$Re = \rho_a V D_p / \mu_a \quad (107)$$

where D_p is the presented diameter and $\mu_a = 1.78 \times 10^{-5}$ kg/m-sec is the viscosity of air. Assuming a nominal debris cloud diameter of 10 cm (i.e. $D_p = 0.1$ m) and a nominal debris cloud axial velocity of 1 km/sec (i.e. $V = 1000$ m/sec) and substituting these values into equation (107) yields a Reynolds number in excess of 10^6 . In this Reynolds number regime, the drag coefficient curve for a sphere is relatively flat with a value between 0.1 and 0.3. The specific value of C_D used in this model will be discussed in a later section.

To solve for the distance H , we note that $A_p = \pi R_{dc}^2$. In addition, at the onset of attenuation (see again Figure 6), the radius of the debris cloud R_{dc} can be obtained using the following relationships between debris cloud spread half-angle, the axial and transverse debris cloud velocities, and the geometry involved:

$$\tan \phi_{dc} = \frac{u_{exp}}{u_{mc}} \quad (108a)$$

$$\sin \phi_{dc} = \frac{R_{dc}}{H - R_{dc}} \quad (108b)$$

Thus, we have

$$\phi_{dc} = \tan^{-1} \left(\frac{u_{exp}}{u_{mc}} \right) \quad (109a)$$

$$R_{dc} = H f_\phi, \quad f_\phi = \frac{\sin \phi_{dc}}{1 + \sin \phi_{dc}} \quad (109b,c)$$

Substituting equations (106b) and (109b) into equation (106a), we obtain

$$E_{debclcd}^{int, ax} = \pi C_D \rho_a f_\phi^2 u_{mc}^2 H^3 / 2 \quad (110)$$

where V , the debris cloud characteristic velocity, has been replaced by u_{mc} . Solving for H yields

$$H = \sqrt[3]{\frac{E_{debcl d}^{int, ax}}{\pi C_D \rho_a f_\phi^2 u_{mc}^2 / 2}} \quad (111)$$

6.2.3 Pressure and Temperature Values at a Specified Location

In order to determine the pressure and temperature values at a specified location within the module due to the passage of the internal debris cloud, several preliminary issues must be addressed. These issues are discussed sequentially, and are followed by a development of the equations required to obtain the desired information.

First, if the point of interest is within the cone angle formed the motion and expansion of the internal debris cloud (region ABC in Figure 7), then personnel at the point of interest will probably be struck by the debris cloud itself; hence, the issue of pressure and temperature becomes secondary to the major concern of surviving the debris cloud impact.

Second, if the point of interest is not within the cone angle characterizing the spread of the debris cloud, but is within the volume of air that is traversed by the shock wave induced by the motion of the debris cloud (region CAD in Figure 7), then personnel at the point of interest will feel the full pressure and temperature associated with the passage of the shock wave itself. Hence, it is not necessary to perform any attenuation of the shock wave induced pressure and temperature increases for such points of interest.

Third, although the shock wave is presumed not to fan out during decay, its growth in the lateral direction (i.e. perpendicular to the axial direction of its motion) can still be observed as shown in Figure 7. If the point of interest is outside region HGEF, i.e. the cylindrical volume of module air whose base corresponds to the maximum extent of the attenuating shock wave, then

personnel at the point of interest will not feel any of the effects of the debris cloud shock wave.

Fourth, once the pressure jump across the decaying shock wave (i.e. in the x-direction) is less than 1% of ambient, it is assumed that we are in fact at ambient conditions and the attenuation process stops. Any point of interest that lies “ahead of” the shock wave in such a state will not experience any of the effects of the debris cloud or the shock wave it creates while a point of interest “behind” it will. Naturally, the attenuation process must first be performed to identify the position of this decayed shock wave, after which it can then be determined whether or not the point of interest lies “behind” it or “ahead of” it. If during the attenuation process the point of interest is traversed by the decaying shock wave, then the attenuation process stops and the pressure and temperature at the point of interest are available.

6.2.4 Definition of Shock Wave Position

Based on the discussion in the preceding section, it is apparent that a functional form of the shock wave at the time attenuation begins and throughout the attenuation process is required. We begin by considering a shock wave in two dimensions and then extend the results to three dimensions. The equation itself derived from the fact that the curve describing the shock wave must satisfy at least the following two conditions. First, far from the leading edge of the shock wave, the angle defining the slope of the curve is given by

$$\mu = \sin^{-1}(1/M) \quad (112)$$

where $M = u_{sd}/c_{0a}$ is the shock wave mach number. Second, at the leading edge, the curve is perpendicular to the direction of travel. Although there are a number of curves that satisfy these conditions, the simplest curve that does so is the hyperbola. The specific form of the hyperbola that is appropriate for shock wave characterization is obtained as follows.

Consider the generic two-dimensional hyperbola shown in Figure 8. We recall the following properties of such a hyperbola in Cartesian coordinates:

$$\text{Equation:} \quad (x/a)^2 - (y/b)^2 = 1 \quad (113a)$$

$$\text{Asymptote Slope:} \quad m = b/a \quad (113b)$$

$$\text{Distance From Origin to Vertex:} \quad a$$

$$\text{Distance From Origin to Focus:} \quad c$$

$$\text{Relationship Between } c \text{ \& } a: \quad c^2 = a^2 + b^2 \quad (113c)$$

Next, we note that equation (112) implies that the slope of the curve can also be written as

$$m = \frac{1}{\sqrt{M^2 - 1}} \quad (114)$$

Equating equations (113b) and (113d) allows us to solve for 'b' in terms 'a', to wit,

$$b = \frac{a}{\sqrt{M^2 - 1}} \quad (115)$$

Finally, as shown in Figure 8, we place the center-of-mass of the debris cloud at the focus of the hyperbola. In this case, we note that the leading edge of the shock wave is located at some distance Δ ahead of the debris cloud, which has some characteristic radius R_{dc} . This distance Δ is obtained from elementary shock physics theory (see, e.g., [15]) and is given by

$$\Delta = 0.8 R_{dc}(\rho_{0a}/\rho_{Ha}) \quad (116)$$

where ρ_{Ha} is given by equation (83) and R_{dc} is given by equation (109b,c).

We note in passing that Region ABC as discussed in Section 6.2 can now also be defined. Specifically, Region ABC in Figure 7 is defined by $\tan\phi_{dc} = u_{exp}/u_{mc}$. If we assume axial symmetry with respect to the x-axis (i.e. the longitudinal axis of the debris cloud), then to determine whether or not the point of interest, whose coordinates are given by $(x_{poi}, y_{poi}, z_{poi})$,

is within Region ABC, we note that the equation of the circle in the y-z plane with its center at $x=x_{poi}$ and lying on the cone subtended by the semi-vertex angle ϕ_{dc} is given by

$$y^2 + z^2 = (x_{poi} \tan \phi_{dc})^2 = R_{x_{poi}}^2 \quad (117)$$

If

$$y_{poi}^2 + z_{poi}^2 \leq R_{x_{poi}}^2 \quad (118)$$

then the point of interest is within Region ABC and personnel at that point will probably be struck by the expanding debris cloud. However, if

$$y_{poi}^2 + z_{poi}^2 > R_{x_{poi}}^2 \quad (119)$$

then the point of interest is outside Region ABC.

Once the center-of-mass of the internal debris cloud is placed at the focus of the hyperbola, it follows that the distance from the origin to the focus can also be written as

$$c = a + \Delta + R_{dc} \quad (120)$$

Substituting for 'b' in terms of a according to equation (115) into equation (113c), solving for 'c', equating the result to equation (120), and solving for 'a' finally yields

$$a = \frac{\Delta + R_{dc}}{\frac{M}{\sqrt{M^2 - 1}} - 1} \quad (121)$$

Since a and b are now both determined, the equation for the hyperbola approximating the shape of the shock wave created by a moving internal debris cloud is also completely determined. To be applicable to the two-dimensional coordinate system shown in Figure 8, the x-coordinate in equation (113a) must be offset by an amount h, that is, the equation for the two-dimensional hyperbola is now written as

$$\left(\frac{x-h}{a}\right)^2 - \left(\frac{y}{b}\right)^2 = 1 \quad (122)$$

The quantity h is obtained by noting that the origin in Figure 7 is shifted over an amount $H + \Delta + a$ when compared to the origin in Figure 8; hence,

$$h = H + \Delta + a \quad (123)$$

In three dimensions, making use of the axial symmetry about the x -axis, equation (123) becomes

$$\left(\frac{x-h}{a}\right)^2 - \left(\frac{y}{b}\right)^2 - \left(\frac{z}{b}\right)^2 = 1 \quad (124)$$

Thus, the position of the shock wave at the onset of attenuation is now defined, and Region CAD as discussed in Section 6.2 can now also be defined. Specifically, the y - and z -coordinates (y_{pw} , z_{pw}) of the circle on the pressure wall with its center at $x=0$ and passing through Point D in Figure 7 is obtained simply by setting $x=0$ in equation (124), to wit,

$$\left(\frac{y_{pw}}{b}\right)^2 + \left(\frac{z_{pw}}{b}\right)^2 = \left(\frac{H + \Delta + a}{a}\right)^2 - 1 \quad (125)$$

To determine whether or not the point of interest, whose coordinates are given by (x_{poi} , y_{poi} , z_{poi}), is within a region like the two-dimensional region CAD, we note that the equation of the circular cross-section of the three-dimensional hyperboloid at $x = x_{poi}$ is given by

$$\left(\frac{y}{b}\right)^2 + \left(\frac{z}{b}\right)^2 = \left[\frac{x_{poi} - (H + \Delta + a)}{a}\right]^2 - 1 = (R_{x_{poi}})^2 \quad (126)$$

If it is true that

$$\left(\frac{y_{poi}}{b}\right)^2 + \left(\frac{z_{poi}}{b}\right)^2 \leq (R_{x_{poi}})^2 \quad (127)$$

then the point of interest is within a region like Region CAD and the full effects of the shock wave are felt at the point of interest. However, if

$$\left(\frac{y_{poi}}{b}\right)^2 + \left(\frac{z_{poi}}{b}\right)^2 > (R_{x_{poi}})^2 \quad (128)$$

then the point of interest is outside a region like Region CAD and only the effects of an attenuated shock wave (or not at all) are experienced at the point of interest.

To define the curve corresponding to the position of the shock wave at the completion of the attenuation process (i.e. pressures and temperatures have decayed to ambient conditions), we recall that we have assumed that the shock wave merely translates axially without fanning out during the attenuation process. In this manner, the x-coordinate of the origin of the hyperbola shifts by an amount η_i , where η_i is the distance away from the full-strength shock wave at the i-th attenuation step. Thus, when $\eta_i = \eta_{amb}$, if we let $(y_{pw,amb}, z_{pw,amb})$ denote the y- and z-coordinates of the circle on the pressure wall that has its center at $x=0$ and that lies on the “ambient” hyperboloid, then equation (125) becomes

$$\left(\frac{y_{pw,amb}}{b}\right)^2 + \left(\frac{z_{pw,amb}}{b}\right)^2 = \left(\frac{H + \Delta + a + \eta_{amb}}{a}\right)^2 - 1 \quad (129)$$

As before, to determine whether personnel at a point of interest defined by the coordinates $(x_{poi}, y_{poi}, z_{poi})$ experience the effects of an attenuated shock wave or not at all, we first calculate the quantity

$$(R'_{x_{poi}})^2 = \left[\frac{x_{poi} - (H + \Delta + a + \eta_i)}{a} \right]^2 - 1 \quad (130)$$

where η_i is the distance away from the full strength shock wave at the i-th attenuation step. If

$$\left(\frac{y_{poi}}{b}\right)^2 + \left(\frac{z_{poi}}{b}\right)^2 \leq (R'_{x_{poi}})^2 \quad (131)$$

then the point of interest is within the “zone of influence” of the attenuating shock wave; if

$$\left(\frac{y_{poi}}{b}\right)^2 + \left(\frac{z_{poi}}{b}\right)^2 > (R'_{x_{poi}})^2 \quad (132)$$

then it is outside this zone of influence at the current attenuation step. If however, equation (132) is true for the entire attenuation procedure, then no shock effects are experienced at the point of interest. Likewise, if the pressure jump across the shock wave has decayed to less than 1% of ambient and the point of interest has not yet been reached, then the attenuation process stops and we again presume that we are at ambient conditions and that personnel at the point of interest do not experience any shock wave effects.

Finally, we note that as the attenuation process progresses, if the point of interest is over-run by the shock wave, then an interpolation procedure is employed to determine the pressure and temperature at the point of interest. However, in the case of a shock wave due to the passage of an internal debris cloud, the interpolation process is somewhat more complicated than the elementary one employed for the spherically expanding shock wave in Section 5.3.1. In this case, since the attenuation proceeds in the x-direction, we must first calculate, x_{fs} , the x-coordinate of the point on the hyperboloid corresponding to the y- and z-coordinates of the point of interest. This is done by solving for x in equation (89c). Once this value is obtained, then the interpolation is performed between the pressures and temperatures at the i-th and (i-1)-th attenuation steps, where the x-coordinate of the point of interest has been over-run in the i-th step, by referencing x_{poi} to $x_{fs} + \eta_{i-1}$.

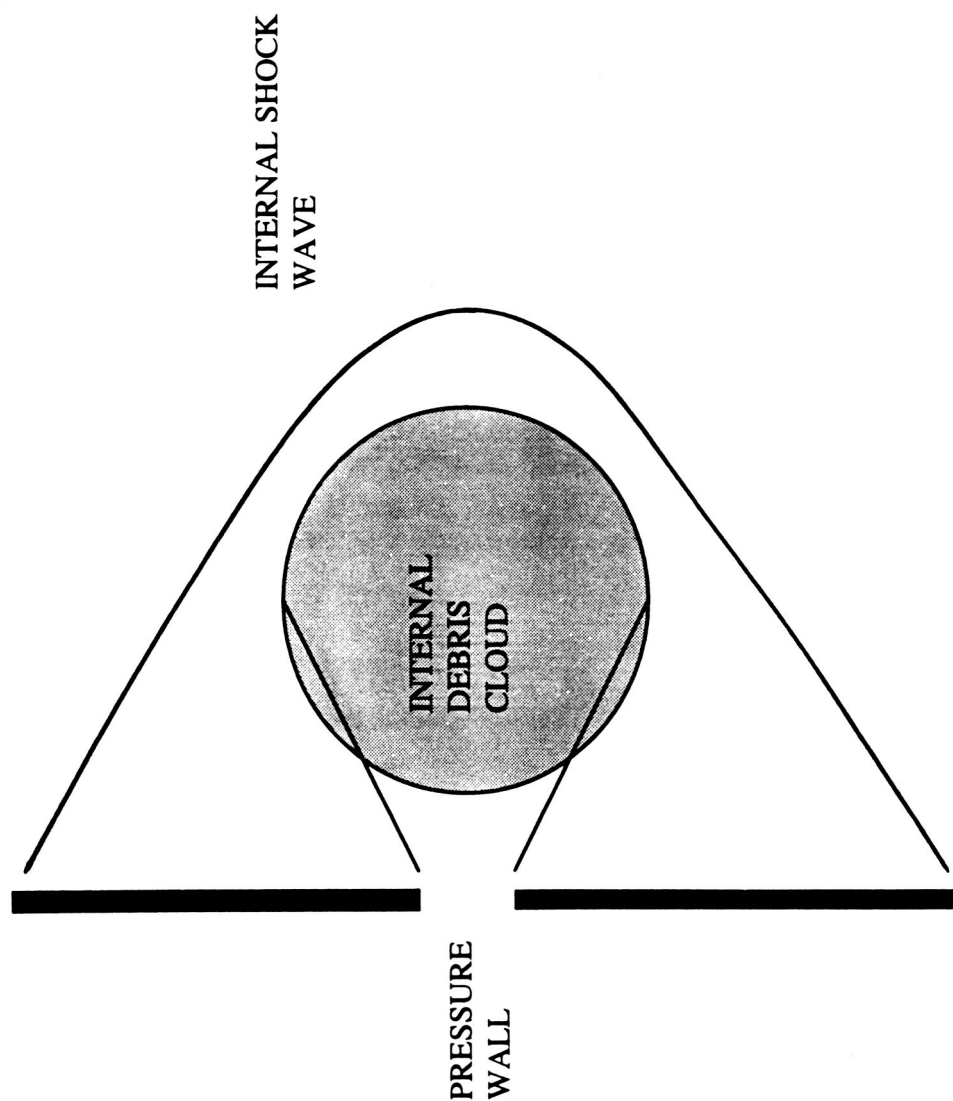


Figure 5. Generic Internal Debris Cloud With Accompanying Shock Wave

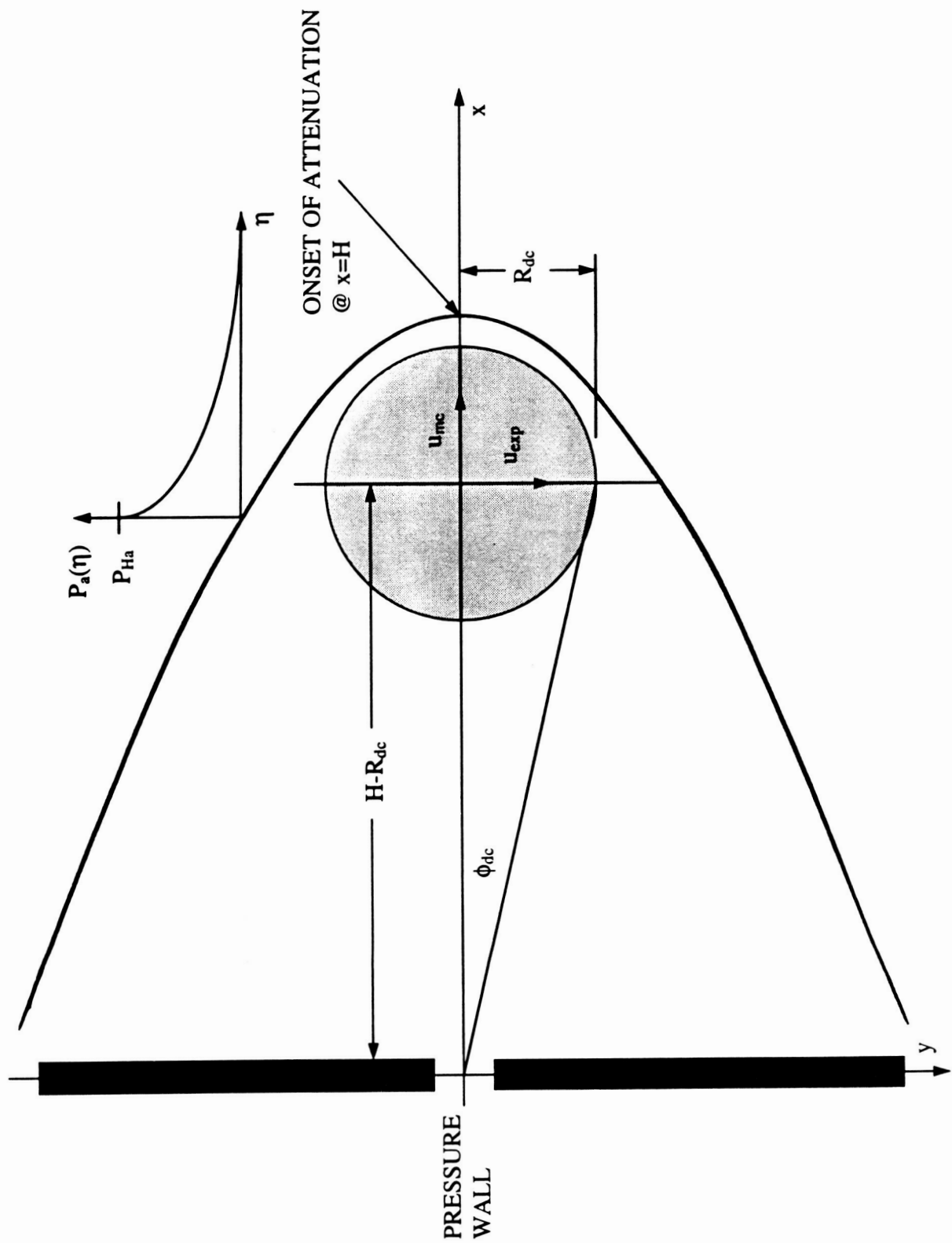


Figure 6. Onset of Internal Debris Cloud Shock Wave Attenuation

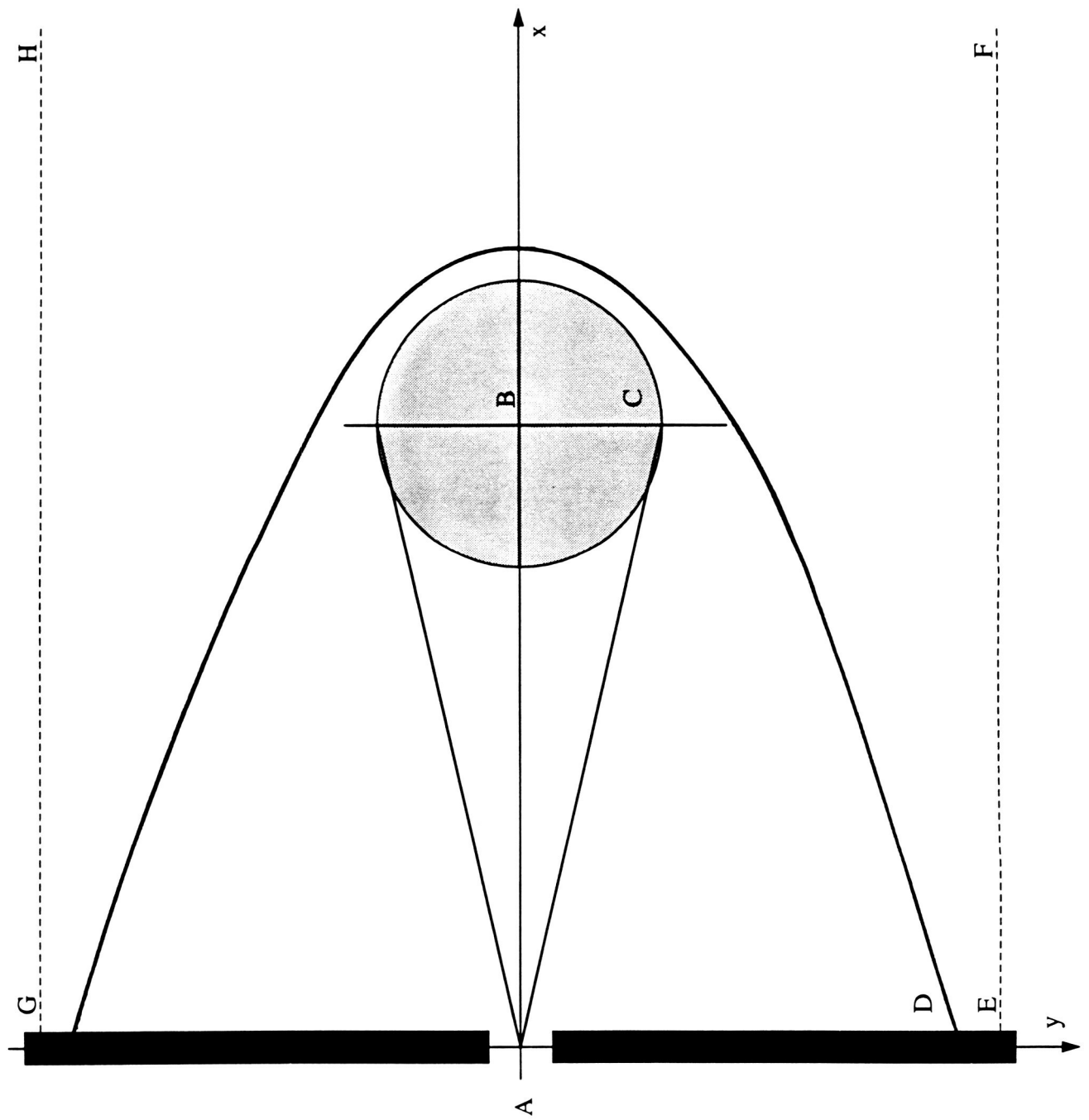


Figure 7. Pressure and Temperature Values at a Specific Location Due to a Debris Cloud Induced Shock Wave

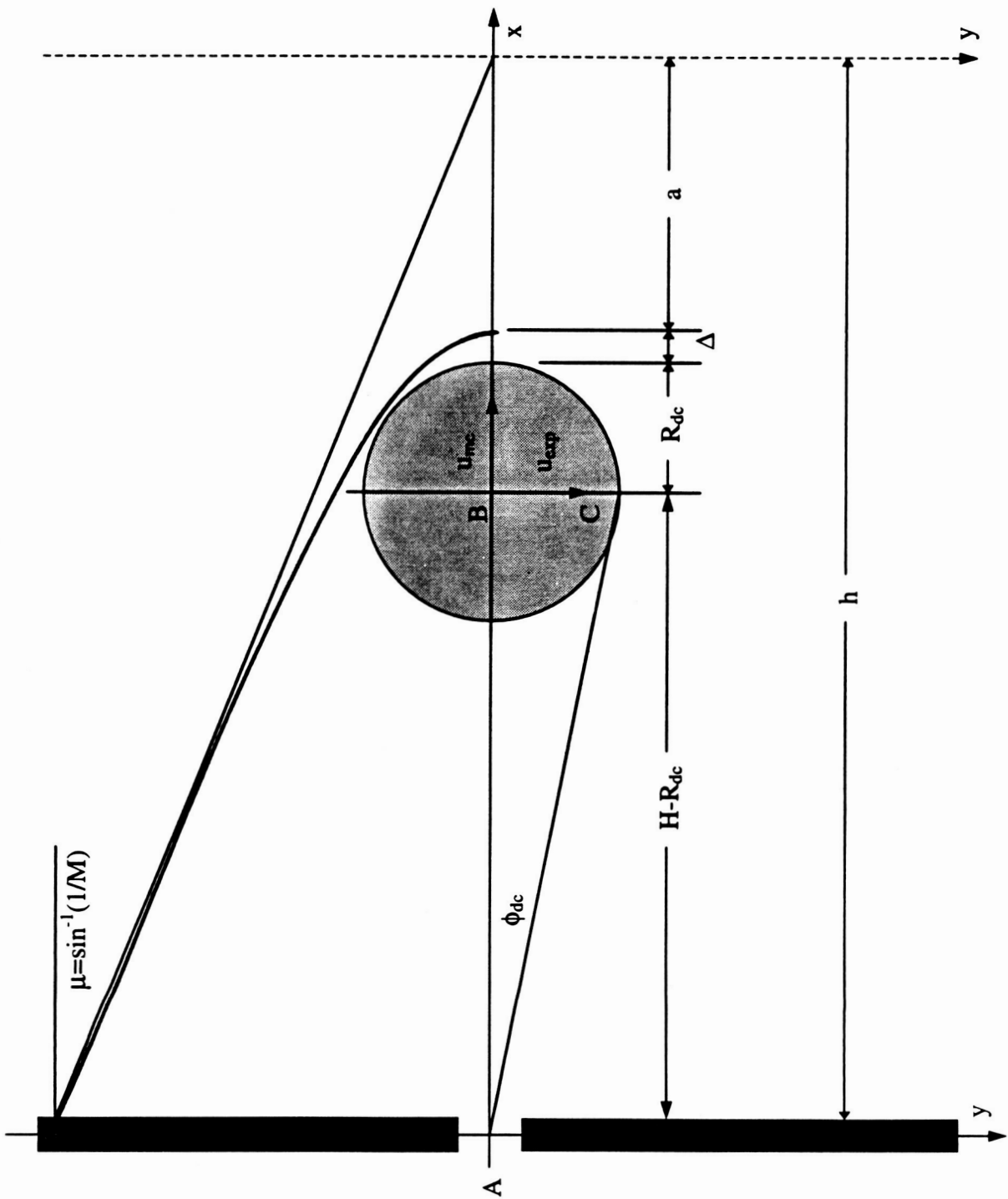


Figure 8. Two-Dimensional Hyperbola as a Model for a Debris Cloud Induced Shock Wave

7.0 SUPERPOSITION OF INDIVIDUAL INTERNAL EFFECTS

In modeling the interaction of the phenomena discussed in Chapters 5 and 6, one of the key issues is the partitioning of the kinetic energy of the initial debris cloud when both a shock wave and an internal debris cloud are created and propagate into the module interior. Once this partitioning is performed, the analysis required to model the interaction of an initial shock wave and an internal debris cloud on the pressure and temperature at a specific point within the module proceeds in a relatively straightforward manner.

7.1 Energy Partitioning

To begin, we write the following energy balance between the energy of the system before and after the impact of the initial debris cloud on the pressure wall:

$$E_{debcl d}^{sec l, ax} + E_{debcl d}^{sec l, exp} = \kappa_2 [E_{pwall}^{sh \& rl} m_{wl} + E_{debcl d}^{sh \& rl} \kappa_1 (m_p + m_b)] + \hat{E}_{shwave}^{initial} + \hat{E}_{debcl d}^{int, ax} + \hat{E}_{debcl d}^{int, exp} \quad (133)$$

We note that equation (133) is very similar to equations (87) and (101) in Section 5.3 and 6.2.

The '^' symbol over the initial shock wave and internal debris cloud energy terms in equation (133) denoted modified values calculated when a shock wave and an internal debris cloud are both present.

As in Section 6.2, the kinetic energy associated with the axial motion of the debris cloud is written as

$$\hat{E}_{debcl d}^{int, ax} = \frac{1}{2} [\kappa_1 (m_p + m_b) + m_{wh}] (\hat{u}_{mc})^2 \quad (134)$$

where \hat{u}_{mc} is the axial velocity of the of the internal debris cloud. If the momentum of the shock wave is ignored in the conservation of momentum before and after the impact of the secondary debris cloud first component on the pressure wall, then this quantity is found by solving equation (99) with the following result:

$$\hat{u}_{mc} = u_{mc} = \frac{\kappa_1(m_p + m_b)v_{mc}^{sec1}}{\kappa_1(m_p + m_b) + m_{wh}} \quad (135)$$

where v_{mc}^{sec1} is the momentum conservation based characteristic velocity of the first component of the secondary debris cloud. We note that, under the assumptions made, the value of u_{mc} does not depend on whether or not an initial shock is created in addition to the internal debris cloud. However, the presence of the initial shock wave does become a factor when we calculate the kinetic energy associated with the expansion of the internal debris cloud. As in Section 6.2, this energy is written as

$$E_{debclcd}^{int,exp} = \frac{1}{2}[\kappa_1(m_p + m_b) + m_{wh}](u_{exp})^2 \quad (136)$$

where, in this case, u_{exp} is still unknown. As such, equation (101) as written in Section 6.2 would have two unknowns and could not be solved directly for u_{exp} . Thus, another equation relating u_{mc} and u_{exp} is required. This equation is obtained by noting that the expansion velocity of a debris cloud, at least near the front of the debris cloud on the trajectory centerline, is also the difference between the leading edge velocity and the center-of-mass velocity of the debris cloud. If we presume this to be true for the entire debris cloud, we can then write

$$u_{exp} = u_{le} - u_{mc} \quad (137)$$

where u_{le} is the leading edge velocity of the internal debris cloud.

We note that if we simply took u_{le} to be equal to the interface particle velocity obtained from the impedance matching calculations as in Section 6.1, i.e. $u_{le}=u_2=u_3=u_{sdc}$, then the interaction between the creation of the initial shock wave and the motion of the internal debris cloud would be minimal. Specifically, if we claim that u_{le} or u_{sdc} is already known, then all that remains to be done is to solve for the energy associated with the initial shock wave using equation (133). Once this value is obtained, we then obtain peak pressures and temperatures and their attenuated values using the techniques presented in Chapters 5 and 6.

However, the presumption that $u_{le}=u_{sdc}$ tacitly implies that the radial expansion as well as the axial motion of the internal debris cloud is independent of the presence of an initial shock wave in addition to the debris cloud. After all, we are using values obtained in Chapter 6 to characterize its motion and expansion, and those values were obtained assuming the presence of only an internal debris cloud. If we wish more of an interaction to exist between the axial motion and radial expansion of the internal debris cloud and the creation of the initial shock wave, then the leading edge velocity of the internal debris cloud should be modified somehow from the value calculated in Chapter 6. Specifically, the modified value should reflect the fact that some portion of the kinetic energy associated with the expansion of the internal debris cloud has been absorbed by the creation of the initial shock wave and vice versa.

To this end, we propose to use the following relationship between debris cloud leading edge velocities and initial shock wave energies:

$$\frac{\left(\hat{u}_{sdc}\right)^2}{E_{shwave}^{initial}} = \frac{(u_{sdc})^2}{E_{shwave}^{initial}} \quad (138)$$

In equation (138), $E_{shwave}^{initial}$ and u_{sdc} refer to the initial shock wave energy and internal debris cloud leading edge velocity that were computed independently in Chapters 5 and 6 while corresponding quantities with a '^' symbol denote a coupled initial shock wave energy and internal debris cloud leading edge velocity. Then, according to equation (138), we can write

$$E_{shwave}^{\wedge initial} = E_{shwave}^{initial} \left(\frac{u_{sdc}^{\wedge}}{u_{sdc}} \right)^2 \quad (139)$$

Substituting for $E_{shwave}^{\wedge initial}$ in equation (133) according to equation (139) and rearranging terms yields the following equation for u_{sdc}^{\wedge} :

$$u_{\Delta E}^2 = E_o (u_{sdc}^{\wedge})^2 + (u_{sdc}^{\wedge} - u_{mc})^2 \quad (140)$$

where

$$E_o = \frac{E_{shwave}^{initial}}{[\kappa_1(m_p + m_b) + m_{wh}] u_{sdc}^2 / 2} \quad (141)$$

$$u_{\Delta E}^2 = \frac{\Delta E}{[\kappa_1(m_p + m_b) + m_{wh}] / 2} \quad (142)$$

and

$$\Delta E = E_{debcl d}^{sec 1, ax} + E_{debcl d}^{sec 2, exp} - \{ \kappa_2 [E_{pwall}^{sh \&rl} m_{wl} + E_{debcl d}^{sh \&rl} \kappa_1(m_p + m_b)] + [\kappa_1(m_p + m_b) + m_{wh}] u_{mc}^2 / 2 \} \quad (143)$$

Solving equation (143) for the leading edge velocity of the internal debris cloud in the presence of an initial shock wave yields

$$\hat{u}_{sdc} = \frac{u_{mc} + \sqrt{u_{mc}^2 - (E_o + 1)(u_{mc}^2 - u_{\Delta E}^2)}}{E_o + 1} \quad (144)$$

Then, once \hat{u}_{sdc} is known, the expansion velocity of the internal debris cloud is found using equation (137) with $u_{le} = \hat{u}_{sdc}$ (which is now also the velocity of the shock wave created by the motion of the internal debris cloud), and the energy associated with the creation of the initial shock wave is found directly using equation (139). Once again, we note that the expression for \hat{u}_{sdc} contains a radical under which is an expression that is in the form of a difference between two quantities. In addition, we note that substituting the value of \hat{u}_{sdc} as obtained using equation (144) into equation (137) may yield a negative expansion velocity. In both cases, adjusting the value of u_{mc} (or, rather, m_{wh}) would improve the results.

7.2 Initial Shock Wave Pressures and Temperatures

7.2.1 Peak Pressures and Temperatures

In the preceding section, a procedure was presented to calculate the leading edge velocity of an internal debris cloud (which is then also the velocity of the shock wave created by the motion of this debris cloud) when an initial shock wave was also present. As was stated during the course of that development, the leading edge velocity so calculated is directly related to the particle velocity at the module wall/air interface when both an initial shock wave and an internal debris cloud are created. Applying this information to the concepts and equations in Chapter 5 allows us to write the total particle velocity in the air immediately adjacent to the module wall as

$$\hat{u}_{pa} = \hat{u}_{sdc} + u_{pw} \quad (145)$$

from which the initial shock wave velocity is given by:

$$\hat{u}_{sa} = c_o + k \hat{u}_{pa} \quad (146)$$

Now that \hat{u}_{pa} and \hat{u}_{sa} are known, the peak pressure and temperature induced by the initial shock wave are readily obtained using the equations in Section 5.2 as follows:

$$\hat{P}_{Ha} = P_{oa} + \rho_{oa} \hat{u}_{sa} \hat{u}_{pa} \quad (147)$$

and

$$\hat{\Delta T} = (\hat{E}_{Ha} - E_{oa}) / C_{pa} \quad (148)$$

where

$$\hat{E}_{Ha} = E_{oa} + \frac{1}{2} (\hat{P}_{Ha} + P_{oa}) (1 / \rho_{oa} - 1 / \rho_{Ha}) \quad (149)$$

and

$$\rho_{Ha} = \frac{\hat{u}_{sa} \rho_{oa}}{\hat{u}_{sa} - \hat{u}_{pa}} \quad (150)$$

7.2.2 Attenuated Pressures and Temperatures

The attenuation of the peak pressure and temperature defined in the preceding section follows a procedure virtually identical to that developed in Section 5.4. The only difference is that we now use the ‘^’ quantities where appropriate to denote the shock wave pressures, velocities, etc. that are calculated considering the presence of an internal debris cloud as well. Specifically, we now have

$$\hat{P}_a(R) = \frac{P_s'(R')}{P_s'(R' = 0.01)} \hat{P}_{Ha} \quad (151)$$

$$R = R' (E / P_{Oa})^{1/3}, E = E_{shwave}^{initial} \quad (152a,b)$$

$$\hat{\Delta T} = [\hat{E}_a(R) - E_{Oa}] / C_{pa} \quad (153)$$

$$\hat{E}_a(R) = E_{Oa} + \frac{1}{2} [\hat{P}_a(R) + P_{Oa}] [1 / \rho_{Oa} - 1 / \rho_a(R)] \quad (154)$$

$$\hat{\rho}_a(R) = \frac{\hat{u}_s(R) \rho_{Oa}}{\hat{u}_s(R) - \hat{u}_p(R)} \quad (155)$$

$$\hat{u}_s(R) = c_{Oa} + k_a \hat{u}_p(R) \quad (156)$$

$$\hat{u}_p(R) = \frac{-\rho_{Oa} c_{Oa} + \sqrt{\hat{D}}}{2k_a \rho_{Oa}} \quad (157)$$

$$\hat{D} = (\rho_{Oa} c_{Oa})^2 - 4k_a \rho_{Oa} [P_{Oa} - \hat{P}_a(R)] \quad (158)$$

7.2.3 Pressure and Temperature Values at a Specified Location

The procedure for calculating the pressure and temperature increase at a specified location within the module for an initial shock wave that has been created in conjunction with an internal debris cloud is identical to that already presented in Section 5.4.1.

7.3 Internal Debris Cloud Pressures and Temperatures

7.3.1 Peak Pressures and Temperatures

As was stated in Section 7.1, the leading edge velocity is also the velocity of the shock wave created by the motion of the internal debris cloud. Following the procedure in Section 6.1,

the particle velocity in the air induced by the motion of the shock wave accompanying the internal debris cloud is given by

$$\hat{u}_{pdc} = (\hat{u}_{sdc} - c_{oa}) / k_a \quad (159)$$

from which the peak pressure behind the shock wave and the corresponding peak temperature increase are given by

$$\hat{P}_{Ha} = P_{oa} + \rho_{oa} \hat{u}_{sdc} \hat{u}_{pdc} \quad (160)$$

$$\hat{\Delta T} = (\hat{E}_{Ha} - E_{oa}) / C_{pa} \quad (161)$$

where

$$\hat{E}_{Ha} = E_{oa} + \frac{1}{2} (\hat{P}_{Ha} + P_{oa}) (1 / \rho_{oa} - 1 / \rho_{Ha}) \quad (162)$$

and

$$\rho_{Ha} = \frac{\hat{u}_{sdc} \rho_{oa}}{\hat{u}_{sdc} - \hat{u}_{pdc}} \quad (163)$$

7.3.2 Attenuated Pressures and Temperatures

The attenuation of the peak pressure and temperature defined in the preceding section follows a procedure virtually identical to that developed in Sections 5.4, 6.2, and 7.2.2. Once again, referring to Figure 6, we use η and not R as the distance parameter for the attenuation process, and, as in Section 7.2.2, we use the ' \wedge ' quantities where appropriate to denote the shock wave pressures, velocities, etc. that are calculated considering the presence of an internal debris cloud as well as an initial shock wave. Finally, as in Section 6.2, the quantity E in equations (86)

and (152a) now refers to the kinetic energy associated with the motion of the internal debris cloud and is given by the sum of the energies in equations (134) and (136).

7.3.3 Pressure and Temperature Values at a Specified Location

The procedure for calculating the pressure and temperature increase at a specified location within the module for shock wave that has been created due to the motion of an internal debris cloud is nearly identical to that presented in Sections 6.2. The major difference lies in the definition of the internal debris cloud spread cone angle and the radius of the internal debris cloud. Specifically, we now have

$$\tan \hat{\phi}_{dc} = \frac{\hat{u}_{sdc} - u_{mc}}{u_{mc}} \quad (164)$$

and

$$\sin \hat{\phi}_{dc} = \frac{\hat{R}_{dc}}{H - \hat{R}_{dc}} \quad (165)$$

from which

$$\hat{\phi}_{dc} = \tan^{-1} \left(\frac{\hat{u}_{sdc} - u_{mc}}{u_{mc}} \right) \quad (166)$$

and

$$\hat{R}_{dc} = \frac{H \sin \hat{\phi}_{dc}}{1 + \sin \hat{\phi}_{dc}} \quad (167)$$

Following these revisions, the process to calculate the temperature and pressure at a specified location due to the motion and attenuation of a shock wave created by an internal debris cloud

follows the same procedure as outlined in Sections 6.2.1 and 6.2.2.

7.4 Cumulative Pressure and Temperature Values at a Specified Location

Once the pressure and temperature values at a specified location have been determined due to the passage of the initial shock wave and the shock created by the passage of the internal debris cloud, their cumulative effect at that point is obtained by merely adding the results together.

8.0 COMPARISON WITH EXPERIMENTAL RESULTS

8.1 Test Configurations and Impact Parameters

The predictions of the model developed herein are compared against the experimental results obtained from 4 high speed impact tests conducted at the University of Alabama in Huntsville Aerophysics Research Center. A detailed description of the test facility has been presented in Volume I of this two volume report. Table 2 below presents a summary of the geometric and impact parameters for the 4 impact tests.

Table 2. Impact Parameters and System Geometries

Test No.	d_p (cm)	V_p (km/s)	t_b (cm)	S (cm)	t_w (cm)	Inner Bumper
1	1.27	6.70	0.16	11.43	0.48	Type A
3	1.59	6.42	0.16	11.43	0.48	Type A
5	1.59	6.58	0.16	11.43	0.48	Type B
6	1.59	6.50	0.16	11.43	0.48	Type A

The MLI in both cases consisted of 20 mylar layers. In the case of the Type B inner bumper, the multi-layer composite material panel consisted of 6 layers of Nextel AF62, 6 layers of Kevlar 710, and a 0.203 cm thick graphite/epoxy panel. Additional information regarding the composition of the Type B inner bumper can be found in Reference [16]. Finally, in all cases the initial ambient temperature behind the pressure wall was 24°C.

Table 3 below presents a summary of the x-, y-, and z-coordinates of the various pressure (P) and temperature (T) sensors that were used to gather the pressure and temperature change data. It is these coordinates that are input into the model to produce the theoretical predictions.

The final column in Table 3 shows the distance from the origin of the coordinate system to the sensor location.

Table 3. Sensor Coordinates

Sensor	Sensor Types	Shot No.	x (cm)	y (cm)	z (cm)	R _d (cm)
1E	P, T	All	18.0	61.0	0.0	63.6
2E	P, T	All	119.0	61.0	0.0	133.7
3E	P, T	All	203.0	61.0	0.0	212.0
1W	P, T	All	18.0	-61.0	0.0	63.6
2W	P, T	All	119.0	-61.0	0.0	133.7
3W	P	All	203.0	-61.0	0.0	212.0
3W	T	1	203.0	-61.0	0.0	212.0
3W	T	3,5,6	203.0	0.0	0.0	203.0

As can be seen in Table 3, Pressure Sensors 1W, 2W, and 3W were mirror images of Pressure Sensors 1E, 2E, and 3E, respectively, with respect to the x-axis for all the tests while the symmetry of the temperature sensors was in effect for Test No. 1 only. For Test Nos. 3,5 and 6, Temperature Sensor 3E was placed in the same position as in Test No. 1 while Temperature Sensor 3W was placed directly on the x-axis at the corresponding distance. Therefore, in subsequent tables, when comparing model predictions to experimental results, the results for Sensors 1E,W, 2E,W, and 3E,W will be grouped together.

8.2 Model Parameter Values

As discussed in the preceding chapters, the results produced by the analytical model depend on the values of the empirical constants ' n ', κ_2 , and κ_3 . Poorly chosen values could lead to either spurious results (e.g. negative or imaginary debris cloud expansion velocities) or unrealistic results (e.g. debris clouds that area either too heavy or too light). In addition, an improper internal debris cloud drag coefficient value could result in debris clouds that stop either

too soon or too late. In the first case, the resulting pressures and temperatures at points far removed from the pressure wall would be far too low while in the second, the shock wave produced by the motion of the internal debris cloud could possibly engulf far removed points of interest and result in pressures and temperatures at those points that are unrealistically high. Naturally, a fairly substantial experimental database is required to determine specific values of the empirical constants and the drag coefficient as functions of projectile diameter, impact velocity, system geometry, etc.

Before determining the actual values of the constants for the analytical model, a series of trial runs were performed to gain insight into the effects of the various constants on the predictions of the analytical model. These trial runs were performed at an impact velocity of 6.5 km/sec, and a dual-wall system with a 0.16 cm bumper, a 0.48 pressure wall, and a 11.43 stand-off distance, and a Type A inner bumper; a drag coefficient of 0.2 was assumed for the purposes of calculating the stopping distance of the internal debris cloud. Results were obtained at coordinates corresponding to those of Sensor 1E as given in Table 3.

Tables 4,5 and 6 present a summary of the output obtained from the trial runs that were performed to determine appropriate empirical constants. Table 4 addresses the effect of changing 'n' while holding κ_2 and κ_3 constant, while Tables 5 and 6 show the effect of varying κ_2 only and κ_3 only, respectively. Because changes in κ_2 and κ_3 affect only the internal debris cloud, comparisons of secondary debris cloud characteristics are omitted in Tables 5 and 6. Examination of these tables reveals the effects on model prediction of changing a given parameter while holding the others fixed.

Table 4. Effect of Changing 'n' on Model Predictions ($\kappa_2=0.2$, $\kappa_3=0.3$)

Parameter	n=0.2	n=1.0
κ_1	0.989	0.945
$\theta_{dc}^{sec 1}$ (deg)	34.54	34.54
$m_{dc}^{sec 1}$ (gms)	4.558	4.355
$v_{mc}^{sec 1}$ (km / s)	4.100	4.080
$v_{exp}^{sec 1}$ (km / s)	2.823	2.810
$\theta_{dc}^{sec 2}$ (deg)	34.54	34.54
$m_{dc}^{sec 2}$ (gms)	2.128	2.128
$v_{mc}^{sec 2}$ (km / s)	0.102	0.525
$v_{exp}^{sec 2}$ (km / s)	0.070	0.361
u_{pw} (km/s)	0.290	0.289
u_{pa} (km/s)	3.301	3.291
u_{sa} (km/s)	3.863	3.852
E_{sw} (J)	2.9×10^4	2.7×10^4
θ_{dc}^{int} (deg)	10.08	11.01
m_{dc}^{int} (gms)	7.476	7.13
u_{mc} (km/s)	2.500	2.496
u_{exp} (km/s)	0.511	0.503
u_{le} (km/s)	3.011	2.999
E_{dc} (J)	2.4×10^4	2.4×10^4
ΔP_{sw} (psi)	0.90	.86
ΔP_{dc} (psi)	13.26	9.58
ΔP_{tot} (psi)	14.16	10.44
ΔT_{sw} (°C)	3.63	3.47
ΔT_{dc} (°C)	37.02	28.42
ΔT_{tot} (°C)	40.65	31.89

For example, in Table 4, we see that increasing 'n' from 0.2 to 1.0 serves to decrease pressure and temperature increases due to both the shock wave and the internal debris cloud. This is due to the fact that an increase in 'n' results in a decrease in κ_1 , which in turn implies that less primary debris cloud mass is passing through the inner bumper. Because of the manner in which the energy and momentum of the primary debris cloud are partitioned among the two secondary debris cloud components, this in turn results in a decrease in the characteristic velocities of the first component of the secondary debris cloud and an increase in the second component velocities. The decrease in the characteristic velocities of the first component are directly responsible for the drop in the shock wave induced pressure and temperature increases. However, the drop in the debris cloud induced pressure and temperature increases is due to the fact that less mass is coming through the inner bumper and hence into the module itself. Because of the manner in which the creation of the module shock wave is presumed to interact with the creation of the internal debris cloud, the velocities of the internal debris cloud are only slightly lower for the larger value of 'n'. Hence, the energy associated with the internal debris cloud in the second case (a larger value of 'n') is less than that in the first case (a smaller value of 'n'), which in turn results in lower pressure and temperature increases.

In Table 5 we see that increasing κ_2 (i.e. increasing the amount of shocked and released secondary debris cloud and pressure wall material) decreases the amount of energy converted into shock wave formation which in turn decreases the pressure and temperature increases due to the module shock wave. However, increasing κ_2 also serves to increase the mass of the internal debris cloud which decreases its axial velocity. This in turn increases the expansion velocity and the spread angle of the debris cloud. The final result is that the shock wave induced by the

internal debris cloud fans out more and affects a larger volume of module air. This could cause remote points to experience higher pressure and temperature increases than if the lower value of κ_2 were used.

Table 5. Effect of Changing κ_2 on Model Predictions ($n=0.5$, $\kappa_3=0.3$)

Parameter	$\kappa_2=0.2$	$\kappa_2=0.8$
u_{pa} (km/s)	3.301	2.800
u_{sa} (km/s)	2.862	3.326
E_{sw} (J)	2.8×10^4	1.5×10^4
θ_{dc}^{int} (deg)	12.06	50.39
m_{dc}^{int} (gms)	7.399	16.154
u_{mc} (km/s)	2.481	1.137
u_{exp} (km/s)	0.530	1.374
u_{le} (km/s)	3.011	2.510
E_{dc} (J)	2.4×10^4	2.6×10^4
ΔP_{sw} (psi)	0.89	0.45
ΔP_{dc} (psi)	10.75	68.31
ΔP_{tot} (psi)	11.64	68.76
ΔT_{sw} (°C)	3.59	1.86
ΔT_{dc} (°C)	31.22	155.40
ΔT_{tot} (°C)	34.81	157.26

In Table 6 we see that increasing κ_3 (i.e. the fraction of shock and released pressure wall material that becomes part of the internal debris cloud) naturally increases the internal debris cloud mass. This again decreases the internal debris cloud axial velocity, increases the expansion velocity and the debris cloud spread angle and has the same net result as that which was observed with an increase in κ_2 .

Table 6. Effect of Changing κ_3 on Model Predictions ($n=0.5$, $\kappa_2=0.2$)

Parameter	$\kappa_3=0.3$	$\kappa_3=0.8$
u_{pa} (km/s)	3.301	3.191
u_{sa} (km/s)	2.862	3.745
E_{sw} (J)	2.8×10^4	2.6×10^4
θ_{dc}^{int} (deg)	12.06	43.16
m_{dc}^{int} (gms)	7.399	12.263
u_{mc} (km/s)	2.481	1.497
u_{exp} (km/s)	0.530	1.404
u_{le} (km/s)	3.011	2.901
E_{dc} (J)	2.4×10^4	2.6×10^4
ΔP_{sw} (psi)	0.89	0.79
ΔP_{dc} (psi)	10.75	16.40
ΔP_{tot} (psi)	11.64	17.19
ΔT_{sw} ($^{\circ}C$)	3.59	3.19
ΔT_{dc} ($^{\circ}C$)	31.22	44.06
ΔT_{tot} ($^{\circ}C$)	34.81	47.25

Based on the trends observed Tables 4, 5, and 6, it appears that if, for example, in contradiction with observed pressure and temperature phenomena, the model predicts a remote point of interest to be engulfed by a full strength debris cloud induced shock wave, then it would be appropriate, for example, to decrease either κ_2 or κ_3 , or both. An alternative means of producing such a result would be to increase the drag coefficient of the internal debris cloud. This would cause the debris cloud to stop sooner so that remote points of interest would feel only attenuated pressures and temperatures.

To determine the values of the constants ' n ', κ_2 , κ_3 , and C_D for use in the initial comparisons between the predictions of the model with experimental results, another series of

runs was performed using the model with various constant combinations. Naturally, the choice of constant combinations was guided by the trends observed in the trial runs and the actual experimental values as recorded by the pressure and temperature sensors at the locations indicated in Table 3. As such, the runs were performed using the system geometries and impact velocities as specified in Table 2. Table 7 presents a summary of the initial empirical constant values as a function of inner bumper type and projectile diameter. These constants should produce reasonable results for the impact velocities, projectile diameters, materials, and system geometries that were tested as part of this study.

Table 7. Initial Empirical Constant Values

Empirical Constant	Type A Inner Bumper		Type B Inner Bumper
Projectile Diameter (cm)	1.27	1.59	1.59
n	0.50	2.50	1.10
κ_2	0.19	0.14	0.23
κ_3	0.30	1.00	0.88
C_D	0.20	0.30	0.11

Naturally, when a sufficiently large amount of test data becomes available, it should be possible to obtain functional expressions for each of the empirical constants in Table 7 in terms of system geometry, materials, impact conditions, etc.

8.3 Comparison of Model Predictions with Experimental Results

Tables 8 through 11 present a comparison of the experimental results and the predictions of the model developed herein for the sensor locations presented previously. It is noted that only initial peak experimental values (i.e. values which occur at times less than approximately 150

msec) are compared against the predictions of the analytical model. In its present stage of development, the model is simply not capable of predicting very late time effects which involve numerous shock wave interactions and reflections. As seen from the complete data presented in Volume I, the temperature at very late times often exceed by a factor of 2 or 3 the initial peak temperature increases.

Tables 8 through 11 also show the times at which the initial peak values occurred at the various sensors. These times are presented to determine whether or not complementary sensors (e.g. Sensors 1E,W) registered peak values at approximately the same time. Ideally, due to the symmetric nature of the impact event and the sensor placement (with the exception of Temperature Sensors 3E,W for Test Nos. 3, 5, and 6), peak values should occur (nearly) simultaneously at complementary sensors and should have (nearly) identical magnitudes. Any significant deviation from nearly identical peak values and their times of occurrence is an indication of an asymmetry in the propagation or composition of the internal debris cloud. Examination of the experimental results in Tables 8 through 11 reveals that the pressure and temperature change magnitudes recorded and their times of occurrence were fairly symmetrical. Naturally, some extreme deviations did exist in certain individual instances, but as a whole the recorded values were fairly symmetrical.

Table 8. Pressure and Temperature Data Comparison (Basic Model) -- Test No. 1

Sensor	Pressure Increase			Temperature Increase		
	Time (msec)	Experimental Result (psi)	Model Prediction (psi)	Time (msec)	Experimental Result (°C)	Model Prediction (°C)
1E	1.12	17	15.2	13.3	18	43.2
1W	1.07	18	15.2	19.0	27	43.2
2E	1.93	4	0.5	21.6	23	2.2
2W	2.15	6	0.5	23.0	20	2.2
3E	2.33	3	0.2	645.8	25	0.7
3W	2.00	2	0.2	n/a	n/a	0.7

Table 9. Pressure and Temperature Data Comparison (Basic Model) -- Test No. 3

Sensor	Pressure Increase			Temperature Increase		
	Time (msec)	Experimental Result (psi)	Model Prediction (psi)	Time (msec)	Experimental Result (°C)	Model Prediction (°C)
1E	0.86	21	24.3	8.5	104	63.9
1W	1.00	21	24.3	6.5	118	63.9
2E	1.33	17	0.7	10.9	139	3.0
2W	1.50	21	0.7	10.8	94	3.0
3E	2.13	8	0.2	n/a	n/a	2.1
3W	2.83	8	0.2	115.0	40	2.1

Table 10. Pressure and Temperature Data Comparison (Basic Model) -- Test No. 5

Sensor	Pressure Increase			Temperature Increase		
	Time (msec)	Experimental Result (psi)	Model Prediction (psi)	Time (msec)	Experimental Result (°C)	Model Prediction (°C)
1E	0.95	34	34.2	13.4	64	82.7
1W	0.80	40	34.2	17.9	54	82.7
2E	2.13	10	0.0	19.6	34	0.0
2W	1.93	15	0.0	20.0	31	0.0
3E	4.07	3	0.0	n/a	n/a	0.0
3W	3.90	4	0.0	n/a	n/a	0.0

Table 11. Pressure and Temperature Data Comparison (Basic Model) -- Test No. 6

Sensor	Pressure Increase			Temperature Increase		
	Time (msec)	Experimental Result (psi)	Model Prediction (psi)	Time (msec)	Experimental Result (°C)	Model Prediction (°C)
1E	1.33	16	24.6	25.0	20	64.8
1W	1.06	31	24.6	26.3	65	64.8
2E	1.71	15	0.8	92.0	52	3.2
2W	1.54	14	0.8	53.0	63	3.2
3E	2.65	12	0.2	52.0	44	1.1
3W	2.66	7	0.2	n/a	n/a	2.1

An examination of the information in Tables 8 through 11 reveals that the model performs reasonably well in predicting the pressures experienced by Sensors 1E,W. However, with regard to the other sensors, the although the model correctly predicts substantial pressure decreases at

Sensors 2E,W and 3E,W, the predicted values are significantly lower than the experimental values. It is almost as if the attenuation of the peak pressures occurs too rapidly with distance away from the shock wave. Based on the significant differences observed between the predictions of the analytical model and the experimental results at Sensors 2E,W and 3E,W, it is apparent that some adjustment of the analytical model is warranted. The modifications made to the model and the constants are presented and discussed in the next section.

8.4 Internal Effects Model Modifications

8.4.1 Model Modifications

As noted in the preceding section, the model performs reasonably well in predicting the pressures experienced by Sensors 1E,W, but at Sensors 2E,W and 3E,W, the predicted values are significantly lower than the experimental values. To lessen the rapidity with which the model predicts the attenuation of the peak pressures and temperatures, it is proposed that equation (152a), which calculate distance using a non-dimensional position quantity, be modified by introducing an empirical constant to control the rate of attenuation as follows:

$$R = \kappa_4 R' (E/P_{0a})^{1/3} \quad (168)$$

where $\kappa_4 > 1$. Choosing a value of $\kappa_4 > 1$ would serve to “stretch out” the attenuation process so that at points far from the shock wave, the pressures are not quite as low as they would be without the empirical factor.

The following expression for κ_4 appears to capture the desired attenuation retardation feature:

$$\kappa_4 = \begin{cases} 1 & , x_{poi} \leq H \\ 1 + m(100R')^m & , x_{poi} > H \end{cases} \quad (169)$$

where m is a positive rational number, R' is the non-dimensional attenuation distance parameter, and H is, as calculated in Section 6.2.2, the distance away from the pressure wall at which internal debris cloud motion stops and attenuation of peak pressures and temperatures begins. This form is motivated by the desire to include “stretching effects” in the attenuation of peak pressures and temperatures only for points of interest that are relatively far removed from the shock wave or the internal debris cloud. Points of interest relatively near the shock wave or debris cloud experience “normally” attenuated pressure and temperature magnitudes. In this manner, some late time effects are included in the analytical model. Additionally, the modification proposed in equations (168) and (169) is applied only to the attenuation of debris cloud induced pressures and temperatures; the attenuation of shock wave induced quantities proceeds without any adjustment or stretching out of the attenuation. It is also noted that when $m=0$ (i.e. no “stretching out”), equation (168) does in fact reduce to its original form given in equation (152a).

8.4.2 Empirical Constant Adjustments

Following the modification of the analytical model as described in the preceding section, a value of m was determined that would extend the effects of the shock wave induced pressure and temperature increases further away from the shock wave and the debris cloud. In doing so, the empirical constants n , κ_2 , and κ_3 as well as the drag coefficient C_D were kept at the values shown in Table 7. The final values of the constant m are presented in Table 12.

Table 12. Final Empirical Constant Values

Empirical Constant	Type A Inner Bumper		Type B Inner Bumper
Projectile Diameter (cm)	1.27	1.59	1.59
m	0.60	0.70	1.25

It must be emphasized that the constants in Tables 7 and 12 will likely yield acceptable results only for the system geometries, projectile diameters, and impact velocities considered in the experimental phase of this effort, the results of which served to determine the actual constant values. While the analytical model will certainly produce results for other system geometries, projectile diameters, and impact velocities, those results may or may not be appropriate for the alternative parameters considered. Additional experimental evidence will be required to validate the analytical model developed herein for impact parameters and systems configurations other than those which produced the empirical data upon which the empirical constants in Tables 7 and 12 were based. It is indeed likely that these will need to be adjusted to accommodate other empirical information as it becomes available.

8.5 Comparison of Modified Model Predictions with Experimental Results

Tables 13 through 16 present a comparison of the experimental results and the predictions of the model developed herein using the empirical constants given in Tables 7 and 12. As can be seen in Tables 13 through 16, the predictions of the model now compare much more favorably with the experimental results.

Table 13. Pressure and Temperature Data Comparison (Improved Model) -- Test No. 1

Sensor	Pressure Increase			Temperature Increase		
	Time (msec)	Experimental Result (psi)	Model Prediction (psi)	Time (msec)	Experimental Result (°C)	Model Prediction (°C)
1E	1.12	17	15.2	13.3	18	43.2
1W	1.07	18	15.2	19.0	27	43.2
2E	1.93	4	7.2	21.6	23	23.0
2W	2.15	6	7.2	23.0	20	23.0
3E	2.33	3	3.2	645.8	25	11.6
3W	2.00	2	3.2	n/a	n/a	11.6

Table 14. Pressure and Temperature Data Comparison (Improved Model) -- Test No. 3

Sensor	Pressure Increase			Temperature Increase		
	Time (msec)	Experimental Result (psi)	Model Prediction (psi)	Time (msec)	Experimental Result (°C)	Model Prediction (°C)
1E	0.86	21	24.3	8.5	104	63.9
1W	1.00	21	24.3	6.5	118	63.9
2E	1.33	17	17.2	10.9	139	46.6
2W	1.50	21	17.2	10.8	94	46.6
3E	2.13	8	8.0	n/a	n/a	25.1
3W	2.83	8	8.0	115.0	40	39.0

Table 15. Pressure and Temperature Data Comparison (Improved Model) -- Test No. 5

Sensor	Pressure Increase			Temperature Increase		
	Time (msec)	Experimental Result (psi)	Model Prediction (psi)	Time (msec)	Experimental Result (°C)	Model Prediction (°C)
1E	0.95	34	34.2	13.4	64	82.7
1W	0.80	40	34.2	17.9	54	82.7
2E	2.13	10	10.2	19.6	34	30.0
2W	1.93	15	10.2	20.0	31	30.0
3E	4.07	3	5.6	n/a	n/a	18.2
3W	3.90	4	5.6	n/a	n/a	21.5

Table 16. Pressure and Temperature Data Comparison (Improved Model) -- Test No. 6

Sensor	Pressure Increase			Temperature Increase		
	Time (msec)	Experimental Result (psi)	Model Prediction (psi)	Time (msec)	Experimental Result (°C)	Model Prediction (°C)
1E	1.33	16	24.6	25.0	20	64.8
1W	1.06	31	24.6	26.3	65	64.8
2E	1.71	15	17.8	92.0	52	48.1
2W	1.54	14	17.8	53.0	63	48.1
3E	2.65	12	8.3	52.0	44	25.8
3W	2.66	7	8.3	n/a	n/a	40.1

The most significant difference between experimental result and model prediction remaining is found for the temperature increases for Test No. 3 as shown in Table 14. Interestingly enough, the corresponding pressure increase values predicted by the model for this

test do agree rather well with the experimental results. A comparison of the test conditions, etc. for Test Nos. 3 and 6 reveals that the two are virtually identical; the only difference is that the velocity for Test No. 6 was 0.8 km/sec higher than that for Test No. 3. Inspection of the experimental results for these two tests as shown in Tables 14 and 16, respectively, shows that the pressure increases sustained during the two tests are in fact very similar. However, with the exception of Sensors 3E,W, the temperature increases are quite different: those recorded in Test No. 6 are substantially lower than those in Test No. 3. Since the analytical model predictions agree well with the pressure readings in both tests as well as the temperature readings in Test No. 6, the inference to be drawn is that the temperature readings in Test No. 3 must be due to some phenomenon not included in the analytical model developed herein.

9.0 SUMMARY AND RECOMMENDATIONS

9.1 Summary

A first-principles-based model has been developed to predict the effects of a perforating orbital debris particle impact within a pressurized habitable module. The model was developed in a way such that it sequentially characterizes the phenomena associated with the impact event, including the initial impact on the outer bumper, the creation and motion of the debris clouds within the module wall system, the impact of the debris clouds on the module pressure wall, the creation and motion of the debris cloud that enters the module interior, and the effects of the debris cloud within the module on module pressure and temperature levels.

The model development has been accomplished through the application of elementary shock physics and thermodynamic theory, as well as the principles of mass, momentum, and energy conservation. The predictions of the model were compared against experimental results obtained from four high-speed impact tests conducted at the University of Alabama in Huntsville. The basic model predictions compared favorably with the experimental data obtained at the sensors located nearest to the impact site; at locations further removed from the impact site, the comparisons were not as favorable even taking into account test-to-test variations in the data. Several modifications were made to the basic model to bring its predictions closer in line with the experimental results, including decreasing the rapidity with which the model predicts the attenuation of peak pressures and accompanying temperature increases. Following the adjustment of several empirical constants, the predictions of the modified internal effects model were in much closer agreement with the experimental results.

9.2 Recommendations

Following a review of the methodology used to develop the internal effects model presented herein, the following recommendations are offered as suggestions for improving the robustness of the model as well as for improving its ability to model the phenomena associated with the high speed impact of a pressurized module. The recommendations are grouped according to the part of the model that would be affected by their implementation.

Outer Bumper Impact

- 1) Include the effects of backslash due to the impact of the projectile on the outer bumper. This would have the effect of decreasing the mass of the primary debris cloud, but, due to momentum conservation, *increasing* its center-of-mass velocity (the so-called “momentum enhancement effect”). Since the energy of the debris cloud is proportional to the square of the velocity, this could have a significant impact on the subsequent effects produced by the primary debris cloud.
- 2) Include the effects of light flash in the energy balance for the initial impact on the outer bumper. This would have the effect of producing more accurate primary debris cloud velocities.

Inner Bumper Impact

- 1) Develop a more suitable equation for the diameter of the hole in the inner bumper produced by the impact of the primary debris cloud. The present approximation is at best an order-of-magnitude estimate. A more appropriate hole-out equation would produce a more accurate mass value for this component of the secondary debris cloud. This in turn would have some effect on the magnitude of the velocity imparted to the

pressure wall by the impact of this component of the secondary debris cloud.

- 2) Include the effects of inner bumper burning and/or melting. This may be a significant energy absorbing mechanism and may have a significant influence on the energy balance that is applied to the system before and after the impact of the primary debris cloud on the inner bumper.

Pressure Wall Impact

- 1) Include the effects of pressure wall deformation, including hole formation, bulging, cracking, etc. This will affect the amount of energy that is available for the motion of the internal debris cloud and the creation of the accompanying shock waves within the module interior.
- 2) Develop an improved mass model for the internal debris cloud. This includes developing a more rigorous means of calculating pressure wall hole-out mass as well as an improved estimate for the amount of secondary debris cloud mass that is trapped by the pressure wall and the amount that enters the module interior.

Internal Effects Modeling

- 1) Improve the shock wave attenuation scheme for the internal debris cloud. This includes adjusting the present model to include an internal debris cloud whose speed decays as it moves into the module interior as opposed to ceasing motion in a rather abrupt manner.

General Comments

- 1) Extend the model to oblique impacts. This would render the model applicable to a much wider variety of impact scenarios.

2) Perform additional internal effects testing at different velocities using alternative system geometries and impact conditions. This would provide additional information that would facilitate the implementation of the recommendations presented herein as well as validate the model for a much larger family of impact events.

In terms of increasing the applicability of the model to a wider class of impact scenarios, additional internal effects testing at different velocities using alternative system geometries and impact conditions is absolutely required. This new information could then be used to, for example, extend the applicability of the model to oblique impacts. In terms of increasing the accuracy of the model developed herein, it would appear that, in order of decreasing importance, the improvements that need to be made are:

- include the effects of pressure wall deformation, including hole formation, bulging, cracking, etc.;
- develop an improved mass model for the internal debris cloud;
- develop a more suitable equation for the diameter of the hole in the inner bumper produced by the impact of the primary debris cloud;
- include the effects of inner bumper burning and/or melting;
- improve the shock wave attenuation scheme for the internal debris cloud;
- include the effects of backsplash due to the impact of the projectile on the outer bumper; and,
- include the effects of light flash in the energy balance for the initial impact on the outer bumper.

10.0 REFERENCES

1. Gehring, J.W., Lathrop, B.L., and Warnica, R.L., Spacecraft Interior Hazards from Hypervelocity Impact, GM Defense Research Laboratories, Report No. TR-66-13, Santa Barbara, California, 1966.
2. Long, L.L., and Hammitt, R.L., "Meteoroid Perforation Effects on Space Cabin Design", *AIAA Hypervelocity Impact Conference*, Paper No. 69-365, Cincinnati, Ohio, April 30 to May 2, 1969.
3. Engler, E.E., "Physiological and Safety Aspects of Penetration", *Space Debris and Meteoroid Technology Workshop*, Marshall Space Flight Center, September, 1984.
4. Weibull, G.W., "A Proposal for Blast Incapacitation Criteria Concerning Soldiers Inside Armored Vehicles", Proceedings of the 9th International Symposium on Ballistics, pp. 2-337 to 2-344, Royal Military College of Science, England, April 29 to May 1, 1986.
5. Rice, M.H., McQueen, R.G., and Walsh, J.M., "Compression of Solids by Strong Shock Waves", Solid State Physics, Volume VI, Seitz, F. and Turnbull, D., eds., Academic Press, New York, 1958.
6. Anderson, C.E., Trucano, T.G., and Mullin, S.A., "Debris Cloud Dynamics", *International Journal of Impact Engineering*, Vol. 9, No. 1, pp. 89-113, 1990.
7. Jolly, W.H., Analytical Prediction of Hole Size Due to Hypervelocity Impact of Spherical Projectiles, Master's Thesis, University of Alabama in Huntsville, Huntsville, Alabama, 1993.
8. Lundeborg, J.F., Stern, P.H., and Bristow, R.J., Meteoroid Protection for Spacecraft Structures, NASA CR-54201, Washington, D.C., 1965.
9. Piekutowski, A.J., "A Simple Dynamic Model for the Formation of Debris Clouds", *International Journal of Impact Engineering*, Vol. 10, pp. 453-471, 1990.
10. Madden, R., Ballistic Limit of Double-Walled Meteoroid Bumper Systems, NASA TN-D-3916, Washington, D.C., 1967.
11. Maiden, C.J., Gehring, J.W., and McMillan, A.R., Investigation of Fundamental Mechanism of Damage to Thin Targets by Hypervelocity Projectiles, GM Defense Research Laboratories, Report No. TR-63-225, Santa Barbara, California, 1963.
12. Piekutowski, A.J., "Debris Clouds Generated by Hypervelocity Impact of Cylindrical Projectiles with Thin Aluminum Plates", *International Journal of Impact Engineering*, Vol. 5,

pp. 509-518, 1987.

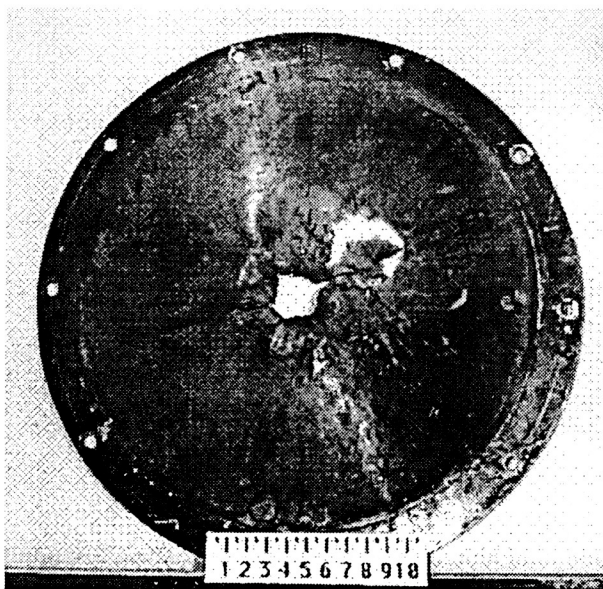
13. Rinehart, J.S., Stress Transients in Solids, HyperDynamics, Santa Fe, New Mexico, 1975.
14. Baker, W., Explosions in Air, Texas University Press, Austin, Texas, 1973.
15. Hayes, W.D. and Probstein, R.F., Hypersonic Flow Theory, Academic Press, New York, 1966.
16. Christiansen, E.L., "Design and Performance Equations for Advanced Meteoroid and Debris Shields", *International Journal of Impact Engineering*, Vol. 14, pp. 145-156, 1993.

11.0 APPENDICES

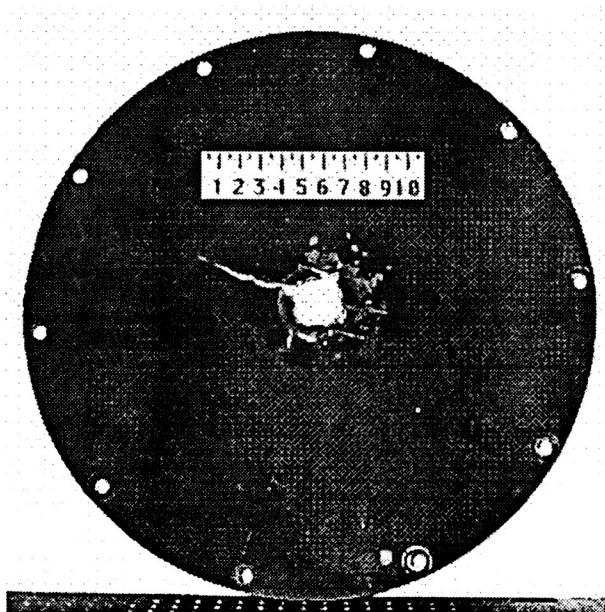
APPENDIX A

Test Data

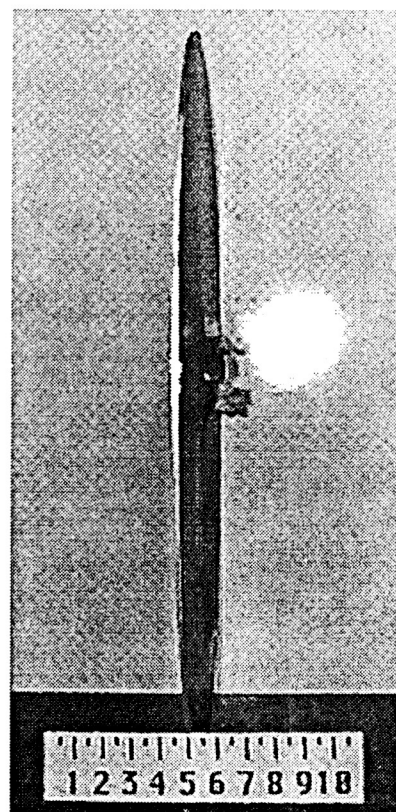
- **TARGET PLATE PHOTOGRAPHS**
- **TEMPERATURE PROFILES**
- **PRESSURE PROFILES**
- **UV AND VISIBLE BAND RADIANT INTENSITY**



Target Plate Front



Target Plate Back



Target Plate Side

Figure A1 Target Plate Photographs - Test #1

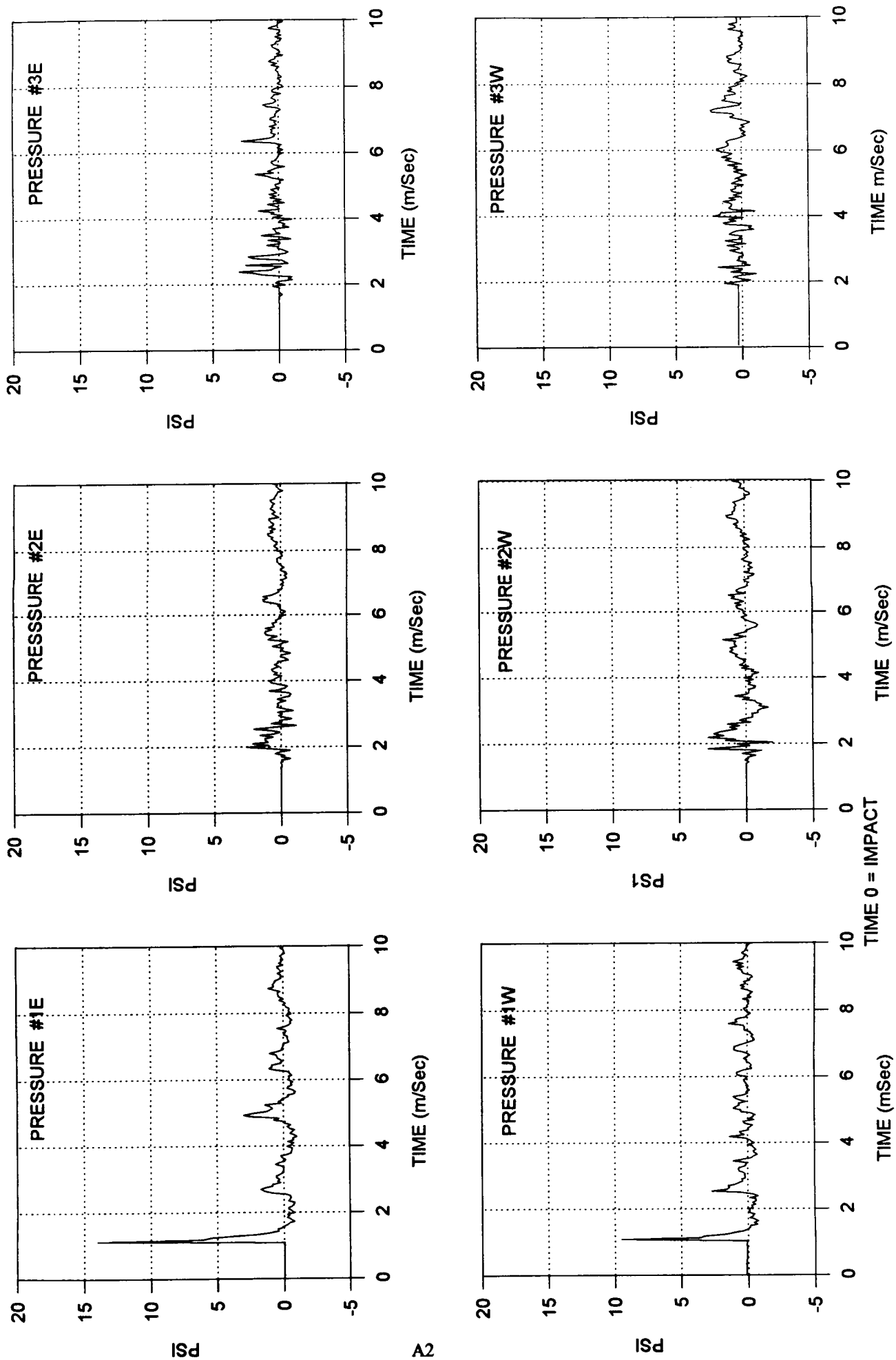


Figure A2 Pressure Profiles - Test #1

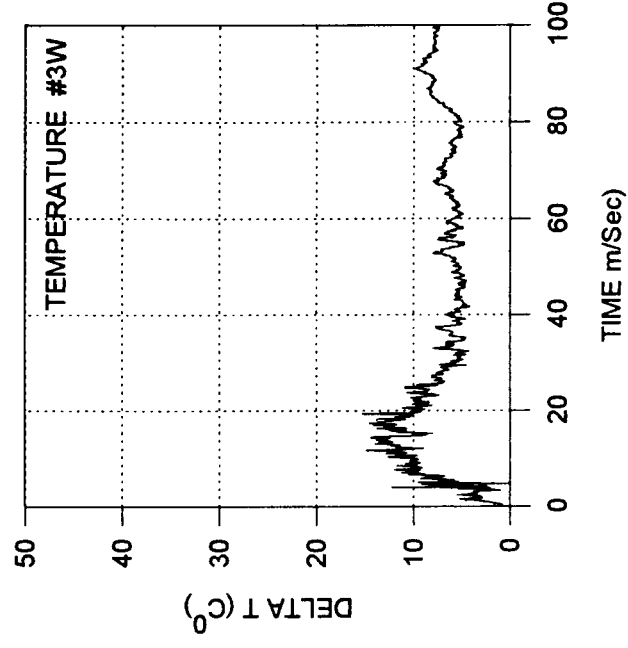
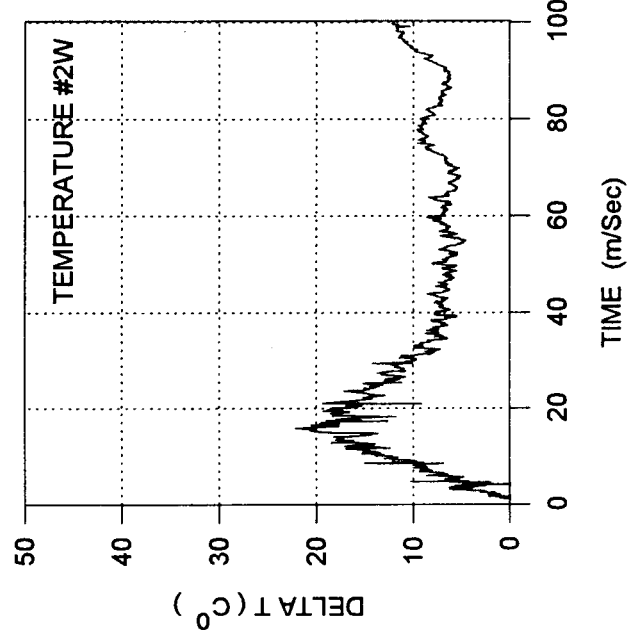
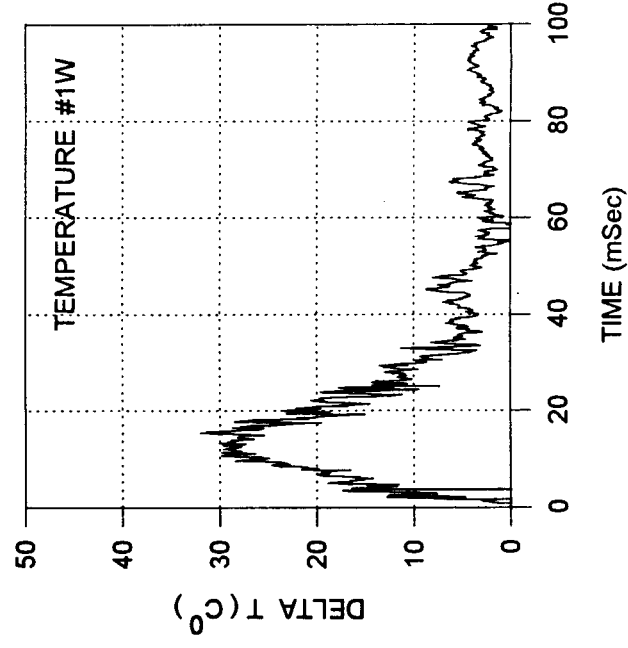
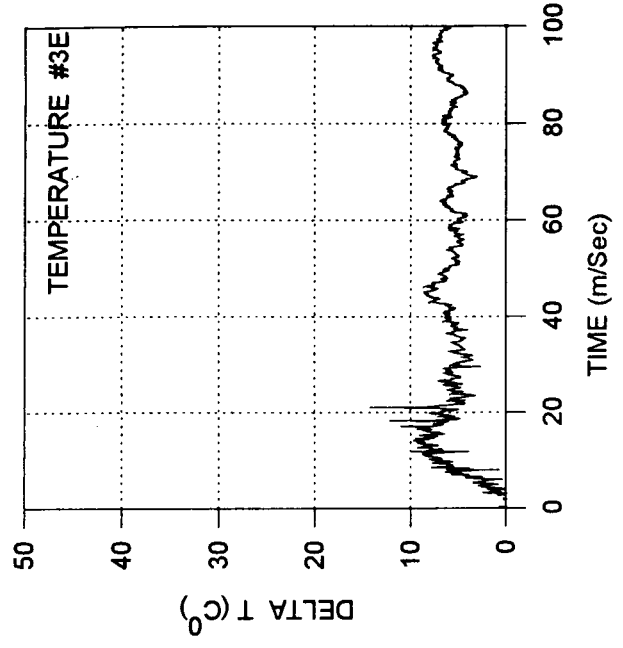
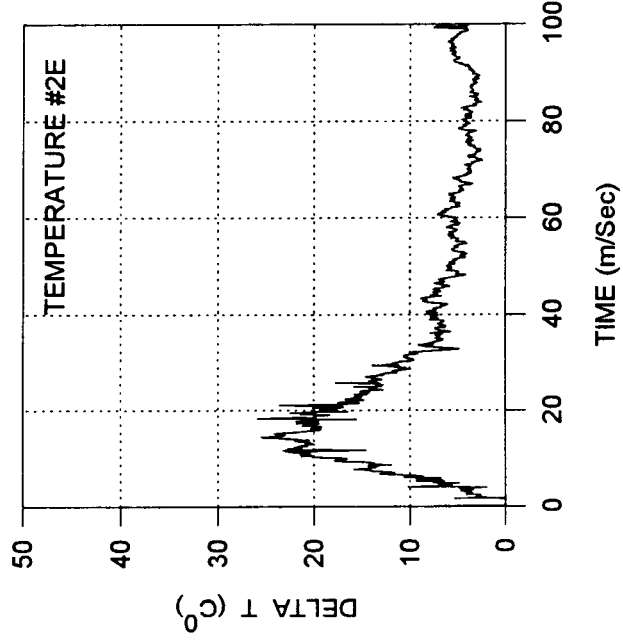
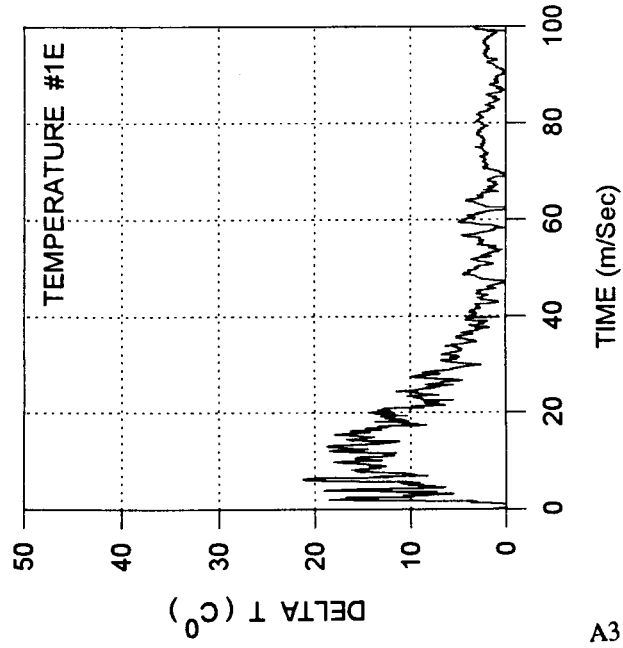
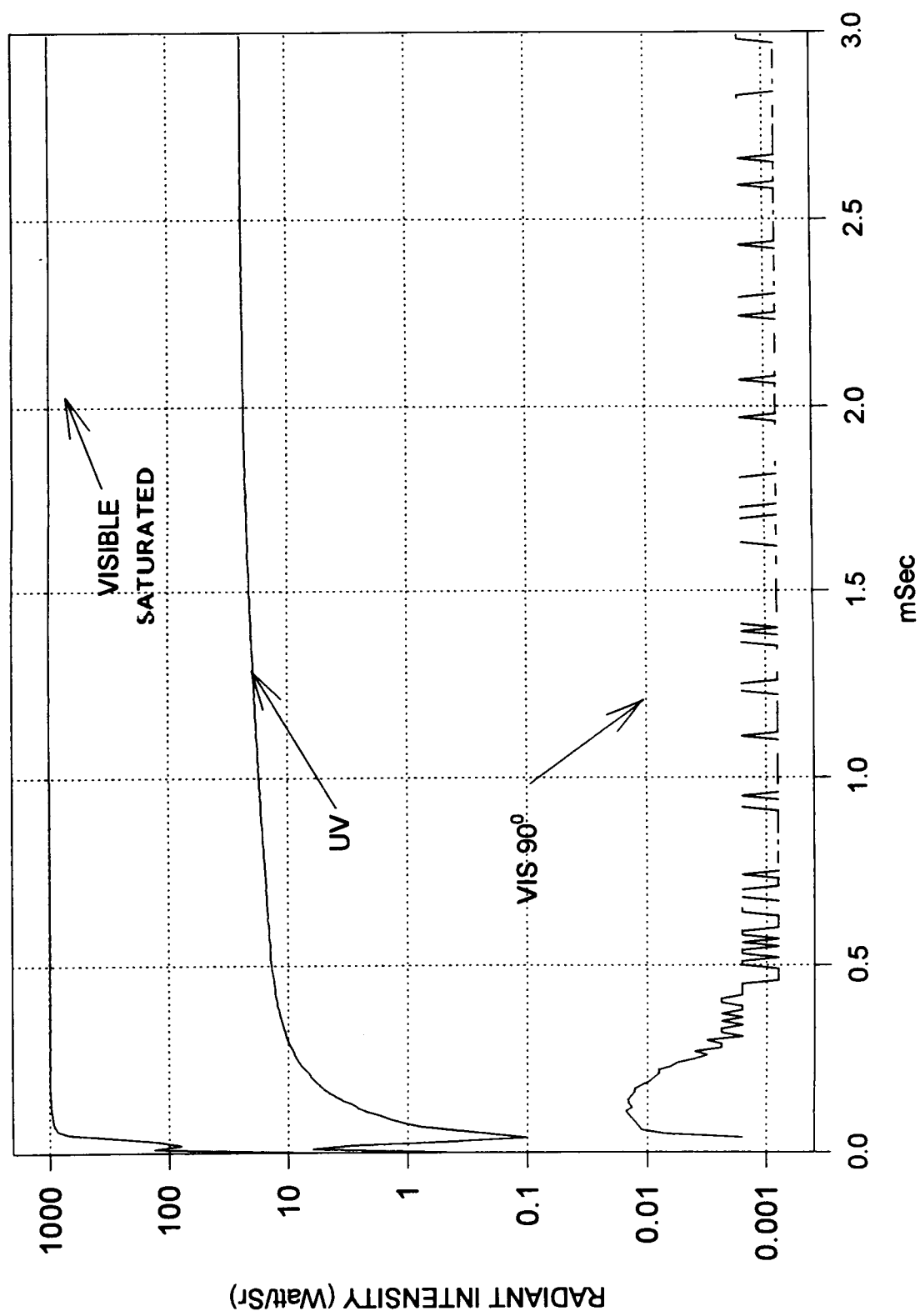
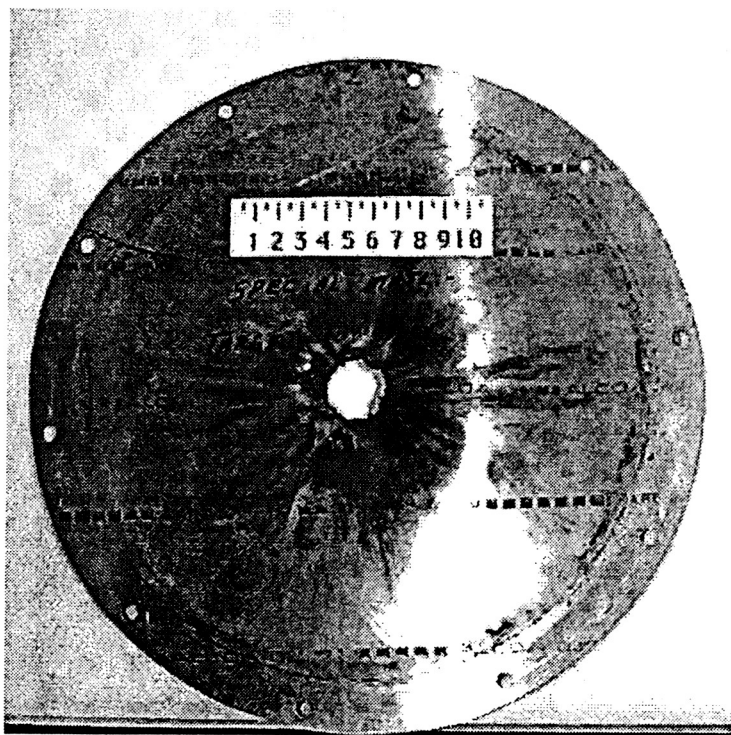
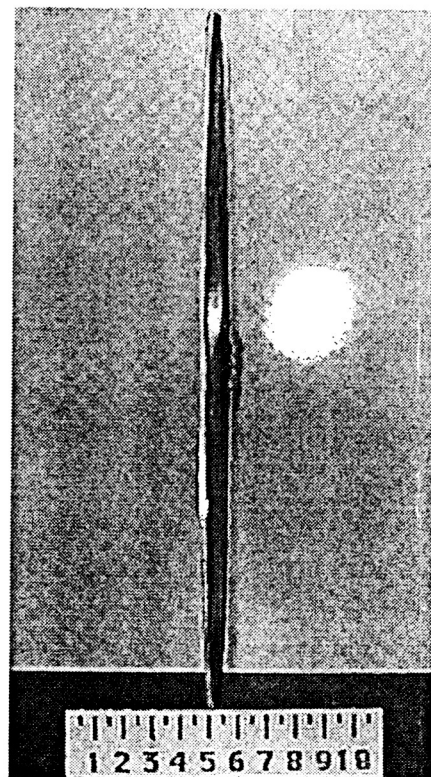


Figure A3 Temperature Profiles - Test #1

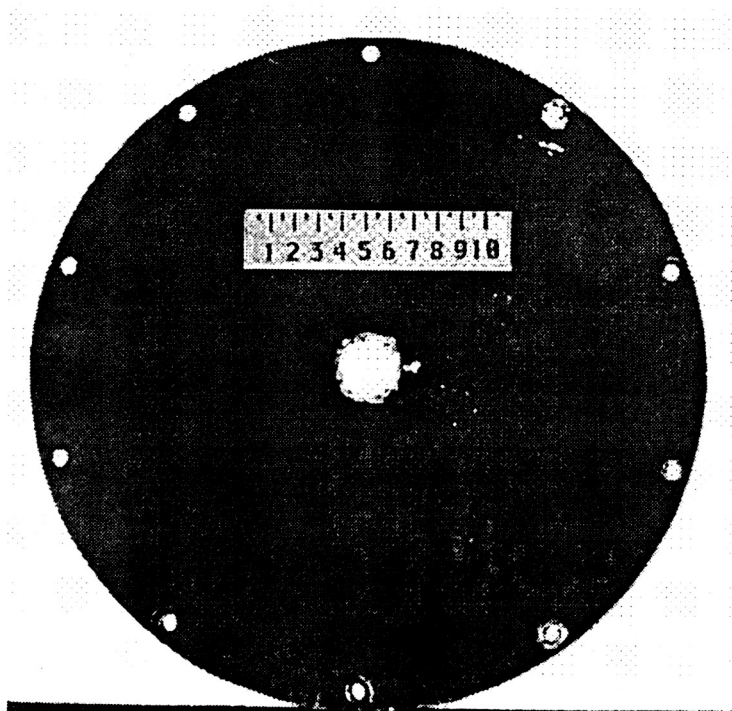




Target Plate Front



Target Plate Side



Target Plate Back

Figure A5 Target Plate Photographs - Test #2

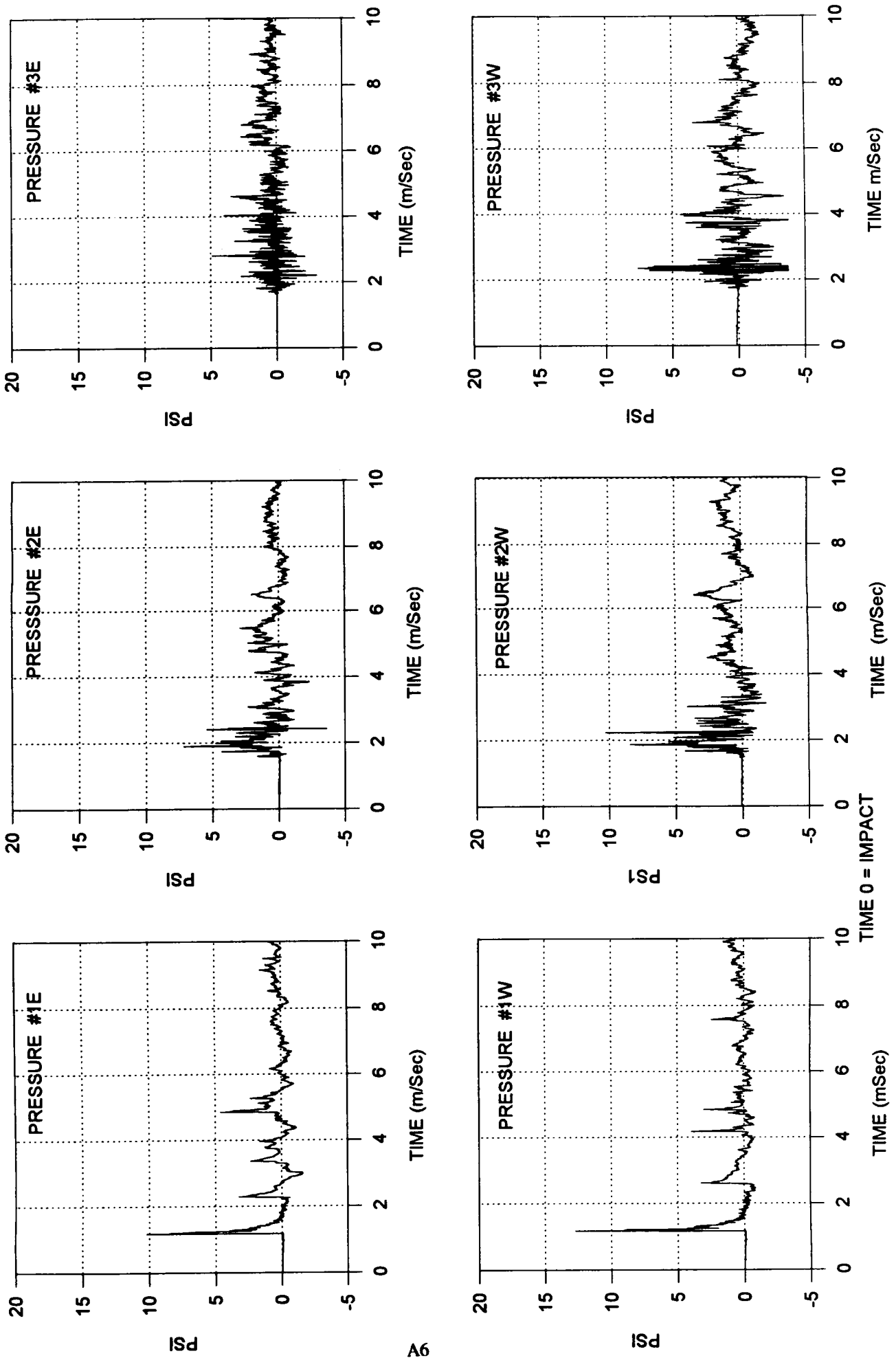


Figure A6 Pressure Profiles - Test #2

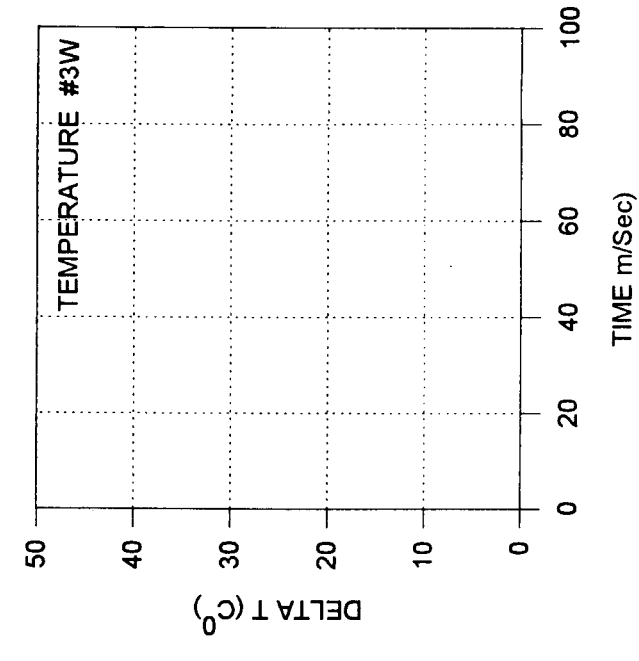
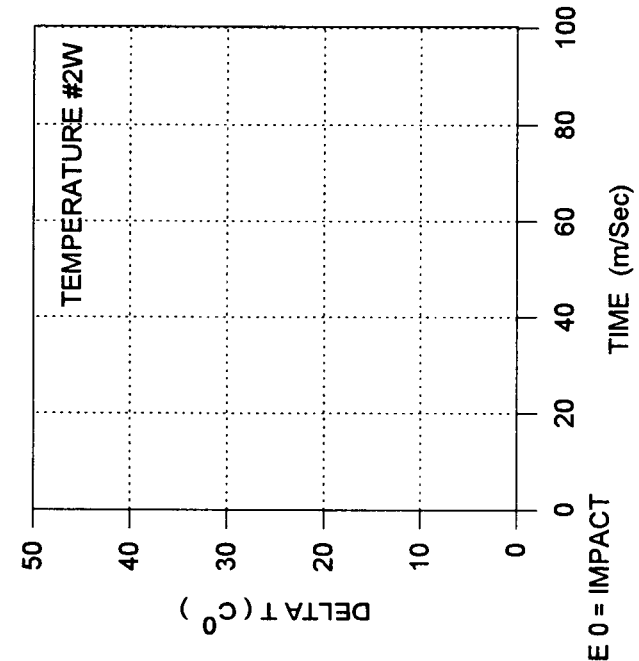
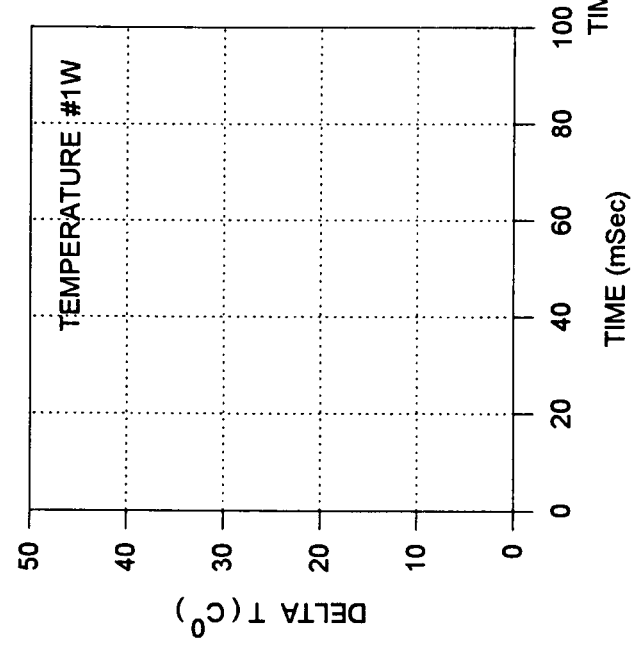
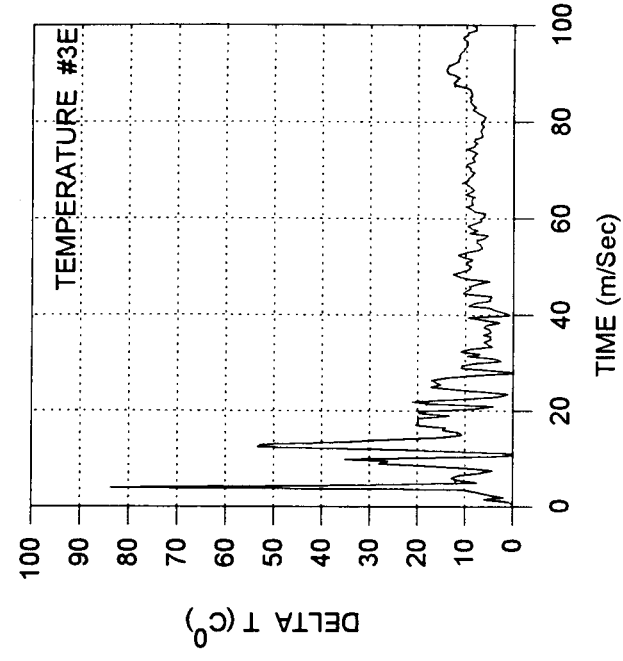
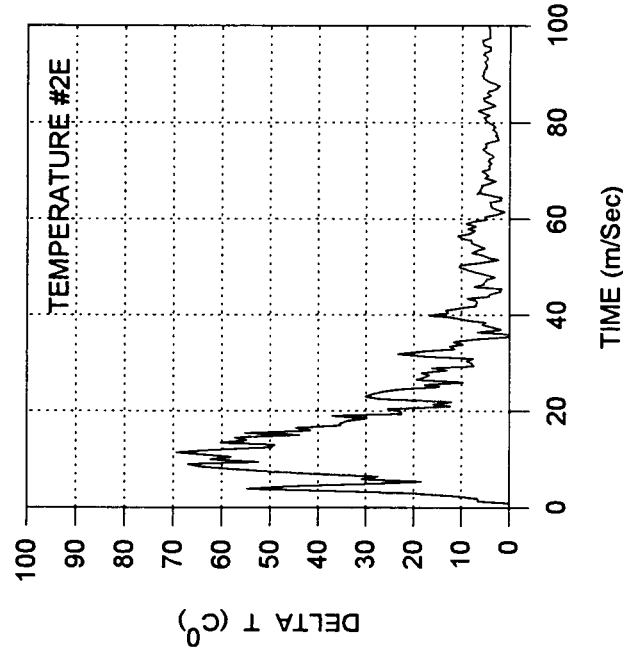
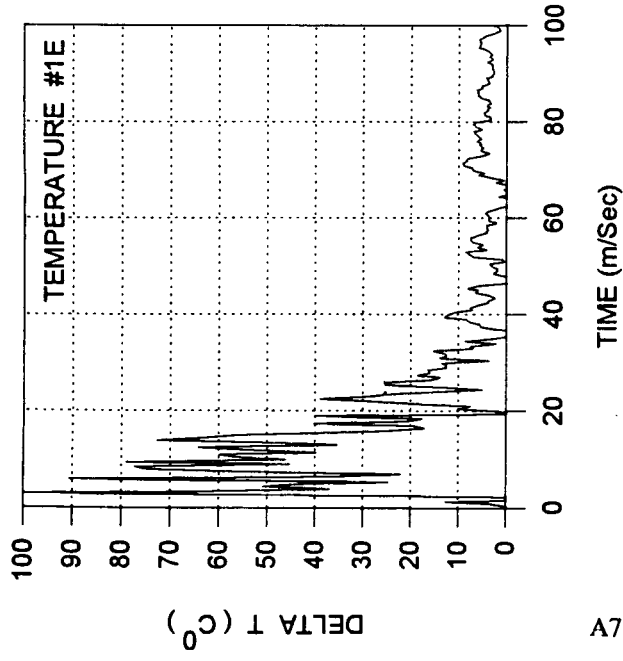
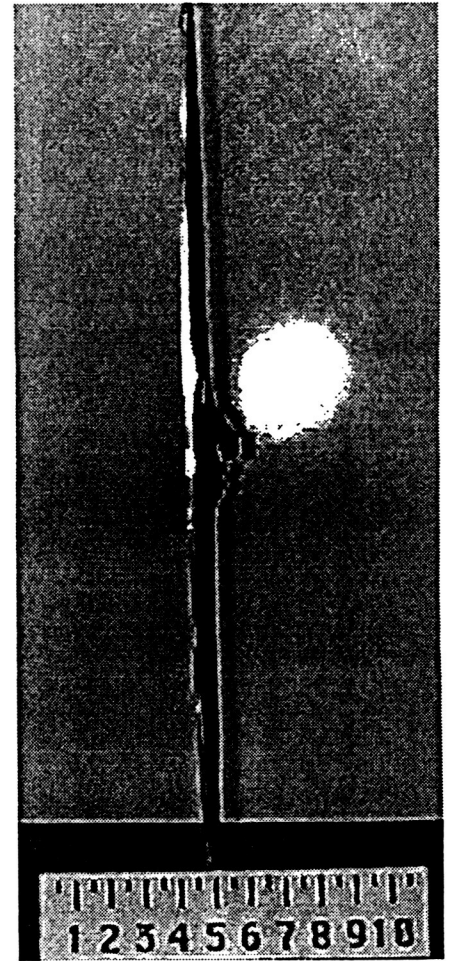


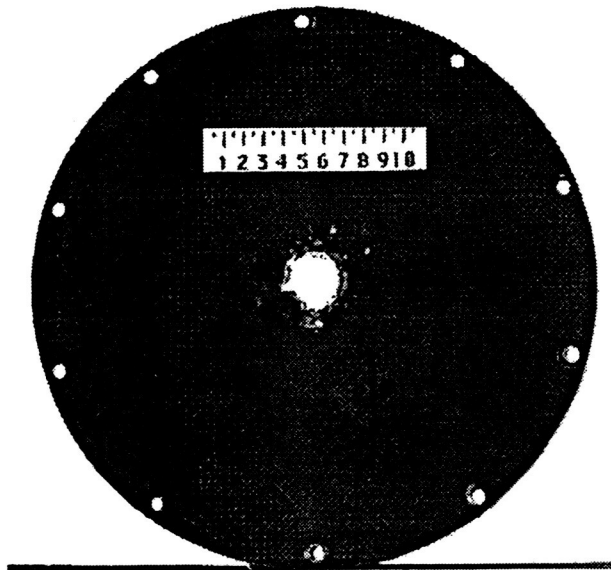
Figure A7 Temperature Profiles - Test #2



Target Plate Front



Target Plate Side



Target Plate Back

Figure A8

Target Plate Photographs - Test #3

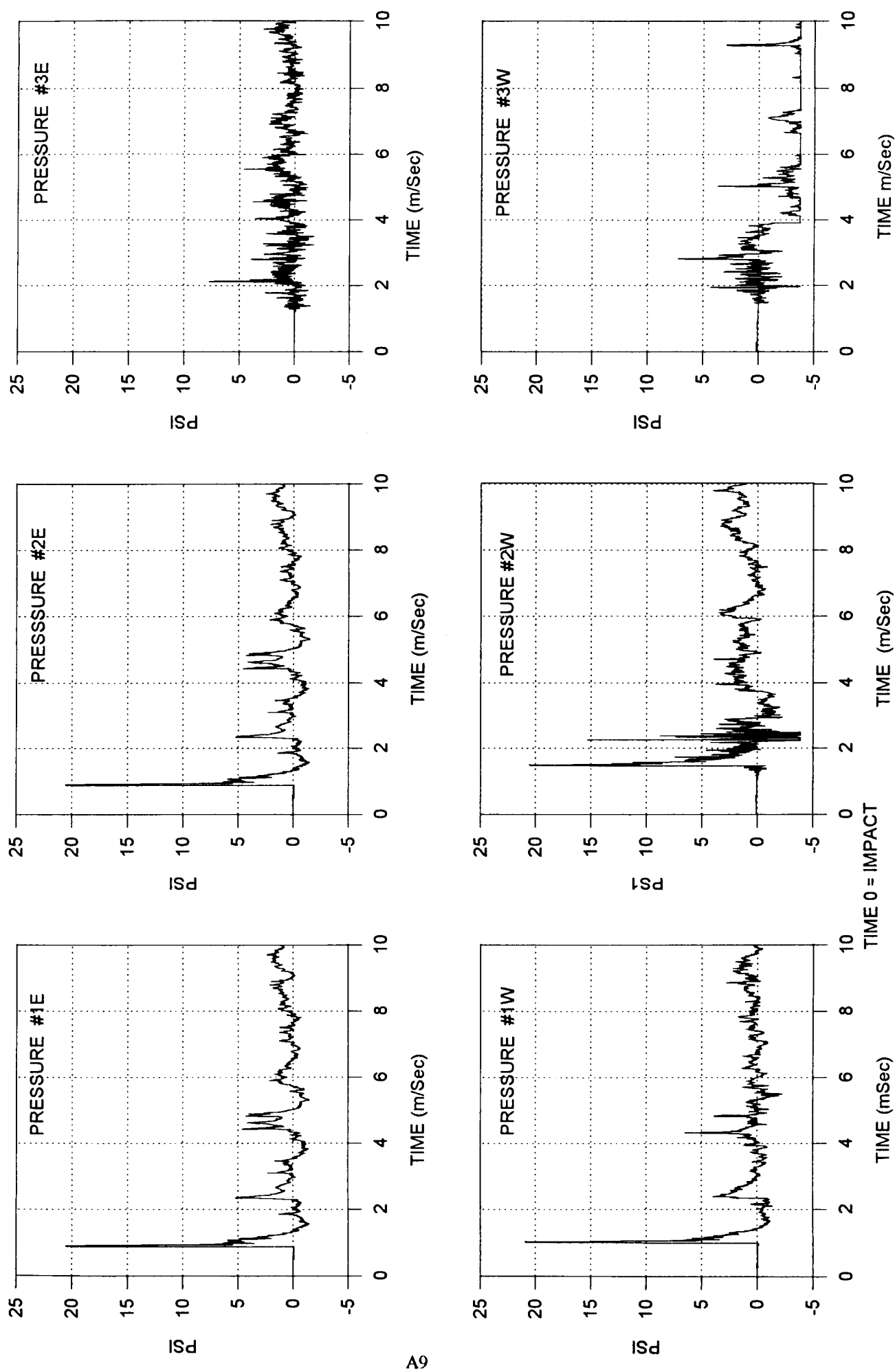
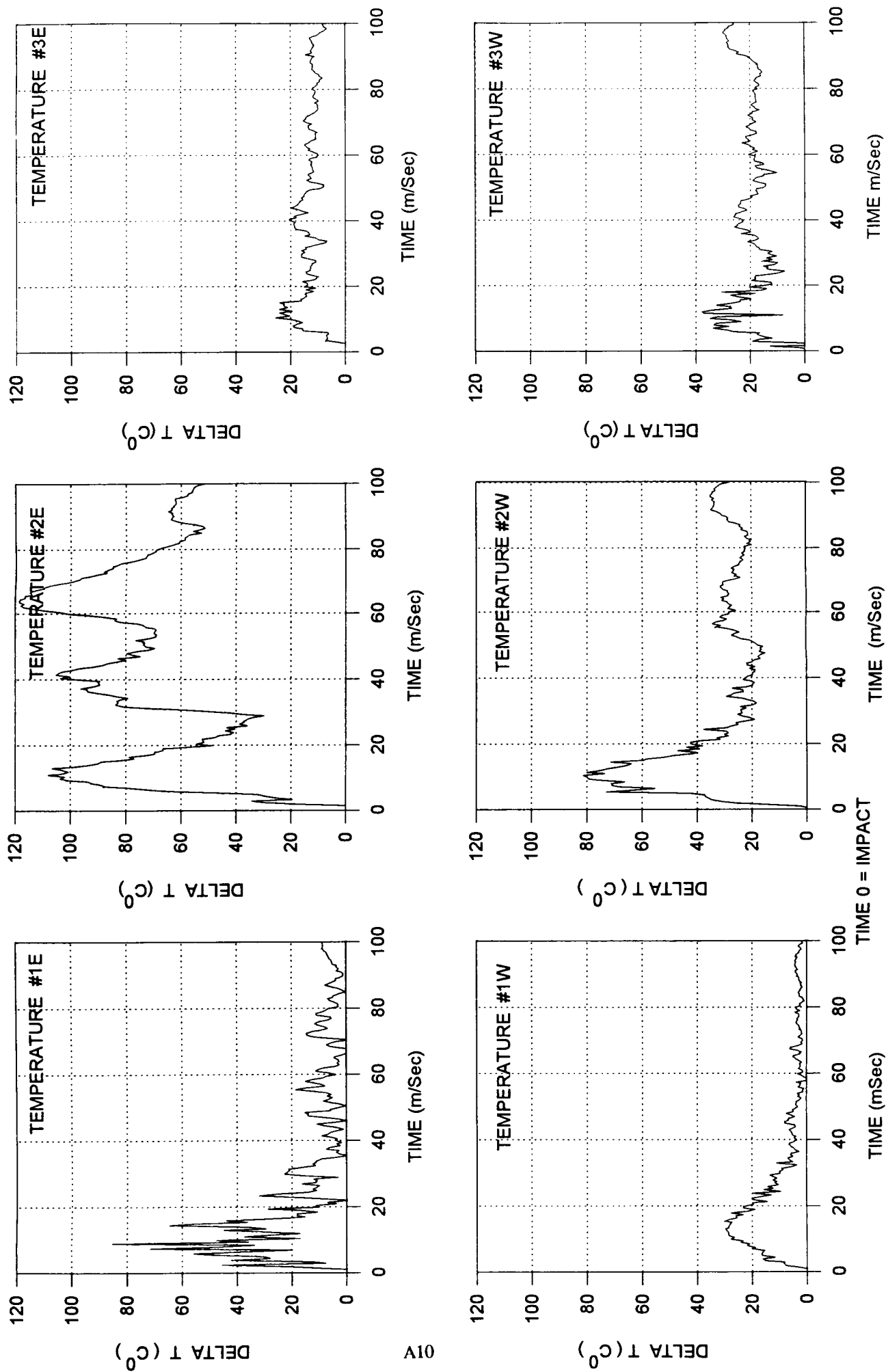
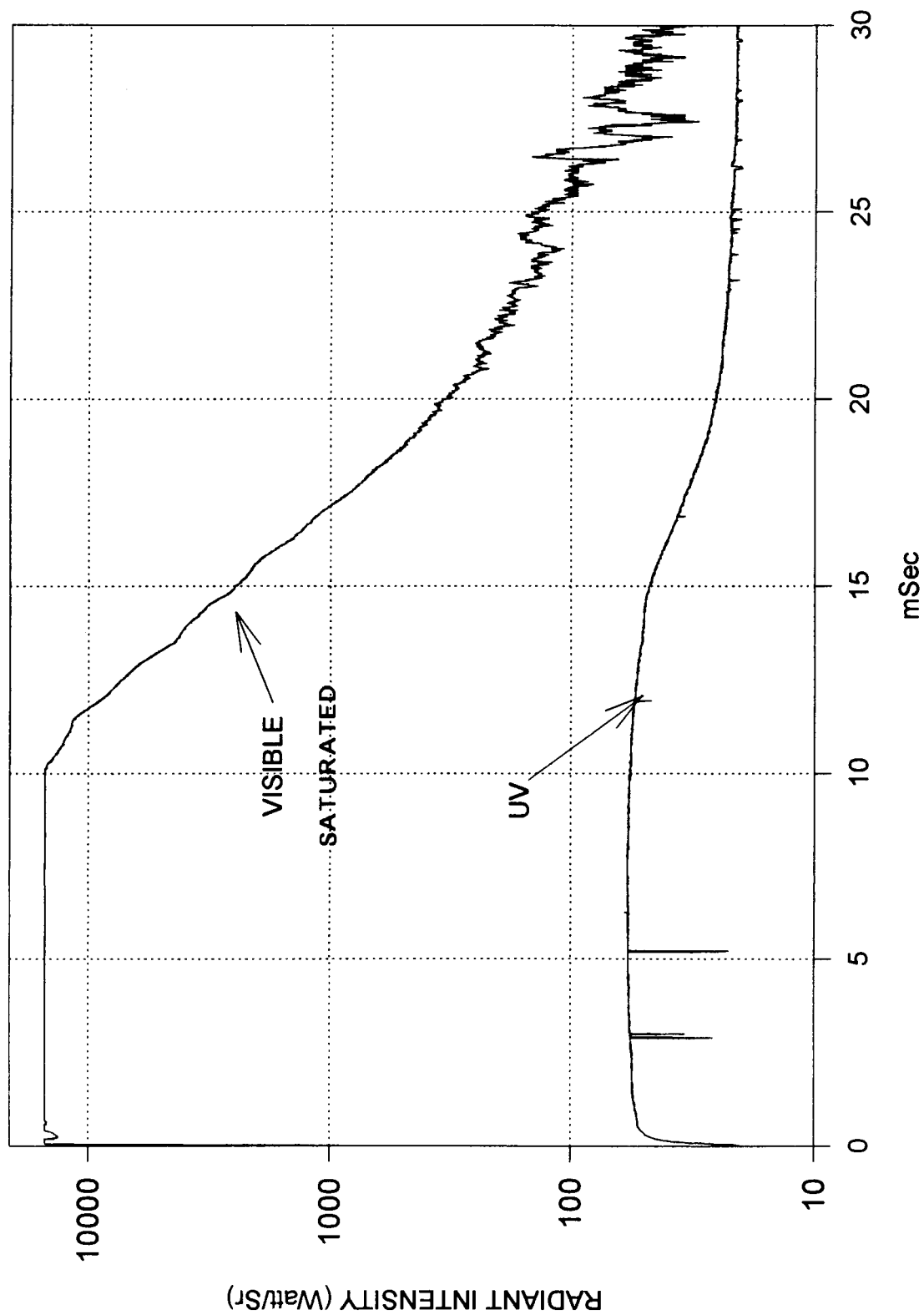
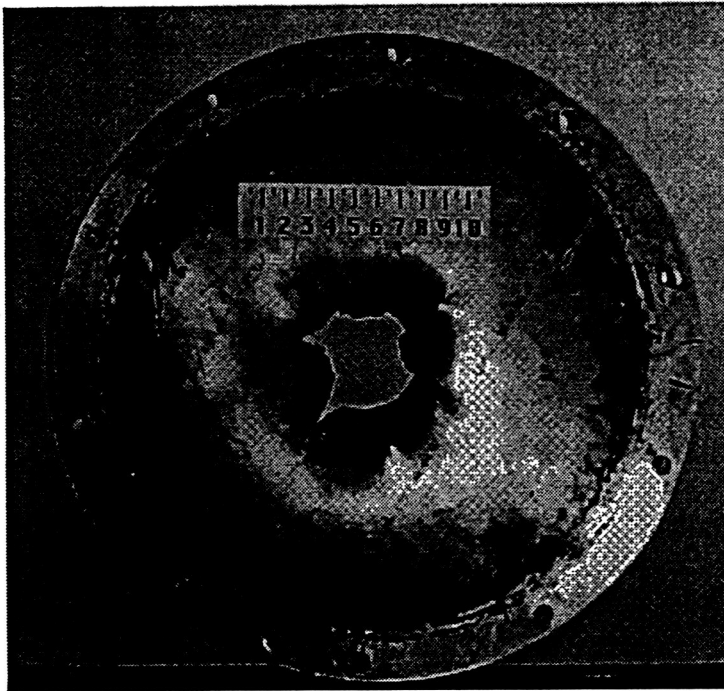


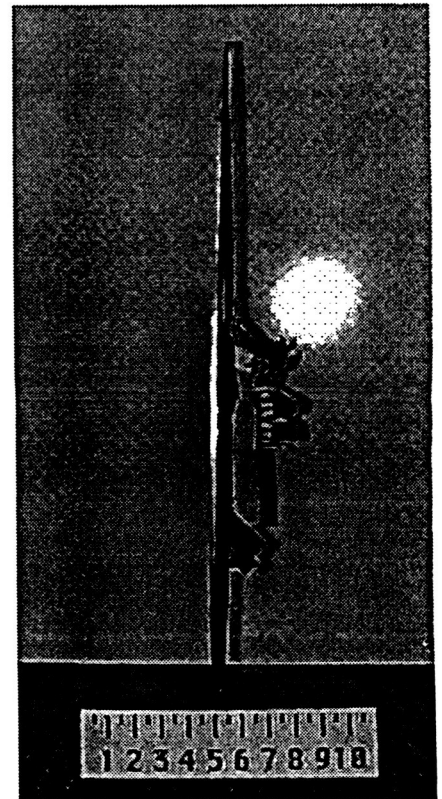
Figure A9 Pressure Profiles - Test #3



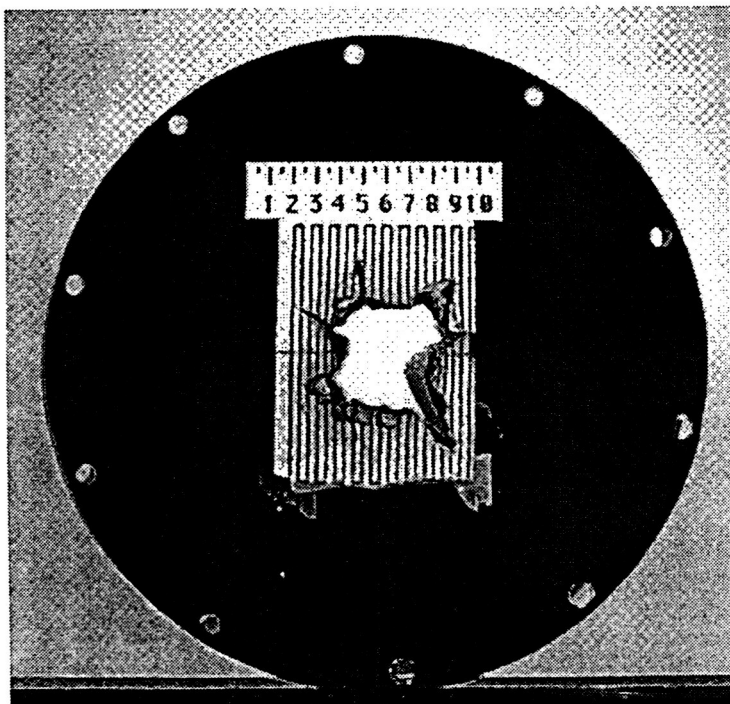




Target Plate Front

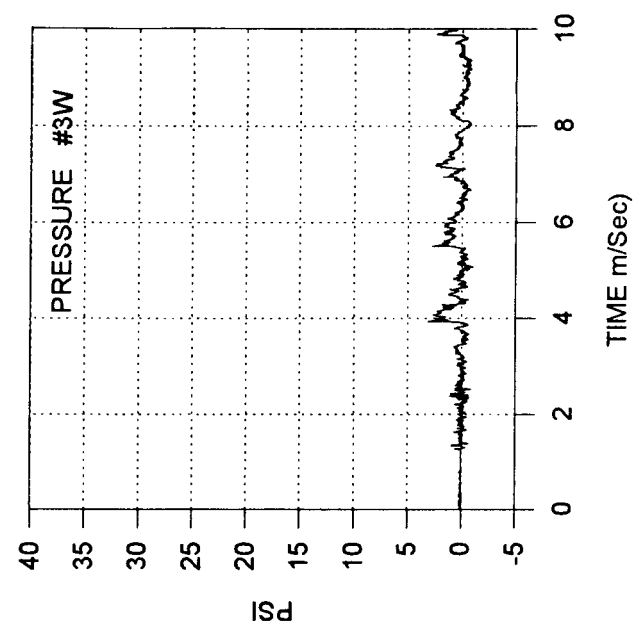
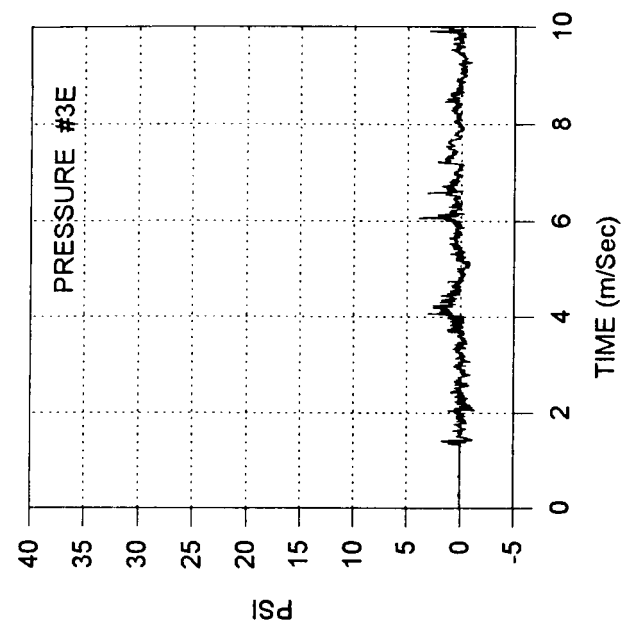
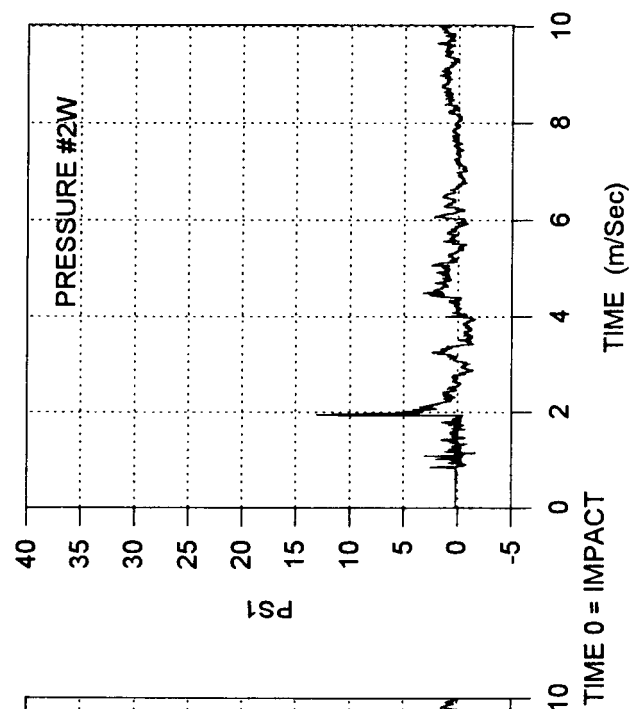
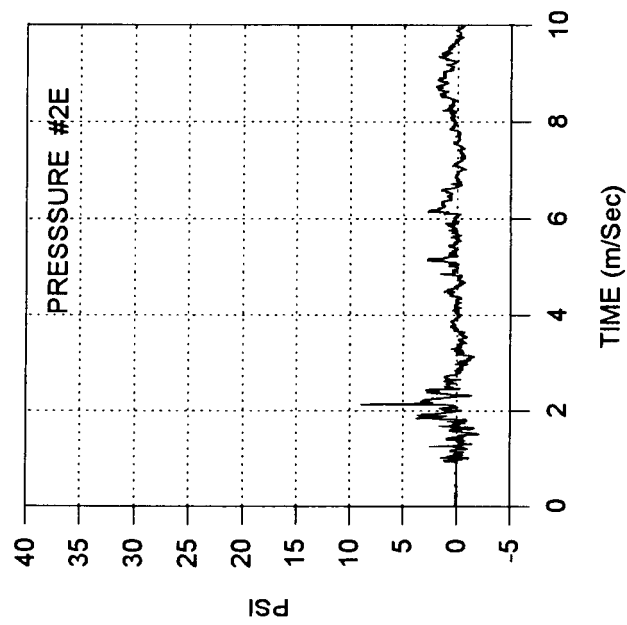
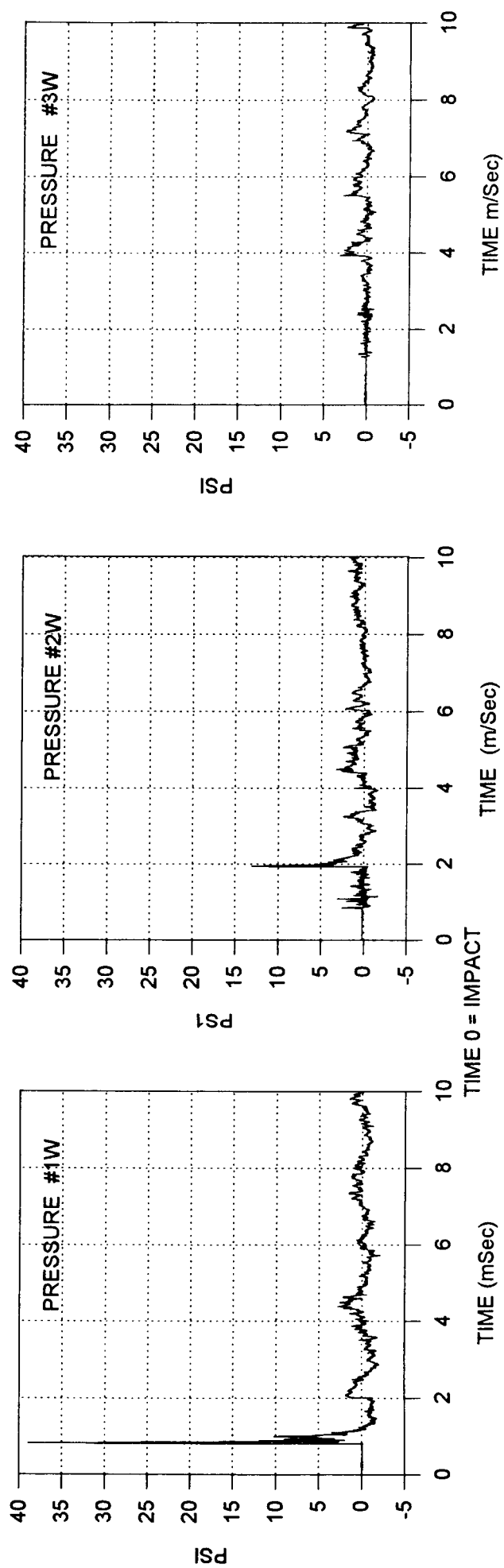
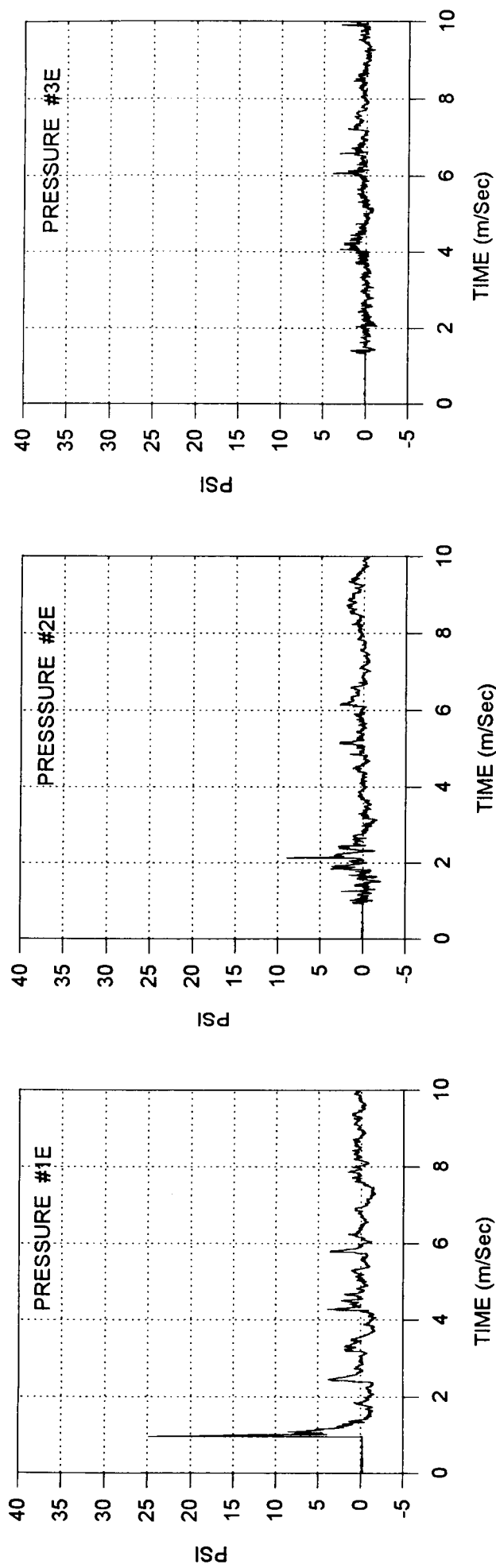


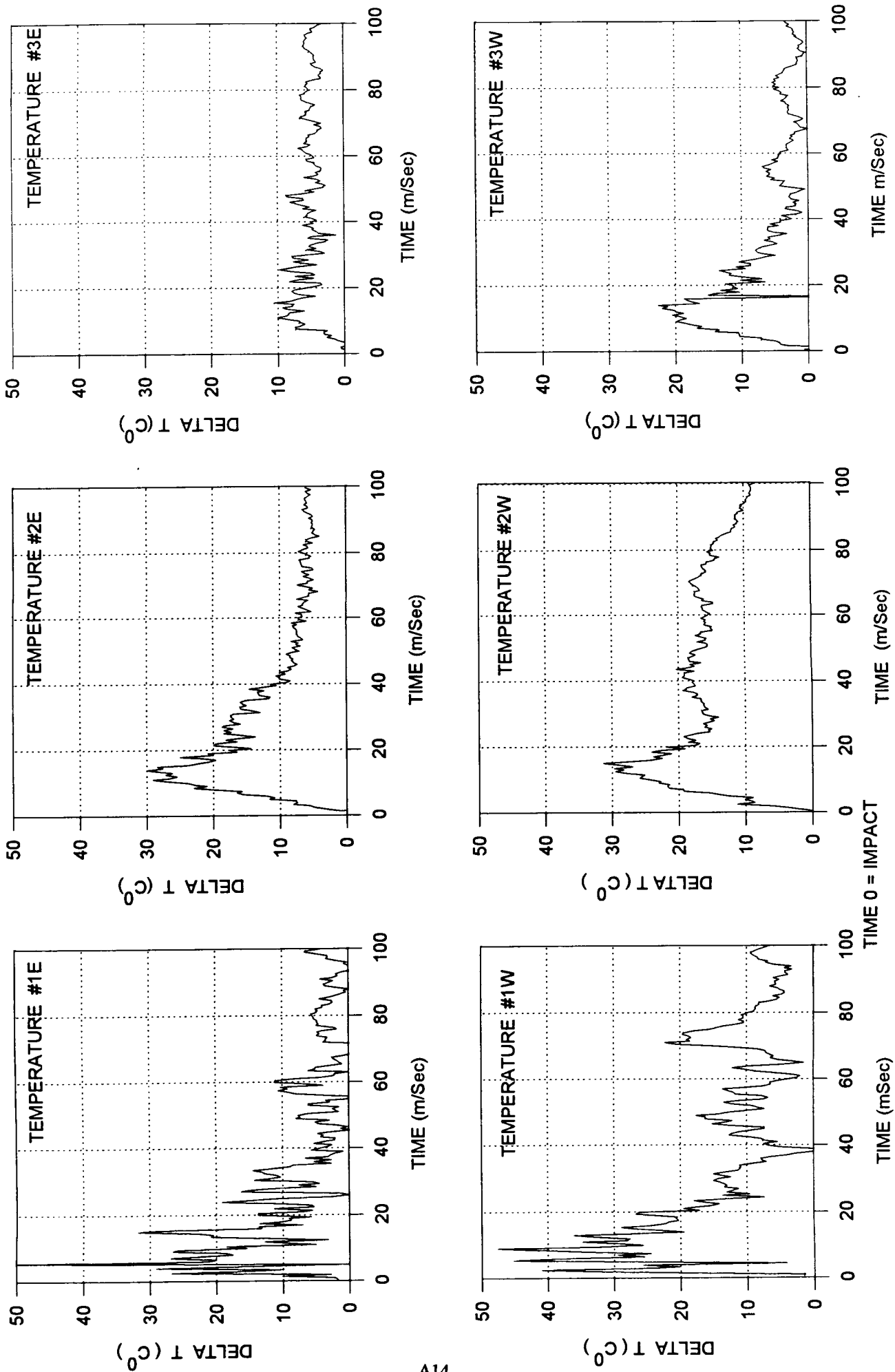
Target Plate Side



Target Plate Back

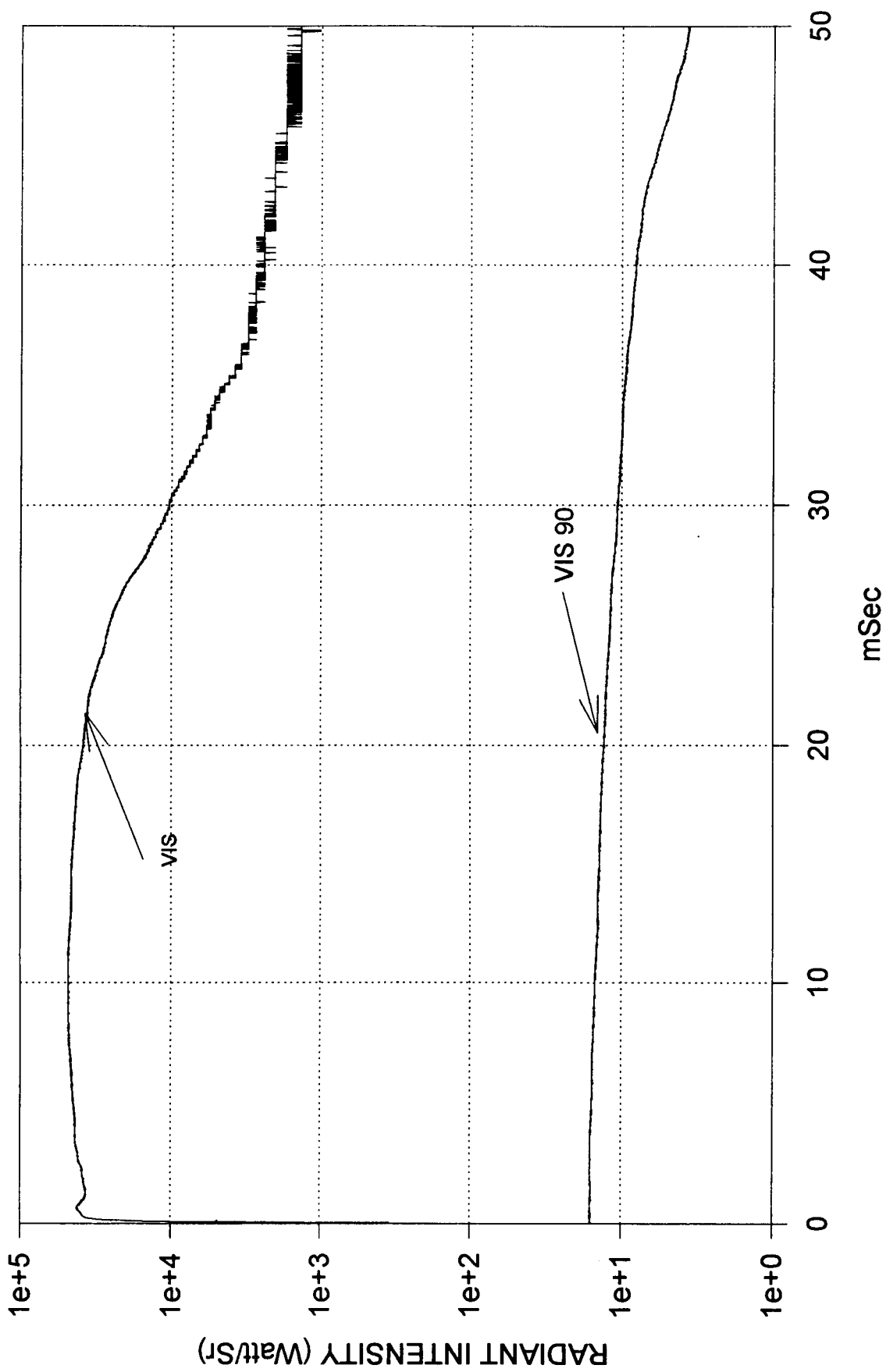
Figure A12 Target Plate Photographs - Test #5

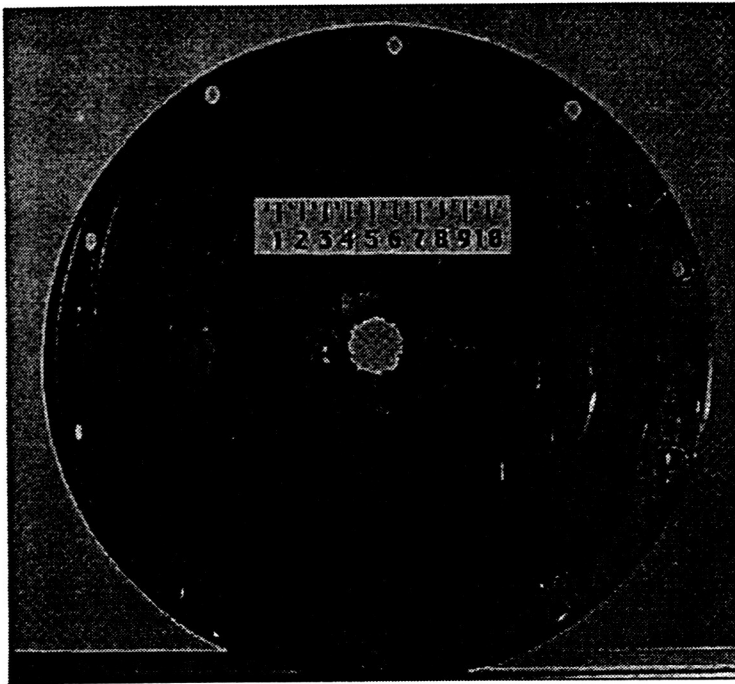




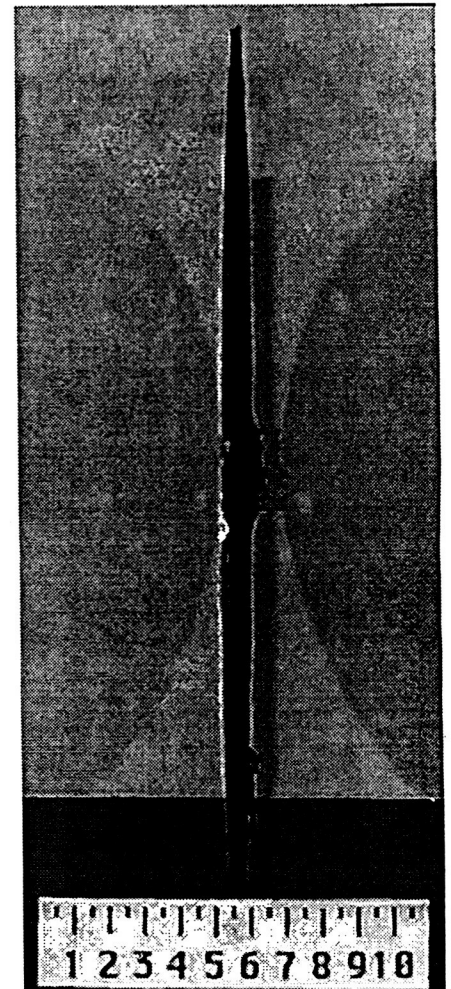
A14

Figure A14 Temperature Profiles - Test #5

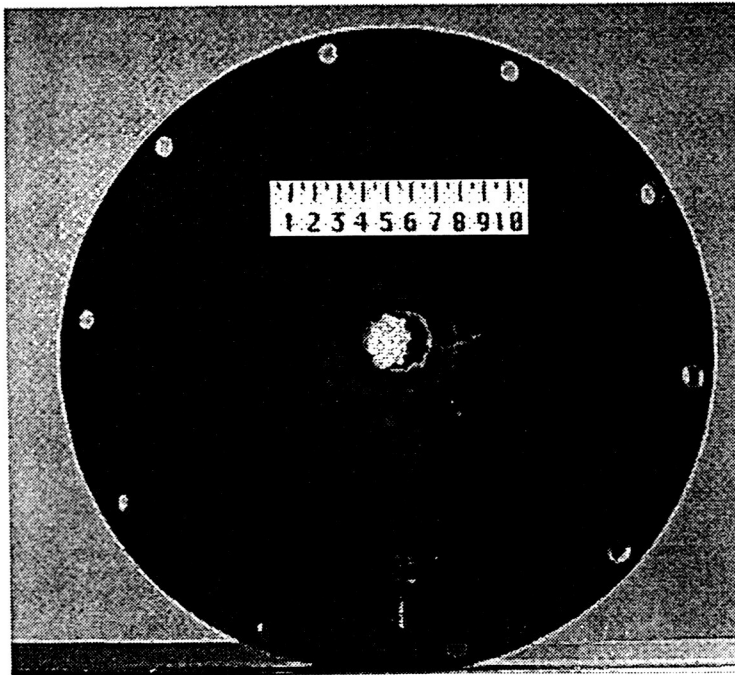




Target Plate Front



Target Plate Side



Target Plate Back

Figure A16 Target Plate Photographs - Test #6

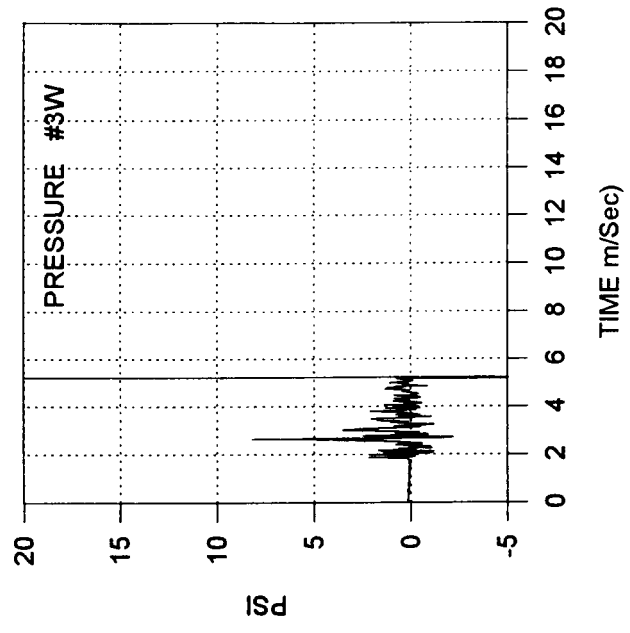
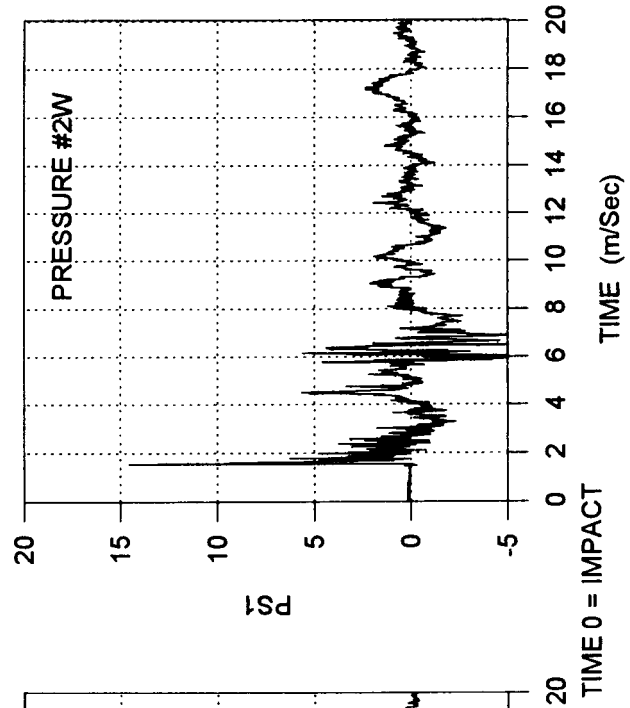
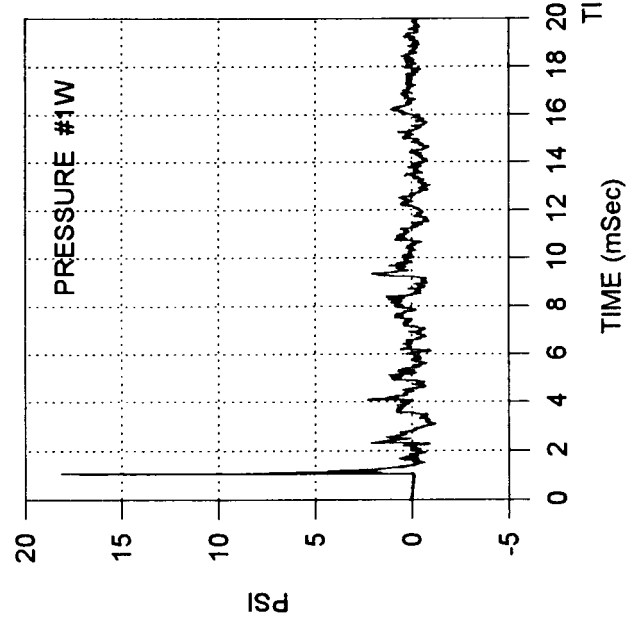
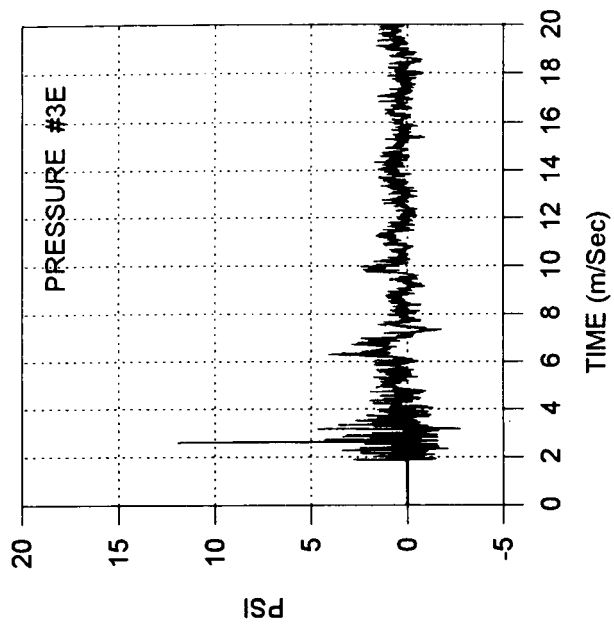
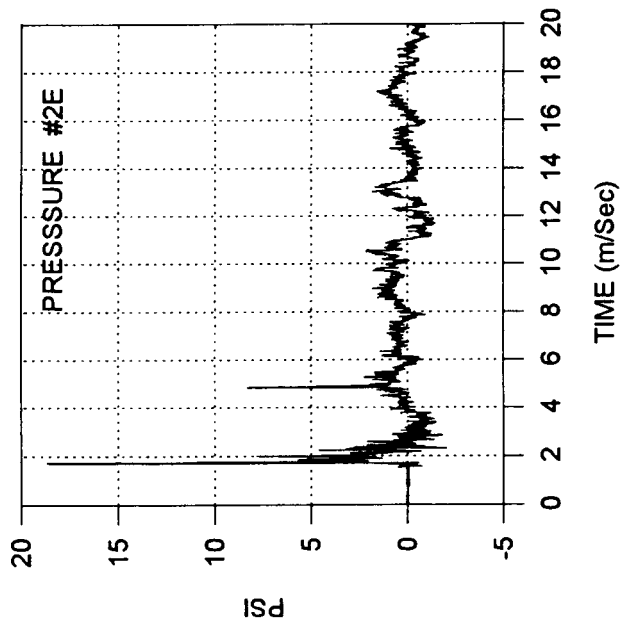
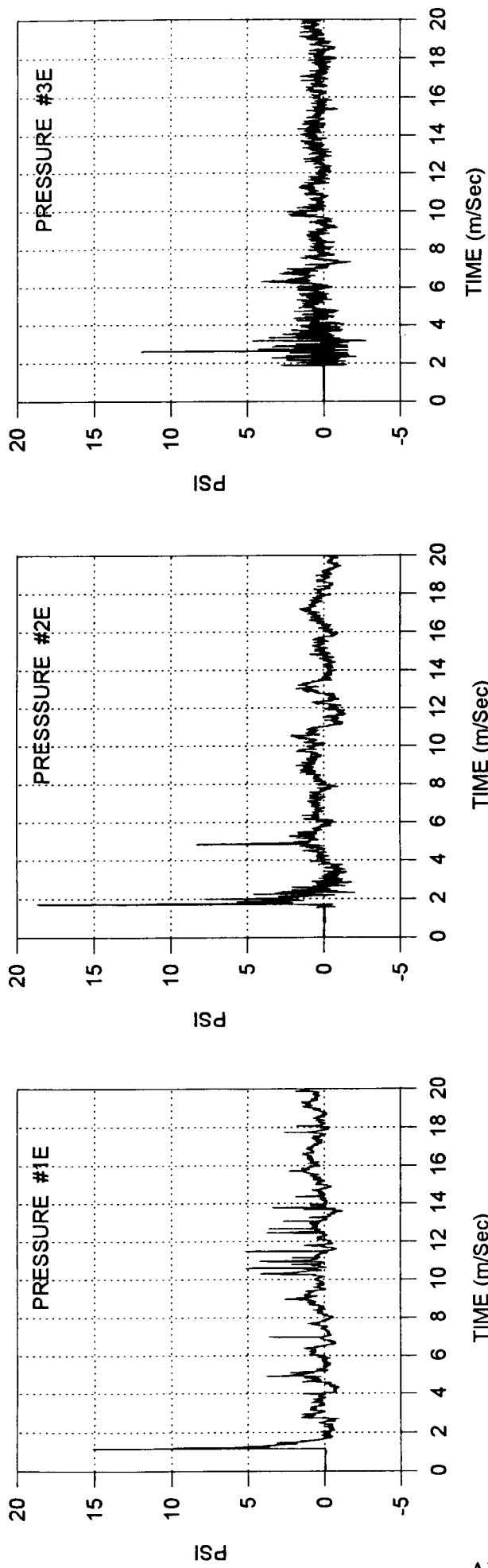
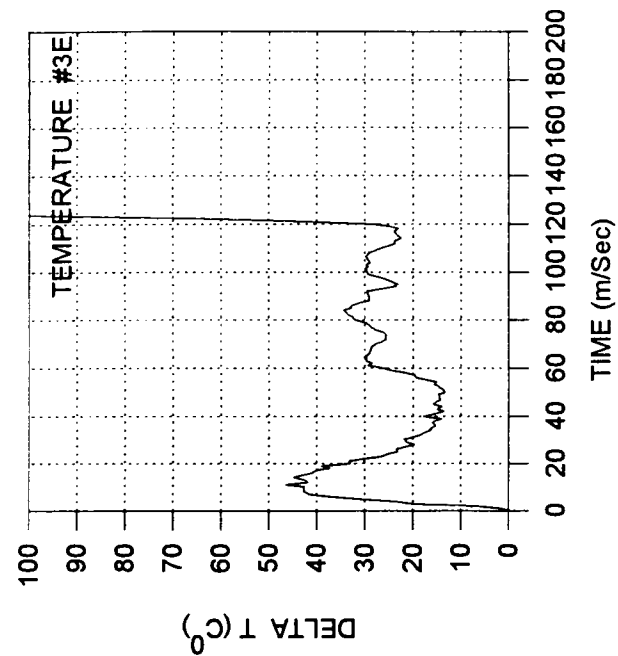
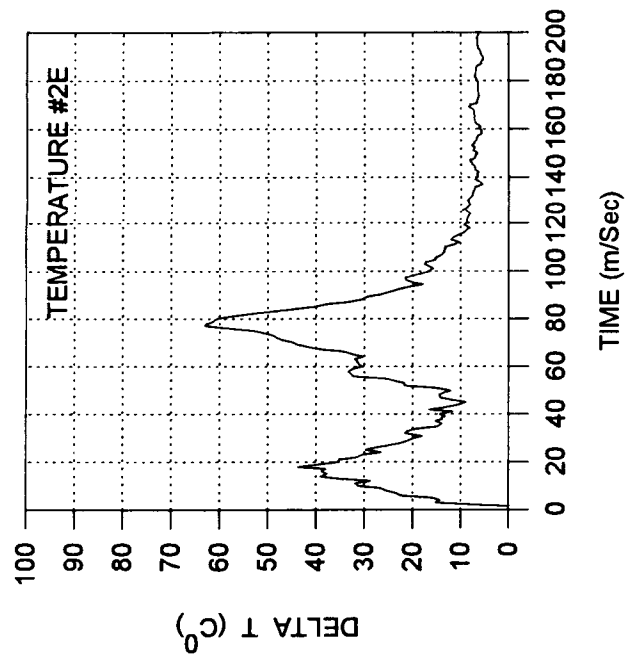
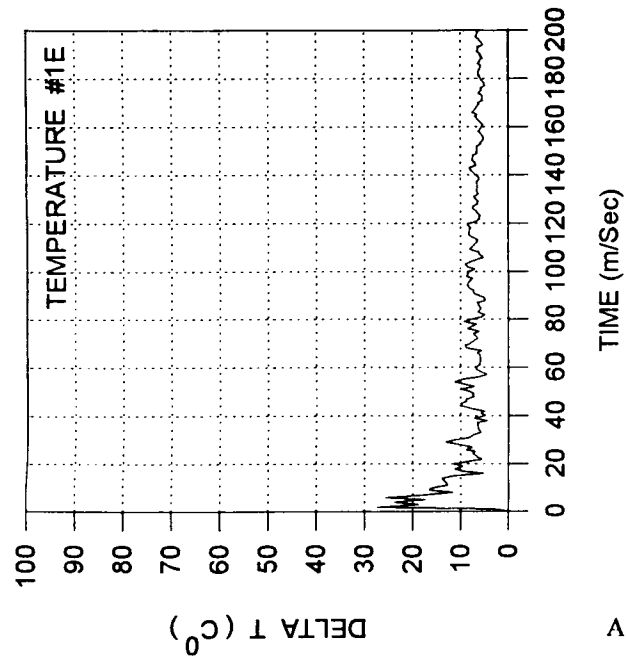


Figure A17 Pressure Profiles - Test #6



81V

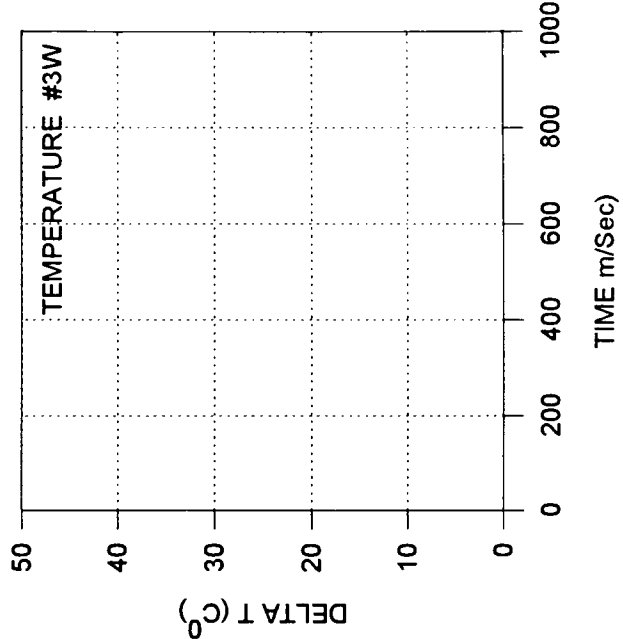
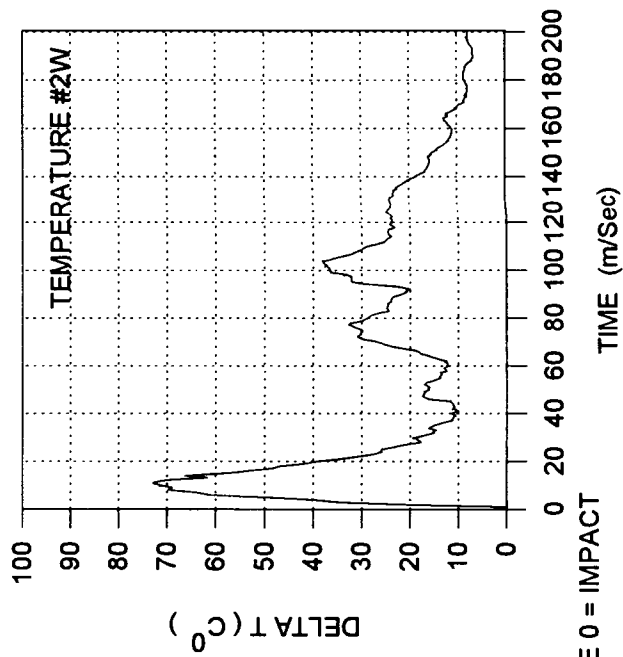
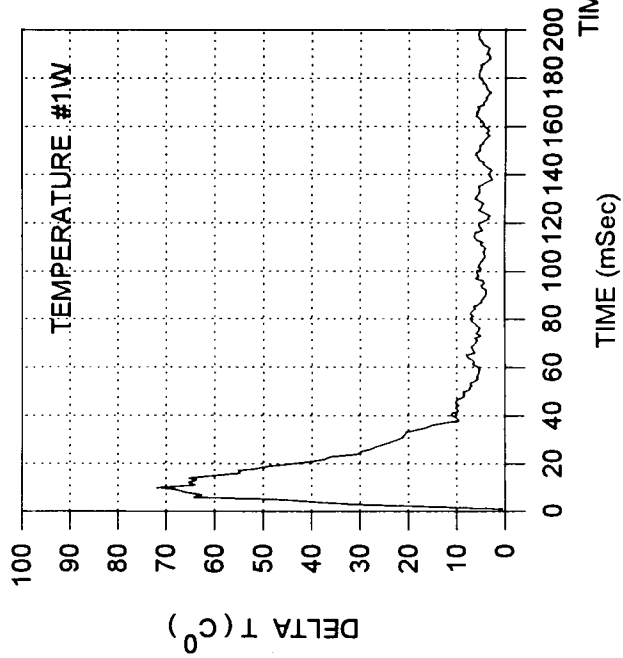


Figure A18 Temperature Profiles - Test #6

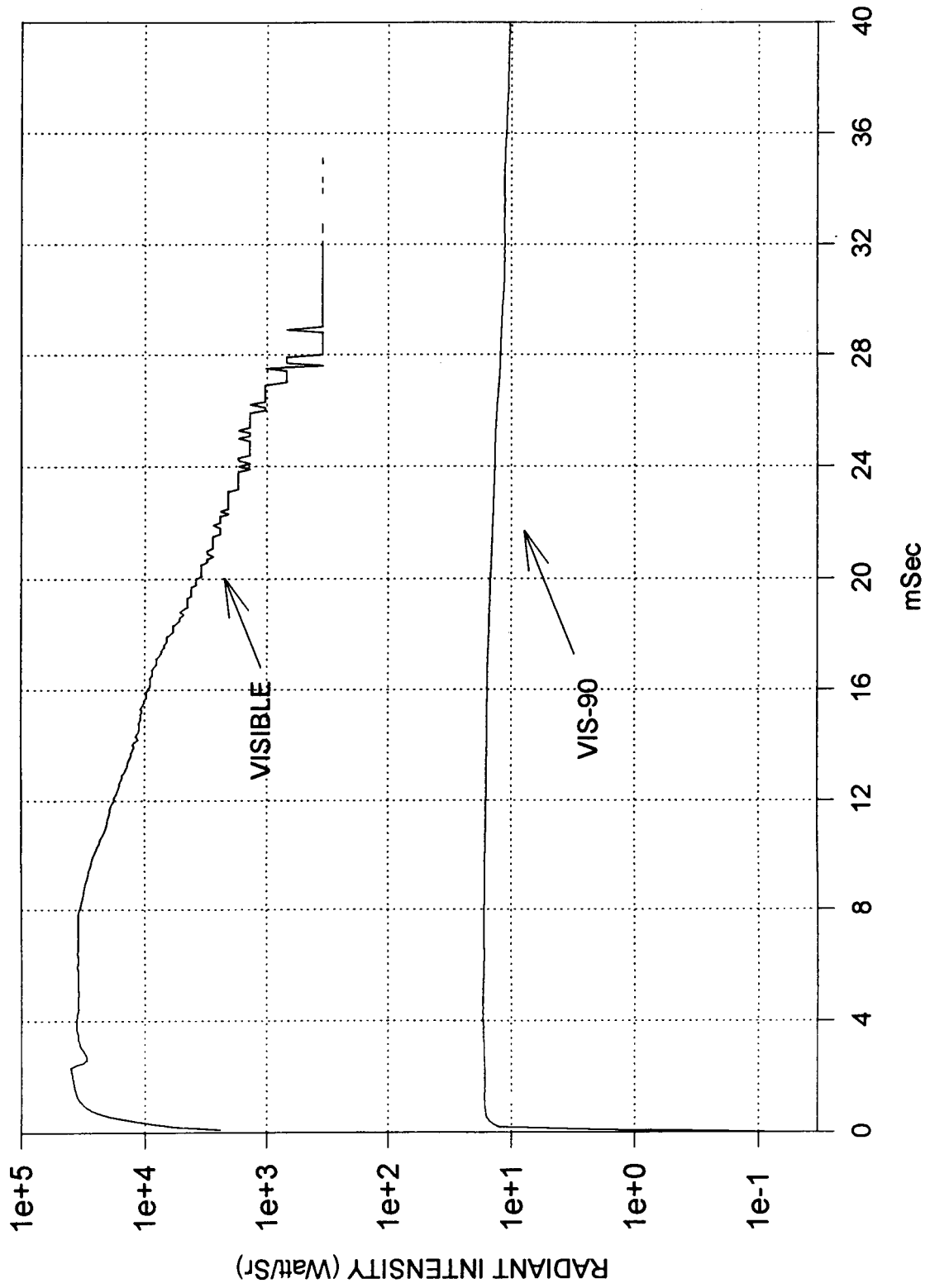
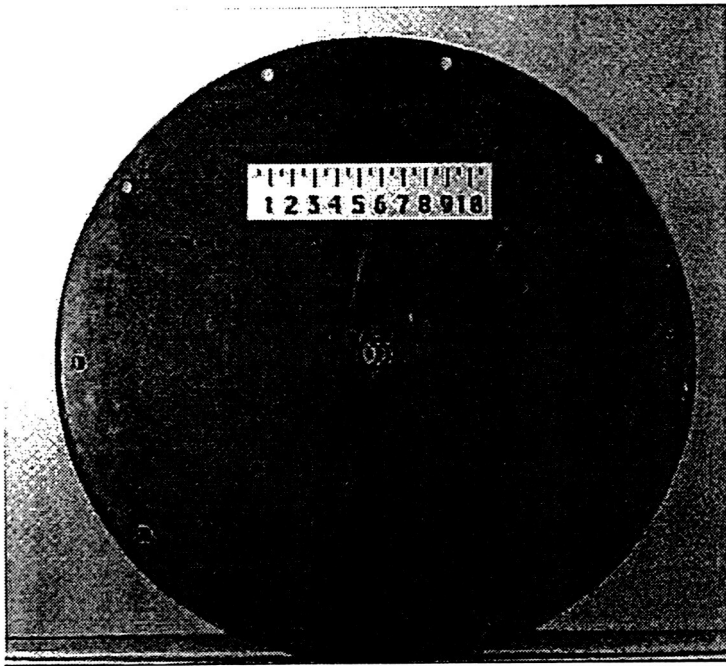
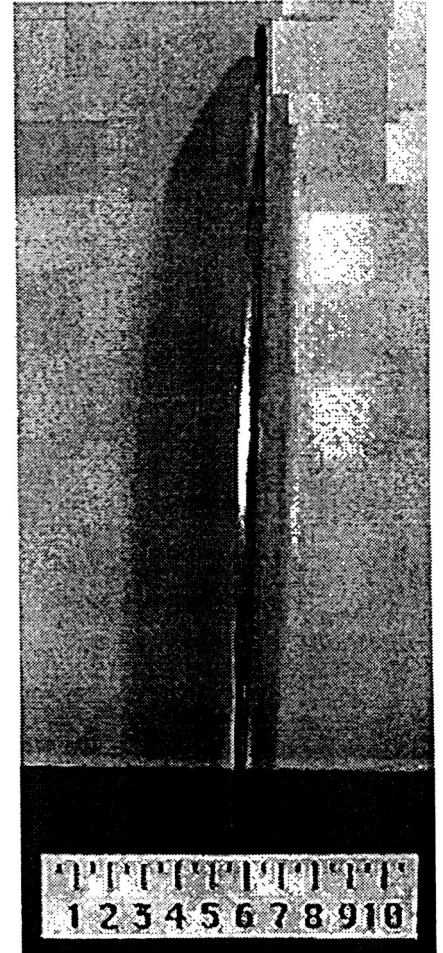


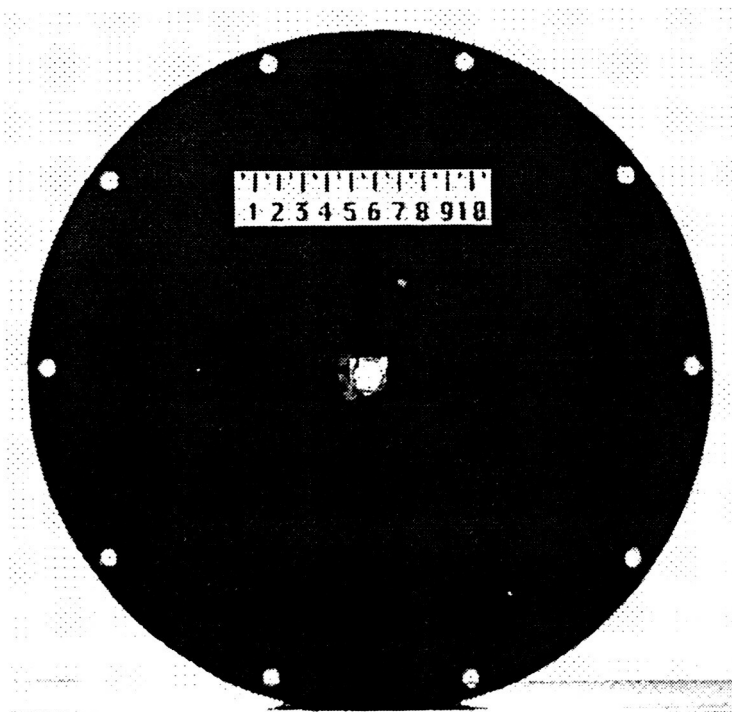
Figure A19 Radiometric Data - Test #6



Target Plate Front

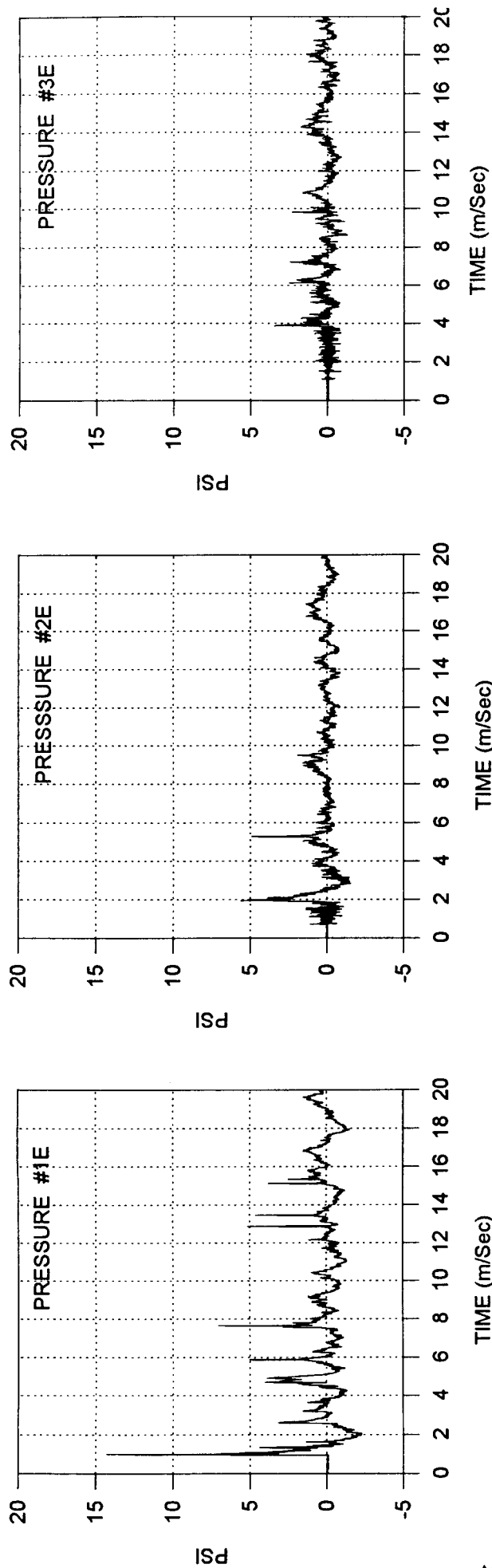


Target Plate Side



Target Plate Back

Figure A20 Target Plate Photographs - Test #8



12V

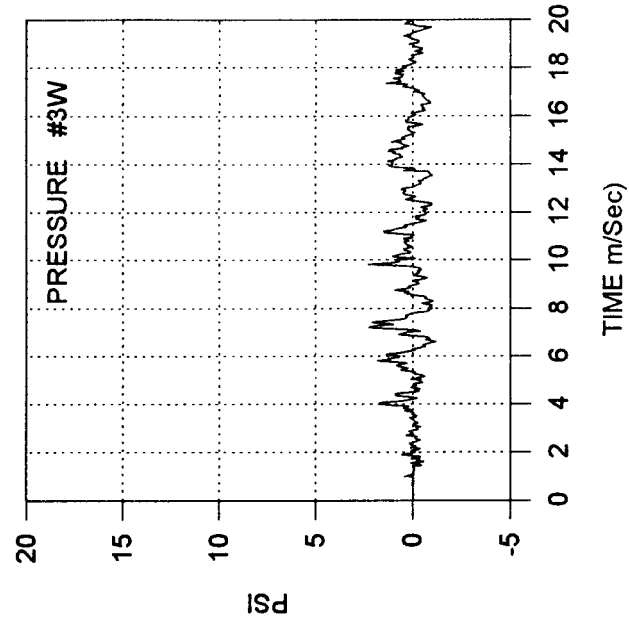
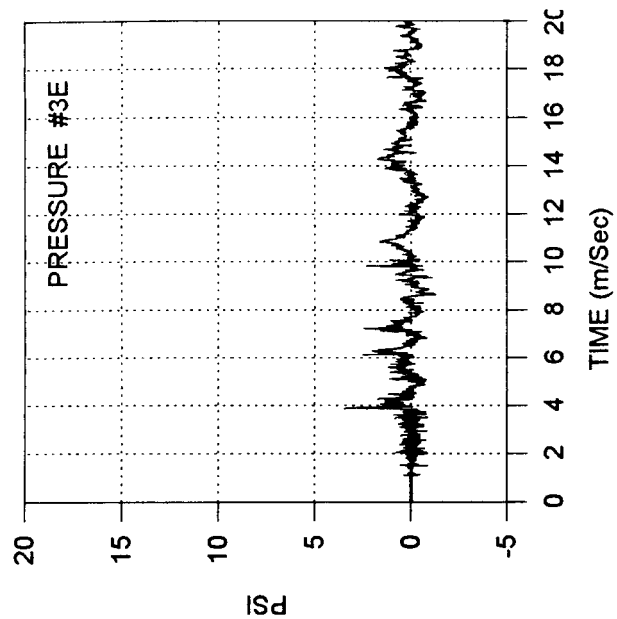
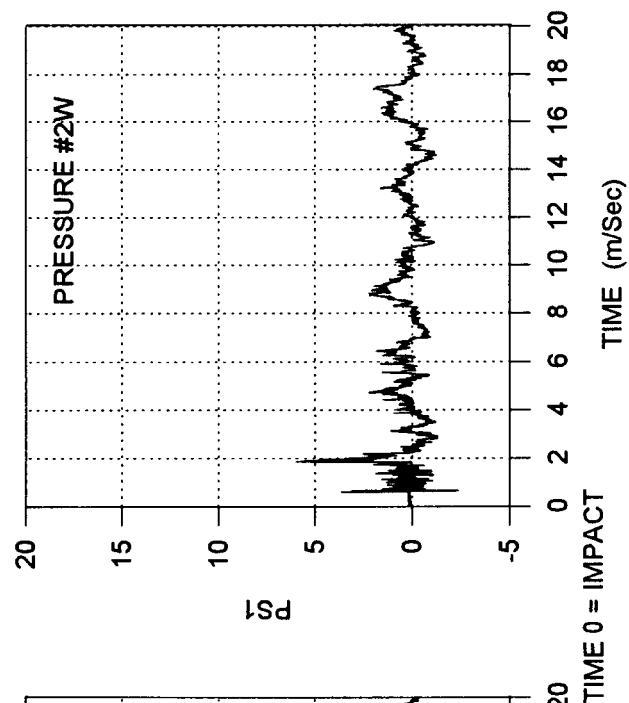
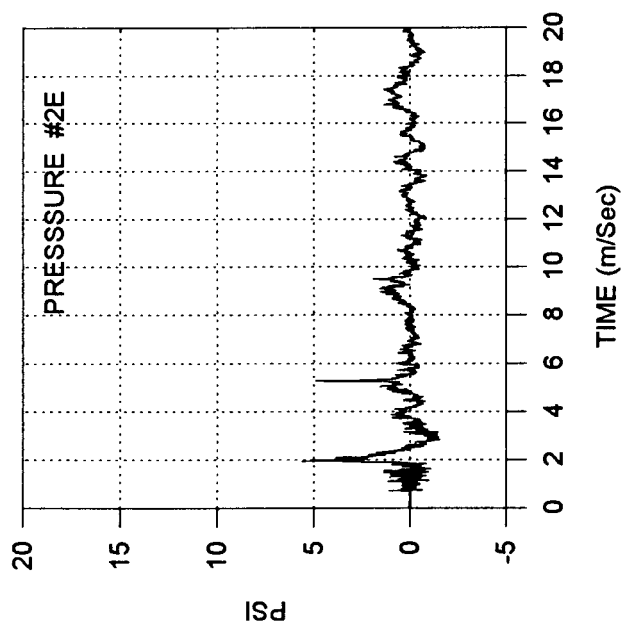
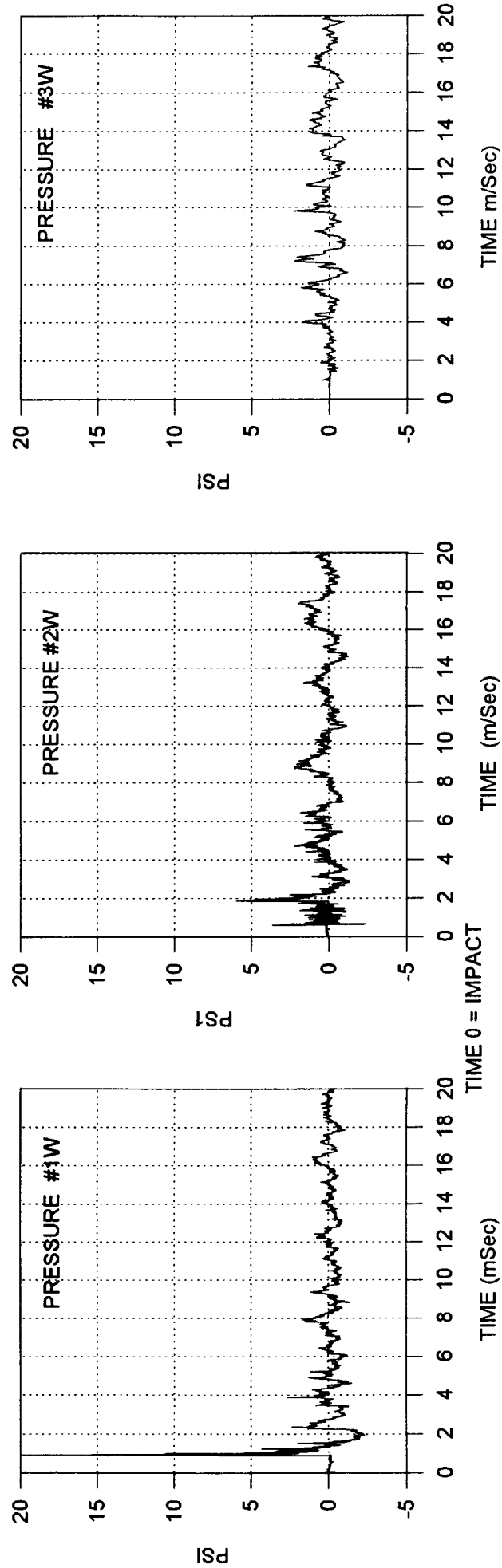
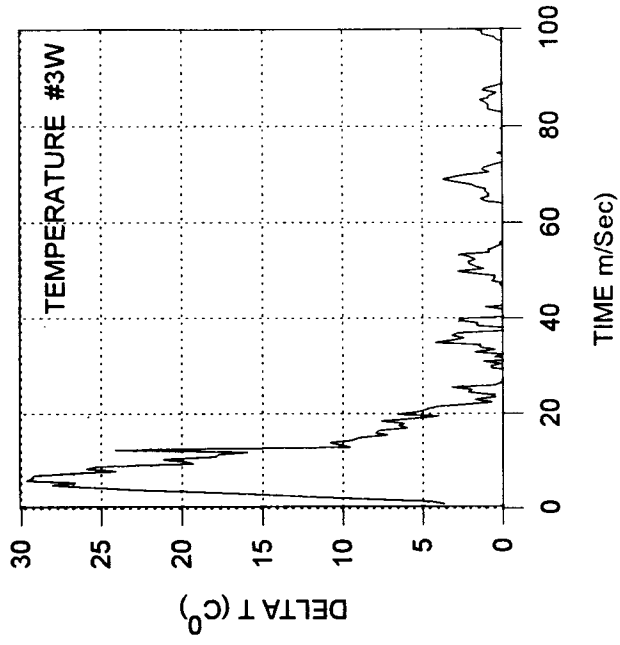
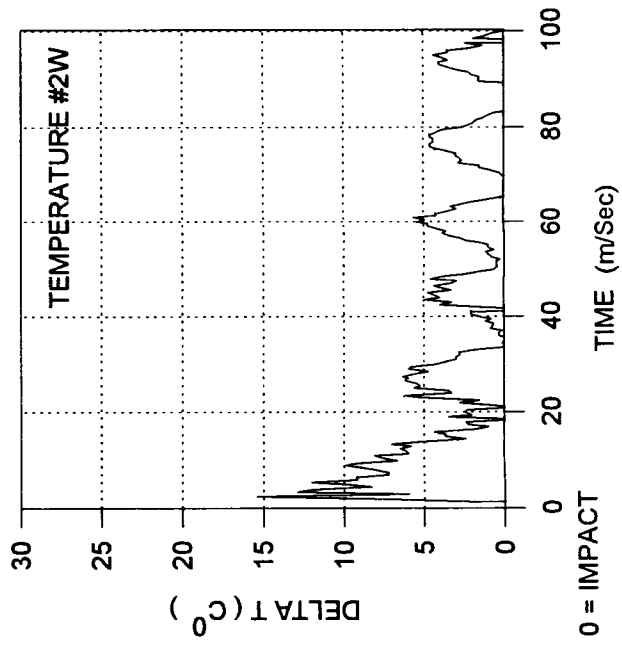
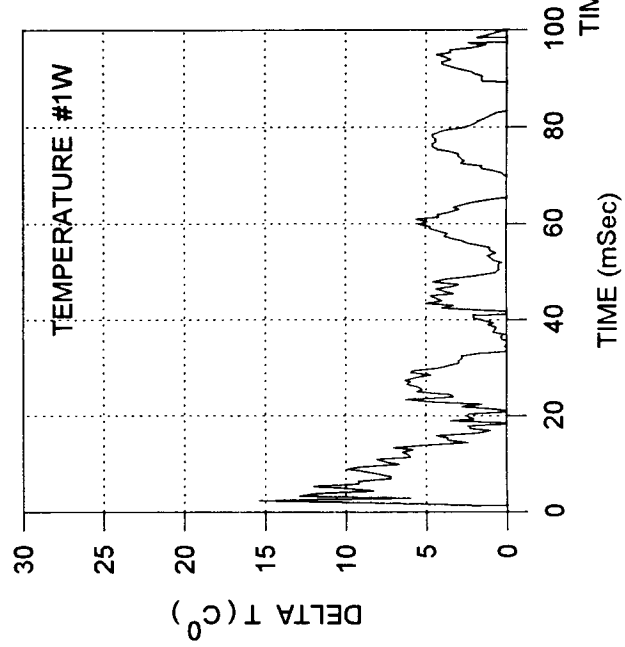
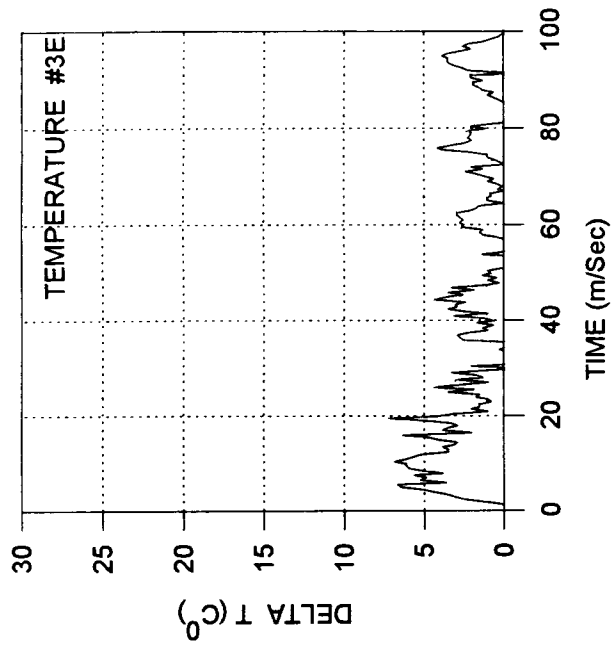
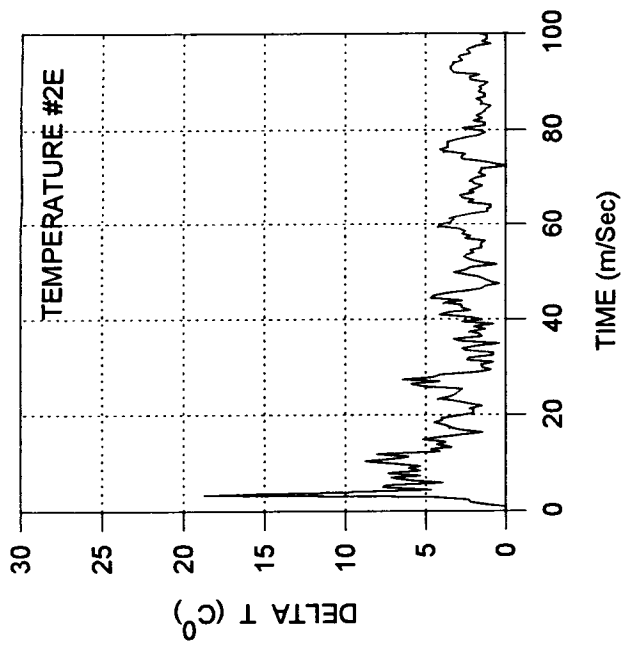
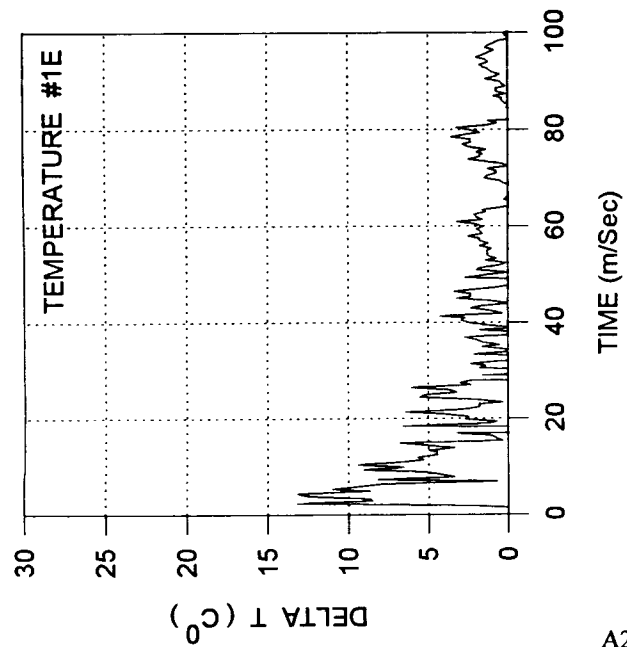


Figure A21 Pressure Profiles - Test #8

TIME 0 = IMPACT



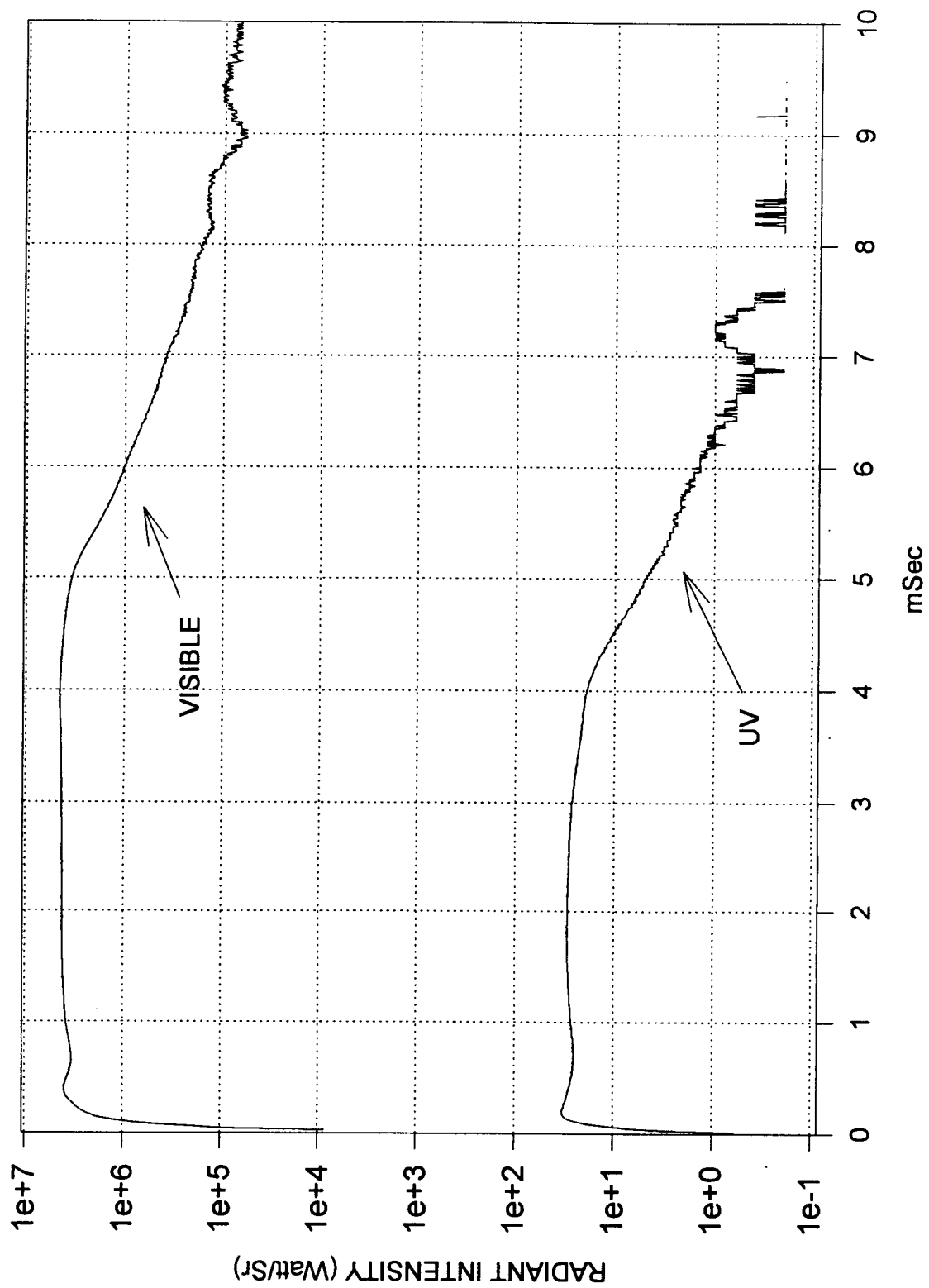
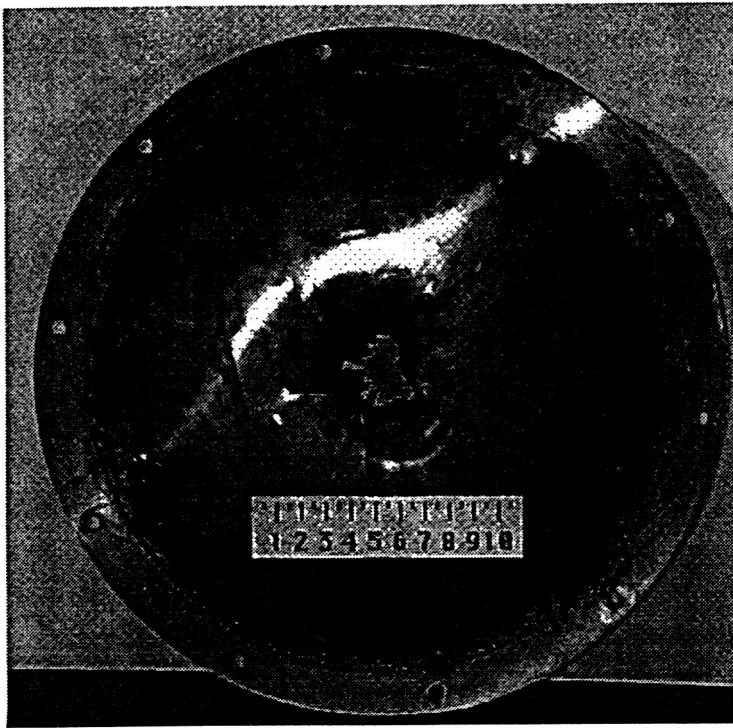


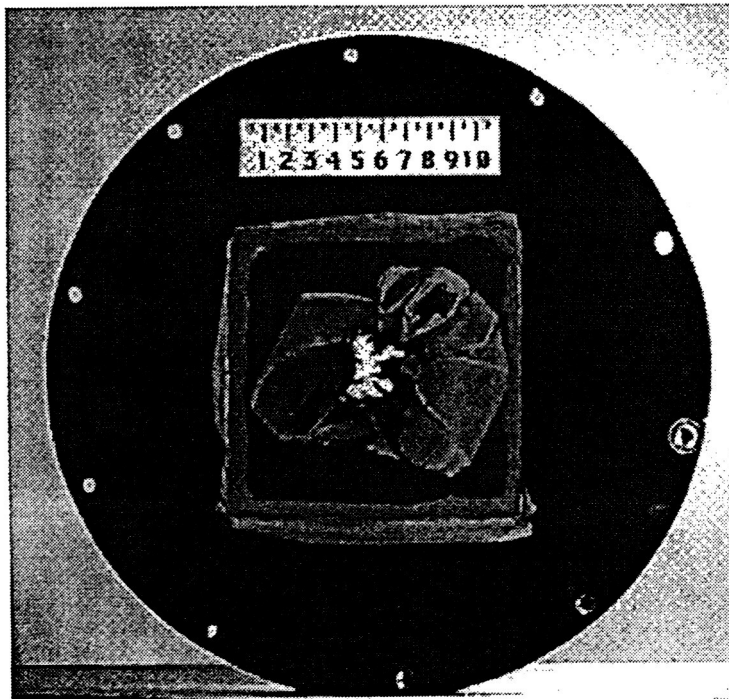
Figure A23 Radiometric Data - Test #8



Target Plate Front



Target Plate Side



Target Plate Back

Figure A24 Target Plate Photographs - Test #9

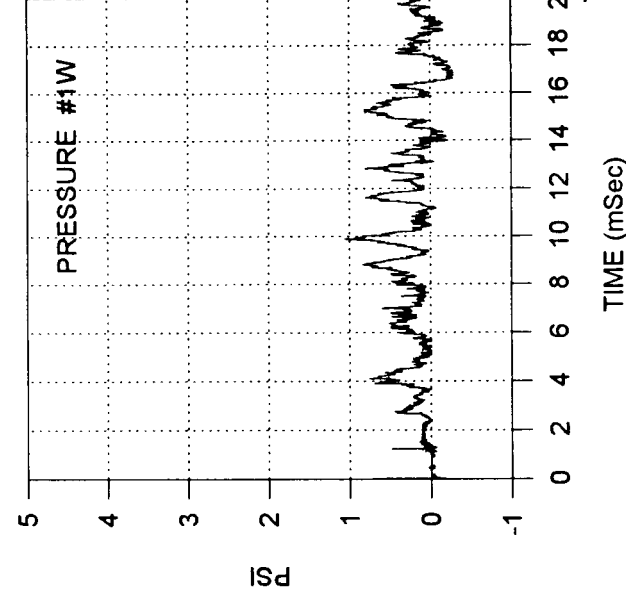
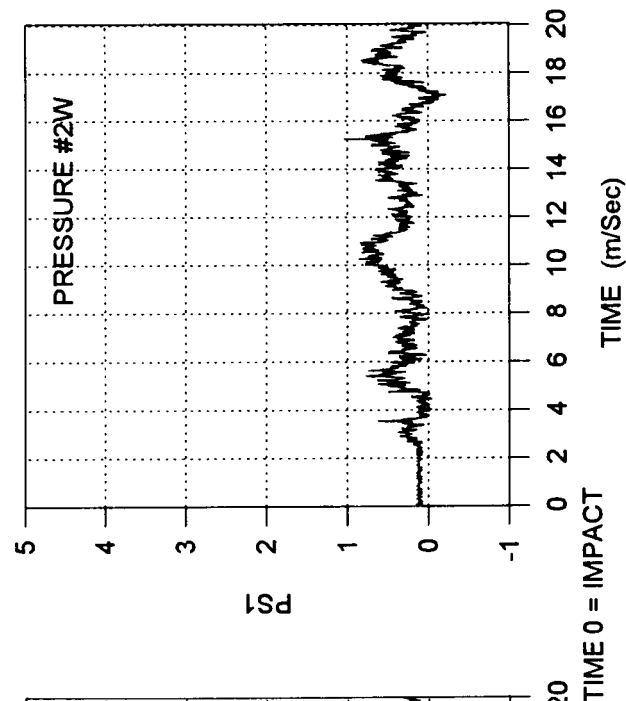
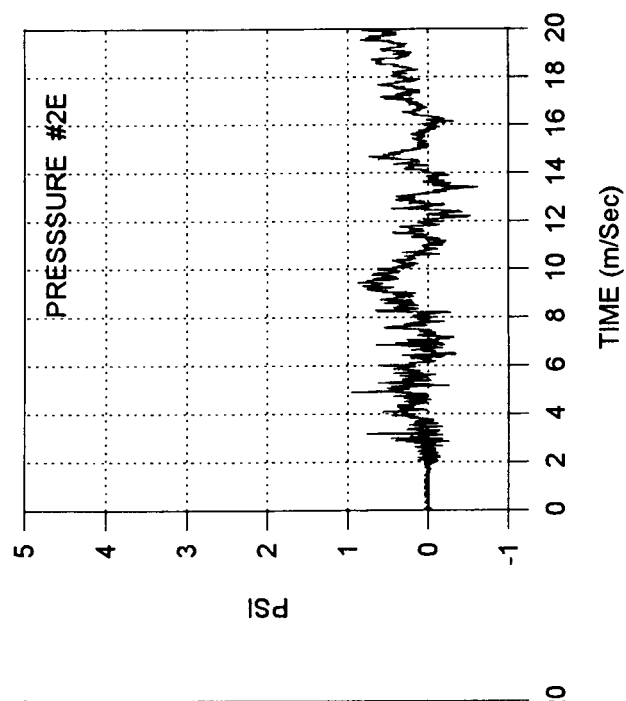
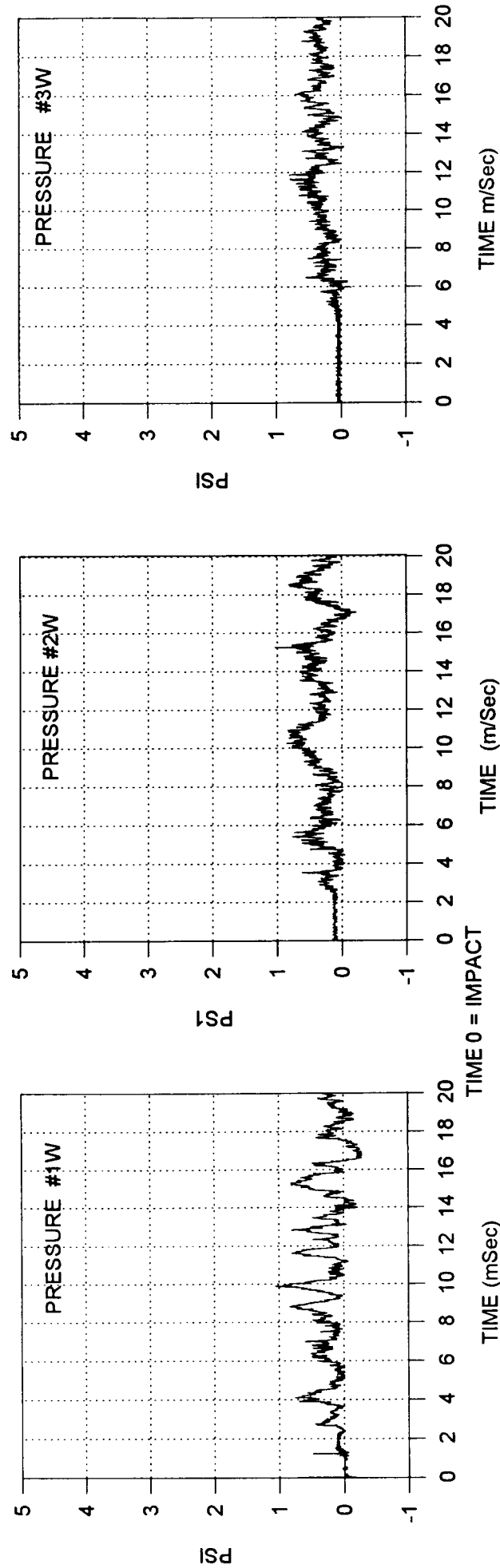
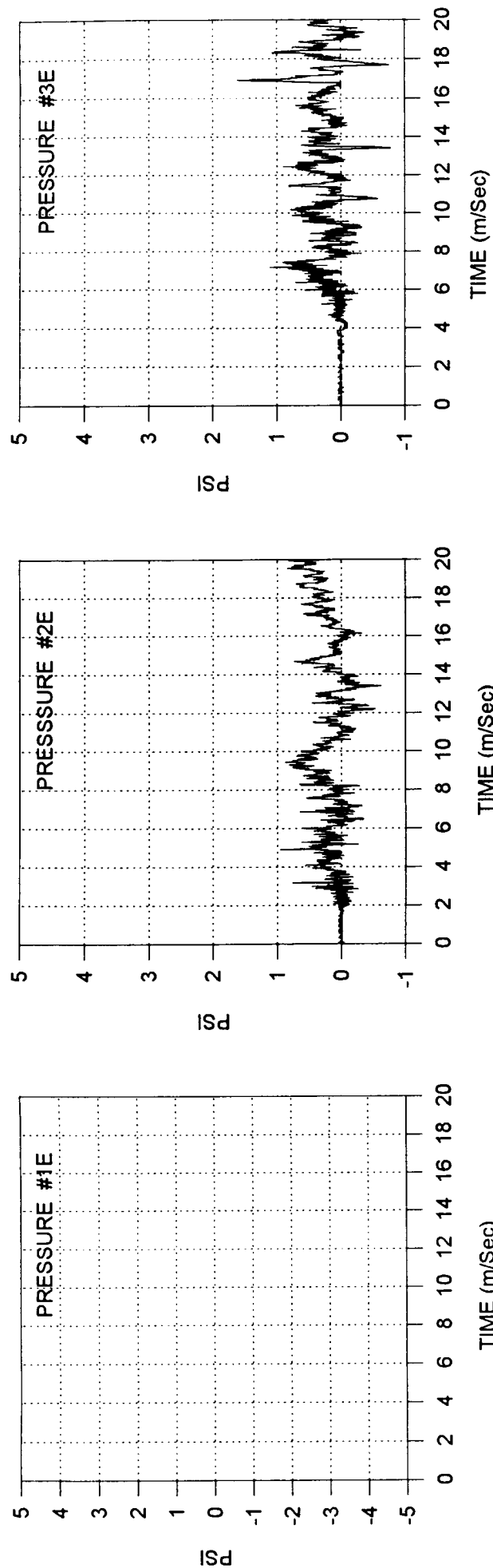
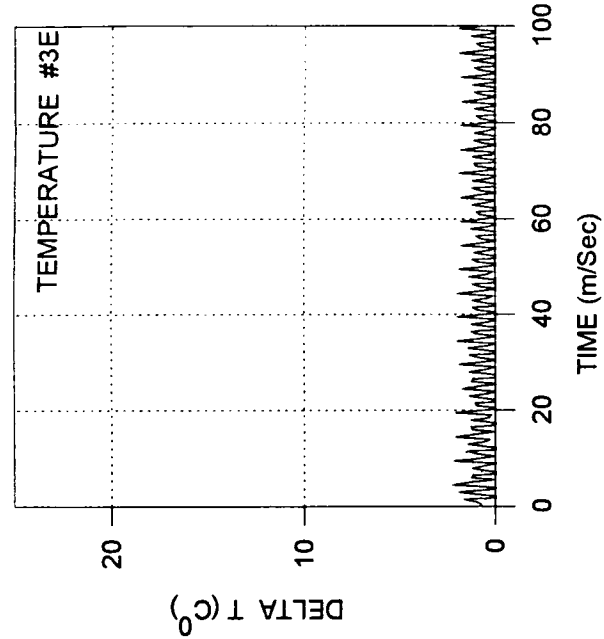
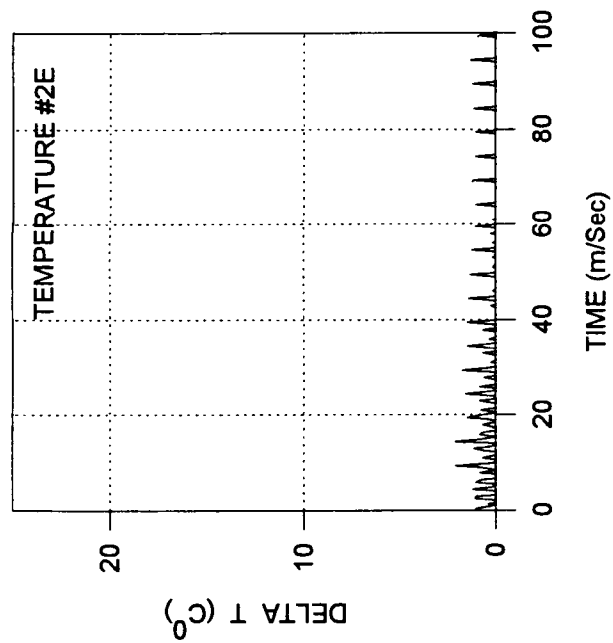
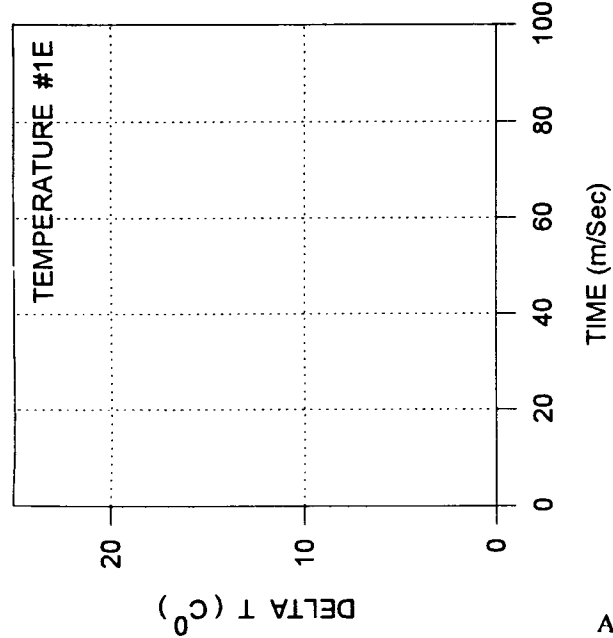


Figure A25 Pressure Profiles - Test #9



A26

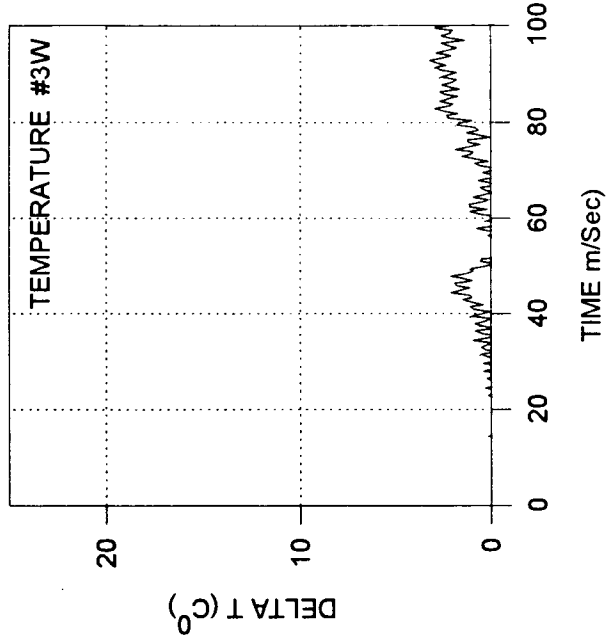
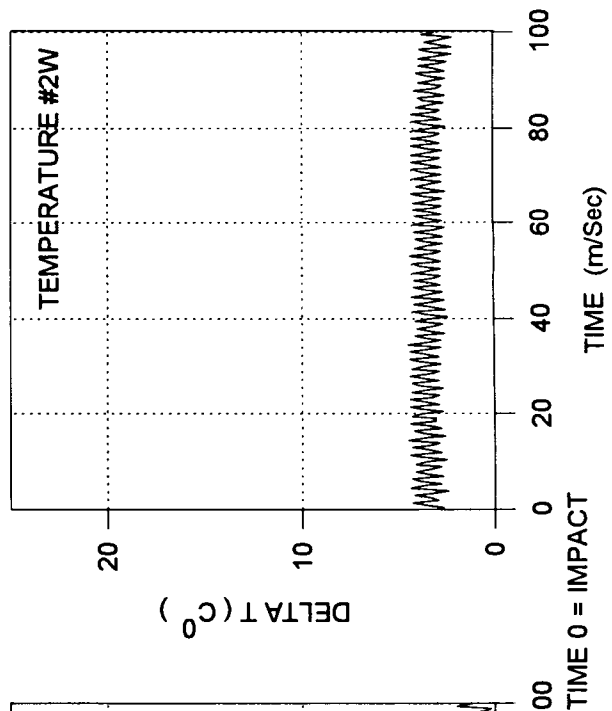
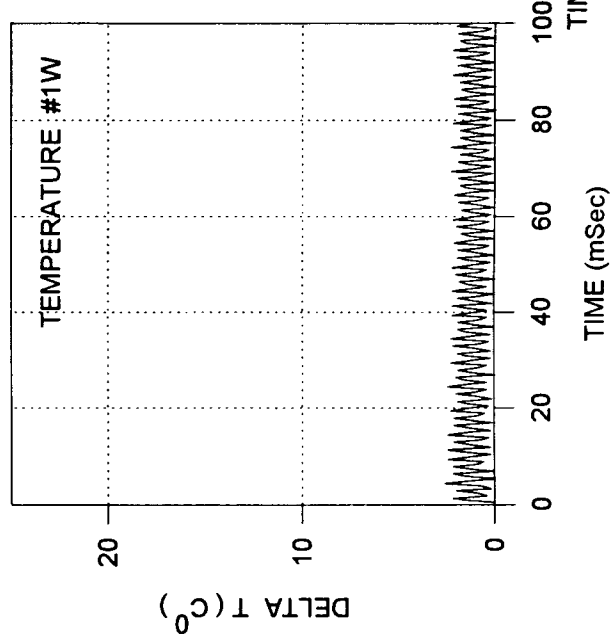


Figure A26 Temperature Profiles - Test #9

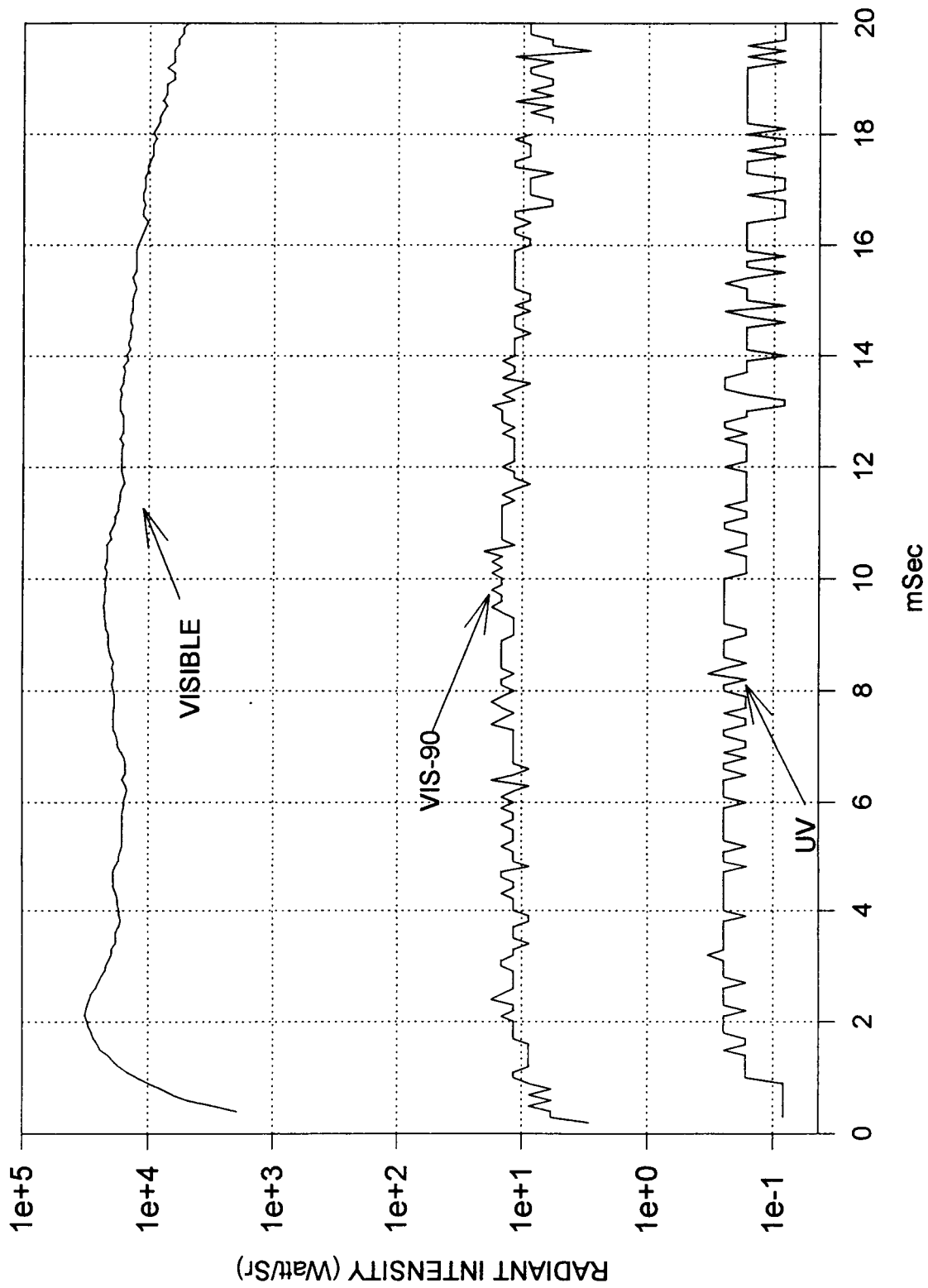
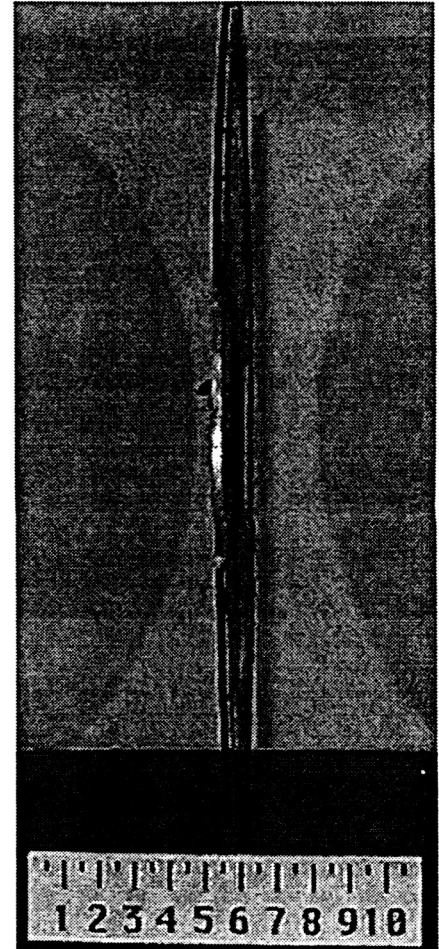


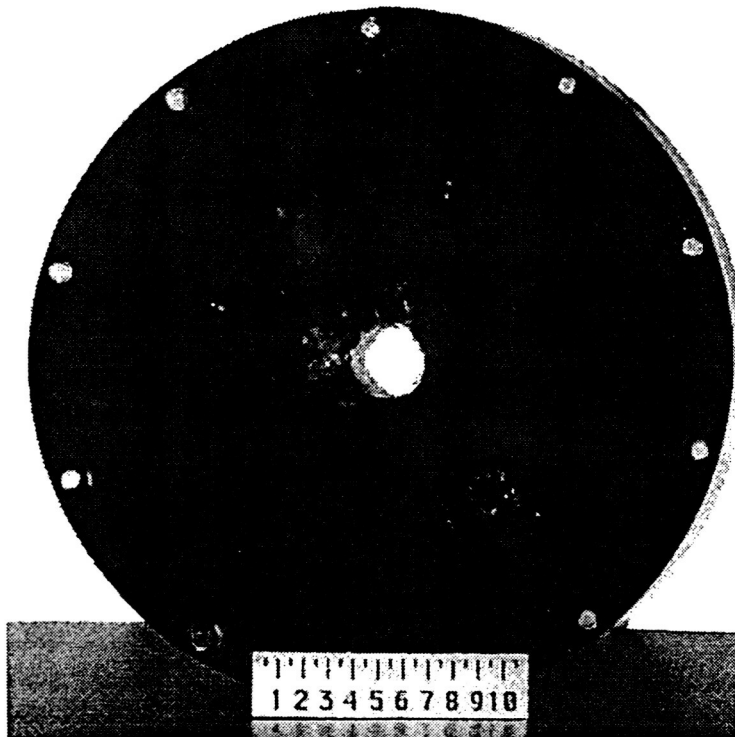
Figure A27 Radiometric Data - Test #9



Target Plate Front



Target Plate Side



Target Plate Back

Figure A28 Target Plate Photographs - Test #10

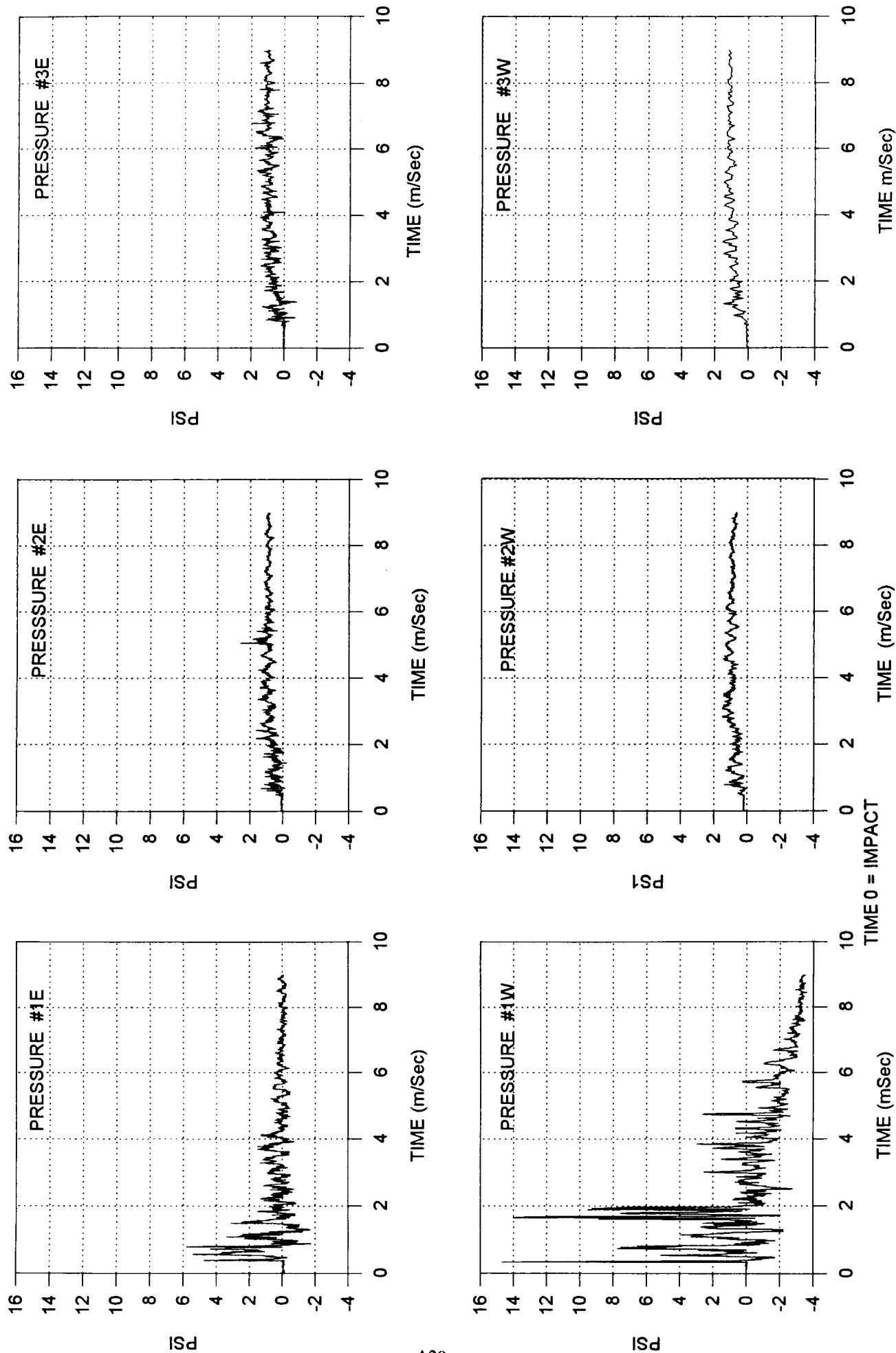
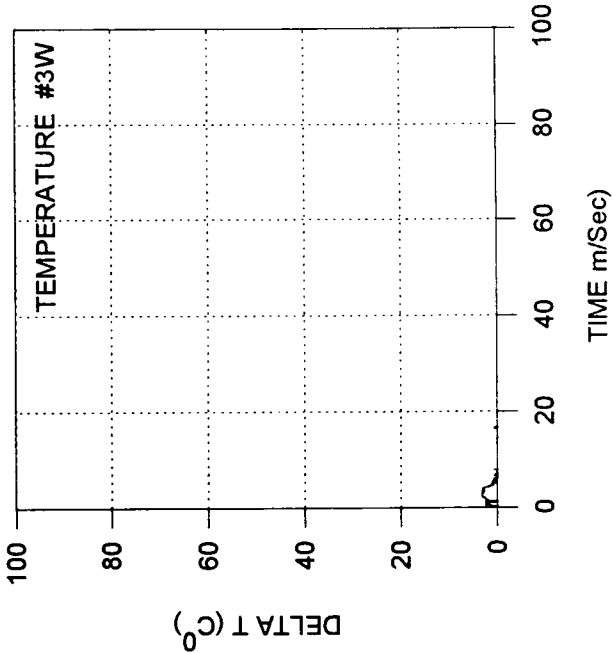
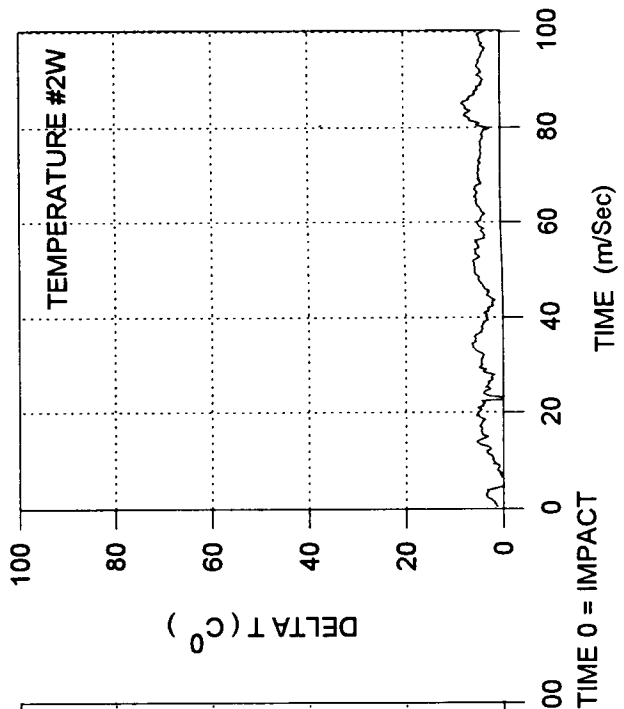
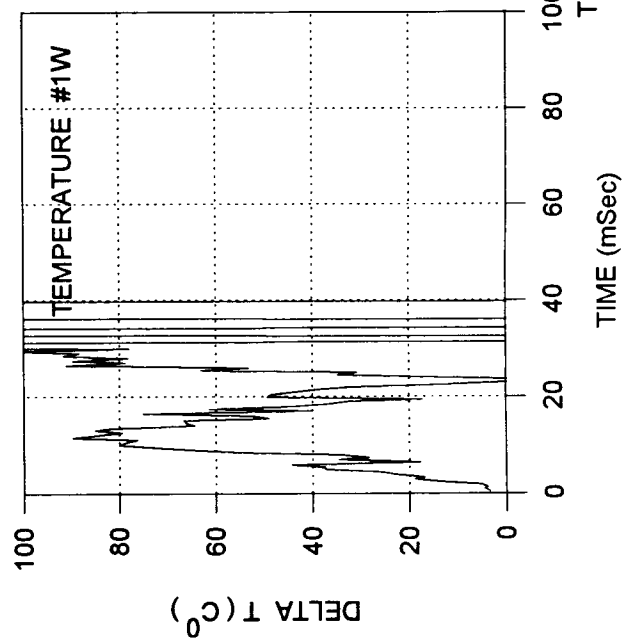
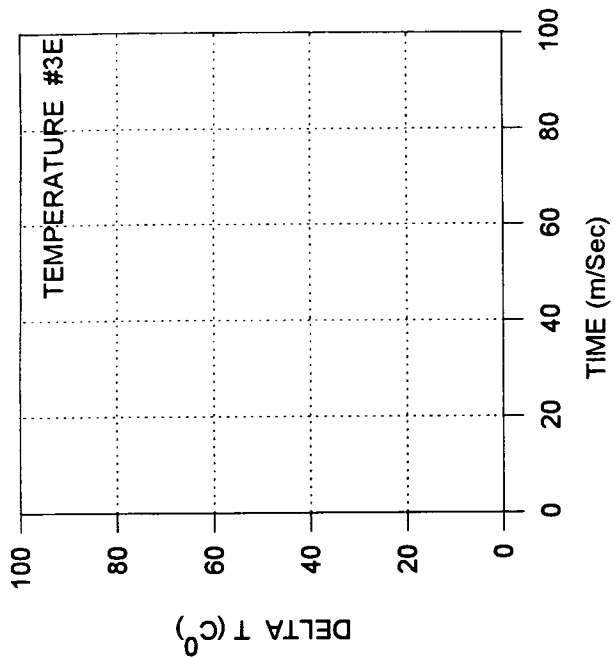
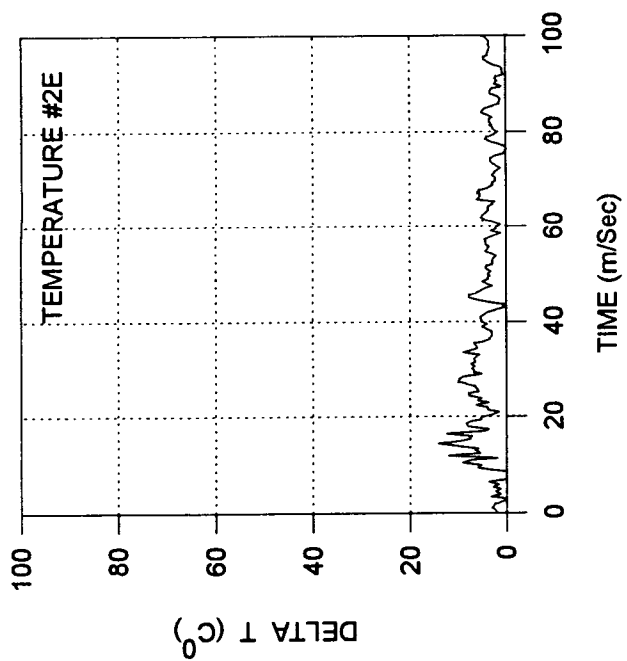
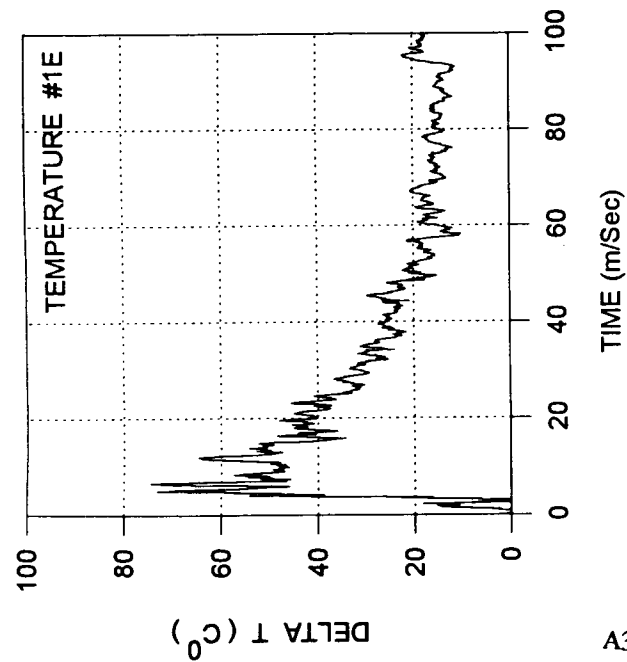


Figure A29 Pressure Profiles - Test #10



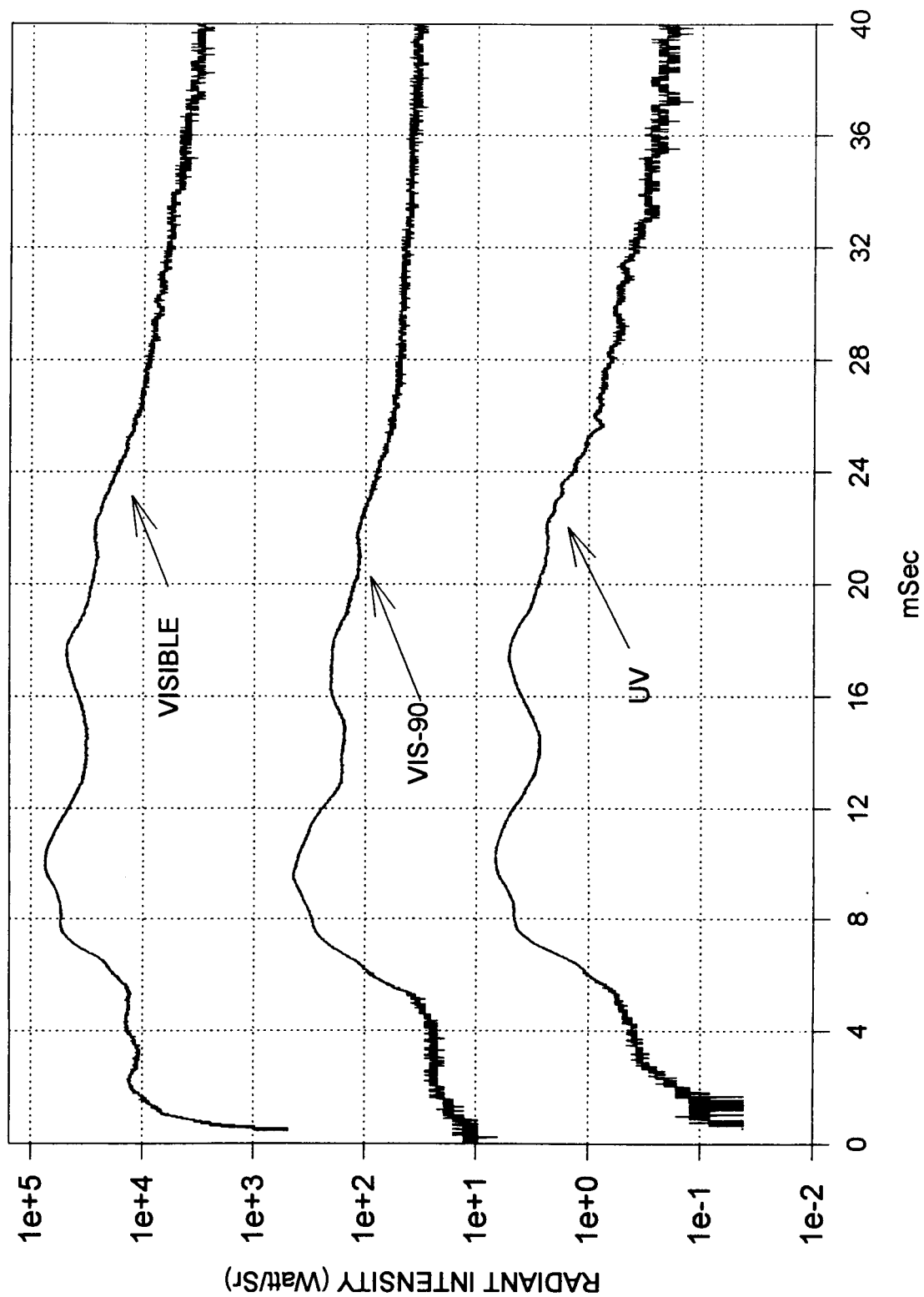
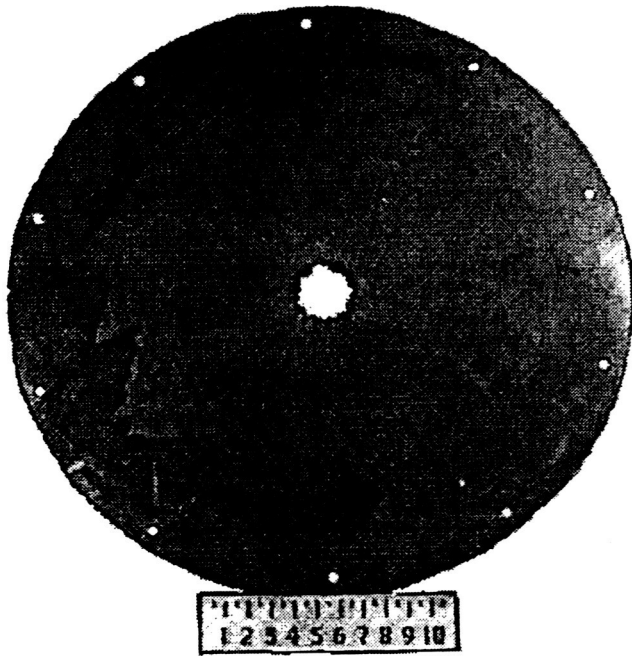
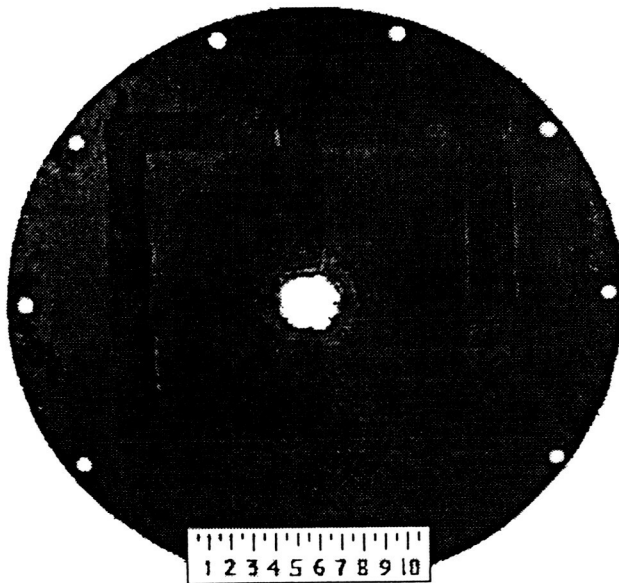


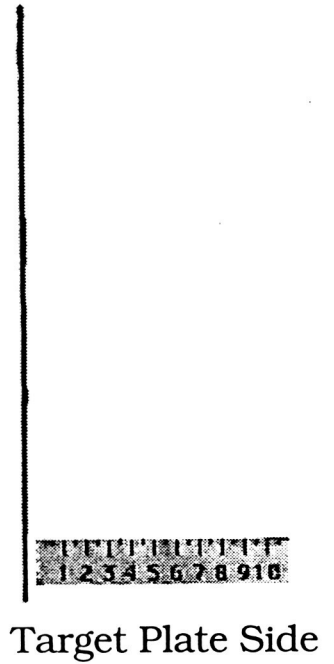
Figure A31 Radiometric Data - Test #10



Target Plate Front

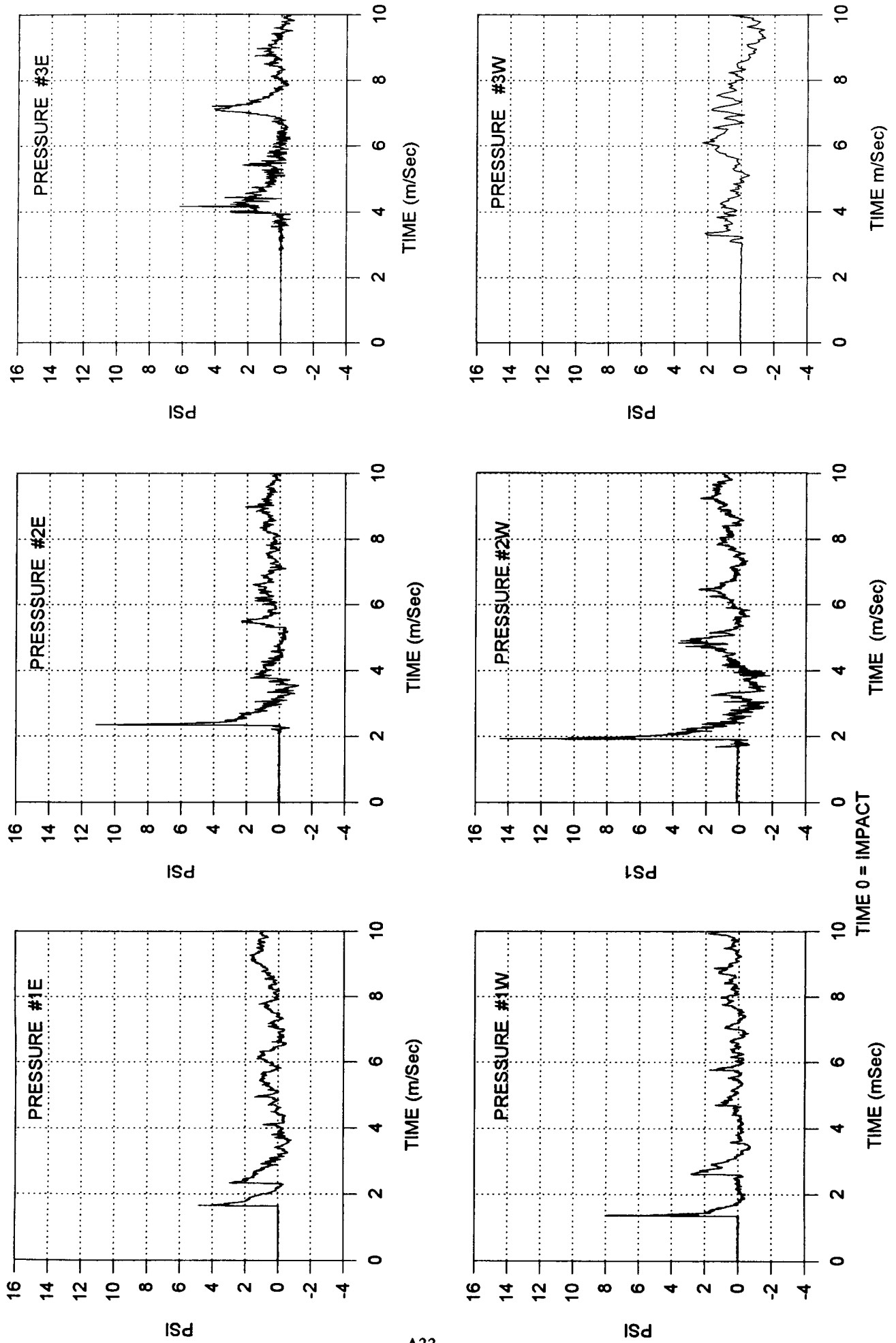


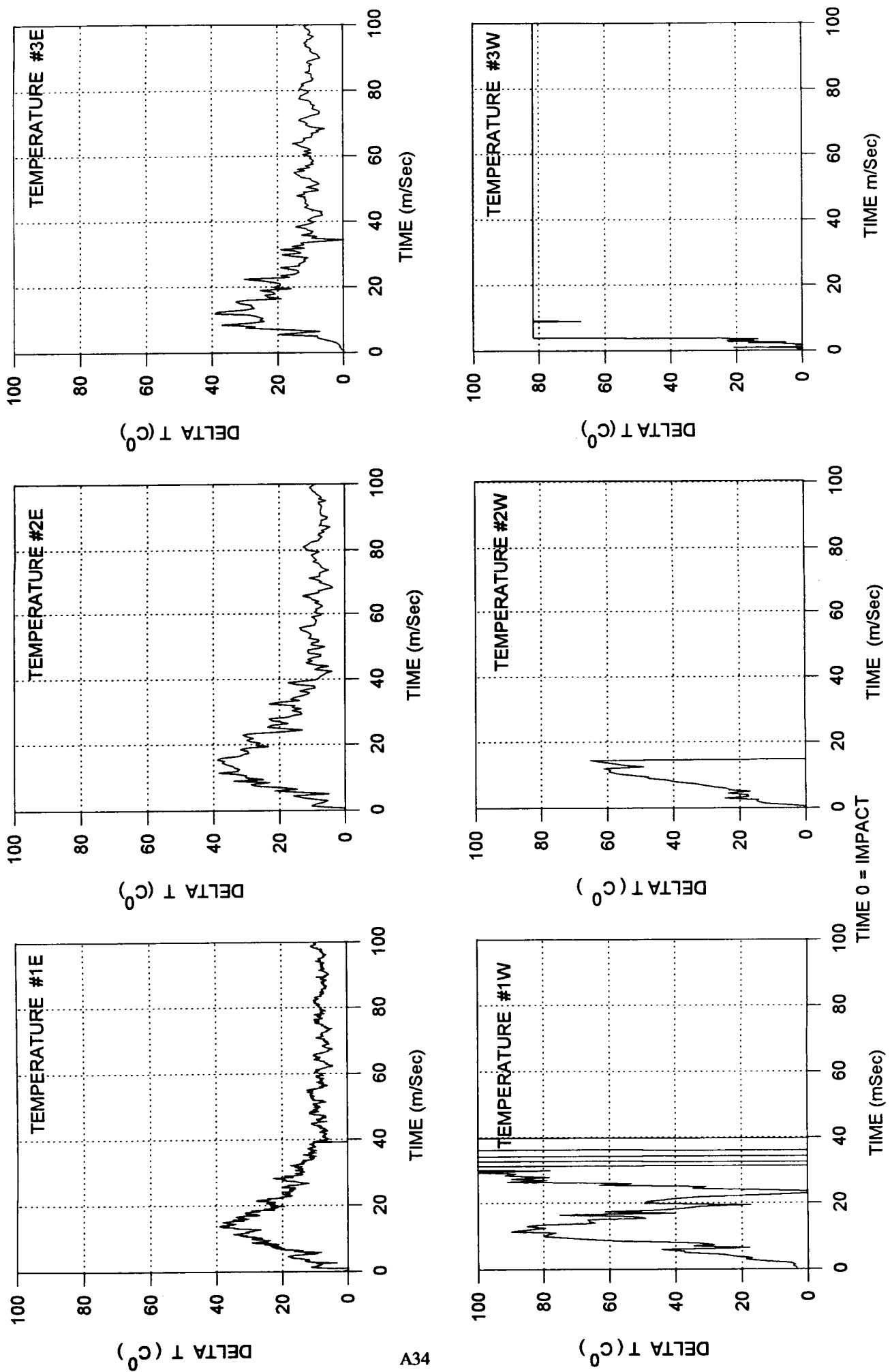
Target Plate Back



Target Plate Side

Figure A32 Target Plate Photographs - Test #11





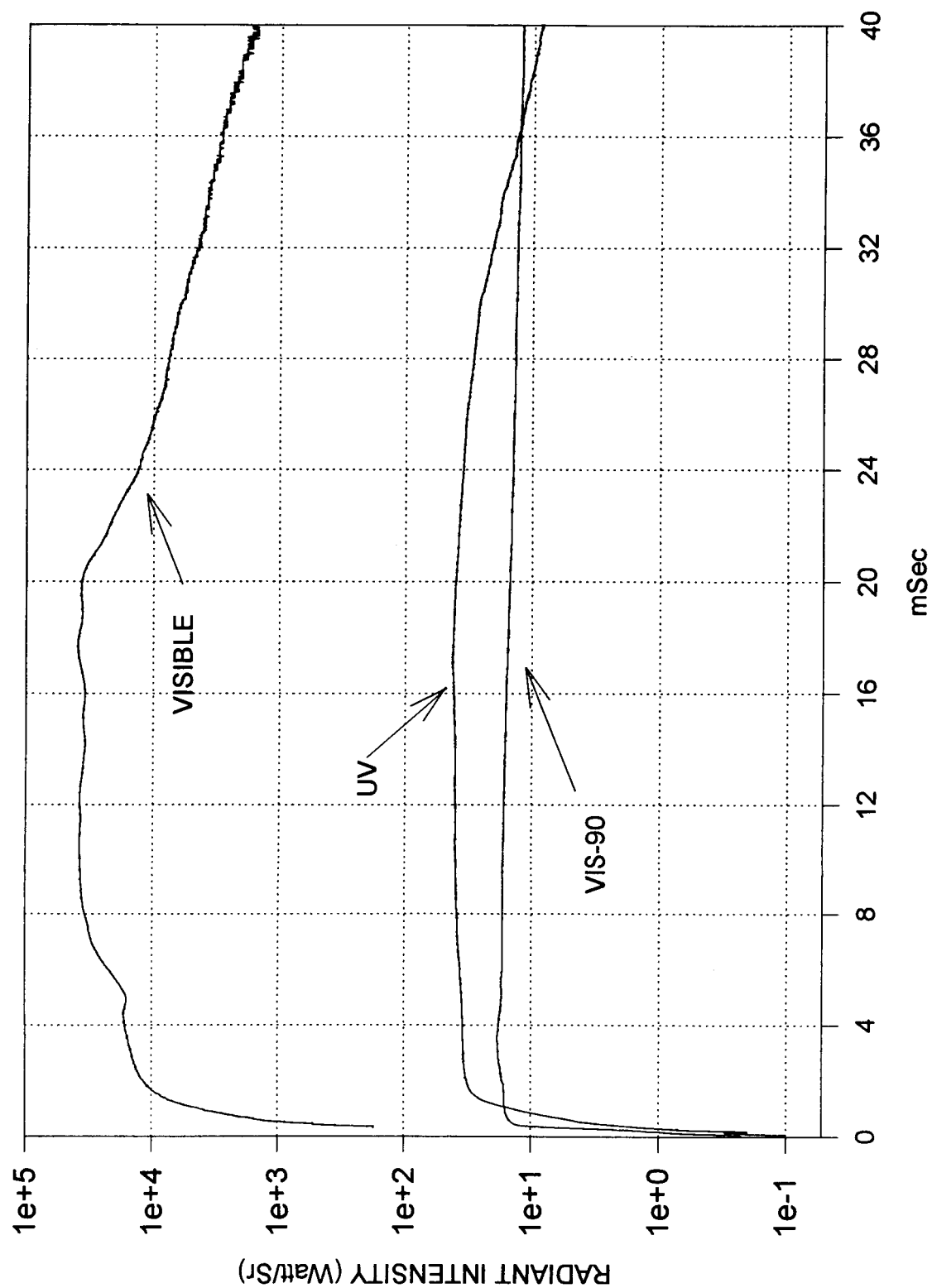
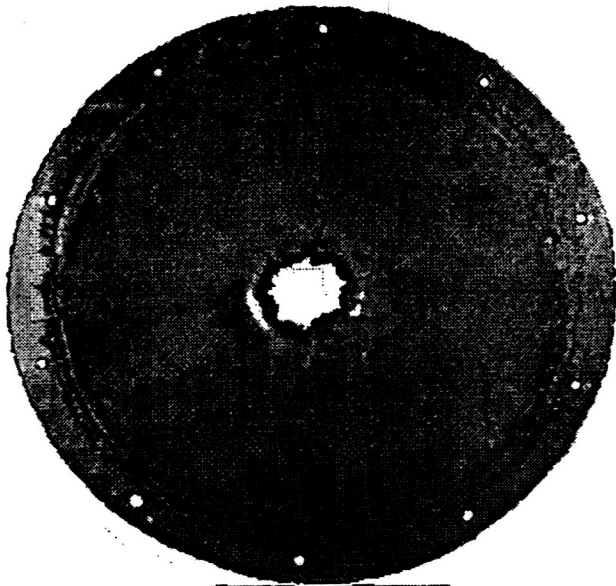
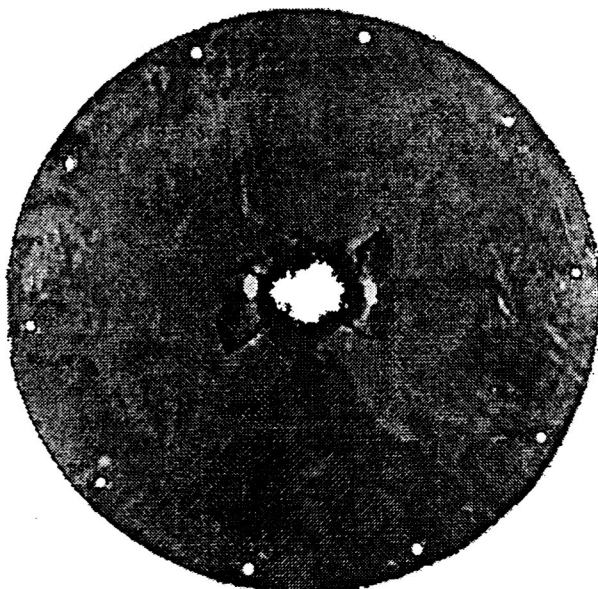


Figure A35 Radiometric Data - Test #11



Target Plate Front



Target Plate Back



Target Plate Side

Figure A36 Target Plate Photographs - Test #13

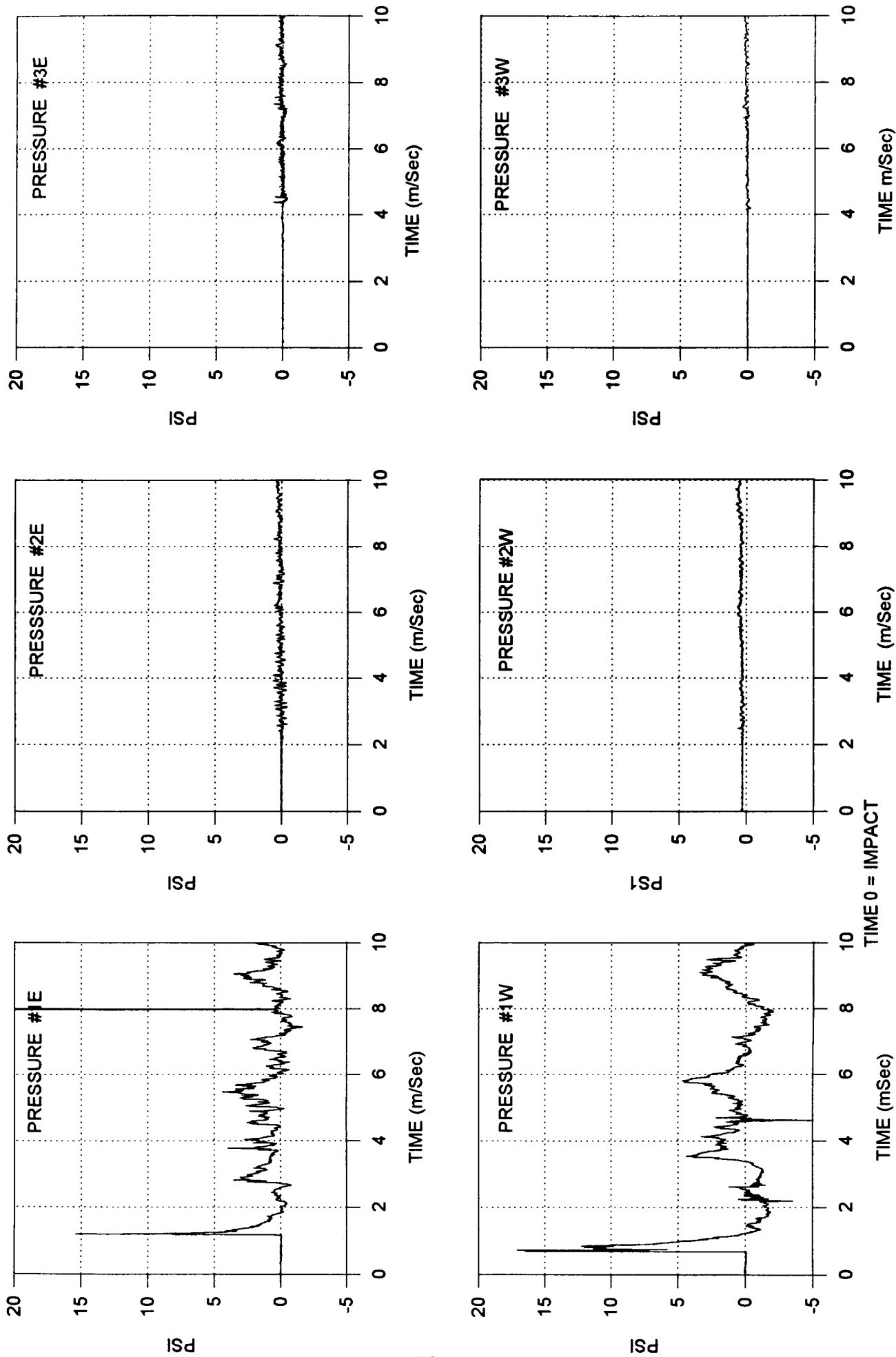


Figure A37 Pressure Profiles - Test #13

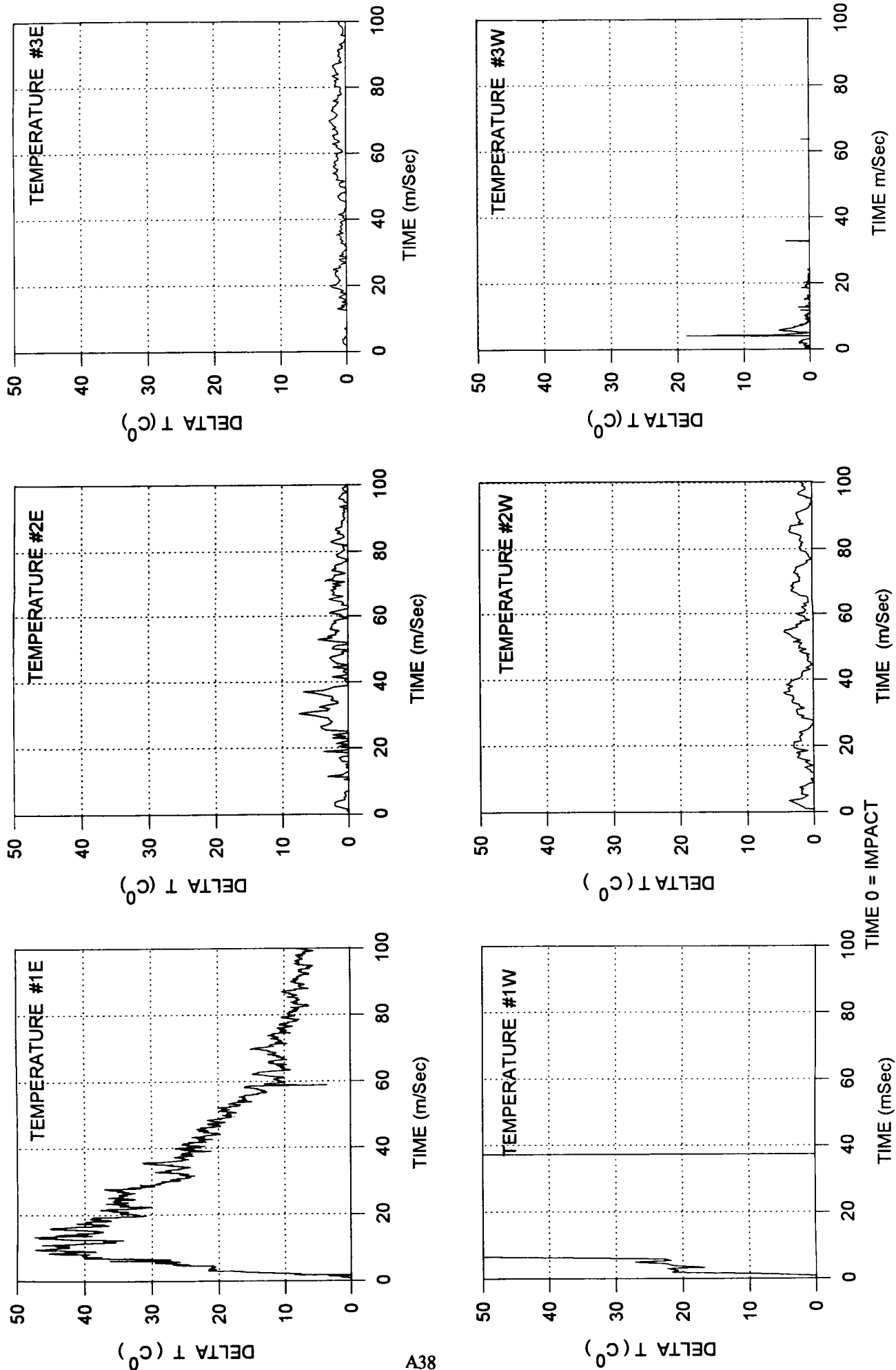


Figure A38 Temperature Profiles - Test #13

Pressure Plate Movement with Atmospheric Change

17 ghz Radar

@ Time=0 Chamber at atmosphere

@ Time=80000 uSec Chamber at 10 tor

360 Degrees = .345 inches

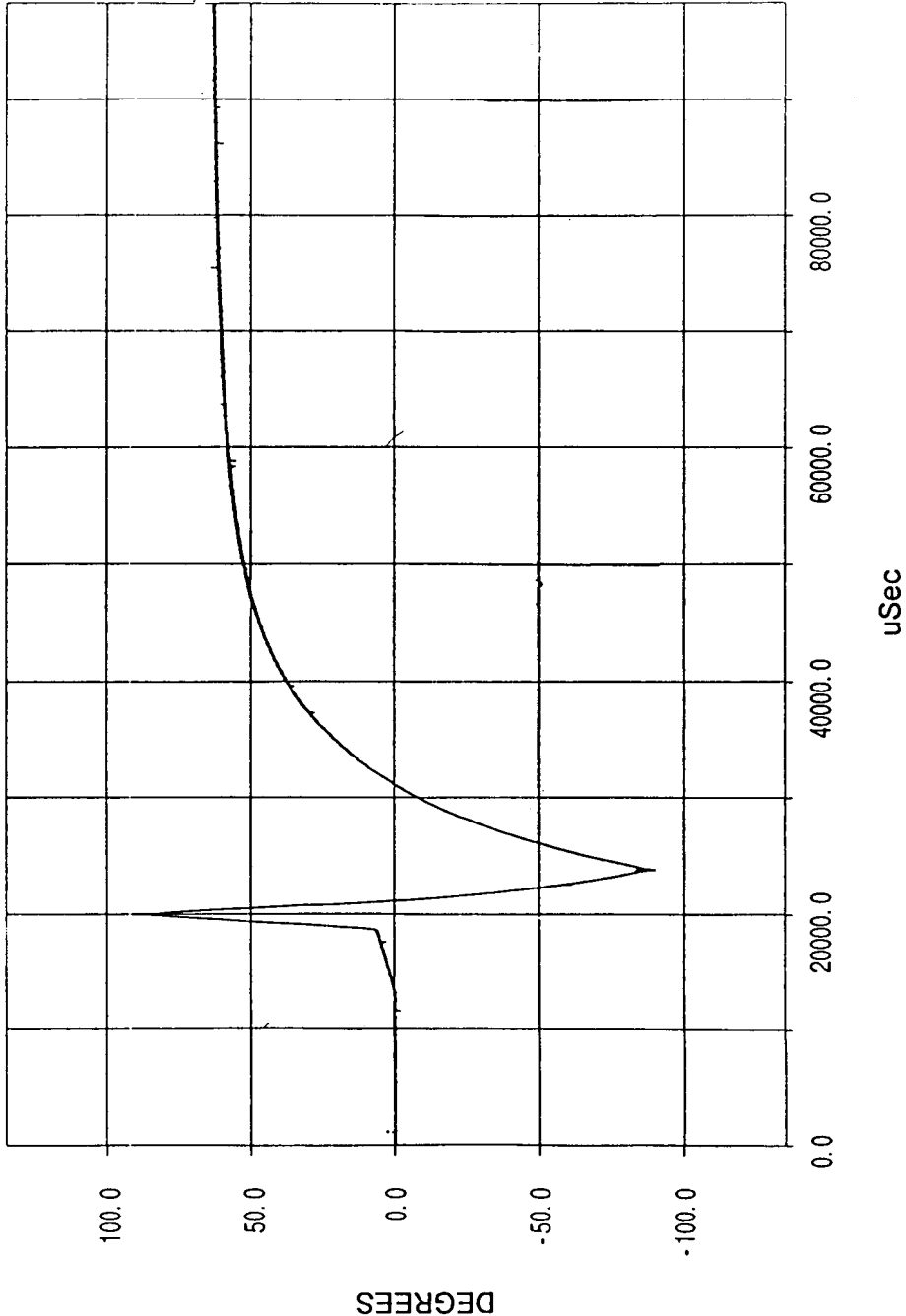


Figure A39 Pressure Plate Movement

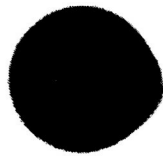
APPENDIX B

• FLASH X-RAY PHOTOGRAPHS

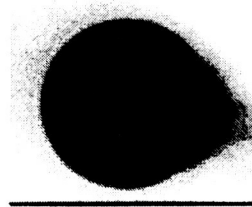
From: Calibration Negative One



extreme correction



light print

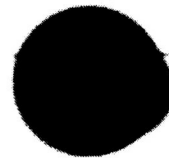


dark print

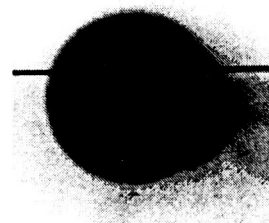
From: Calibration Negative Two



extreme correction



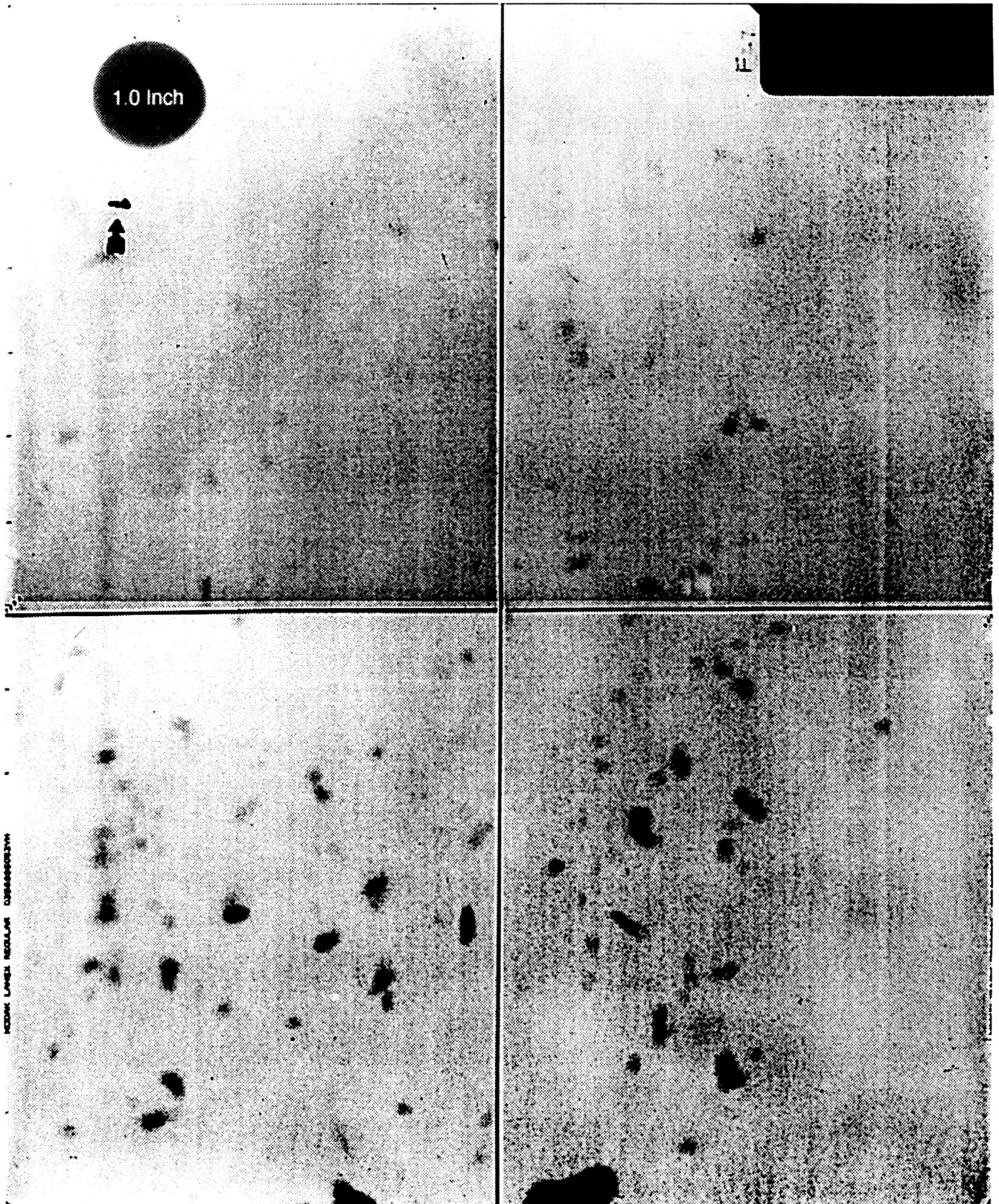
light print



dark print

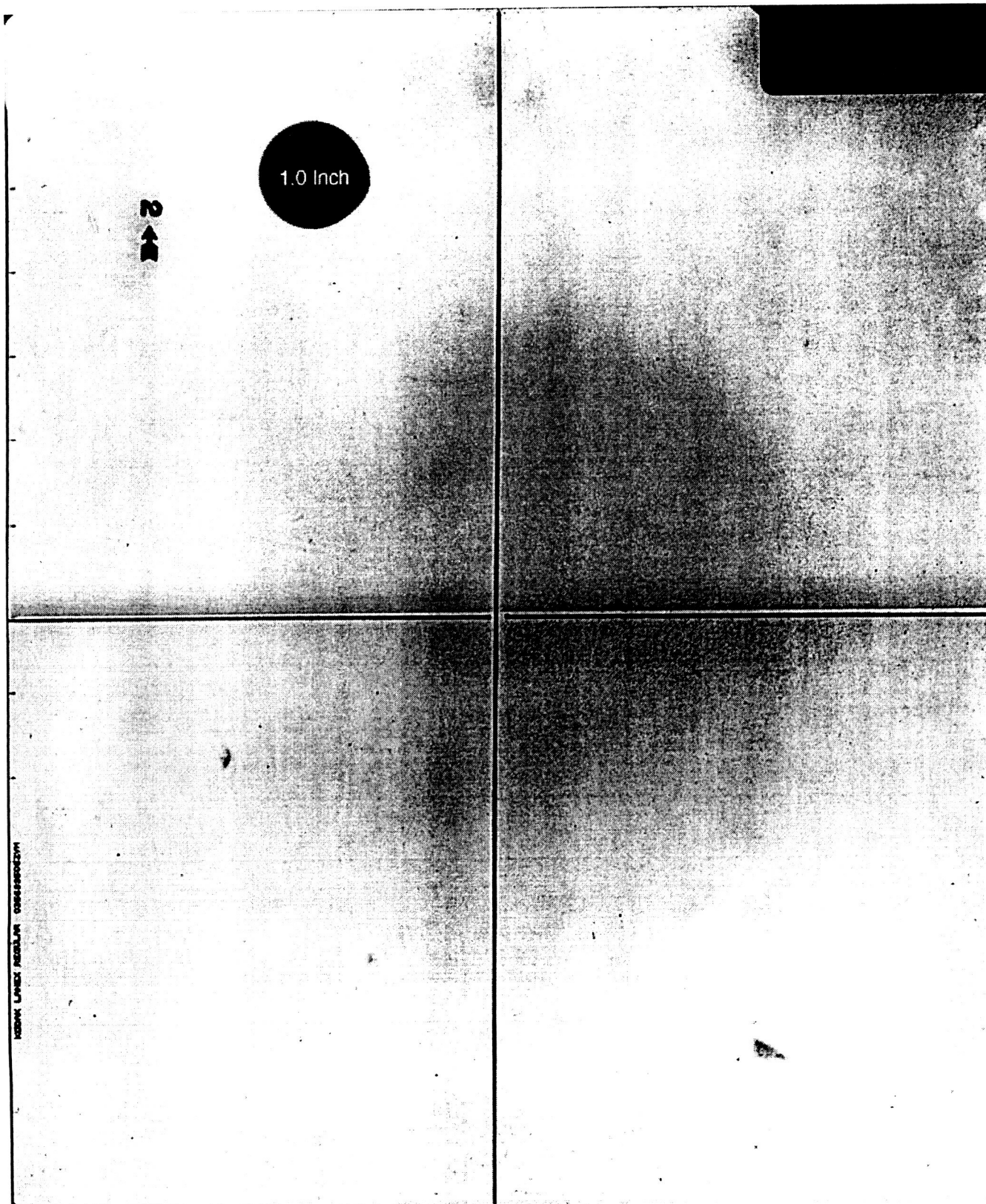
Images of a one inch calibration sphere placed in the target center.
The variation of size is due to several factors
inherent to the image manipulation process.

Figure B1 X-Ray Photograph Size Calibration



Flash X-Ray of Debris Cloud: UAH 94-26: Print One

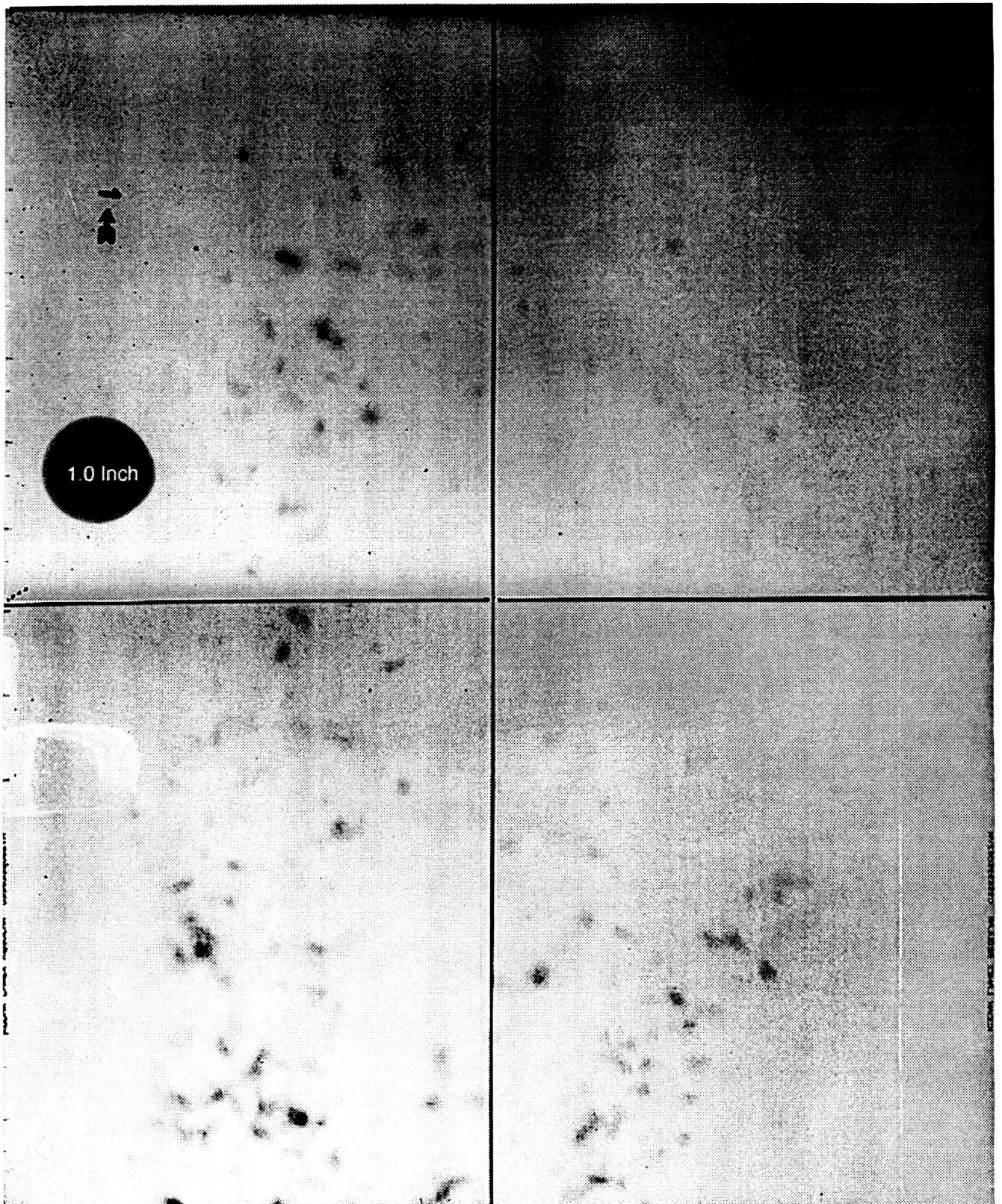
Figure B2 X-Ray Photograph of Debris Cloud, Test # 01 X-Ray #1



Flash X-Ray of Debris Cloud: UAH 94-26; Print Two

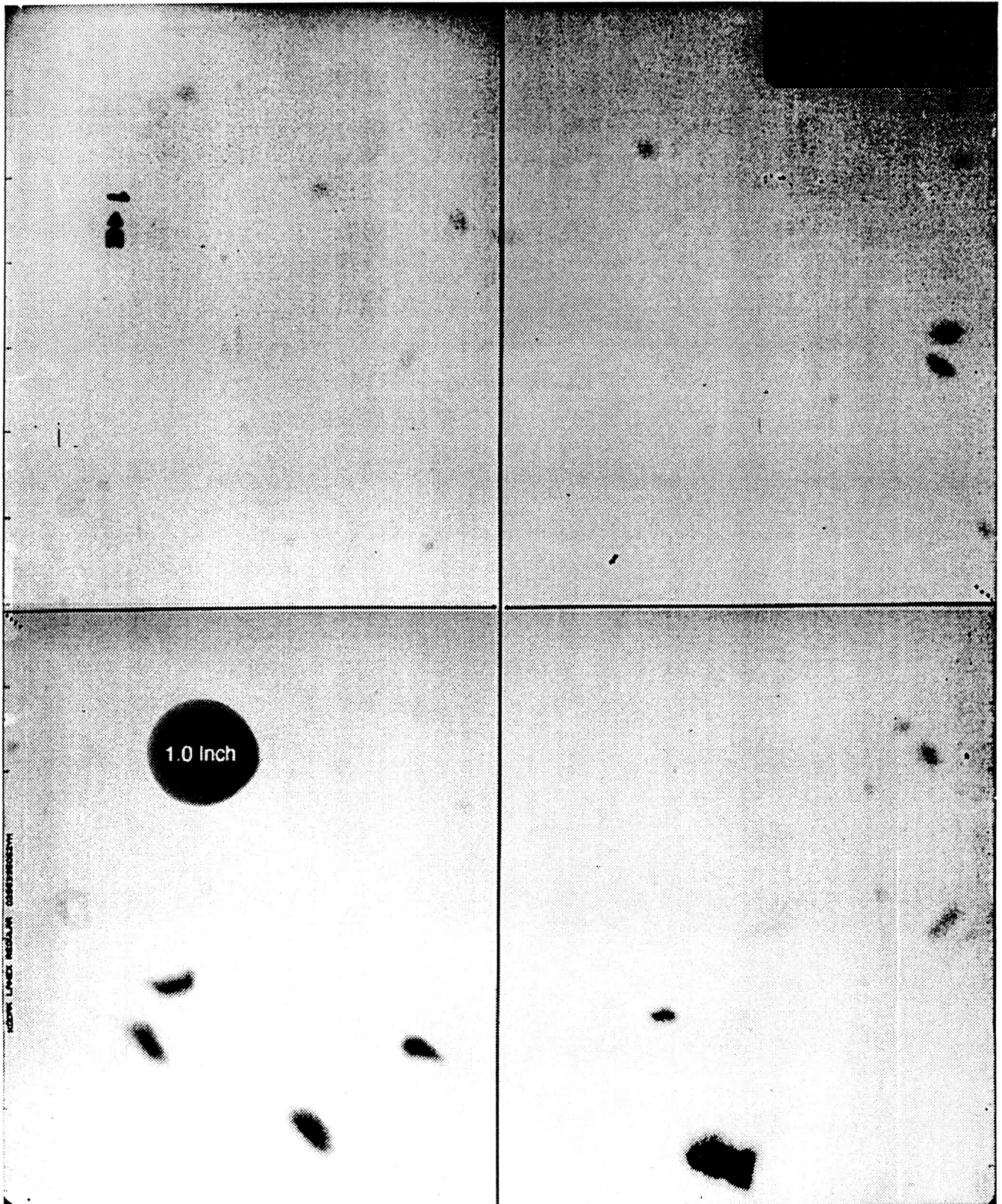
Figure B3

X-Ray Photograph of Debris Cloud, Test # 01 X-Ray #2



Flash X-Ray of Debris Cloud: UAH 94-30

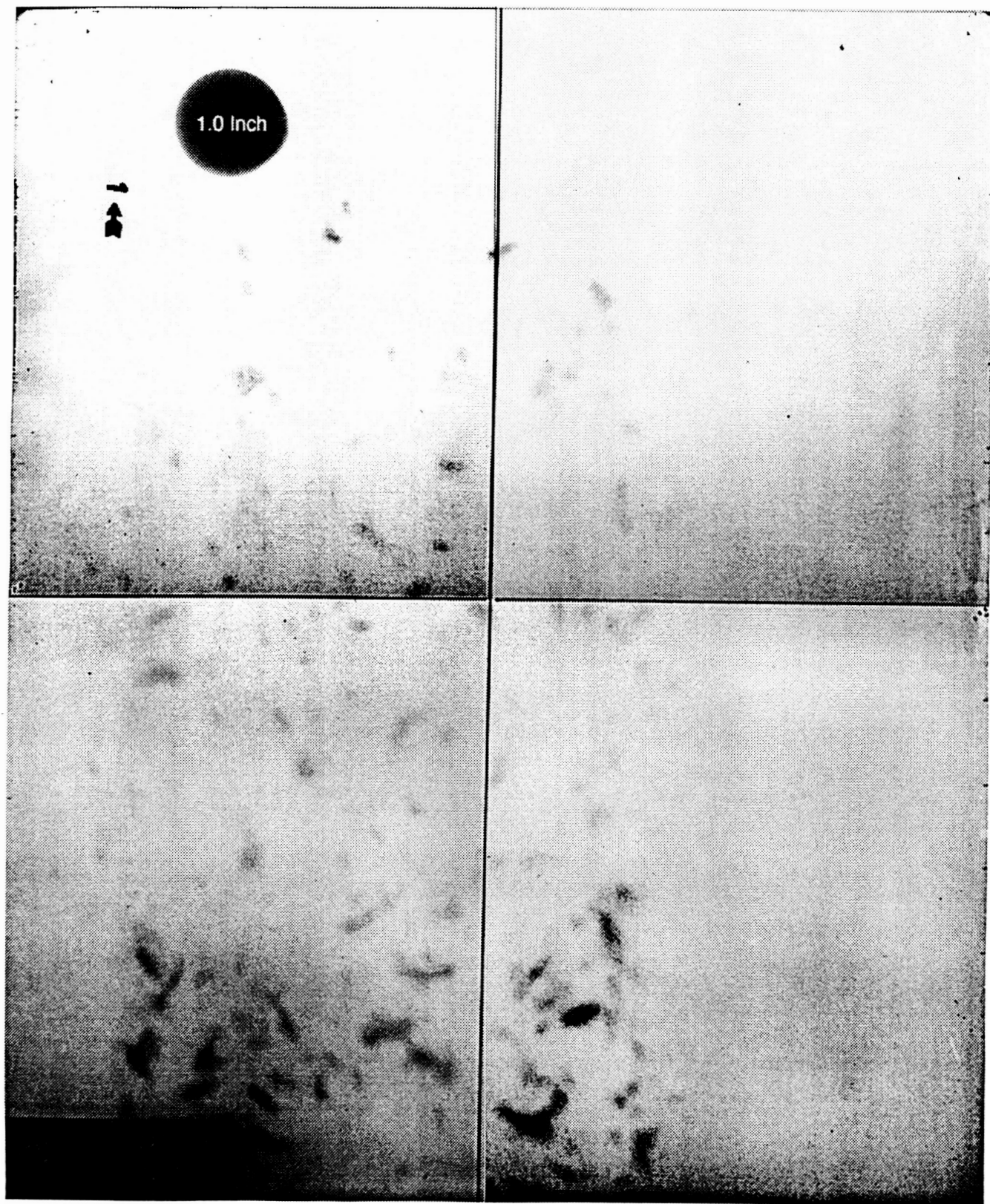
Figure B4 X-Ray Photograph of Debris Cloud, Test # 03 X-Ray #1



Flash X-Ray of Debris Cloud: UAH 94-33

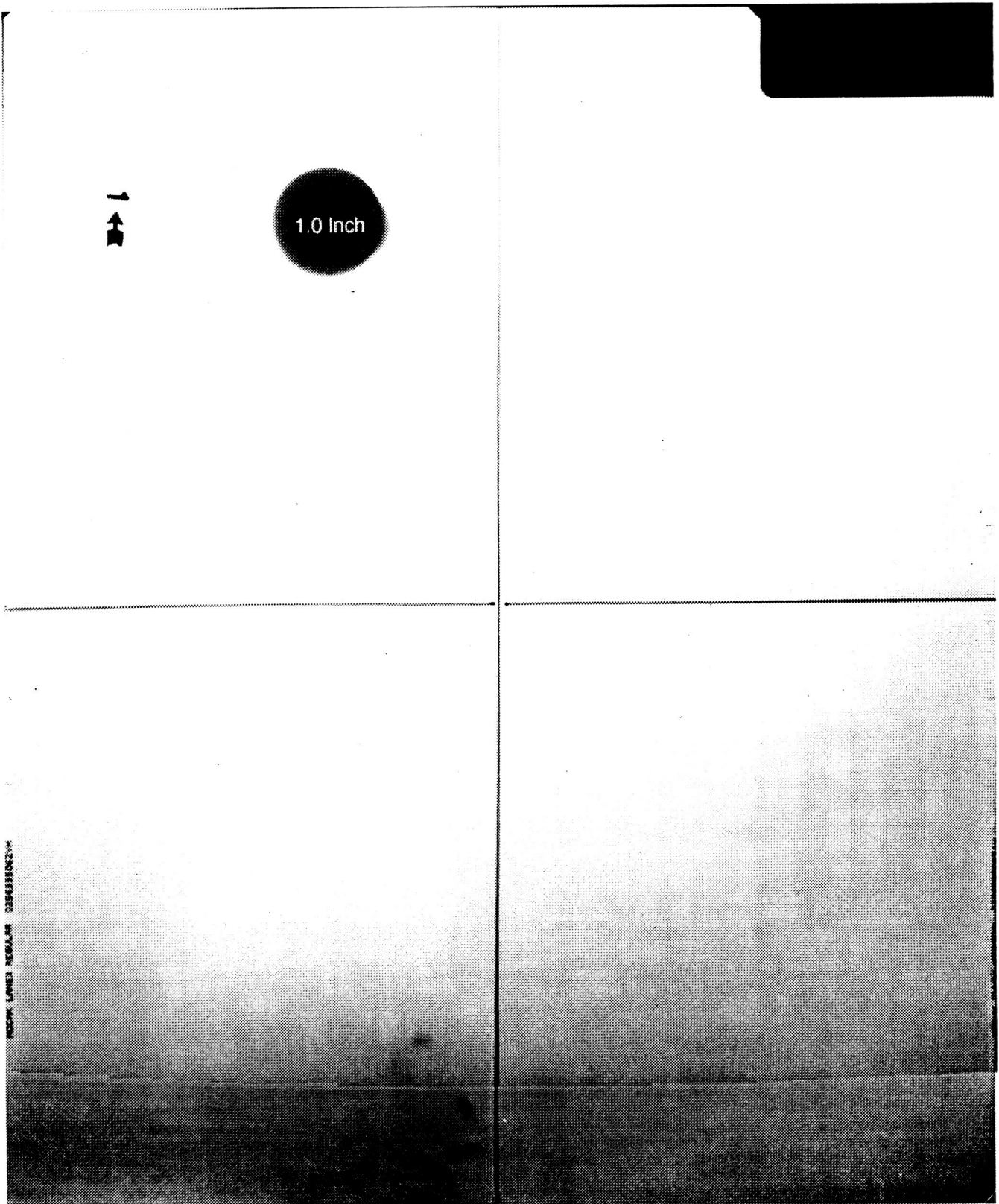
Figure B5

X-Ray Photograph of Debris Cloud, Test # 05 X-Ray #1



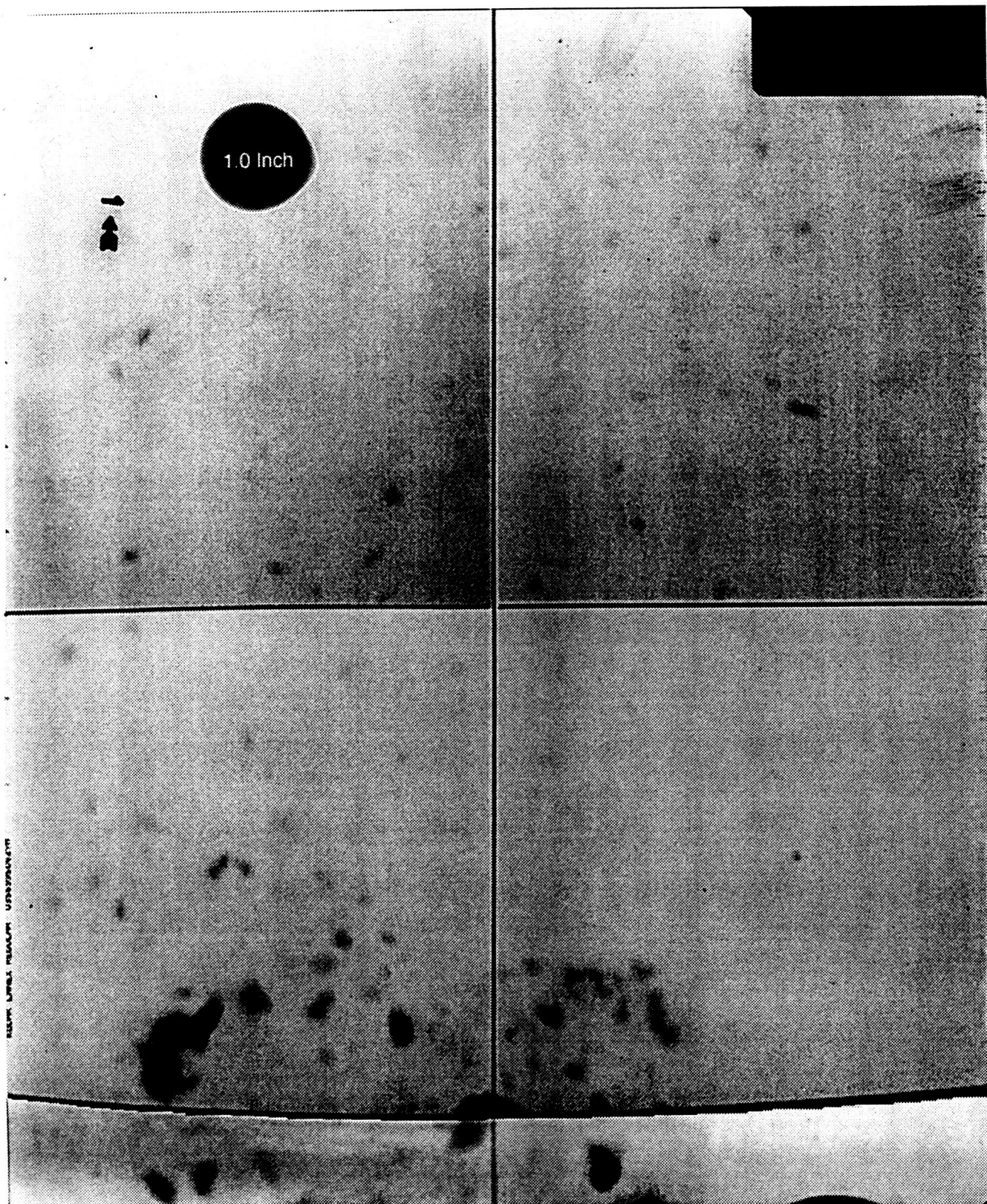
Flash X-Ray of Debris Cloud: UAH 94-42

Figure B6 X-Ray Photograph of Debris Cloud, Test # 06 X-Ray #1



Flash X-Ray of Debris Cloud: UAH 94-56

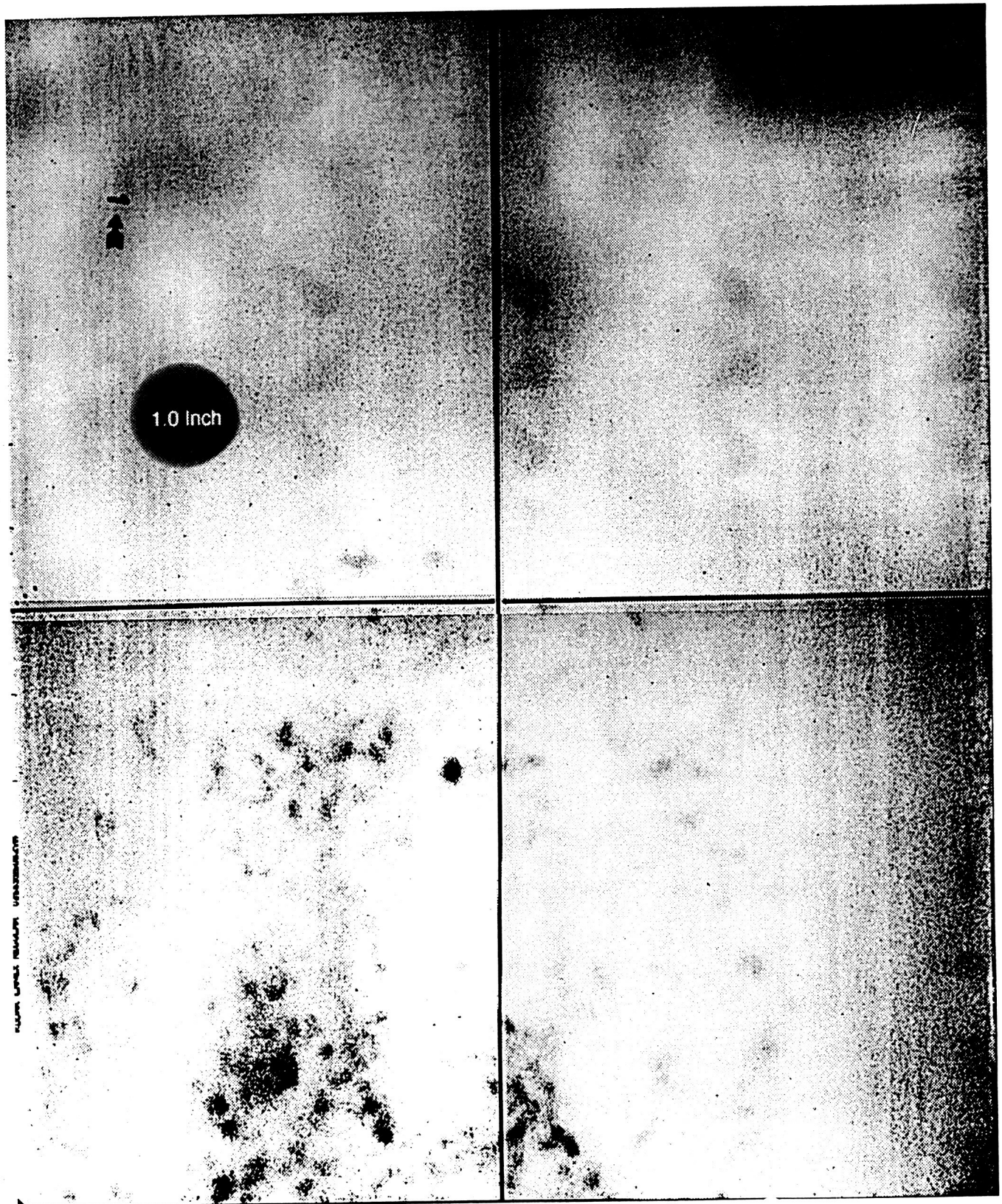
Figure B7 X-Ray Photograph of Debris Cloud, Test # 09 X-Ray #1



Flash X-Ray of Debris Cloud: UAH 94-57

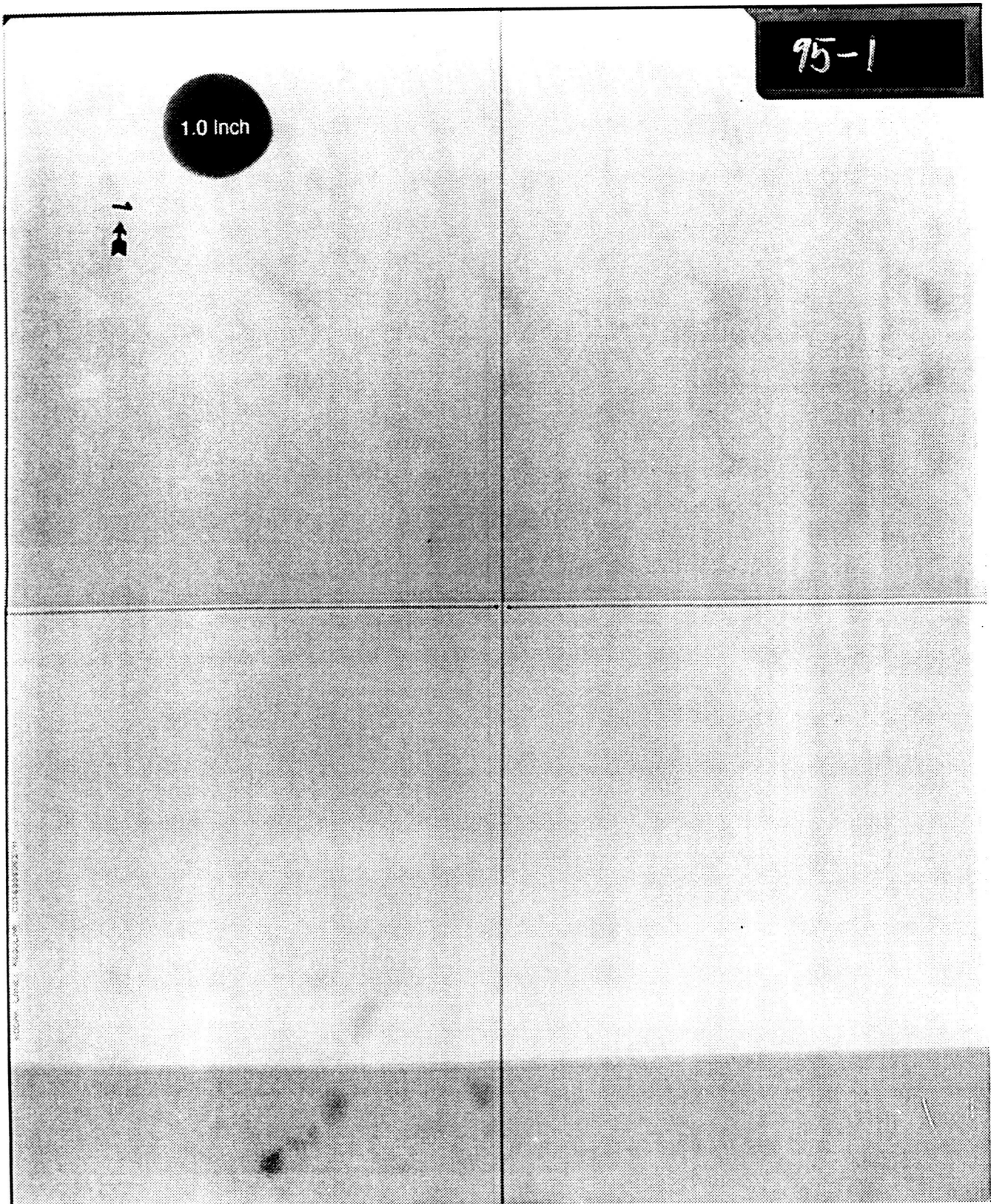
Figure B8

X-Ray Photograph of Debris Cloud, Test # 10 X-Ray #1



Flash X-Ray of Debris Cloud: UAH 94-61

Figure B9 X-Ray Photograph of Debris Cloud, Test # 11 X-Ray #1



Flash X-Ray of Debris Cloud: UAH 95-01

Figure B10 X-Ray Photograph of Debris Cloud, Test # 13 X-Ray #1

APPENDIX C -- INTEFF.FOR

```

$DEBUG
PROGRAM EFFCALC
IMPLICIT DOUBLE PRECISION (A-H,O-Z)
DOUBLE PRECISION KSB,KSP,KST,KA,KB,KP,KDC,KT,NUB,NUP,NUT,MB,MIB
DOUBLE PRECISION MP,MW,MW1,MW2,MWH,MDC,MDC1,MDCT,PRT(10,2)
CHARACTER*2 BID,PID,TID,IB,BIDCHK,PIDCHK,TIDCHK
CHARACTER*10 BMAT,PMAT,TMAT,IBMAT
INTEGER VOPT

C
COMMON/HYPERB/A,B,DEL,H

C
OPEN(1,FILE='IMPDAT')
OPEN(2,FILE='IMPOUT')
OPEN(4,FILE='GPARAM')

C
PI=3.141592

C
C..... READ DEBRIS CLOUD, PRESSURE WALL, AND AIR MATERIAL PROPERTIES.
C..... THE PARAMETERS MUST BE IN THE FOLLOWING UNITS:
C.....
C.....      BID,PID,TID,IB ..... MATERIAL ID CODES
C.....      BMAT,PMAT,TMAT,IBMAT ... MATERIALS
C.....      COB,COP,COT..... BULK SOUND SPEED, KM/S
C.....      RB,RP,RT ..... AMBIENT MATL DENSITY, GM/CUCM
C.....      ARIB ..... INNER BMPR AREAL DNSTY,GM/SQCM
C.....      KB,KP,KT ..... SLOPE OF US-UP LINE
C.....      EB,EP,ET..... ELASTIC MODULUS, LBS/SQ.IN.
C.....      ALFAB,ALFAP,ALFAT ..... LINEAR COEFF OF THERMAL EXP, 1/C
C.....      CPSB,CPSP,CPST ..... SPECIFIC HEAT (SOLID), CAL/GM-C
C.....      CPLB,CPLP,CPLT ..... SPECIFIC HEAT (LIQD), CAL/GM/C
C.....      TMB,TMP,TMT ..... MELT TEMPERATURE, C
C.....      TVB,TVP,TVT ..... VAPORIZATION TEMPERATURE, C
C.....      HFB,HFP,HFT ..... LATENT HEAT OF FUSION, CAL/GM
C.....      HVB,HVP,HVT ..... LATENT HEAT OF VPRZTN, CAL/GM
C
C      WRITE(*,3)
C      3 FORMAT(' ENTER PROJECTILE MATERIAL ID CODE (A2) AND HIT ENTER')
C      READ(4,5) PID
C      5 FORMAT(A2)
C      WRITE(*,31)
C      31 FORMAT(' ENTER BUMPER MATERIAL ID CODE (A2) AND HIT ENTER')
C      READ(4,51) BID
C      51 FORMAT(A2)
C      WRITE(*,7)
C      7 FORMAT(' ENTER PRESSURE WALL MATERIAL ID CODE (A2) AND HIT ENTER')
C      READ(4,9) TID
C      9 FORMAT(A2)
C      WRITE(*,11)
C      11 FORMAT(' ENTER INNER BUMPER ID CODE (A2) AND HIT ENTER')
C      READ(4,111) IB
C      111 FORMAT(A2)
C      IF (IB.EQ.'AA') THEN
C      IBMAT='MLI-BLNKT'
C      RIBA=0.072
C      ENDIF
C      IF (IB.EQ.'BB') THEN
C      IBMAT='MLI/K/N/GE'
C      RIBA=1.02
C      ENDIF
C

```

```

        REWIND 1
        READ(1,4)
    4  FORMAT(////)
C
    99  READ(1,1) PIDCHK
        1  FORMAT(A2)
        IF (PID.EQ.PIDCHK) THEN
            READ(1,10) PMAT,COP,KP,RP,GPI
    10  FORMAT(A10,4F10.5)
            READ(1,100) EP,NUP,ALPHAP,CPSP,CPLP
    100  FORMAT(2(E10.3,F10.5),F10.5)
            READ(1,102) TMP,TVP,HFP,HVP
    102  FORMAT(4F10.5)
            ENDIF
            IF (PID.NE.PIDCHK) THEN
                IF (PIDCHK.EQ.'XX') THEN
                    WRITE (*,17)
    17  FORMAT(' PROJECTILE MATERIAL NOT FOUND IN MATERIAL LIBRARY.',/,
$' PLEASE CHECK DEBRIS CLOUD MATERIAL ID CODE AND BEGIN AGAIN.')
                    STOP
                ENDIF
                IF (PIDCHK.NE.'XX') THEN
                    READ (1,2)
    2  FORMAT(////)
                    GOTO 99
                ENDIF
            ENDIF
C
        REWIND 1
        READ(1,4)
    999  READ(1,1) BIDCHK
        IF (BID.EQ.BIDCHK) THEN
            READ(1,10) BMAT,COB,KB,RB,GBI
            READ(1,100) EB,NUB,ALPHAB,CPSP,CPLB
            READ(1,102) TMB,TVB,HFB,HVB
            ENDIF
            IF (BID.NE.BIDCHK) THEN
                IF (BIDCHK.EQ.'XX') THEN
                    WRITE (*,117)
    117  FORMAT(' BUMPER MATERIAL NOT FOUND IN MATERIAL LIBRARY.',/, ' PLEAS
$E CHECK BUMPER MATERIAL ID CODE AND BEGIN AGAIN.')
                    STOP
                ENDIF
                IF (BIDCHK.NE.'XX') THEN
                    READ (1,2)
                    GOTO 999
                ENDIF
            ENDIF
C
        REWIND 1
        READ(1,4)
    9999  READ(1,1) TIDCHK
        IF (TID.EQ.TIDCHK) THEN
            READ(1,10) TMAT,COT,KT,RT,GTI
            READ(1,100) ET,NUT,ALPHAT,CPST,CPLT
            READ(1,102) TMT,TVT,HFT,HVT
            ENDIF
            IF (TID.NE.TIDCHK) THEN
                IF (TIDCHK.EQ.'XX') THEN
                    WRITE (*,1117)

```

```

1117 FORMAT(' PRESSURE WALL MATERIAL NOT FOUND IN MATERIAL LIBRARY.',/
$, ' PLEASE CHECK PRESSURE WALL MATERIAL ID CODE AND BEGIN AGAIN.')
STOP
ENDIF
IF (TIDCHK.NE.'XX') THEN
READ (1,2)
GOTO 9999
ENDIF
ENDIF

C
C..... REQUIRED PROPERTIES OF AIR AND THEIR UNITS:
C
C..... COA ... ADIABATIC BULK SOUND SPEED, KM/S
C..... CPA ... AMBIENT SPECIFIC HEAT, CAL/GM/DEG-C
C..... RP .... AMBIENT DENSITY, GM/CU.CM.
C..... KA .... SLOPE OF US-UP LINE, DIMENSIONLESS
C..... TOA ... AMBIENT TEMPERATURE, DEG-C
C..... POA ... AMBEINT PRESSURE, ATM
C..... CD .... DRAG COEFFICIENT
C
CPA=0.24
COA=0.33
KA=1.07
RA=1.22E-03
TOA=24.0
POA=1.0
TA=TOA+273.0
PA=POA*101325.0
EOA=(CPA*4186.0)*TA

C
C..... READ GEOMETRIC PARAMETERS AND ASSUMPTIONS
C
C..... DP .... PROJECTILE DIAMETER, CM
C..... TS .... BUMPER THICKNESS, CM
C..... TW .... PRESSURE WALL THICKNESS, CM
C..... S ..... BUMPER-TO-PRESSURE WALL STAND-OFF DISTANCE, CM
C..... S2 .... INNER BUMPER-TO-PRESSURE WALL DISTANCE, CM
C..... HMOD .. MODULE DIAMETER, CM
C
READ (4,113) DP,TS,TW,S,S2,HMOD,CD
113 FORMAT(7F10.5)

C
C..... READ PROJECTILE IMPACT VELOCITY IN KM/S
C
WRITE(*,29)
29 FORMAT(' INPUT PROJECTILE IMPACT VELOCITY IN KM/SEC (F5.2) AND HIT
$ ENTER')
READ(*,30) VP
30 FORMAT(F5.2)

C
C..... CALCULATE PROJECTILE AND BUMPER HOLE-OUT MASSES
C
MP=(PI/6.0)*(DP/100.0)*(DP/100.0)*(DP/100.0)*(RP*1000.0)
R1=VP/COB
R2=TS/DP
R3=RB/RP
DBDP=3.4*(R2**0.33333)*(R1**0.33333)*(1.0-0.0308*R3)
DB=DP*DBDP
MB=(PI/4.0)*(DB/100.0)*(DB/100.0)*(TS/100.0)*(RP*1000.0)
C

```



```

EB=EB*68947.0
BETAB=3.0*ALPHAB
IF (NUB.LT.0.5) THEN
KSB=EB/3.0/(1.0-2.0*NUB)
COBC=DSQRT((KSB/10.0)/(RB*1000.0))/1000.0
ENDIF
IF (NUB.EQ.0.5) THEN
KSB=-1.0
COBC=-1.0
ENDIF
IF (NUB.LT.0.5) GB=2.3885E-08*KSB*BETAB/CPSB/RB
IF (NUB.EQ.0.5) GB=GBI
GRB=GB*RB*1000.0

```

C

```

EP=EP*68947.0
BETAP=3.0*ALPHAP
IF (NUP.LT.0.5) THEN
KSP=EP/3.0/(1.0-2.0*NUP)
COPC=DSQRT((KSP/10.0)/(RP*1000.0))/1000.0
ENDIF
IF (NUP.EQ.0.5) THEN
KSP=-1.0
COPC=-1.0
ENDIF
IF (NUP.LT.0.5) GP=2.3885E-08*KSP*BETAP/CPSP/RP
IF (NUP.EQ.0.5) GP=GPI
GRP=GP*RP*1000.0

```

C

```

WRITE(2,40) PMAT,BMAT,IBMAT,TMAT
40 FORMAT('NORMAL IMPACT OF A ',A10,' PROJECTILE ON A DUAL-WALL SYSTE
$M WITH A ',/,A10,' BUMPER, A ',A10,' INNER BUMPER, AND A ',A10,' PR
$ESSURE WALL')
WRITE (2,45) PMAT,COP,KP,RP,DP,MP*1000.0,VP,BMAT,COT,KT,RT,TS,DB
$
$,MB*1000.0
45 FORMAT(/,'PROJECTILE PROPERTIES ...',/,3X,'MAT = ',A10,/,3X,
$'CO = ',F6.3,' KM/S',/,3X,'K = ',F6.3,/,3X,'RHO = ',F6.3,' GM/C
$U.CM.',/,3X,'DP = ',F6.3,' CM',/,3X,'MP = ',F6.3,' GMS',/,3X,
$'VP = ',F6.3,' KM/S',/,3X,'BUMPER PROPERTIES ...',/,3X,'MAT = ',A10
$,/,3X,'CO = ',F6.3,' KM/S',/,3X,'K = ',F6.3,/,3X,'RHO = ',F6.3,
$' GM/CU.CM.',/,3X,'TS = ',F6.3,' CM',/,3X,'DH = ',F6.3,' CM',/,
$3X,'MB = ',F6.3,' GMS')

```

C

```

C..... CALCULATE PARTICLE AND SHOCK WAVE VELOCITIES AND HUGONIOT
C..... PRESSURE DUE TO PROJECTILE IMPACT

```

C

```

V=VP
IF (BMAT.EQ.PMAT) GOTO 35
A=KP-KB*(RB/RP)
B=2.0*KP*V+COP+COB*(RB/RP)
C=COP*V+KP*V*V
D=B*B-4.0*A*C
UBP=(B-SQRT(D))/(2.0*A)
GOTO 38
35 UBP=V/2.0
38 UPP=V-UBP
UBS=COB+KB*UBP
UPS=COP+KP*UPP
PP=RP*UPS*UPP
PB=RB*UBS*UBP

```

C

```

C..... PROJECTILE AND BUMPER SHOCK LOADING RESPONSE AND RELEASE
C..... CALCULATION PHASE
C
  WRITE(*,5080)
5080 FORMAT(/,' BEGINNING PROJECTILE AND BUMPER SHOCK LOADING RESPONSE
  $AND',/, ' RELEASE CALCULATIONS ...')
  WRITE(2,509)
509 FORMAT(/,'**** PROJECTILE AND BUMPER SHOCK LOADING RESPONSE AND RE
  $LEASE CALCULATIONS ****')
  WRITE(2,6011) VP,UPP,UPS,PP,UBP,UBS,PB
6011 FORMAT(/,'PROJECTILE IMPACT VELOCITY .... VP = ',F7.3,' KM/S',/,
  $'PROJ MATL PARTICLE VELOCITY ... UP = ',F7.3,' KM/S',/, 'PROJ MATL
  $SHOCK WAVE SPEED .... US = ',F7.3,' KM/S',/, 'HUGONIOT IMPACT PRESS
  $URE ..... PH = ',F7.3,' GPA',/, 'BMPR MATL PARTICLE VELOCITY ... U
  $P = ',F7.3,' KM/S',/, 'BMPR MATL SHOCK WAVE SPEED .... US = ',F7.3,
  $' KM/S',/, 'HUGONIOT IMPACT PRESSURE ..... PH = ',F7.3,' GPA')
C
  VPO=1.0/RP
  VP1=RP*UPS/(UPS-UPP)
  VP1=1.0/VP1
C
  PH=PP*1.0E09
C
  WRITE(2,705) EP/10.0,NUP,KSP/10.0,ALPHAP,CPSP,CPLP
705 FORMAT(/,'PARAMETERS REQUIRED FOR CALCULATING PROJECTILE MATERIAL
  $RESPONSE AND',/, 'RELEASE FROM SHOCKED STATE USING THE MIE-GRUNEISE
  $N E-O-S:',/,3X,'ELASTIC MODULUS ..... E =',E10.4,' N/SQ
  $.M.',/,3X,'POISSON RATIO ..... NU =',F10.3,/,3X,'BULK
  $MODULUS ..... K =',E10.4,' N/SQ.M.',/,3X,'LIN. COEF.
  $ OF THERM. EXP. ... ALFA =',E10.4,' /DEG-C',/,3X,'SP HEAT (SOLID)
  $ ..... CPS =',F10.3,' CAL/GM/DEG-C',/,3X,'SP HEAT (LIQUID)
  $ ..... CPL =',F10.3,' CAL/GM/DEG-C')
  PHMB=PH/100.0E+09
  WRITE(2,800) PH,PHMB,VPO,VP1,GP,GPI
800 FORMAT(3X,'HUGON IMP PRESS (PA,MBAR) ... PH =',E10.4,',',F5.3,/,
  $3X,'SP VOL AT REST ..... V0 =',F10.3,' CU.CM./GM',/,3X,
  $'SP VOL AT IMPACT ..... V1 =',F10.3,' CU.CM./GM',/,3X,'AM
  $B M-GRUN COEF (CAL,INP) ... GAM0 =',F10.3,',',F5.3)
  WRITE(2,805) TMP,TVP,HFP,HVP
805 FORMAT(3X,'MELT TEMPERATURE ..... TM =',F10.2,' DEG-C',/,
  $3X,'VAPOR TEMPERATURE ..... TV =',F10.2,' DEG-C',/,3X,'HEA
  $T OF FUSION ..... HF =',F10.2,' CAL/GM',/,3X,'HEAT OF V
  $APORIZATION ..... HV =',F10.2,' CAL/GM')
C
C..... CALCULATE RELEASE OF PROJECTILE MATERIAL UP UNTIL ZERO PRESSURE
C..... IS REACHED
C
  WRITE (2,1701)
1701 FORMAT(/,'RELEASE OF SHOCKED PROJECTILE MATERIAL ...')
  PFIN=0.0
  CALL RELS(COP,KP,RP,GRP,VPO,VP1,PH,EXTP,UPP,PFIN,VFP)
C
C..... CALCULATE TEMPERATURE INCREASE IN PROJECTILE MATERIAL
C
  CALL TINC(CPSP,CPLP,TMP,TVP,HFP,HVP,EXTP)
C
  VBO=1.0/RB
  VB1=RB*UBS/(UBS-UBP)
  VB1=1.0/VB1
C

```

```

      PH=PB*1.0E+09
C
      WRITE(2,7051) EB/10.0,NUB,KSB/10.0,ALPHAB,CPSB,CPLB
7051 FORMAT(/,'PARAMETERS REQUIRED FOR CALCULATING BUMPER MATERIAL RESP
$ONSE AND',/, 'RELEASE FROM SHOCKED STATE USING THE MIE-GRUNEISEN E-
$O-S:',/,3X,'ELASTIC MODULUS ..... E      =',E10.4,' N/SQ.M.'
$,/,3X,'POISSON RATIO ..... NU      =',F10.3,/,3X,'BULK MODU
$LUS ..... K      =',E10.4,' N/SQ.M.',/,3X,'LIN. COEF. OF
$THERM. EXP. ... ALFA =',E10.4,' /DEG-C',/,3X,'SP HEAT (SOLID) ....
$..... CPS      =',F10.3,' CAL/GM/DEG-C',/,3X,'SP HEAT (LIQUID) ...
$..... CPL      =',F10.3,' CAL/GM/DEG-C')
      PHMB=PH/100.0E+09
      WRITE(2,8001) PH,PHMB,VBO,VB1,GB,GBI
8001 FORMAT(3X,'HUGON IMP PRESS (PA,MBAR) ... PH      =',E10.4,',',F5.3,/,
$,3X,'SP VOL AT REST ..... V0      =',F10.3,' CU.CM./GM',/,3X,
$'SP VOL AT IMPACT ..... V1      =',F10.3,' CU.CM./GM',/,3X,'AM
$B M-GRUN COEF (CAL,INP) ... GAM0 =',F10.3,',',F5.3)
      WRITE(2,8051) TMB,TVB,HFB,HVB
8051 FORMAT(3X,'MELT TEMPERATURE ..... TM      =',F10.2,' DEG-C',/,
$,3X,'VAPOR TEMPERATURE ..... TV      =',F10.2,' DEG-C',/,3X,'HEA
$T OF FUSION ..... HF      =',F10.2,' CAL/GM',/,3X,'HEAT OF V
$APORIZATION ..... HV      =',F10.2,' CAL/GM')
C
C.....  CALCULATE RELEASE OF BUMPER MATERIAL UP UNTIL ZERO PRESSURE IS
C.....  REACHED
C
      WRITE (2,1703)
1703 FORMAT(/,'RELEASE OF SHOCKED BUMPER MATERIAL ...')
      PFIN=0.0
      CALL RELS(COB,KB,RB,GRB,VBO,VB1,PH,EXTB,UBP,PFIN,VFB)
C
C.....  CALCULATE TEMPERATURE INCREASE IN BUMPER MATERIAL
C
      CALL TINC(CPSB,CPLB,TMB,TVB,HFB,HVB,EXTB)
C
      WRITE(*,1707)
1707 FORMAT(' PROJECTILE AND BUMPER MATERIALS SHOCK LOADING AND RELEASE
$',/, ' CALCULATIONS COMPLETE.')
C
      WRITE(*,58)
58  FORMAT(/,' BEGINNING PRESSURE WALL RESPONSE AND IMPEDANCE MATCH CA
$LCULATIONS ...')
C
C.....  CALCULATE PRIMARY DEBRIS CLOUD MASS AXIAL VELOCITY, AND EXP VEL
C
      MDC=MP+MB
      RATIOF=MP/MDC
      RATIOB=MB/MDC
C
      VCOM=MP*VP/(MP+MB)
C
      EINIT=0.5*MP*(VP*1000.0)*(VP*1000.0)
      EDIFF=EINIT-EXTB*MB-EXTP*MP-0.5*MDC*(VCOM*1000.0)*(VCOM*1000.0)
      IF (EDIFF.LE.0.0) THEN
        WRITE (2,991)
        WRITE (*,991)
991  FORMAT('*** FATAL ERROR 001: INSUFFICIENT ENERGY AVAILABLE FOR PRI
$MARY DEB CLD EXPANSION ***)
        STOP
        ENDIF

```

```

      VEXP=DSQRT(EDIFF/(0.5*MDC))/1000.0
C
C..... CALCULATE PRIMARY DEBRIS CLOUD LEADING EDGE VELOCITY
C
      VLE=2.0*UBP
C
C..... CALCULATE PRIMARY DEBRIS CLOUD 1/2-ANGLE SPREAD, PRESSURE WALL
C..... LOADING AREA, MASS OF SHOCKED AND RELEASED PRESSURE WALL MATL,
C..... AND MASS OF PRESSURE WALL HOLE-OUT MATERIAL
C
      THDC=ATAN(VEXP/VCOM)
      THDEG=180.0*THDC/PI
C
      DW=2.0*S*DTAN(THDC)
      RW=DW/2.0
      MW=(PI/4.0)*(DW/100.0)*(DW/100.0)*(TW/100.0)*(RT*1000.0)
C
      READ (4,49) AK2,AK3,AN,AMEXP
49 FORMAT(4F10.5)
C
C..... CALCULATE DEBRIS CLOUD IMPACT VELOCITY BASED ON MOMENTUM
C..... CONSERVATION AT THE PRESSURE WALL
C
      VPW=MDC*VLE/(MDC+MW)
C
C..... ASSIGN DEBRIS CLOUD IMPACT VELOCITY
C
      READ (4,1709) VOPT
1709 FORMAT(I1)
C
      IF (VOPT.EQ.1) V=VCOM
      IF (VOPT.EQ.2) V=VLE
      IF (VOPT.EQ.3) V=VPW
C
      WRITE (2,1710) VEXP,VCOM,VLE,VPW,V
1710 FORMAT(/,'PRIMARY DEBRIS CLOUD CHARACTERISTIC VELOCITIES ...',/,3X
$, 'VEXP = ',F6.3,' KM/S',/,3X,'VCOM = ',F6.3,' KM/S',/,3X,'VLE = '
$,F6.3,' KM/S',/,3X,'VPW = ',F6.3,' KM/S',/, 'SELECTED PRIMARY DEBR
$IS CLOUD IMPACT VELOCITY ...',/,3X,'VDC = ',F6.3,' KM/S')
C
      ET=ET*68947.0
      BETAT=3.0*ALPHAT
      IF (NUT.LT.0.5) THEN
        KST=ET/3.0/(1.0-2.0*NUT)
        COTC=DSQRT((KST/10.0)/(RT*1000.0))/1000.0
      ENDIF
      IF (NUT.EQ.0.5) THEN
        KST=-1.0
        COTC=-1.0
      ENDIF
      IF (NUT.LT.0.5) GT=2.3885E-08*KST*BETAT/CPST/RT
      IF (NUT.EQ.0.5) GT=GTI
      GRT=GT*RT*1000.0
C
      KDC=KP*RATIOF+KB*RATIOB
      RPSR=1.0/VFP
      RBSR=1.0/VFB
      RDC=RPSR*RATIOF+RBSR*RATIOB
      CODC=COP*RATIOF+COB*RATIOB
      GRDC=GRP*RATIOF+GRB*RATIOB

```

```

C      WRITE(2,50) THDEG,RATIO,P,PSR,RATIO,B,RSR,CODC,KDC,RDC,MDC*1000.
50  FORMAT(/,'PRIMARY DEBRIS CLOUD PROPERTIES ...',/,3X,'1/2-ANG = ',
$F6.3,' DEG',/,3X,'RATIO-P = ',F6.3,/,3X,'PSR      = ',F6.3,
$' GM/CU.CM.',/,3X,'RATIO-B = ',F6.3,/,3X,'RSR      = ',F6.3,
$' GM/CU.CM.',/,3X,'CO      = ',F6.3,' KM/S (AVG)',/,3X,'K      =
$',F6.3,' (AVG)',/,3X,'RHO      = ',F6.3,' GM/CU.CM. (AVG)',/,3X,
$'MDC      = ',F6.3,' GMS')
C
C.....  CALCULATE SECONDARY DEBRIS CLOUD COMPONENT MASSES, AXIAL MOTION
C.....  VELOCITIES, AND EXPANSION VELOCITIES
C
      DH1=(0.45*V+0.90)*DB
      MIB=PI*(RIBA*10.0)*(DH1/100.0)*(DH1/100.0)/4.0
      RWA=RT*TW
      AK1=(1.0-RIBA/RWA)**AN
      GAM=MIB/MDC
      AKMN=(-GAM+DSQRT(GAM*GAM+4.0))/2.0
      IF (AKMN.GT.AK1) AK1=AKMN
      MDC1=AK1*MDC
      MDCT=MDCT+MIB
C
      VMCA=MDC*V/MDCT
C
      R2=V/VMCA
      CALL ROOTS(AK1,R2,MIB,MDC,MDC1,C1AX,C2AX)
      VMC1=C1AX*VMCA
      VMC2=C2AX*VMCA
C
      EPA=MDC*(V*1000.0)*(V*1000.0)/2.0
      EPE=MDC*(VEXP*1000.0)*(VEXP*1000.0)/2.0
      EL1=MDCT*(VMCA*1000.0)*(VMCA*1000.0)/2.0
      EL21=MDC*(1.0-AK1)*(V*1000.0)*(V*1000.0)/2.0
      EL22=MDC*(1.0-AK1)*(VEXP*1000.0)*(VEXP*1000.0)/2.0
      EDIF=EPA+EPE-EL1-(EL21+EL22)
      IF (EDIF.LE.0.0) THEN
        WRITE (2,9921)
        WRITE (*,9921)
9921  FORMAT('*** FATAL ERROR 002: INSUFFICIENT ENERGY AVAILABLE FOR SEC
$ONDARY DEBRIS CLOUD EXPANSION ***')
        STOP
        ENDIF
      VEXPA=DSQRT(EDIF/(MDCT/2.0))/1000.0
C
      R2=VEXP/VEXPA
      CALL ROOTS(AK1,R2,MIB,MDC,MDC1,C1EXP,C2EXP)
      VEXP1=C1EXP*VEXPA
      VEXP2=C2EXP*VEXPA
C
C.....  CALCULATE SECONDARY DEBRIS CLOUD SPREAD ANGLES
C
      THDC1=ATAN(VEXP1/VMC1)
      TH1DEG=180.0*THDC1/PI
      THDC2=ATAN(VEXP2/VMC2)
      TH2DEG=180.0*THDC2/PI
      DW1=2.0*S2*THDC1
      DW2=2.0*S2*THDC2
      RW1=DW1/2.0
      RW2=DW2/2.0
      MW1=(PI/4.0)*(DW1/100.0)*(DW1/100.0)*(TW/100.0)*(RT*1000.0)

```

```

      MW2=(PI/4.0)*(DW2/100.0)*(DW2/100.0)*(TW/100.0)*(RT*1000.0)
C
C..... CALCULATE ADDITIONAL PRESSURE WALL VELOCITY
C
      MDC=MDC1
      MW=MW1
      MWH=AK3*(MW1*AK2)
      V=VMC1
      VEXP=VEXP1
      UPW=MIB*(V+VEXP)/(MIB+MW2)
C
      WRITE (2,450) RIBA,DH1,S2
450 FORMAT(/,'INNER BUMPER PROPERTIES ...',/,3X,'RHO-A = ',F6.3,
$' GM/SQ.CM.',/,3X,'DH = ',F6.3,' CM',/,3X,'S2 = ',F6.3,
$' CM')
      WRITE (2,451) VMCA,EPA,EPE,EL1,EL21,EL22,EDIF,VEXPA,UPW
451 FORMAT(/,'SECONDARY DEBRIS CLOUD PROPERTIES (GENERAL) ...',/,3X,
$'SEC DEB CLD AVG AXL VEL .... ',F6.3,' KM/S',/,3X,'PRIM DEB CLD AX
$L ENERGY .... ',E11.4,' J',/,3X,'PRIM DEB CLD EXP ENERGY .... ',
$E11.4,' J',/,3X,'SEC DEB CLD AXL ENERGY ..... ',E11.4,' J',/,3X,
$'PRIM DEB CLD AXL EN LOST ... ',E11.4,' J',/,3X,'PRIM DEB CLD EXP
$EN LOST ... ',E11.4,' J',/,3X,'EN AVAIL SEC DEB CLD EXP ... ',
$E11.4,' J',/,3X,'SEC DEB CLD AVG EXP VEL .... ',F6.3,' KM/S',/,3X,
$'ADDL PRESS WALL VEL ..... ',F6.3,' KM/S')
      WRITE (2,452) TH1DEG,RDC,AN,AK1,AKMN,MDC*1000.0,C1AX,C1EXP,V,VEXP
452 FORMAT(/,'SECONDARY DEBRIS CLOUD PROPERTIES (1ST COMP) ...',
$,/,3X,'1/2-ANG = ',F6.3,' DEG',/,3X,'RHO = ',F6.3,' GM/CU.CM.',
$,/,3X,'N = ',F6.3,/,3X,'K1 = ',F6.3,' (>',F5.3,')',/,3X,
$'MDC1 = ',F6.3,' GMS',/,3X,'C#1 = ',F6.3,/,3X,'C#2 = ',
$F6.3,/,3X,'VMC = ',F6.3,' KM/S',/,3X,'VEXP = ',F6.3,' KM/S'
$)
      WRITE (2,453) TH2DEG,RIBA,MIB*1000.0,C2AX,C2EXP,VMC2,VEXP2
453 FORMAT(/,'SECONDARY DEBRIS CLOUD PROPERTIES (2ND COMP) ...',/,3X,
$'1/2-ANG = ',F6.3,' DEG',/,3X,'RHO-A = ',F6.3,' GM/CU.CM.',/,3X,
$'MIB = ',F6.3,' GMS',/,3X,'C#1 = ',F6.3,/,3X,'C#2 = ',
$F6.3,/,3X,'VMC = ',F6.3,' KM/S',/,3X,'VEXP = ',F6.3,
$' KM/S')
      WRITE (2,454) TMAT,COT,KT,RT,TW,S,COA,KA,RA,CPA,T0A,P0A,HMOD
454 FORMAT(/,'PRESSURE WALL PROPERTIES ...',/,3X,'MAT = ',A10,/,3X,
$'CO = ',F6.3,' KM/S',/,3X,'K = ',F6.3,/,3X,'RHO = ',F6.3,
$' GM/CU.CM.',/,3X,'TW = ',F6.3,' CM',/,3X,'S = ',F6.3,' CM',/,
$'MODULE AIR PROPERTIES ...',/,3X,'CO = ',F6.3,' KM/S',/,3X,
$'K = ',F6.3,/,3X,'RHO = ',E10.3,' GM/CU.CM.',/,3X,'CP = ',F6.3,
$' CAL/GM/DEG-C',/,3X,'T0 = ',F6.3,' DEG-C',/,3X,'P0 = ',F6.3,
$' ATM',/,/, 'MODULE DIAMETER ...',/,3X,'HMOD = ',F7.2,' CM')
C
C..... CALCULATE PARTICLE AND SHOCK WAVE VELOCITIES AND HUGONIOT
C..... PRESSURE DUE TO SECONDARY DEBRIS CLOUD IMPACT
C
      IF (TMAT.EQ.BMAT.AND.BMAT.EQ.PMAT) GOTO 351
      A=KDC-KT*(RT/RDC)
      B=2.0*KDC*V+CODC+COT*(RT/RDC)
      C=CODC*V+KDC*V*V
      D=B*B-4.0*A*C
      UTP=(B-SQRT(D))/(2.0*A)
      GOTO 381
351   UTP=V/2.0
381   UDCP=V-UTP
      UTS=COT+KT*UTP
      UDCS=CODC+KDC*UDCP

```

```

PDC=RDC*UDCS*UDCP
PT=RT*UTS*UTP
C
C..... PRESSURE WALL RESPONSE AND IMPEDANCE MATCH CALCULATION PHASE
C
WRITE(2,59)
59 FORMAT(/,'**** PRESSURE WALL RESPONSE AND IMPEDANCE MATCH CALCULAT
$IONS ****')
WRITE(2,60) V,UTP,UTS,PT
60 FORMAT(/,'ASSIGNED PRESS WALL IMP VEL ..... VW = ',F7.3,' KM/S',
$/,'PRESSURE WALL PARTICLE VELOCITY ... UP = ',F7.3,' KM/S',/,'PRES
$SURE WALL SHOCK WAVE SPEED .... US = ',F7.3,' KM/S',/,'HUGONIOT IM
$PACT PRESSURE ..... PH = ',F7.3,' GPA')
C
VTO=1.0/RT
VT1=RT*UTS/(UTS-UTP)
VT1=1.0/VT1
VDCO=1.0/RDC
VDC1=RDC*UDCS/(UDCS-UDCP)
VDC1=1.0/VDC1
C
PH=PT*1.0E09
C
WRITE(2,75) ET/10.0,NUT,KST/10.0,ALPHAT,CPST,CPLT
75 FORMAT(/,'PARAMETERS REQUIRED FOR CALCULATING PRESSURE WALL MATERI
$AL RESPONSE AND',/,'RELEASE FROM SHOCKED STATE USING THE MIE-GRUNE
$ISEN E-O-S:',/,'3X','MATL ELASTIC MODULUS ..... E =',
$E10.4,' N/SQ.M.',/,'3X','MATL POISSON RATIO ..... NU =',
$F10.3,/,'3X','MATL BULK MODULUS ..... K =',E10.4,
$' N/SQ.M.',/,'3X','MATL LIN. COEF. OF THERM. EXP. ... ALFA =',E10.4,
$' /DEG-C',/,'3X','MATL SP HEAT (SOLID) ..... CPS =',F10.3,
$' CAL/GM/DEG-C',/,'3X','MATL SP HEAT (LIQUID) ..... CPL =',
$,F10.3,' CAL/GM/DEG-C')
PHMB=PH/100.0E+09
WRITE(2,80) PH,PHMB,VTO,VT1,GT,GTI
80 FORMAT(3X,'MATL HUGON IMP PRESS (PA,MBAR) ... PH =',E10.4,',',
$F5.3,/,'3X','MATL SP VOL AT REST ..... V0 =',F10.3,' CU.C
$M./GM',/,'3X','MATL SP VOL AT IMPACT ..... V1 =',F10.3,' CU
$.CM./GM',/,'3X','MATL AMB M-GRUN COEF (CAL,INP) ... GAM0 =',F10.3,',',
$,F5.3)
WRITE(2,85) TMT,TVT,HFT,HVT
85 FORMAT(3X,'MATL MELT TEMPERATURE ..... TM =',F10.2,' DEG-
$C',/,'3X','MATL VAPOR TEMPERATURE ..... TV =',F10.2,' DEG-C'
$,/,'3X','MATL HEAT OF FUSION ..... HF =',F10.2,' CAL/GM'
$,/,'3X','MATL HEAT OF VAPORIZATION ..... HV =',F10.2,' CAL/GM')
C
C..... PERFORM IMPEDANCE MATCH CALCULATIONS TO DETERMINE SHOCK WAVE
C..... PROPERTIES FOR WAVE TRANSMITTED INTO MODULE AND REFLECTED INTO
C..... PRESSURE WALL
C
CALL IMPMTCH(RT,RA,KT,KA,COT,COA,UTP,PA,UAP)
UAS=COA+KA*UAP
PHA=RA*UAS*UAP
PHAB=(PHA/101325.0)*1.0E+09
C
WRITE(2,175) UAP,UAS,PHA,PHAB
175 FORMAT(/,'RESULTS OF IMPEDANCE MATCH CALCULATIONS ...',/,'3X,
$'INTERFACE (REFL & TRANS) PARTICLE VEL ...',F8.5,' KM/S',/,'3X,
$'TRANSMITTED SHOCK WAVE SPEED .....',F8.5,' KM/S',/,'3X,
$'INTERFACE (REFL & TRANS) PRESSURE .....',E12.5,' GPA ('F5.1,

```

```

$' ATM) ')
C
C..... CALCULATE RELEASE OF SECONDARY DEBRIS CLOUD MATERIAL UP UNTIL
C..... ZERO PRESSURE IS REACHED
C
      WRITE (2,171)
171 FORMAT(/,'RELEASE OF SHOCKED SECONDARY DEBRIS CLOUD MATERIAL ...')
      PFIN=0.0
      CALL RELS(CODC,KDC,RDC,GRDC,VDCO,VDC1,PH,EXTDC,UDCP,PFIN,VFDC)
C
C..... CALCULATE RELEASE OF PRESSURE WALL MATERIAL UP UNTIL INTERFACE
C..... PRESSURE IS REACHED
C
      WRITE (2,173)
173 FORMAT(/,'RELEASE OF SHOCKED PRESSURE WALL MATERIAL ...')
      PFIN=PHA*1.0E+09
      CALL RELS(COT,KT,RT,GRT,VTO,VT1,PH,EXTPW,UTP,PFIN,VFPW)
C
C..... CALCULATE TEMPERATURE INCREASE IN PRESSURE WALL MATERIAL
C
      CALL TINC(CPST,CPLT,TMT,TVT,HFT,HVT,EXTPW)
C
      WRITE(*,177)
177 FORMAT(' PRESSURE WALL & IMPEDANCE MATCH CALCULATIONS COMPLETE.')
C
C..... MODULE INTERNAL EFFECTS CALCULATION PHASE
C
      WRITE (*,181)
181 FORMAT(/,' BEGINNING MODULE INTERNAL EFFECTS CALCULATION PHASE ...
$')
C
      READ (4,183) IOPT
183 FORMAT(I1)
C
      WRITE (2,186)
186 FORMAT(/,'***** MODULE INTERNAL EFFECTS CALCULATION *****',//,
$'CALCULATION OPTION SELECTED ...')
      IF (IOPT.EQ.1) WRITE (2,1871)
1871 FORMAT(/,3X,'SHOCK WAVE PASSAGE ONLY')
      IF (IOPT.EQ.2) WRITE (2,1872)
1872 FORMAT(/,3X,'INTERNAL DEBRIS CLOUD PASSAGE ONLY')
      IF (IOPT.EQ.3) WRITE (2,1874)
1874 FORMAT(/,3X,'COMBINED SHOCK WAVE AND INTERNAL DEB CLD PASSAGE')
C
      IF (IOPT.EQ.1.OR.IOPT.EQ.3) THEN
        ESDCA=0.5*MDC*(V*1000.0)*(V*1000.0)
        ESDCE=0.5*MDC*(VEXP*1000.0)*(VEXP*1000.0)
        EL1=EXTDC*(MDC*AK2)
        EL2=EXTPW*(MW*AK2)
        ESW=ESDCA+ESDCE-(EL1+EL2)
        SWR1=EL1/(ESDCA+ESDCE)
        SWR2=EL2/(ESDCA+ESDCE)
        SWR3=ESW/(ESDCA+ESDCE)
        WRITE (2,306) MDC*1000.0,V,ESDCA,ESDCE,ESDCA+ESDCE,EXTDC,
$          AK2*MDC*1000.0,AK2,EL1,SWR1*100.0,EXTPW,
$          AK2*MW*1000.0,AK2,EL2,SWR2*100.0
306 FORMAT(/,3X,'SECONDARY DEBRIS CLOUD MASS ..... ',F10.3,
$' GMS',/,3X,'SECONDARY DEBRIS CLOUD VELOCITY ..... ',F10.3,
$' KM/S',/,3X,'AXIAL ENERGY OF SECONDARY DEBRIS CLOUD ... ',E10.4,
$' JOULES',/,3X,'EXPAN ENERGY OF SECONDARY DEBRIS CLOUD ... ',E10.4,

```



```

$' JOULES',/,3X,'TOTAL ENERGY OF SECONDARY DEBRIS CLOUD ... ',E10.4,
$' JOULES',/,3X,'SDC SHOCK HEATING WASTE HEAT ..... ',E10.4
$, ' JOULES/KG',/,3X,'SDC MASS SUBJECTED TO SHOCK HEATING ..... ',
$F10.3,' GMS ('F4.2','MDC)',/,3X,'ENERGY LOST TO SDC SHOCK HEATING
$..... ',E10.4,' JOULES ('F5.2','%)',/,3X,'PWALL SHOCK HEATING
$WASTE HEAT ..... ',E10.4,' JOULES/KG',/,3X,'PWALL MASS SUBJE
$CTED TO SHOCK HEATING .... ',F10.3,' GMS ('F4.2','MW)',/,3X,'ENERG
$Y LOST TO PWALL SHOCK HEATING ..... ',E10.4,' JOULES ('F5.2','%
$')
  IF (IOPT.EQ.1) WRITE (2,3601) ESW,SWR3*100.0
3601 FORMAT(3X,'ENERGY TRANSFORMED INTO SW MOTION ..... ',E10.4,
$' JOULES ('F5.2','%')
  IF (ESW.LE.0.0) THEN
    WRITE (2,990)
    WRITE (*,990)
990 FORMAT('*** FATAL ERROR 003: INSUFFICIENT ENERGY AVAILABLE FOR SHO
$CK WAVE FORMATION ***')
    STOP
    ENDIF
    ENDIF
C
  IF (IOPT.EQ.2.OR.IOPT.EQ.3) THEN
    ESDCA=0.5*MDC*(V*1000.0)*(V*1000.0)
    ESDCE=0.5*MDC*(VEXP*1000.0)*(VEXP*1000.0)
    EL1=EXTDC*(MDC*AK2)
    EL2=EXTPW*(MW*AK2)
    DDCM=MDC*MWH
    UMC=MDC*V/DDCM
    EL3=0.5*DDCM*(UMC*1000.0)*(UMC*1000.0)
    DELE=ESDCA+ESDCE-(EL1+EL2+EL3)
    IF (DELE.LE.0.0) THEN
      WRITE (2,992)
      WRITE (*,992)
992 FORMAT('*** FATAL ERROR 004: INSUFFICIENT ENERGY AVAILABLE FOR INT
$ DEB CLD EXPANSION ***')
      STOP
      ENDIF
      UEXP=DSQRT(DELE/(DDCM/2.0))/1000.0
      ENDIF
C
C..... READ COORDINATES OF THE POINT OF INTEREST
C
  READ (4,1854) NPOI
1854 FORMAT(I2)
  DO 9099 IPOI=1,NPOI
C
C..... INITIALIZE TOTAL PRESSURE AND TEMPERATURE INCREASES
C
  PINCTOT=0.0
  TINCTOT=0.0
C
  READ (4,1855) XPOI,YPOI,ZPOI
1855 FORMAT(3F10.5)
C
  WRITE (2,1856) IPOI,NPOI
1856 FORMAT(5X,/, '***** NOW ANALYZING POINT-OF-INTEREST NO.',I2, '/',
$I2, ' *****',/)
C
  IF (IOPT.EQ.1) CONTINUE
  IF (IOPT.EQ.2) GOTO 1000

```

```

      IF (IOPT.EQ.3) THEN
      UAPOLD=UAP
      UASOLD=UAS
      ESWOLD=ESW
      EON=ESW
      EOD=(MDC+MWH)*(UAP*1000.0)*(UAP*1000.0)/2.0
      E0=EON/EOD
      UMC2=(UMC*1000.0)*(UMC*1000.0)
      UDE2=DELE/(0.5*(MDC+MWH))
      SQ1=UMC2
      SQ2=(E0+1)*(UMC2-UDE2)
      SQ=SQ1-SQ2
      IF (SQ.LE.0.0) THEN
      WRITE (2,994)
      WRITE (*,994)
994  FORMAT('*** FATAL ERROR 005: INAPPROPRIATE SHOCK WAVE/DEBRIS CLOUD
$ INTERACTION MODELING ***')
      STOP
      ENDIF
      UAP=(UMC*1000.0+DSQRT(SQ))/(E0+1)/1000.0
      ESW=ESWOLD*(UAP/UAPOLD)*(UAP/UAPOLD)
      SWR3=ESW/(ESDCA+ESDCE)
      IF (IOPT.EQ.3) WRITE (2,3611) ESW,SWR3*100.0
3611 FORMAT(3X,'ENERGY TRANSFORMED INTO SW MOTION ..... ',E10.4,
$' JOULES (' ,F5.2,'%')')
      UAS=COA+KA*UAP
      PHA=RA*UAS*UAP
      PHAB=(PHA/101325.0)*1.0E+09
      WRITE (2,1751) UAP,UAS,PHA,PHAB
1751 FORMAT(/,'MODIFIED INTERFACE VALUES ...',/,3X,'INTERFACE PARTICLE
$VEL ...',F8.5,' KM/S',/,3X,'TRANS SHOCK WAVE SPEED ...',F8.5,
$' KM/S',/,3X,'INTERFACE PRESSURE .....',E12.5,' GPA (' ,F5.1,
$' ATM)')
      ENDIF
C
      UAPT=UAP+UPW
      UAST=COA+KA*UAPT
      PHAT=RA*UAST*UAPT
      PHATB=(PHAT/101325.0)*1.0E+09
      WRITE (2,1752) UAPT,UAST,PHAT,PHATB
1752 FORMAT(3X,'TOT TRANS PARTICLE VELOCITY .....',F8.5,' KM/S',/,3X,
$'TOT TRANS SHOCK WAVE SPEED .....',F8.5,' KM/S',/,3X,'TOT TRANS
$PRESSURE .....',E12.5,' GPA (' ,F5.1,' ATM)')
C
      WRITE (*,184)
184  FORMAT(/,' BEGINNING SHOCK WAVE PASSAGE CALCULATIONS ...')
C
      CALL INTEFF(UAST,COA,KA,RA,E0A,PA,CPA,SWUS,SWPHB,DELT,RHA)
C
      WRITE (2,300) UAST,SWUS
300  FORMAT(/,'INITIAL SHOCK WAVE PASSAGE ...',/,3X,'TOTAL SHOCK WAVE V
$ELOCITY ..... ',F10.3,' KM/S',/,3X,'INTERNAL SHOCK WAVE V
$ELOCITY ..... ',F10.3,' KM/S')
C
      IF (SWUS.LT.COA) THEN
      DPPOI=0.0
      DELTPOI=0.0
      WRITE (2,303)
303  FORMAT(/,3X,'*** SHOCK WAVE SPEED LESS THAN SPEED OF SOUND ***')
      GOTO 309

```

```

        ENDIF
C
        SWPINC=SWPHB-POA
        SWTINC=DELT
        WRITE (2,3061) SWPINC,SWTINC
3061  FORMAT(3X,'INITAL PRESSURE INCREASE ..... ',F10.3,
        $' ATM',/,3X,'INITIAL TEMPERATURE INCREASE ..... ',F10.3,
        $' DEG-C')
C
        IF (IOPT.EQ.1) JOPT=1
        IF (IOPT.EQ.3) JOPT=31
        CALL ATTEN(AMEXP,SWPINC,COA,KA,SWUS,RA,PA,E0A,CPA,ESW,XPOI,YPOI,
        $          ZPOI,JOPT,DPPOI,DELTPOI)
C
309   WRITE (*,310)
310  FORMAT(' SHOCK WAVE PASSAGE CALCULATIONS COMPLETE.')
C
        IF (IOPT.EQ.1) GOTO 9099
C
        IF (IOPT.EQ.3) THEN
        PINCTOT=PINCTOT+DPPOI
        TINCTOT=TINCTOT+DELTPOI
        GOTO 1000
        ENDIF
C
1000  WRITE (*,311)
311  FORMAT(/,' BEGINNING DEBRIS CLOUD PASSAGE CALCULATIONS ...')
C
        UEXP=UAP-UMC
        IF (UEXP.LE.0.0) THEN
        WRITE (2,9922)
        WRITE (*,9922)
9922  FORMAT(/,'*** FATAL ERROR 006: INSUFFICIENT ENERGY AVAILABLE FOR
        $INT DEB CLD EXPANSION ***')
        WRITE (2,4060) MWH*1000.0,AK3,AK2,DDCM*1000.0,UMC,UAP,UEXP
4060  FORMAT(3X,'PR WALL MASS CONTRIB TO DIFF DEB CLD ..... ',F10.3,
        $' GMS (' ,F4.2,'*',F4.2,'MW1)',/,3X,'DIFFUSE DEBRIS CLOUD MASS ....
        $..... ',F10.3,' GMS',/,3X,'DIFF DEB CLD AXIAL CHARACT VELOC
        $ITY ..... ',F10.3,' KM/S',/,3X,'DIFF DEB CLD LEADING EDGE VELOCIT
        $Y ..... ',F10.3,' KM/S',/,3X,'DIFF DEB CLD EXPANSION VELOCITY ..
        $..... ',F10.3,' KM/S')
        STOP
        ENDIF
C
        CALL INTEFF(UAP,COA,KA,RA,E0A,PA,CPA,DCUS,DCPHB,DELT,RHA)
C
        WRITE (2,400) UAP,DCUS
400  FORMAT(/,'DEBRIS CLOUD PASSAGE ...',/,3X,'INT DEB CLD LEADING EDGE
        $ VELOCITY ..... ',F10.3,' KM/S',/,3X,'DEB CLD INDUCED SHOCK WAV
        $E VELOCITY ..... ',F10.3,' KM/S')
C
        IF (DCUS.LT.COA) THEN
        DPPOI=0.0
        DELTPOI=0.0
        WRITE (2,403)
403  FORMAT(/,3X,'*** SHOCK WAVE SPEED LESS THAN SPEED OF SOUND ***')
        GOTO 409
        ENDIF
C
        DCPINC=DCPHB-POA

```

```

DCTINC=DELT
EDDCA=0.5*DDCM*(UMC*1000.0)*(UMC*1000.0)
EDDCE=0.5*DDCM*(UEXP*1000.0)*(UEXP*1000.0)
EDDC=EDDCA+EDDCE
DDCR3=EDDCA/(ESDCA+ESDCE)
DDCR4=EDDCE/(ESDCA+ESDCE)
DDCR5=EDDC/(ESDCA+ESDCE)
WRITE (2,4061) DCPINC,DCTINC,MWH*1000.0,AK3,AK2,DDCM*1000.0,UMC,
$          EDDCA,DDCR3*100.0,UEXP,EDDCE,DDCR4*100.0,EDDC,
$          DDCR5*100.0
4061 FORMAT(3X,'INIT PRESS INCR BEH DEB CLD INDUCED SW ... ',F10.3,
$' ATM',/,3X,'INIT TEMP INCR BEH DEB CLD INDUCED SW .... ',F10.3,
$' DEG-C',/,3X,'PR WALL MASS CONTRIB TO DIFF DEB CLD ..... ',F10.3,
$' GMS (' ,F4.2,'*',F4.2,'MW1)',/,3X,'DIFFUSE DEBRIS CLOUD MASS ....
$..... ',F10.3,' GMS',/,3X,'DIFF DEB CLD AXIAL CHARACT VELOC
$ITY ..... ',F10.3,' KM/S',/,3X,'DIFFUSE DEB CLD AXIAL KINETIC ENE
$RGY ..... ',E10.4,' JOULES (' ,F5.2,'%)',/,3X,'DIFF DEB CLD EXPAN C
$HARACT VELOCITY ..... ',F10.3,' KM/S',/,3X,'DIFFUSE DEB CLD EXPAN
$ KINETIC ENERGY ..... ',E10.4,' JOULES (' ,F5.2,'%)',/,3X,'DIFFUSE
$DEB CLD TOTAL KINETIC ENERGY ..... ',E10.4,' JOULES (' ,F5.2,'%)' )
C
C.....  CALCULATE INTERNAL DEBRIS CLOUD SPREAD, ATTENUATION INITIATION
C.....  DISTANCE, AND DEBRIS CLOUD RADIUS AT ATTENUATION ONSET
C
TPHDC=UEXP/UMC
ANG=(180.0/PI)*ATAN(TPHDC)
SPHDC=DSIN(PI*ANG/180.0)
FCNPHI=SPHDC/(1.0+SPHDC)
DEN=PI*CD*(RA*1000.0)*FCNPHI*FCNPHI*(UMC*1000.0)
$          *(UMC*1000.0)/2.0
H=100.0*(EDDCA/DEN)**0.3333333333
IF (H.GT.HMOD) H=HMOD
RDC=H*FCNPHI
DEL=0.8*RDC*RA/RHA
AM=DCUS/COA
AN=DEL+RDC
AD=AM/DSQRT(AM*AM-1.0)-1.0
A=AN/AD
B=A/DSQRT(AM*AM-1.0)
C
C.....  CHECK IF POINT OF INTEREST WITHIN DEBRIS CLOUD PATH
C
IF (XPOI.GE.H) GOTO 4023
RXPOI=XPOI*TPHDC
QCHK1=YPOI*YPOI+ZPOI*ZPOI
QCHK2=RXPOI*RXPOI
WRITE (2,4011) UMC,UEXP,ANG,RDC,H,AM,DEL,A,B
4011 FORMAT(/,'INTERNAL DEBRIS CLOUD CHARACTERISTICS ...',/,3X,'UCOM =
$',F6.3,' KM/S',/,3X,'UEXP = ',F6.3,' KM/S',/,3X,'1/2-ANG = ',F6.2,
$' DEG',/,3X,'MAX RDC = ',F6.2,' CM',/,3X,'H-DIST = ',F6.2,' CM',
$//,'INT DEB CLD SHOCK WAVE CHARACTERISTICS ...',/,3X,'M# = ',F6.2
$//,3X,'DEL = ',F6.2,' CM',/,3X,'A = ',F10.2,' CM',/,3X,'B = ',
$F10.2,' CM')
IF(QCHK1.LE.QCHK2) THEN
WRITE (2,4012) XPOI,YPOI,ZPOI
4012 FORMAT(/,'*** WARNING: PT OF INT (' ,F6.2,',',F6.2,',',F6.2,') LIES
$ WITHIN DEB CLD CONE ***')
WRITE (*,410)
GOTO 9099
ENDIF

```

```

C
C..... IF POINT OF INTEREST IS OUTSIDE DEBRIS CLOUD CONE ANGLE, CHECK IF
C..... POINT OF INTEREST IS OVER-RUN BY FULL STRENGTH BOW SHOCK
C
      IF (XPOI.GE.H) GOTO 4023
      T1=XPOI-(H+DEL+A)
      RXPOI2=(T1/A)*(T1/A)-1.0
      RXPOI=DSQRT(RXPOI2)
      QCHK1=(YPOI/B)*(YPOI/B)+(ZPOI/B)*(ZPOI/B)
      QCHK2=RXPOI*RXPOI
      T11=-(H+DEL+A)
      RPWP2=(T11/A)*(T11/A)-1.0
      RPWP=DSQRT(RPWP2)
      WRITE (2,4021) B*RPWP
4021  FORMAT(3X,'RPW-MIN = ',F6.2,' CM')
      IF (QCHK1.LE.QCHK2) THEN
        WRITE (2,4022) XPOI,YPOI,ZPOI
4022  FORMAT(/,'*** WARNING: PT OF INT (',F6.2,',',F6.2,',',F6.2,') LIES
      $ OUTSIDE DEB CLD CONE',/,13X,'BUT WITHIN FULL STRENGTH BOW SHOCK *
      $**')
      DPPOI=DCPHB-P0A
      DELTPOI=DCTINC
      GOTO 409
      ENDIF
C
C..... IF POINT OF INTEREST OUTSIDE DEBRIS CLOUD CONE AND OUTSIDE BOW
C..... SHOCK, PROCEED WITH ATTENUATION OF PEAK PRESSURE AND TEMPERATURE
C
4023  IF (IOPT.EQ.2) JOPT=2
      IF (IOPT.EQ.3) JOPT=32
      CALL ATTEN(AMEXP,DCPINC,COA,KA,DCUS,RA,PA,E0A,CPA,EDDC,XPOI,YPOI
      $           ,ZPOI,JOPT,DPPOI,DELTPOI)
C
409   WRITE (*,410)
410   FORMAT(' DEBRIS CLOUD PASSAGE CALCULATIONS COMPLETE.')
C
      IF (IOPT.EQ.2) GOTO 9099
C
      IF (IOPT.EQ.3) THEN
        PINCTOT=PINCTOT+DPPOI
        TINCTOT=TINCTOT+DELTPOI
        WRITE (2,421) PINCTOT,PINCTOT*14.7,TINCTOT
421   FORMAT(/,'CUMULATIVE EFFECT OF SHOCK WAVE AND DEBRIS CLOUD PASSAGE
      $ .....',/,3X,'TOT PRESSURE INCREASE ...',F7.2,' ATM (',F9.3,
      $ ' PSI)',/,3X,'TOT TEMPERATURE INCREASE ...',F7.2,' DEG-C')
        PRT(IPOI,1)=PINCTOT*14.7
        PRT(IPOI,2)=TINCTOT
        GOTO 9099
      ENDIF
C
9099  CONTINUE
C
      DO 9199 IPOI=1,NPOI
        WRITE (*,422) IPOI,PRT(IPOI,1),PRT(IPOI,2)
422   FORMAT(' POI #',I2,5X,' TOT PRES INCR ...',F7.3,' PSI',5X,'TOT TEM
      $P INCR ...',F7.2,' C')
9199  CONTINUE
C
      CLOSE(1)
      CLOSE(2)

```

```

      CLOSE(4)
C
      STOP
      END
C
      SUBROUTINE RELS(CO,K,R,G,VO,V1,PHO,EX,UP,PHA,VF)
      IMPLICIT DOUBLE PRECISION (A-H,O-Z)
      DOUBLE PRECISION K,PH(201),EH(201),V(201),P(201),E(201)
C
C..... THIS SUBROUTINE CALCULATES THE RELEASE OF A SHOCKED MATERIAL
C..... USING THE MIE-GRUNHEISEN EQUATION OF STATE. INCLUDED IS A
C..... CALCULATION OF THE FINAL SPECIFIC VOLUME AND THE WASTE HEAT
C..... GENERATED BY THE RELEASE PROCESS. WHEN THE PRESSURE ALONG THE
C..... ISENTROPE DROPS BELOW THE REFLECTED PRESSURE ARE CALCULATED BY
C..... THE IMPEDANCE MATCH PROCESS, THE RELEASE PROCESS IS TERMINATED
C
      V(1)=V1
      PH(1)=PHO
      EH(1)=0.5*PH(1)*(VO-V1)/1000.0
      DV=(VO-V1)/50.0
      DE=0.0
      DV2=DV/1000.0
      E(1)=EH(1)
      P(1)=PH(1)
      DEN1=1.0+G*DV2*0.5
C
      II=0
      UR=0.0
      DO 10 I=2,201
      V(I)=V(I-1)+DV
      PH(I)=CO**2*R*1000.0*(1.0-V(I)/VO)/(1.0-K*(1.0-V(I)/VO))**2
      PH(I)=PH(I)*1.0E06
      EH(I)=0.5*PH(I)*(VO-V(I))/1000.0
      P(I)=(PH(I)+G*(E(I-1)-EH(I)-0.5*P(I-1)*DV2))/DEN1
      E(I)=E(I-1)-0.5*(P(I)+P(I-1))*DV2
      DP=P(I)-P(I-1)
      DUR=DSQRT(-DP*(DV/1000.0))
      UR=UR+DUR/1000.0
      II=II+1
      IF (P(I).GE.0.0) DE=DE+0.5*DV2*(P(I)+P(I-1))
      IF (P(I).LT.0.0) GOTO 15
      IF (P(I).LE.PHA) GOTO 15
10 CONTINUE
C
15 Q=P(II)/(P(II)-P(II+1))
      DE=DE+0.5*Q*DV2*P(II)
      EX=EH(1)-DE
      VF=V(II)+Q*(V(II+1)-V(II))
      UFS1=UP+UR
      UFS2=2.0*UP
C
      WRITE(2,20) VF,EH(1),DE,EX
20 FORMAT(/,'SPECIFIC VOL AFTER RELEASE ..... VF =',F5.3,
$' CU.CM./GM',/,'ENERGY DUE TO DEB CLD IMPACT .... ',E10.4,
$' JOULES/KG',/,'ENERGY RECOVERED BY RELEASE ..... ',E10.4,
$' JOULES/KG',/,'WASTE HEAT GENERATED ..... ',E10.4,
$' JOULES/KG')
C
      RETURN
      END

```

```

C
SUBROUTINE TINC(SHS,SHL,TM,TV,HF,HV,EXH)
IMPLICIT DOUBLE PRECISION (A-H,O-Z)
DOUBLE PRECISION IME,IVE

C
C..... THIS SUBROUTINE CALCULATES THE RESIDUAL TEMPERATURE INCREASE
C..... IN A MATERIAL THAT HAS BEEN RELEASED FROM THE SHOCKED STATE
C..... ESTIMATES THE PERCENTAGE OF VAPORIZED, MELTED, AND SOLID
C..... MATERIAL DUE TO THE RELEASE PROCESS
C
SHS=SHS*4186.0
SHL=SHL*4186.0
HF=HF*4186.0
HV=HV*4186.0

C
C..... CALCULATE ENERGIES REQUIRED TO INITIATE MATERIAL MELT AND
C..... VAPORIZATION.
C
IME=TM*SHS
IVE=IME+HF+(TV-TM)*SHL

C
C..... IF WASTE HEAT IS LESS THAN THE ENERGY REQ'D TO START MELT,
C..... CALCULATE TEMPERATURE RISE USING W.H.=S.H.*(TEMP.INCR.)
C
IF (EXH.LT.IME) THEN
DT=EXH/SHS
TR=DT
DEL=0.0
WRITE(2,50) IME,DEL,EXH
50 FORMAT('ENERGY REQ, INCIPIENT MELT ... ',E10.4,' JOULES/KG',/,
$'ENERGY AVAILABLE FOR MELT .... ',E10.4,' JOULES/KG',/,
$'EXCESS ENERGY AVAILABLE ..... ',E10.4,' JOULES/KG')
PV=0.0
PL=0.0
PS=100.0
GOTO 100
ENDIF

C
C..... IF WASTE HEAT EXCEEDS THE ENERGY REQ'D TO START MELT, BUT IS
C..... LESS THAN THAT REQ'D TO COMPLETE MELT, RESET THE VALUE OF THE
C..... ENERGY AVAILABLE FROM THE WASTE HEAT VALUE TO THE VALUE REQ'D
C..... TO START MELT. THIS IMPLIES THAT SOME ENERGY IS AVAILABLE FOR
C..... MELTING A PORTION OF THE MATERIAL. NOTE: THE TEMPERATURE RISE
C..... EQUALS THE MELT TEMPERATURE OF THE MATERIAL.
C
IF (EXH.GE.IME.AND.EXH.LT.IME+HF) THEN
TR=TM
DEL=EXH-IME
REQM=IME+HF
WRITE(2,60) IME,REQM,DEL
60 FORMAT('ENERGY REQ, INCIPIENT MELT ... ',E10.4,' JOULES/KG',/,
$'ENERGY REQ, COMPLETE MELT .... ',E10.4,' JOULES/KG',/,
$'ENERGY AVAILABLE FOR MELT .... ',E10.4,' JOULES/KG')
PV=0.0
PL=100.0*DEL/HF
PS=100.0-PL
GOTO 100
ENDIF

C
C..... IF THE WASTE HEAT EXCEEDS THE ENERGY REQ'D TO COMPLETELY MELT

```

```

C..... THE MATERIAL, BUT IS LESS THAN THAT REQ'D TO START VAPORIZA-
C..... TION, COMPUTE THE TEMPERATURE INCREASE CAUSED BY THE EXCESS
C..... ENERGY AND ADD IT TO THE MELT TEMPERATURE OF THE MATERIAL.
C
      IF (EXH.GE.IME+HF.AND.EXH.LT.IVE) THEN
      DEL=EXH-IME-HF
      DT=DEL/SHL
      TR=TM+DT
      REQM=IME+HF
      WRITE(2,70) IME,REQM,DEL
70  FORMAT('ENERGY REQ, INCIPIENT MELT ... ',E10.4,' JOULES/KG',/,
$'ENERGY REQ, COMPLETE MELT .... ',E10.4,' JOULES/KG',/,
$'EXCESS ENERGY AVAILABLE ..... ',E10.4,' JOULES/KG')
      PV=0.0
      PL=100.0
      PS=100.0-PL
      GOTO 100
      ENDIF
C
      IF (EXH.GE.IVE.AND.EXH.LT.IVE+HV) THEN
      DEL=EXH-IVE
      REQV=IVE+HV
      TR=TV
      WRITE(2,80) IVE,REQV,DEL
80  FORMAT('ENERGY REQ, INCIPIENT VAP .... ',E10.4,' JOULES/KG',/,
$'ENERGY REQ, COMPLETE VAP ..... ',E10.4,' JOULES/KG',/,
$'EXCESS ENERGY AVAILABLE ..... ',E10.4,' JOULES/KG')
      PV=100.0*DEL/HV
      PL=100.0-PV
      PS=100.0-PL
      GOTO 100
      ENDIF
C
      IF (EXH.GE.IVE+HV) THEN
      ECVAP=IVE+HV
      PV=100.0
      PL=0.0
      PS=0.0
      WRITE (2,90) ECVAP
90  FORMAT('ENERGY REQ, COMPLETE VAP .... ',E10.4,' JOULES/KG',/,
$'*** THE MATERIAL IS COMPLETELY VAPORIZED ***')
      GOTO 120
      ENDIF
C
100 WRITE(2,110) TR,PS,PL,PV
110 FORMAT('RESIDUAL MATERIAL TEMP ..... ',F10.3,' DEG-C',//,'PERCENT
$T SHKD AND REL PRESS WALL MATERIAL ...',/,3X,'IN SOLID STATE ... '
$,F6.2,'% ',/,3X,'IN MOLTEN FORM ... ',F6.2,'% ',/,3X,'IN VAPOR FORM
$.... ',F6.2,'% ')
C
120 RETURN
      END
C
      SUBROUTINE IMPMTC(RMA,RMB,KMA,KMB,COMA,COMB,V1,P4,UPMB)
      IMPLICIT DOUBLE PRECISION (A-H,O-Z)
      DOUBLE PRECISION KMA,KMB
C
      A=RMA*KMA-RMB*KMB
      B=RMA*COMA+RMB*COMB+4.0*RMA*KMA*V1
      P1=2.0*RMA*V1*(COMA+2.0*KMA*V1)

```



```

P1=P1-P4/1.0E+09
DISC=B*B-4.0*A*P1
UPMB=(B-DSQRT(DISC))/(2.0*A)
C
RETURN
END
C
SUBROUTINE INTEFF(V,CO,K,R0,E0,P,CP,US,PHB,DT,R)
IMPLICIT DOUBLE PRECISION (A-H,O-Z)
DOUBLE PRECISION K
C
US=V
UP=(US-CO)/K
PH=P/1.0E+09+R0*US*UP
PHB=(PH/101325.0)*1.0E+09
R=US*R0/(US-UP)
EH=E0+0.5*(PH*1.0E+09+P)*(1.0/R0-1.0/R)/1000.0
DT=(EH-E0)/(CP*4186.0)
C
RETURN
END
C
SUBROUTINE ATTEN(AM,DP1,CO,K,US,R0,P0,E0,CP,ES,XP,YP,ZP,JOPT,
$ DPPOI,DELTPOI)
IMPLICIT DOUBLE PRECISION (A-H,O-Z)
DOUBLE PRECISION K
COMMON/HYPERB/A,B,DEL,H
C
PI=3.141592
C
IF (JOPT.EQ.1.OR.JOPT.EQ.31) RPOI=DSQRT(XP*XP+YP*YP+ZP*ZP)
C
WRITE (2,5)
5 FORMAT(/,'PEAK SHOCK VALUES ...',/,2X,'DIST (CM)',3X,'SW VEL (KM/S
$)',3X,'SH DEN (GM/CC)',4X,'PR INC (ATM)',3X,'T INC (DEG-C)')
C
PB1=3.803/(0.01**1.2627)
DO 100 I=1,2000
RB=I/100.0
IF (RB.LE.0.1) PB=3.803/(RB**1.2627)
IF (RB.GT.0.1.AND.RB.LE.1.0) PB=0.476/(RB**2.2416)
IF (RB.GT.1.0.AND.RB.LE.10.0) PB=0.441/(RB**1.3821)
IF (RB.GT.10.0) PB=0.241/(RB**1.1120)
RATIO=PB/PB1
PH=(DP1*RATIO+1.0)*101325.0
DP=PH/101325.0-1.0
IF (DP.LT.0.01.AND.JOPT.EQ.1) GOTO 200
IF (DP.LT.0.01.AND.JOPT.EQ.31) GOTO 200
IF (DP.LT.0.01.AND.JOPT.EQ.2) GOTO 300
IF (DP.LT.0.01.AND.JOPT.EQ.32) GOTO 300
IF (I.EQ.1) THEN
UP=(US-CO)/K
GOTO 7
ENDIF
AA=R0*K
BB=R0*CO
CC=(P0-PH)/1.0E+09
UP=(-BB+DSQRT(BB*BB-4.0*AA*CC))/(2.0*AA)
US=CO+K*UP
7 R=R0*US/(US-UP)

```

```

E=E0+0.5*(PH+P0)*(1.0/R0-1.0/R)/1000.0
RA1=RB*((ES/P0)**0.3333333333)*100.0
IF (JOPT.EQ.1.OR.JOPT.EQ.31) AK4=1.0
IF (JOPT.EQ.2.OR.JOPT.EQ.32) THEN
  IF (XP.LE.H) AK4=1.0
  IF (XP.GT.H) AK4=1.0+AM*((RB/0.01)**AM)
ENDIF
RA=AK4*RA1
DELT=(E-E0)/(CP*4186.0)
IF (I.EQ.1) WRITE (2,10) RA,US,R,DP,DELT
10 FORMAT(3X,F6.2,9X,F5.3,9X,E9.3,10X,F7.3,6X,F9.3)
C
  IF (JOPT.EQ.1.OR.JOPT.EQ.31) THEN
    IF (RPOI.GT.RA) GOTO 90
    IF (RPOI.EQ.RA) THEN
      DPPOI=DP
      DELTPOI=DELT
      GOTO 150
    ENDIF
    IF (RPOI.LT.RA) THEN
      T1=(RPOI-RAF)/(RA-RAF)
      DPPOI=DPF+(DP-DPF)*T1
      DELTPOI=DELTF+(DELT-DELTF)*T1
      GOTO 150
    ENDIF
  ENDIF
C
  IF (JOPT.EQ.2.OR.JOPT.EQ.32) THEN
    T1=XP-(H+DEL+A+RA)
    RXP2=(T1/A)*(T1/A)-1.0
    QCHK1=(YP/B)*(YP/B)+(ZP/B)*(ZP/B)
    QCHK2=RX2
    XFS=H+DEL+A-A*DSQRT(QCHK1+1.0)
    IF (QCHK1.GT.QCHK2) GOTO 90
    IF (QCHK1.EQ.QCHK2) THEN
      DPPOI=DP
      DELTPOI=DELT
      GOTO 150
    ENDIF
    IF (QCHK1.LT.QCHK2) THEN
      T1=(XP-(XFS+RAF))/(RA-RAF)
      DPPOI=DPF+(DP-DPF)*T1
      DELTPOI=DELTF+(DELT-DELTF)*T1
      GOTO 150
    ENDIF
  ENDIF
C
90 RAF=RA
   USF=US
   RF=R
   DPF=DP
   DELTF=DELT
C
100 CONTINUE
C
150 WRITE (2,15) XP,YP,ZP,AM
15 FORMAT(/,'POINT-OF-INTEREST COORDINATES ...',/,3X,'X-COORD = ',
$F6.2,' CM',/,3X,'Y-COORD = ',F6.2,' CM',/,3X,'Z-COORD = ',F6.2,
$' CM',/,3X,'M-CONST = ',F6.2)
  IF (JOPT.EQ.1.OR.JOPT.EQ.31) WRITE (2,16) RPOI

```

```

16 FORMAT(3X,'R-DIST = ',F6.2,' CM')
   IF (JOPT.EQ.2.OR.JOPT.EQ.32) WRITE (2,161) XP-XFS
161 FORMAT(3X,'ETA-DST = ',F6.2,' CM')
   WRITE (2,17) US,R,DPPOI,DPPOI*14.7,DELTPOI
17 FORMAT(/,'ATTENUATED SHOCK VALUES ...',/,3X,'SH WAVE VEL = ',F9.3,
$' KM/S',/,3X,'SH DENSITY = ',E13.3,' GM/CC',/,3X,'PRESS INCR = '
$,F9.3,' ATM (' ,F9.3,' PSI)',/,3X,'TEMP INCR = ',F9.3,' DEG-C')
   RETURN

```

C

```

200 WRITE (2,10) RAF,USF,RF,DPF,DELTF
   DPPOI=0.0
   DELTPOI=0.0
   WRITE (2,205) XP,YP,ZP
205 FORMAT(/,'POINT-OF-INTEREST COORDINATES ...',/,3X,'X-COORD = ',
$F6.2,' CM',/,3X,'Y-COORD = ',F6.2,' CM',/,3X,'Z-COORD = ',F6.2,
$' CM')
   WRITE (2,210) RPOI,RAF
210 FORMAT('*** NOTE: DIST TO PT OF INT (' ,F6.2,' CM) BEYOND DP=1%ATM
$DIST (' ,F6.2,' CM) ***')
   RETURN

```

C

```

300 WRITE (2,10) RAF,USF,RF,DPF,DELTF
   DPPOI=0.0
   DELTPOI=0.0
   WRITE (2,305) XP,YP,ZP
305 FORMAT(/,'POINT-OF-INTEREST COORDINATES ...',/,3X,'X-COORD = ',
$F7.2,' CM',/,3X,'Y-COORD = ',F7.2,' CM',/,3X,'Z-COORD = ',F7.2,
$' CM')

```

C

```

   AP=A+RAF
   QCHK22=(H+DEL+AP)*(H+DEL+AP)/(A*A)-1.0
   QCHK2=DSQRT(QCHK22)
   QCHK12=(YP/B)*(YP/B)+(ZP/B)*(ZP/B)
   QCHK1=DSQRT(QCHK12)
   RPW=B*QCHK2
   IF (QCHK1.GE.QCHK2) WRITE (2,310) RPW
310 FORMAT('*** NOTE: PT OF INT OUTSIDE MAX SHOCK WAVE CYL (RPW-MAX =
$' ,F6.2,' CM) ***')
   IF (QCHK1.LT.QCHK2) WRITE (2,315) XP-XFS,XP,XFS,RAF
315 FORMAT('*** NOTE: X-DIR DIST (' ,F6.2,' CM) TO PT OF INT (X-COORD =
$' ,F6.2,' CM) FROM',/,10X,'FULL STRENGTH SHOCK (X-COORD = ',F6.2,
$' CM) BEYOND DP=1%ATM',/,10X,'DIST (' ,F6.2,' CM) ***')
   RETURN
END

```

C

```

SUBROUTINE ROOTS(AK1,R2,MIB,MDC,MDC1,C1,C2)
IMPLICIT DOUBLE PRECISION(A-H,O-Z)
DOUBLE PRECISION MIB,MDC,MDC1
R1=MIB/MDC1
T0=(R1+1.0)*AK1*AK1
DD=(MDC*R2)*(MDC*R2)*R1*(T0-1.0)
T11=MDC*R2*R1
T12=DSQRT(DD)
C2N=T11-T12
C2D=MIB*(R1+1.0)
C2=C2N/C2D
C1=(MDC*R2-MIB*C2)/MDC1
RETURN
END

```

APPENDIX D – SAMPLE INPUT FILES

INPUT FILE: *IMPDAT*

```

-----
--MAT'L--|----C0---|----K----|---RHO---|--GAM0---|
--EL.MOD.-|----NU---|--ALFA---|---CPS---|--CPL---|
--T.MELT--|--T.VAP--|--H.FUS--|--H.VAP--|
-----

```

AL

```

ALUMINUM      5.380      1.340      2.712      2.130
0.103E+08      0.35 0.240E-04      0.235      0.255
660.0      2450.0      95.0      2450.0
-----

```

A1

```

2XXX ALUM      5.350      1.340      2.800      2.000
0.106E+08      0.33 0.209E-04      0.212      0.242
640.0      2450.0      85.0      2450.0
-----

```

A2

```

5XXX ALUM      5.310      1.340      2.670      2.000
0.101E+08      0.33 0.225E-04      0.215      0.245
641.0      2450.0      85.0      2450.0
-----

```

A3

```

6XXX ALUM      5.380      1.340      2.700      2.000
0.100E+08      0.33 0.233E-04      0.212      0.242
652.0      2450.0      85.0      2450.0
-----

```

A4

```

7XXX ALUM      5.290      1.340      2.810      2.000
0.103E+08      0.33 0.221E-04      0.217      0.245
636.0      2450.0      85.0      2450.0
-----

```

BE

```

BERYLLIUM      7.975      1.124      1.820      1.160
0.419E+08      0.08 0.140E-04      0.570      0.832
1281.0      2884.0      260.0      8195.0
-----

```

CD

```

CADMIUM      2.307      1.640      8.640      2.270
0.672E+07      0.33 0.343E-04      0.058      0.063
321.0      765.0      13.5      212.0
-----

```

CU

```

COPPER      3.940      1.489      8.930      2.000
0.190E+08      0.34 0.170E-04      0.097      0.114
1083.0      2590.0      49.0      1150.0
-----

```

EP

```

EPOXY      3.020      1.520      1.180      0.800
0.650E+06      0.50 0.500E-04      0.250      0.285
350.0      -1.0      -1.0      -1.0
-----

```

FE

```

IRON      4.580      1.490      7.870      1.570
0.290E+08      0.30 0.120E-04      0.120      0.150
1539.0      3035.0      65.0      1591.0
-----

```

PB					
LEAD	2.030	1.470	11.340	2.770	
0.200E+07	0.45	0.293E-04	0.031	0.036	
327.0	1740.0	6.0	210.0		

LX					
LEXAN	2.750	1.480	1.180	0.860	
0.345E+06	0.50	0.650E-04	0.290	0.315	
225.0	-1.0	-1.0	-1.0		

MO					
MOLYBDENUM	5.173	1.220	10.200	1.520	
0.460E+08	0.31	0.061E-04	0.079	0.104	
2610.0	5555.0	70.0	1242.0		

NI					
NICKEL	4.667	1.530	8.860	1.800	
0.330E+08	0.30	0.143E-04	0.130	0.157	
1454.0	2865.0	74.0	1523.0		

PT					
PLATINUM	3.680	1.500	21.370	2.940	
0.277E+08	0.39	0.110E-04	0.037	0.042	
1769.0	4349.0	26.0	632.0		

S1					
304 STEEL	4.590	1.550	7.910	1.670	
0.284E+08	0.28	0.112E-04	0.110	0.125	
1425.0	3035.0	65.0	1590.0		

S2					
430 STEEL	4.680	1.550	7.830	1.670	
0.299E+08	0.29	0.104E-04	0.110	0.125	
1470.0	3035.0	65.0	1590.0		

S3					
4340 STEEL	4.570	1.550	7.830	1.670	
0.290E+08	0.30	0.112E-04	0.110	0.125	
1510.0	3070.0	65.0	1590.0		

TA					
TANTALUM	3.374	1.201	16.650	1.690	
0.260E+08	0.35	0.065E-04	0.033	0.039	
2996.0	5425.0	38.0	1007.0		

SN					
TIN	2.560	1.520	7.280	1.850	
0.603E+07	0.33	0.269E-04	0.058	0.062	
235.0	2450.0	14.0	580.0		

TI					
TITANIUM	4.786	1.049	4.512	1.100	
0.180E+08	0.30	0.100E-04	0.150	0.167	
1676.0	3260.0	99.0	2182.0		

W					
TUNGSTEN	4.150	1.237	19.170	1.480	
0.590E+08	0.30	0.040E-04	0.035	0.046	
3410.0	5900.0	53.0	1054.0		

ZN				
ZINC	3.042	1.500	7.140	2.150
0.108E+08	0.33	0.274E-04	0.100	0.115
420.0	907.0	25.0	420.0	

AU				
GOLD	3.060	1.570	19.240	3.100
0.124E+08	0.42	0.161E-04	0.034	0.038
1063.0	2960.0	16.0	413.0	

AG				
SILVER	3.230	2.500	10.490	2.500
0.120E+08	0.37	0.211E-04	0.062	0.071
961.0	2210.0	25.0	554.0	

MG				
MAGNESIUM	4.490	1.240	1.740	1.500
0.640E+07	0.29	0.300E-04	0.295	0.336
650.0	1110.0	88.0	1326.0	

XX

INPUT FILE: *GPARAM*

AL
AL
AL
AA

	1.27	0.16	0.48	11.43	5.72	400.0	0.20
	0.19	0.30	0.50	0.60			
1							
3							
4							
	18.0	61.0	0.0				
	119.0	61.0	0.0				
	203.0	61.0	0.0				
	203.0	0.0	0.0				

APPENDIX E -- SAMPLE OUTPUT FILE

NORMAL IMPACT OF A ALUMINUM PROJECTILE ON A DUAL-WALL SYSTEM WITH A
ALUMINUM BUMPER, A MLI-BLNKT INNER BUMPER, AND A ALUMINUM PRESSURE WALL

PROJECTILE PROPERTIES ...

MAT = ALUMINUM
CO = 5.380 KM/S
K = 1.340
RHO = 2.712 GM/CU.CM.
DP = 1.270 CM
MP = 2.909 GMS
VP = 6.700 KM/S

BUMPER PROPERTIES ...

MAT = ALUMINUM
CO = 5.380 KM/S
K = 1.340
RHO = 2.712 GM/CU.CM.
TS = .160 CM
DH = 2.257 CM
MB = 1.736 GMS

**** PROJECTILE AND BUMPER SHOCK LOADING RESPONSE AND RELEASE CALCULATIONS

PROJECTILE IMPACT VELOCITY VP = 6.700 KM/S
PROJ MATL PARTICLE VELOCITY ... UP = 3.350 KM/S
PROJ MATL SHOCK WAVE SPEED US = 9.869 KM/S
HUGONIOT IMPACT PRESSURE PH = 89.662 GPA
BMPR MATL PARTICLE VELOCITY ... UP = 3.350 KM/S
BMPR MATL SHOCK WAVE SPEED US = 9.869 KM/S
HUGONIOT IMPACT PRESSURE PH = 89.662 GPA

PARAMETERS REQUIRED FOR CALCULATING PROJECTILE MATERIAL RESPONSE AND
RELEASE FROM SHOCKED STATE USING THE MIE-GRUNEISEN E-O-S:

ELASTIC MODULUS E = .7102E+11 N/SQ.M.
POISSON RATIO NU = .350
BULK MODULUS K = .7891E+11 N/SQ.M.
LIN. COEF. OF THERM. EXP. ... ALFA = .2400E-04 /DEG-C
SP HEAT (SOLID) CPS = .235 CAL/GM/DEG-C
SP HEAT (LIQUID) CPL = .255 CAL/GM/DEG-C
HUGON IMP PRESS (PA,MBAR) ... PH = .8966E+11, .897
SP VOL AT REST V0 = .369 CU.CM./GM
SP VOL AT IMPACT V1 = .244 CU.CM./GM
AMB M-GRUN COEF (CAL,INP) ... GAM0 = 2.129,2.130
MELT TEMPERATURE TM = 660.00 DEG-C
VAPOR TEMPERATURE TV = 2450.00 DEG-C
HEAT OF FUSION HF = 95.00 CAL/GM
HEAT OF VAPORIZATION HV = 2450.00 CAL/GM

RELEASE OF SHOCKED PROJECTILE MATERIAL ...

SPECIFIC VOL AFTER RELEASE VF = .399 CU.CM./GM
ENERGY DUE TO DEB CLD IMPACT5611E+07 JOULES/KG
ENERGY RECOVERED BY RELEASE4616E+07 JOULES/KG
WASTE HEAT GENERATED9957E+06 JOULES/KG
ENERGY REQ, INCIPIENT MELT6492E+06 JOULES/KG
ENERGY REQ, COMPLETE MELT1047E+07 JOULES/KG
ENERGY AVAILABLE FOR MELT3464E+06 JOULES/KG
RESIDUAL MATERIAL TEMP 660.000 DEG-C

PERCENT SHKD AND REL PRESS WALL MATERIAL ...

IN SOLID STATE ... 12.89%
IN MOLTEN FORM ... 87.11%
IN VAPOR FORM00%

PARAMETERS REQUIRED FOR CALCULATING BUMPER MATERIAL RESPONSE AND
RELEASE FROM SHOCKED STATE USING THE MIE-GRUNEISEN E-O-S:

ELASTIC MODULUS E = .7102E+11 N/SQ.M.
POISSON RATIO NU = .350
BULK MODULUS K = .7891E+11 N/SQ.M.
LIN. COEF. OF THERM. EXP. ... ALFA = .2400E-04 /DEG-C
SP HEAT (SOLID) CPS = .235 CAL/GM/DEG-C
SP HEAT (LIQUID) CPL = .255 CAL/GM/DEG-C
HUGON IMP PRESS (PA,MBAR) ... PH = .8966E+11, .897
SP VOL AT REST V0 = .369 CU.CM./GM
SP VOL AT IMPACT V1 = .244 CU.CM./GM
AMB M-GRUN COEF (CAL,INP) ... GAMO = 2.129,2.130
MELT TEMPERATURE TM = 660.00 DEG-C
VAPOR TEMPERATURE TV = 2450.00 DEG-C
HEAT OF FUSION HF = 95.00 CAL/GM
HEAT OF VAPORIZATION HV = 2450.00 CAL/GM

RELEASE OF SHOCKED BUMPER MATERIAL ...

SPECIFIC VOL AFTER RELEASE VF = .399 CU.CM./GM
ENERGY DUE TO DEB CLD IMPACT5611E+07 JOULES/KG
ENERGY RECOVERED BY RELEASE4616E+07 JOULES/KG
WASTE HEAT GENERATED9957E+06 JOULES/KG
ENERGY REQ, INCIPIENT MELT6492E+06 JOULES/KG
ENERGY REQ, COMPLETE MELT1047E+07 JOULES/KG
ENERGY AVAILABLE FOR MELT3464E+06 JOULES/KG
RESIDUAL MATERIAL TEMP 660.000 DEG-C

PERCENT SHKD AND REL PRESS WALL MATERIAL ...

IN SOLID STATE ... 12.89%
IN MOLTEN FORM ... 87.11%
IN VAPOR FORM00%

PRIMARY DEBRIS CLOUD CHARACTERISTIC VELOCITIES ...

VEXP = 2.918 KM/S
VCOM = 4.196 KM/S
VLE = 6.700 KM/S
VPW = .118 KM/S

SELECTED PRIMARY DEBRIS CLOUD IMPACT VELOCITY ...

VDC = 4.196 KM/S

PRIMARY DEBRIS CLOUD PROPERTIES ...

1/2-ANG = 34.821 DEG
RATIO-P = .626
RPSR = 2.504 GM/CU.CM.
RATIO-B = .374
RBSR = 2.504 GM/CU.CM.
CO = 5.380 KM/S (AVG)
K = 1.340 (AVG)
RHO = 2.504 GM/CU.CM. (AVG)
MDC = 4.645 GMS

INNER BUMPER PROPERTIES ...

RHO-A = .072 GM/SQ.CM.
DH = 6.293 CM

S2 = 5.720 CM

SECONDARY DEBRIS CLOUD PROPERTIES (GENERAL) ...

SEC DEB CLD AVG AXL VEL 2.885 KM/S
PRIM DEB CLD AXL ENERGY4088E+05 J
PRIM DEB CLD EXP ENERGY1978E+05 J
SEC DEB CLD AXL ENERGY2812E+05 J
PRIM DEB CLD AXL EN LOST1147E+04 J
PRIM DEB CLD EXP EN LOST5548E+03 J
EN AVAIL SEC DEB CLD EXP3084E+05 J
SEC DEB CLD AVG EXP VEL 3.022 KM/S
ADDL PRESS WALL VEL308 KM/S

SECONDARY DEBRIS CLOUD PROPERTIES (1ST COMP) ...

1/2-ANG = 34.821 DEG
RHO = 2.504 GM/CU.CM.
N = .500
K1 = .972 (> .788)
MDC1 = 4.515 GMS
C#1 = 1.453
C#2 = .965
VMC = 4.192 KM/S
VEXP = 2.916 KM/S

SECONDARY DEBRIS CLOUD PROPERTIES (2ND COMP) ...

1/2-ANG = 34.821 DEG
RHO-A = .072 GM/CU.CM.
MIB = 2.239 GMS
C#1 = .087
C#2 = .058
VMC = .252 KM/S
VEXP = .175 KM/S

PRESSURE WALL PROPERTIES ...

MAT = ALUMINUM
CO = 5.380 KM/S
K = 1.340
RHO = 2.712 GM/CU.CM.
TW = .480 CM
S = 11.430 CM

MODULE AIR PROPERTIES ...

CO = .330 KM/S
K = 1.070
RHO = .122E-02 GM/CU.CM.
CP = .240 CAL/GM/DEG-C
T0 = 24.000 DEG-C
P0 = 1.000 ATM

MODULE DIAMETER ...

HMOD = 400.00 CM

**** PRESSURE WALL RESPONSE AND IMPEDANCE MATCH CALCULATIONS ****

ASSIGNED PRESS WALL IMP VEL VW = 4.192 KM/S
PRESSURE WALL PARTICLE VELOCITY ... UP = 2.096 KM/S
PRESSURE WALL SHOCK WAVE SPEED US = 8.188 KM/S
HUGONIOT IMPACT PRESSURE PH = 46.543 GPA

PARAMETERS REQUIRED FOR CALCULATING PRESSURE WALL MATERIAL RESPONSE AND

RELEASE FROM SHOCKED STATE USING THE MIE-GRUNEISEN E-O-S:

MATL ELASTIC MODULUS	E	=	.7102E+11 N/SQ.M.
MATL POISSON RATIO	NU	=	.350
MATL BULK MODULUS	K	=	.7891E+11 N/SQ.M.
MATL LIN. COEF. OF THERM. EXP. ...	ALFA	=	.2400E-04 /DEG-C
MATL SP HEAT (SOLID)	CPS	=	.235 CAL/GM/DEG-C
MATL SP HEAT (LIQUID)	CPL	=	.255 CAL/GM/DEG-C
MATL HUGON IMP PRESS (PA,MBAR) ...	PH	=	.4654E+11, .465
MATL SP VOL AT REST	V0	=	.369 CU.CM./GM
MATL SP VOL AT IMPACT	V1	=	.274 CU.CM./GM
MATL AMB M-GRUN COEF (CAL,INP) ...	GAM0	=	2.129,2.130
MATL MELT TEMPERATURE	TM	=	660.00 DEG-C
MATL VAPOR TEMPERATURE	TV	=	2450.00 DEG-C
MATL HEAT OF FUSION	HF	=	95.00 CAL/GM
MATL HEAT OF VAPORIZATION	HV	=	2450.00 CAL/GM

RESULTS OF IMPEDANCE MATCH CALCULATIONS ...

INTERFACE (REFL & TRANS) PARTICLE VEL ...	4.19006 KM/S
TRANSMITTED SHOCK WAVE SPEED	4.81337 KM/S
INTERFACE (REFL & TRANS) PRESSURE24605E-01 GPA (242.8 ATM)

RELEASE OF SHOCKED SECONDARY DEBRIS CLOUD MATERIAL ...

SPECIFIC VOL AFTER RELEASE	VF = .414 CU.CM./GM
ENERGY DUE TO DEB CLD IMPACT2379E+07 JOULES/KG
ENERGY RECOVERED BY RELEASE1950E+07 JOULES/KG
WASTE HEAT GENERATED4289E+06 JOULES/KG

RELEASE OF SHOCKED PRESSURE WALL MATERIAL ...

SPECIFIC VOL AFTER RELEASE	VF = .379 CU.CM./GM
ENERGY DUE TO DEB CLD IMPACT2196E+07 JOULES/KG
ENERGY RECOVERED BY RELEASE1847E+07 JOULES/KG
WASTE HEAT GENERATED3496E+06 JOULES/KG
ENERGY REQ, INCIPIENT MELT6492E+06 JOULES/KG
ENERGY AVAILABLE FOR MELT0000E+00 JOULES/KG
EXCESS ENERGY AVAILABLE3496E+06 JOULES/KG
RESIDUAL MATERIAL TEMP	355.374 DEG-C

PERCENT SHKD AND REL PRESS WALL MATERIAL ...

IN SOLID STATE ...	100.00%
IN MOLTEN FORM00%
IN VAPOR FORM00%

***** MODULE INTERNAL EFFECTS CALCULATION *****

CALCULATION OPTION SELECTED ...

COMBINED SHOCK WAVE AND INTERNAL DEB CLD PASSAGE

SECONDARY DEBRIS CLOUD MASS	4.515 GMS
SECONDARY DEBRIS CLOUD VELOCITY	4.192 KM/S
AXIAL ENERGY OF SECONDARY DEBRIS CLOUD3966E+05 JOULES
EXPAN ENERGY OF SECONDARY DEBRIS CLOUD1919E+05 JOULES
TOTAL ENERGY OF SECONDARY DEBRIS CLOUD5885E+05 JOULES
SDC SHOCK HEATING WASTE HEAT4289E+06 JOULES/KG
SDC MASS SUBJECTED TO SHOCK HEATING858 GMS (.19MDC)
ENERGY LOST TO SDC SHOCK HEATING3679E+03 JOULES (.63%)
PWALL SHOCK HEATING WASTE HEAT3496E+06 JOULES/KG
PWALL MASS SUBJECTED TO SHOCK HEATING	9.390 GMS (.19MW)

ENERGY LOST TO PWALL SHOCK HEATING3283E+04 JOULES (5.58%)

***** NOW ANALYZING POINT-OF-INTEREST NO. 1/ 4 *****

ENERGY TRANSFORMED INTO SW MOTION2986E+05 JOULES (50.74%)

MODIFIED INTERFACE VALUES ...

INTERFACE PARTICLE VEL ...	3.08170 KM/S
TRANS SHOCK WAVE SPEED ...	3.62742 KM/S
INTERFACE PRESSURE13638E-01 GPA (134.6 ATM)
TOT TRANS PARTICLE VELOCITY	3.38979 KM/S
TOT TRANS SHOCK WAVE SPEED	3.95708 KM/S
TOT TRANS PRESSURE16365E-01 GPA (161.5 ATM)

INITIAL SHOCK WAVE PASSAGE ...

TOTAL SHOCK WAVE VELOCITY	3.957 KM/S
INTERNAL SHOCK WAVE VELOCITY	3.957 KM/S
INITIAL PRESSURE INCREASE	161.507 ATM
INITIAL TEMPERATURE INCREASE	5789.626 DEG-C

PEAK SHOCK VALUES ...

DIST (CM)	SW VEL (KM/S)	SH DEN (GM/CC)	PR INC (ATM)	T INC (DEG-C)
.67	3.957	.851E-02	161.507	5789.626

POINT-OF-INTEREST COORDINATES ...

X-COORD = 18.00 CM
Y-COORD = 61.00 CM
Z-COORD = .00 CM

M-CONST = .60
R-DIST = 63.60 CM

ATTENUATED SHOCK VALUES ...

SH WAVE VEL =	.347 KM/S
SH DENSITY =	.128E-02 GM/CC
PRESS INCR =	.067 ATM (.981 PSI)
TEMP INCR =	3.931 DEG-C

DEBRIS CLOUD PASSAGE ...

INT DEB CLD LEADING EDGE VELOCITY	3.082 KM/S
DEB CLD INDUCED SHOCK WAVE VELOCITY	3.082 KM/S
INIT PRESS INCR BEH DEB CLD INDUCED SW ...	95.422 ATM
INIT TEMP INCR BEH DEB CLD INDUCED SW	3360.483 DEG-C
PR WALL MASS CONTRIB TO DIFF DEB CLD	2.817 GMS (.30* .19MW1)
DIFFUSE DEBRIS CLOUD MASS	7.332 GMS
DIFF DEB CLD AXIAL CHARACT VELOCITY	2.581 KM/S
DIFFUSE DEB CLD AXIAL KINETIC ENERGY2442E+05 JOULES (41.50%)
DIFF DEB CLD EXPAN CHARACT VELOCITY501 KM/S
DIFFUSE DEB CLD EXPAN KINETIC ENERGY9183E+03 JOULES (1.56%)
DIFFUSE DEB CLD TOTAL KINETIC ENERGY2534E+05 JOULES (43.06%)

INTERNAL DEBRIS CLOUD CHARACTERISTICS ...

UCOM =	2.581 KM/S
UEXP =	.501 KM/S
1/2-ANG =	10.97 DEG
MAX RDC =	11.52 CM
H-DIST =	72.05 CM

INT DEB CLD SHOCK WAVE CHARACTERISTICS ...

M# = 9.34

DEL = 1.53 CM
A = 2256.06 CM
B = 242.98 CM
RPW-MIN = 62.56 CM

PEAK SHOCK VALUES ...

DIST (CM)	SW VEL (KM/S)	SH DEN (GM/CC)	PR INC (ATM)	T INC (DEG-C)
.63	3.082	.737E-02	95.422	3360.483

POINT-OF-INTEREST COORDINATES ...

X-COORD = 18.00 CM
Y-COORD = 61.00 CM
Z-COORD = .00 CM

M-CONST = .60
ETA-DST = 14.43 CM

ATTENUATED SHOCK VALUES ...

SH WAVE VEL = .501 KM/S
SH DENSITY = .179E-02 GM/CC
PRESS INCR = .970 ATM (14.258 PSI)
TEMP INCR = 39.274 DEG-C

CUMULATIVE EFFECT OF SHOCK WAVE AND DEBRIS CLOUD PASSAGE

TOT PRESSURE INCREASE ... 1.04 ATM (15.239 PSI)
TOT TEMPERATURE INCREASE ... 43.20 DEG-C

***** NOW ANALYZING POINT-OF-INTEREST NO. 2/ 4 *****

ENERGY TRANSFORMED INTO SW MOTION2986E+05 JOULES (50.74%)

MODIFIED INTERFACE VALUES ...

INTERFACE PARTICLE VEL ... 3.08170 KM/S
TRANS SHOCK WAVE SPEED ... 3.62742 KM/S
INTERFACE PRESSURE13638E-01 GPA (134.6 ATM)
TOT TRANS PARTICLE VELOCITY 3.38979 KM/S
TOT TRANS SHOCK WAVE SPEED 3.95708 KM/S
TOT TRANS PRESSURE16365E-01 GPA (161.5 ATM)

INITIAL SHOCK WAVE PASSAGE ...

TOTAL SHOCK WAVE VELOCITY 3.957 KM/S
INTERNAL SHOCK WAVE VELOCITY 3.957 KM/S
INITIAL PRESSURE INCREASE 161.507 ATM
INITIAL TEMPERATURE INCREASE 5789.626 DEG-C

PEAK SHOCK VALUES ...

DIST (CM)	SW VEL (KM/S)	SH DEN (GM/CC)	PR INC (ATM)	T INC (DEG-C)
.67	3.957	.851E-02	161.507	5789.626

POINT-OF-INTEREST COORDINATES ...

X-COORD = 119.00 CM
Y-COORD = 61.00 CM
Z-COORD = .00 CM

M-CONST = .60
R-DIST = 133.72 CM

ATTENUATED SHOCK VALUES ...

SH WAVE VEL = .336 KM/S
SH DENSITY = .124E-02 GM/CC

PRESS INCR = .021 ATM (.313 PSI)
TEMP INCR = 1.312 DEG-C

DEBRIS CLOUD PASSAGE ...

INT DEB CLD LEADING EDGE VELOCITY 3.082 KM/S
DEB CLD INDUCED SHOCK WAVE VELOCITY 3.082 KM/S
INIT PRESS INCR BEH DEB CLD INDUCED SW ... 95.422 ATM
INIT TEMP INCR BEH DEB CLD INDUCED SW 3360.483 DEG-C
PR WALL MASS CONTRIB TO DIFF DEB CLD 2.817 GMS (.30* .19MW1)
DIFFUSE DEBRIS CLOUD MASS 7.332 GMS
DIFF DEB CLD AXIAL CHARACT VELOCITY 2.581 KM/S
DIFFUSE DEB CLD AXIAL KINETIC ENERGY2442E+05 JOULES (41.50%)
DIFF DEB CLD EXPAN CHARACT VELOCITY501 KM/S
DIFFUSE DEB CLD EXPAN KINETIC ENERGY9183E+03 JOULES (1.56%)
DIFFUSE DEB CLD TOTAL KINETIC ENERGY2534E+05 JOULES (43.06%)

PEAK SHOCK VALUES ...

DIST (CM)	SW VEL (KM/S)	SH DEN (GM/CC)	PR INC (ATM)	T INC (DEG-C)
1.01	3.082	.737E-02	95.422	3360.483

POINT-OF-INTEREST COORDINATES ...

X-COORD = 119.00 CM
Y-COORD = 61.00 CM
Z-COORD = .00 CM

M-CONST = .60
ETA-DST = 115.43 CM

ATTENUATED SHOCK VALUES ...

SH WAVE VEL = .426 KM/S
SH DENSITY = .154E-02 GM/CC
PRESS INCR = .468 ATM (6.872 PSI)
TEMP INCR = 21.694 DEG-C

CUMULATIVE EFFECT OF SHOCK WAVE AND DEBRIS CLOUD PASSAGE

TOT PRESSURE INCREASE49 ATM (7.185 PSI)
TOT TEMPERATURE INCREASE ... 23.01 DEG-C

***** NOW ANALYZING POINT-OF-INTEREST NO. 3/ 4 *****

ENERGY TRANSFORMED INTO SW MOTION2986E+05 JOULES (50.74%)

MODIFIED INTERFACE VALUES ...

INTERFACE PARTICLE VEL ... 3.08170 KM/S
TRANS SHOCK WAVE SPEED ... 3.62742 KM/S
INTERFACE PRESSURE13638E-01 GPA (134.6 ATM)
TOT TRANS PARTICLE VELOCITY 3.38979 KM/S
TOT TRANS SHOCK WAVE SPEED 3.95708 KM/S
TOT TRANS PRESSURE16365E-01 GPA (161.5 ATM)

INITIAL SHOCK WAVE PASSAGE ...

TOTAL SHOCK WAVE VELOCITY 3.957 KM/S
INTERNAL SHOCK WAVE VELOCITY 3.957 KM/S
INITIAL PRESSURE INCREASE 161.507 ATM
INITIAL TEMPERATURE INCREASE 5789.626 DEG-C

PEAK SHOCK VALUES ...

DIST (CM)	SW VEL (KM/S)	SH DEN (GM/CC)	PR INC (ATM)	T INC (DEG-C)
.67	3.957	.851E-02	161.507	5789.626

POINT-OF-INTEREST COORDINATES ...

X-COORD = 203.00 CM
Y-COORD = 61.00 CM
Z-COORD = .00 CM

M-CONST = .60
R-DIST = 211.97 CM

ATTENUATED SHOCK VALUES ...

SH WAVE VEL = .333 KM/S
SH DENSITY = .123E-02 GM/CC
PRESS INCR = .011 ATM (.166 PSI)
TEMP INCR = .701 DEG-C

DEBRIS CLOUD PASSAGE ...

INT DEB CLD LEADING EDGE VELOCITY 3.082 KM/S
DEB CLD INDUCED SHOCK WAVE VELOCITY 3.082 KM/S
INIT PRESS INCR BEH DEB CLD INDUCED SW ... 95.422 ATM
INIT TEMP INCR BEH DEB CLD INDUCED SW 3360.483 DEG-C
PR WALL MASS CONTRIB TO DIFF DEB CLD 2.817 GMS (.30* .19MW1)
DIFFUSE DEBRIS CLOUD MASS 7.332 GMS
DIFF DEB CLD AXIAL CHARACT VELOCITY 2.581 KM/S
DIFFUSE DEB CLD AXIAL KINETIC ENERGY2442E+05 JOULES (41.50%)
DIFF DEB CLD EXPAN CHARACT VELOCITY501 KM/S
DIFFUSE DEB CLD EXPAN KINETIC ENERGY9183E+03 JOULES (1.56%)
DIFFUSE DEB CLD TOTAL KINETIC ENERGY2534E+05 JOULES (43.06%)

PEAK SHOCK VALUES ...

DIST (CM)	SW VEL (KM/S)	SH DEN (GM/CC)	PR INC (ATM)	T INC (DEG-C)
1.01	3.082	.737E-02	95.422	3360.483

POINT-OF-INTEREST COORDINATES ...

X-COORD = 203.00 CM
Y-COORD = 61.00 CM
Z-COORD = .00 CM

M-CONST = .60
ETA-DST = 199.43 CM

ATTENUATED SHOCK VALUES ...

SH WAVE VEL = .378 KM/S
SH DENSITY = .138E-02 GM/CC
PRESS INCR = .207 ATM (3.043 PSI)
TEMP INCR = 10.941 DEG-C

CUMULATIVE EFFECT OF SHOCK WAVE AND DEBRIS CLOUD PASSAGE

TOT PRESSURE INCREASE22 ATM (3.208 PSI)
TOT TEMPERATURE INCREASE ... 11.64 DEG-C

***** NOW ANALYZING POINT-OF-INTEREST NO. 4/ 4 *****

ENERGY TRANSFORMED INTO SW MOTION2986E+05 JOULES (50.74%)

MODIFIED INTERFACE VALUES ...

INTERFACE PARTICLE VEL ... 3.08170 KM/S
TRANS SHOCK WAVE SPEED ... 3.62742 KM/S
INTERFACE PRESSURE13638E-01 GPA (134.6 ATM)
TOT TRANS PARTICLE VELOCITY 3.38979 KM/S
TOT TRANS SHOCK WAVE SPEED 3.95708 KM/S
TOT TRANS PRESSURE16365E-01 GPA (161.5 ATM)

INITIAL SHOCK WAVE PASSAGE ...

TOTAL SHOCK WAVE VELOCITY	3.957 KM/S
INTERNAL SHOCK WAVE VELOCITY	3.957 KM/S
INITIAL PRESSURE INCREASE	161.507 ATM
INITIAL TEMPERATURE INCREASE	5789.626 DEG-C

PEAK SHOCK VALUES ...

DIST (CM)	SW VEL (KM/S)	SH DEN (GM/CC)	PR INC (ATM)	T INC (DEG-C)
.67	3.957	.851E-02	161.507	5789.626

POINT-OF-INTEREST COORDINATES ...

X-COORD = 203.00 CM
Y-COORD = .00 CM
Z-COORD = .00 CM

M-CONST = .60
R-DIST = 203.00 CM

ATTENUATED SHOCK VALUES ...

SH WAVE VEL = .333 KM/S
SH DENSITY = .123E-02 GM/CC
PRESS INCR = .012 ATM (.176 PSI)
TEMP INCR = .744 DEG-C

DEBRIS CLOUD PASSAGE ...

INT DEB CLD LEADING EDGE VELOCITY	3.082 KM/S
DEB CLD INDUCED SHOCK WAVE VELOCITY	3.082 KM/S
INIT PRESS INCR BEH DEB CLD INDUCED SW ...	95.422 ATM
INIT TEMP INCR BEH DEB CLD INDUCED SW	3360.483 DEG-C
PR WALL MASS CONTRIB TO DIFF DEB CLD	2.817 GMS (.30* .19MW1)
DIFFUSE DEBRIS CLOUD MASS	7.332 GMS
DIFF DEB CLD AXIAL CHARACT VELOCITY	2.581 KM/S
DIFFUSE DEB CLD AXIAL KINETIC ENERGY2442E+05 JOULES (41.50%)
DIFF DEB CLD EXPAN CHARACT VELOCITY501 KM/S
DIFFUSE DEB CLD EXPAN KINETIC ENERGY9183E+03 JOULES (1.56%)
DIFFUSE DEB CLD TOTAL KINETIC ENERGY2534E+05 JOULES (43.06%)

PEAK SHOCK VALUES ...

DIST (CM)	SW VEL (KM/S)	SH DEN (GM/CC)	PR INC (ATM)	T INC (DEG-C)
1.01	3.082	.737E-02	95.422	3360.483

POINT-OF-INTEREST COORDINATES ...

X-COORD = 203.00 CM
Y-COORD = .00 CM
Z-COORD = .00 CM

M-CONST = .60
ETA-DST = 129.43 CM

ATTENUATED SHOCK VALUES ...

SH WAVE VEL = .411 KM/S
SH DENSITY = .150E-02 GM/CC
PRESS INCR = .394 ATM (5.790 PSI)
TEMP INCR = 18.842 DEG-C

CUMULATIVE EFFECT OF SHOCK WAVE AND DEBRIS CLOUD PASSAGE

TOT PRESSURE INCREASE41 ATM (5.966 PSI)
TOT TEMPERATURE INCREASE ... 19.59 DEG-C

REPORT DOCUMENTATION PAGE

Form Approved
OMB No. 0704-0188

Public reporting burden for this collection of information is estimated to average 1 hour per response, including the time for reviewing instructions, searching existing data sources, gathering and maintaining the data needed, and completing and reviewing the collection of information. Send comments regarding this burden estimate or any other aspect of this collection of information, including suggestions for reducing this burden, to Washington Headquarters Services, Directorate for Information Operations and Reports, 1215 Jefferson Davis Highway, Suite 1204, Arlington, Va 22202-4302, and to the Office of Management and Budget, Paperwork Reduction Project (0704-0188), Washington, DC 20503.

1. AGENCY USE ONLY (Leave Blank)		2. REPORT DATE February 1996	3. REPORT TYPE AND DATES COVERED Contractor Report (Final)
4. TITLE AND SUBTITLE Vulnerability of Space Station Freedom Modules: A Study of the Effects of Module Perforation on Crew and Equipment			5. FUNDING NUMBERS NCC8-28
6. AUTHOR(S) J. Serrano, D. Liquornik, and W. P. Schonberg			
7. PERFORMING ORGANIZATION NAME(S) AND ADDRESS(ES) University of Alabama in Huntsville Huntsville, Alabama 35899			8. PERFORMING ORGANIZATION REPORT NUMBERS M-803
9. SPONSORING/MONITORING AGENCY NAME(S) AND ADDRESS(ES) George C. Marshall Space Flight Center Marshall Space Flight Center, Alabama 35812			10. SPONSORING/MONITORING AGENCY REPORT NUMBER NASA CR-4716
11. SUPPLEMENTARY NOTES Technical Monitor: Joel Williamsen, Structures and Dynamics Laboratory, Science and Engineering Directorate			
12a. DISTRIBUTION/AVAILABILITY STATEMENT Unclassified-Unlimited Subject Category 18			12b. DISTRIBUTION CODE
13. ABSTRACT (Maximum 200 words) Orbital debris penetration of manned spacecraft is accompanied by a number of atmospheric effects that can pose a serious hazard to spacecraft and crew survival. These atmospheric effects can include overpressure, light flash, and temperature rise as hot particles formed during the penetration process impinge into the atmosphere of a manned spacecraft. This report presents the results of a combined experimental/analytical study sponsored by the NASA/Marshall Space Flight Center and performed by the University of Alabama in Huntsville (UAH). The experimental effort consisted of a series of light gas gun tests in which orbital debris particle simulants were fired through space station module wall mock-ups into a large test chamber simulating the interior cabin of a spacecraft at 1 atm. The test chamber was instrumented with pressure transducers, light sensors, and temperature gauges to measure the level of blast hazard associated with differing target and impact conditions. The analytical effort consisted of the development of an analytical model for the various internal effects that accompany the perforation of a habitable module by an orbital debris particle. The model characterizes the phenomena comprising the impact event, including the initial impact, the creation and motion of a debris cloud within the module wall, the impact of the debris cloud on the inner wall, the creation and motion of the debris cloud that enters the module interior, and the effects of the debris cloud within the module on module pressure and temperature levels.			
14. SUBJECT TERMS kinetic energy penetration, hypervelocity impact, blast pressure, air blast, light flash, orbital debris, impact modeling			15. NUMBER OF PAGES 220
			16. PRICE CODE A10
17. SECURITY CLASSIFICATION Unclassified	18. SECURITY CLASSIFICATION OF THIS PAGE Unclassified	19. SECURITY CLASSIFICATION OF ABSTRACT Unclassified	20. LIMITATION OF ABSTRACT Unlimited